Influence of casting defects on the fatigue behaviour of an A357-T6 aerospace alloy

Itziar Serrano Munoz

N° d'ordre 2014-ISAL–0117 Année 2014

THÈSE

Influence of casting defects on the fatigue behaviour of an A357-T6 aerospace alloy

Étude de l'influence des défauts de fonderie sur le comportement en fatigue de l'alliage aéronautique A357-T6

Présentée devant

l'Institut National des Sciences Appliquées de Lyon

pour obtenir

le GRADE DE DOCTEUR

École doctorale :

ED Matériaux

par

Itziar SERRANO MUNOZ

Ingénieur

Thèse soutenue le 28 Novembre 2014 devant la Commission d'examen

Jury

Veronique AUBIN	Professeur	Rapporteur
Myriam BROCHU	Maître de Conférences	Rapporteur
Jean-Yves BUFFIERE	Professeur	Directeur de thèse
Yves GAILLARD	Ingénieur	Examinateur
Yves NADOT	Professeur	Examinateur
Catherine VERDU	Professeur	Directeur de thèse

MatéIS - UMR CNRS 5510 - INSA de Lyon
25 avenue Jean Capelle, 69621 Villeurbanne Cedex (FRANCE)

*INSA Direction de la **Recherche** – Écoles Doctorales – Quinquennal 2011-2015*

SIGLE	ECOLE DOCTORALE	NOM ET COORDONNEES DU RESPONSABLE
CHIMIE	**CHIMIE DE LYON** **http://www.edchimie-lyon.fr** Sec :Renée EL MELHEM Bat Blaise Pascal 3e etage Insa : R. GOURDON	M. Jean Marc LANCELIN Université de Lyon – Collège Doctoral Bât ESCPE 43 bd du 11 novembre 1918 69622 VILLEURBANNE Cedex Tél : 04.72.43 13 95 directeur@edchimie-lyon.fr
E.E.A.	**ELECTRONIQUE, ELECTROTECHNIQUE, AUTOMATIQUE** **http://edeea.ec-lyon.fr** Secrétariat : M.C. HAVGOUDOUKIAN eea@ec-lyon.fr	M. Gérard SCORLETTI Ecole Centrale de Lyon 36 avenue Guy de Collongue 69134 ECULLY Tél : 04.72.18 60.97 Fax : 04 78 43 37 17 Gerard.scorletti@ec-lyon.fr
E2M2	**EVOLUTION, ECOSYSTEME, MICROBIOLOGIE, MODELISATION** **http://e2m2.universite-lyon.fr** Insa : H. CHARLES	Mme Gudrun BORNETTE CNRS UMR 5023 LEHNA Université Claude Bernard Lyon 1 Bât Forel 43 bd du 11 novembre 1918 69622 VILLEURBANNE Cédex Tél : 06.07.53.89.13 e2m2@ univ-lyon1.fr
EDISS	**INTERDISCIPLINAIRE SCIENCES-SANTE** **http://www.ediss-lyon.fr** Sec : Insa : M. LAGARDE	Mme Emmanuelle CANET-SOULAS INSERM U1060, CarMeN lab, Univ. Lyon 1 Bâtiment IMBL 11 avenue Jean Capelle INSA de Lyon 696621 Villeurbanne Tél : 04.72.68.49.09 Fax :04 72 68 49 16 Emmanuelle.canet@univ-lyon1.fr
INFOMATHS	**INFORMATIQUE ET MATHEMATIQUES** **http://infomaths.univ-lyon1.fr** Sec :Renée EL MELHEM Bat Blaise Pascal 3e etage infomaths@univ-lyon1.fr	Mme Sylvie CALABRETTO LIRIS – INSA de Lyon Bat Blaise Pascal 7 avenue Jean Capelle 69622 VILLEURBANNE Cedex Tél : 04.72. 43. 80. 46 Fax 04 72 43 16 87 Sylvie.calabretto@insa-lyon.fr
Matériaux	**MATERIAUX DE LYON** **http://ed34.universite-lyon.fr** Secrétariat : M. LABOUNE PM : 71.70 –Fax : 87.12 Bat. Saint Exupéry Ed.materiaux@insa-lyon.fr	M. Jean-Yves BUFFIERE INSA de Lyon MATEIS Bâtiment Saint Exupéry 7 avenue Jean Capelle 69621 VILLEURBANNE Cedex Tél : 04.72.43 83 18 Fax 04 72 43 85 28 Jean-yves.buffiere@insa-lyon.fr
MEGA	**MECANIQUE, ENERGETIQUE, GENIE CIVIL, ACOUSTIQUE** **http://mega.universite-lyon.fr** Secrétariat : M. LABOUNE PM : 71.70 –Fax : 87.12 Bat. Saint Exupéry mega@insa-lyon.fr	M. Philippe BOISSE INSA de Lyon Laboratoire LAMCOS Bâtiment Jacquard 25 bis avenue Jean Capelle 69621 VILLEURBANNE Cedex Tél :04.72 .43.71.70 Fax : 04 72 43 72 37 Philippe.boisse@insa-lyon.fr
ScSo	**ScSo*** **http://recherche.univ-lyon2.fr/scso/** Sec : Viviane POLSINELLI Brigitte DUBOIS Insa : J.Y. TOUSSAINT	M. OBADIA Lionel Université Lyon 2 86 rue Pasteur 69365 LYON Cedex 07 Tél : 04.78.77.23.86 Fax : 04.37.28.04.48 Lionel.Obadia@univ-lyon2.fr

*ScSo : Histoire, Géographie, Aménagement, Urbanisme, Archéologie, Science politique, Sociologie, Anthropologie

Ametsik gabeko bizia, izarrik gabeko gaua.

(Basque proverb)

Acknowledgments

Many people helped me carry out the work presented in this PhD. I feel extraordinarily lucky to have benefited from these individuals expertise, advise and guidance. I will start by thanking my two supervisors (Jean-Yves Buffière and Catherine Verdu) and many colleagues (particularly Joël Lachambre and Sylvain Dancette for their collaboration and Vincent Chomiene, le grand *animateur*) from Mateis laboratory. Special thanks to CTIF (Yves Gaillard and Amaury Chabod) for its expertise, assistance and being able to deliver new cast rods on such a sort notice as thy did. Likewise, gratitude is expressed to ENSMA partners (Yves Nadot and Peng Fei Mu) mainly for their vacuum testing and wise advise. Also, many thanks to all the people that assisted me during the challenging periods of synchrotron experiments. The night shifts would have been just unbearable without a companion (Cristina Revilla, la reine de la soudure) and tons of coffee and sweets.

Un apartado propio merecen mi familia y amigos que desde la distancia se las han arreglado para apoyarme y animarme, siempre con buen humor e incluso con bastante sorna. Llevar a cabo este trabajo hubiese sido mucho menos interesante sin ellos.

Abstract

The excellent castability, relatively low production costs, and high strength to weight ratios make Al-Si-Mg cast alloys an attractive choice for use in cheaper and lighter engineering components, in both automotive and aerospace industries. However, it is well known that High Cycle Fatigue (HCF) lives ($10^5 < N_f < 10^7$ cycles) of cast components are influenced when casting defects (such as pores and oxides) are present at the free surface or subsurface. They act as stress raisers which can considerably reduce the crack incubation period depending on their size, shape and the microstructural features of the surrounding material. Internal casting defects are of special interest to this work. The application of safety coefficients considers that all casting defects present in a component have the same deleterious effect and no attention is paid, for example, to their distance to the free surface. In other words, internal defects (corresponding to the case where the depth of the defect allows crack nucleation and propagation to essentially occur without interaction with the air environment) are considered as damaging to fatigue life as surface defects (those placed at the free surface and in contact with the air environment).

Surface crack monitoring performed on uniaxial fatigue specimens indicates that the presence of a surface microshrinkage exceeding the size of microstructurally small cracks ($\sqrt{A} \approx 500$ μm, controlled by the SDAS) readily nucleates a fatigue cracks producing steady crack propagation and remarkable reduction in the expected fatigue life. A smaller surface defect ($\sqrt{A} \approx 300$ μm) nucleated a crack that did not reduced the expected fatigue life as in this case early stages of propagation are still influenced by the SDAS.

Pure torsional cycling reveals that the morphology of fracture surfaces is highly influenced by the stress level. In general, torsional fatigue behaviour is described by having reduced (with respect to uniaxial testing) and multisite crack nucleation periods. Several dominant cracks can evolve simultaneously and the final failure occurs by the linkage of some of those cracks. Crack propagation is controlled by the crystallography and pores do not appear to be preferential nucleation sites.

S-N curves show that macroscopic specimens containing $\varnothing_{eq} \approx 2$ mm internal artificial defect produce similar fatigue lives to those obtained with a *defect-free* material. Internal crack nucleation was rarely observed during synchrotron tomography experiments; instead the fatal cracks initiated from much smaller surface defects. Tomographic images show that, in the case of internal propagation, crystallographic paths are formed while surface cracks propagate in mode I. The crack growth rate of internal cracks is much smaller than that of cracks propagating from the free surface. Finally, FE simulations of realistic pore morphologies obtained using the 3D images indicate that the K_t parameter can be used as indicator of the severity of the pore.

Keywords: A357-T6 cast aluminium alloy, small fatigue cracks, surface and internal casting defects, uniaxial and torsional cycling, FE simulations, tomographic techniques, EBSD.

Résumé

L'excellente coulabilité, les coûts de production relativement bas, et leurs ratios poids/résistance mécanique élevés des alliages de fonderie Al-Si-Mg une des solutions les plus intéressantes dans le secteur automobile ainsi que l'aérospatiale. Toutefois, il est bien connu que la durée de vie de ces composants moulés à haut nombre de cycles ($10^5 < N_f < 10^7$ cycles) résulte sévèrement réduite lorsque des défauts de fonderie (notamment pores et oxydes) sont débouchants et/ou subsurfaciques. Ces défauts concentrent les contraintes et peuvent considérablement réduire la période d'incubation de fissures de fatigue en fonction de leur taille, forme et des caractéristiques microstructurales du matériau. Les défauts de fonderie dénommés *internes* sont d'un intérêt particulier à ce travail car l'application de coefficients de sécurité ne tient pas compte de leur distance à la surface. C'est-à-dire, les défauts internes (correspondant au cas où l'emplacement du défaut permettrait les fissures d'amorcer et propager essentiellement sans interaction avec l'air ambiance) et les défauts de surface (ceux qui sont placés à la surface et en contact direct avec l'air ambiance) vont également nuire la durée de vie des composants moulés.

Le suivi de fissures surfaciques (effectué en éprouvettes macroscopiques de traction) indique que la présence d'un microdéfaut avec une taille supérieure à celle de petites fissures microstructurelles ($\sqrt{A} = 500$ μm, contrôlée par le SDAS) produit une remarquable réduction de la durée vie. En revanche, la durée de vie n'est pas affectée lorsqu'un défaut plus petit ($\sqrt{A} = 280$ μm) en présent à la surface car l'amorçage et les premiers stades de propagation sont encore influencés par le SDAS.

Les essaies en torsion pure montrent que la morphologie des surfaces de rupture est fortement influencée par le niveau de contrainte. En général, le comportement en torsion correspond à des périodes à l'amorçage relativement réduits (par rapport à la traction). Cet amorçage et multisite et plusieurs fissures peuvent évoluer simultanément, la rupture finale se produisant par liaison de certaines de ces fissures. La propagation de fissures en torsion est contrôlée par la cristallographie et les retassures ne semblent pas être des sites de nucléation préférentiels, contrairement à ce qui a été observé en fatigue uni-axiale.

Les durées de vie obtenues en utilisant des spécimens macroscopiques contenant défauts artificiel internes de $\varnothing_{eq} \approx 2$ mm sont similaires à celles obtenues avec un matériau de référence. L'amorçage de fissures internes a été rarement observé lors d'essais fatigue in situ caracterisés par tomographie synchrotron. Les images tomographiques montrent que, dans le cas de la propagation interne, les fissures ont une propagation cristallographique alors que les fissures surfaciques se propagent sans influence apparente de l'orientation cristalline locale (mode I). La vitesse de propagation des fissures internes est très inférieure à celle des fissures se propageant à partir de la surface. Enfin, les simulations EF obtenues en utilisant les images en 3D indiquent que le paramètre K_t est capable d'indiquer le grade de sévérité d'un pore, mais seulement quand les défauts sont d'une taille similaire.

Mot Clés: alliage d'aluminium moulé A357-T6, fissures de fatigue courtes, défaut de fonderie

surfaciques et internes, essais de fatigue en traction ou en torsion, simulations par éléments finis, techniques de tomographie, EBSD.

Contents

Table des matières

List of Figures

List of Tables

Introduction

The excellent castability, relatively low production costs, and high strength to weight ratios make Al-Si-Mg cast alloys an attractive choice for use in cheaper and lighter engineering components, in both automotive and aerospace industries. However, it is well known that High Cycle Fatigue (HCF) lives ($10^5 < N_f < 10^7$ cycles; where N_f stands for the numbers of cycles to failure) of cast components are severely reduced when casting defects (notably pores and oxides) are present at the free surface or subsurface. Such defects act as stress raisers which can considerably reduce the crack incubation period depending on their size, shape and the microstructural features of the surrounding material.

Restrictive safety coefficients must be imposed in order to ensure the safety of cast structural components which mostly results in an over-sizing of these components (negatively impacting both cost-effectiveness and fuel consumption). With regard to quality controls, Non-Destructive Test (NDT) methods offers relatively unexpensive inspections of cast components. On the one hand, they allow to eliminate those components with critical flaws before subsequent costly manufacturing steps. On the other hand, components with defects that can be demonstrated non-critical can be retained and not scrapped.

Nowadays, the inspection of castings is based on standards (*e.g.,* reference radiographs ASTM-E155-10) that are almost exclusively focused on the size of the defect. No attention is paid to the position of defects within components although it has been shown that surface defects (those intercepting the free surface and in direct contact with the ambient air) produce different fatigue response than internal[1] defects. Another point of interest is the material fatigue behaviour under torsion loads. Not much work have been done on the multiaxial behaviour of cast aluminium allows and it is unknown if the influence of casting defects is the same under torsion loadings than that observed and for uniaxial loadings. It seems clear that a better knowledge of the actual influence of defects is a key issue in order to increase the cost-effectiveness of castings solutions. Moreover, it would allow to expand their use and replace some wrought assembled components whose production results more expensive but safer from an engineering standpoint.

This PhD work is ascribed to the scientific project known as IDEFFAAR (standing for Influence des DEfauts de Fonderie sur la Fatigue des Alliages Aéronautiques by its name in French, *i.e.,* influence of casting defects on fatigue behaviour of aerospace alloys) and was funded by The French National Research Agency (ANR) during 36 months. Six different partners take part in it (CTIF, ENSMA and INSA as academic partners and Fonderie MESSIER, SAFRAN, and AIRBUS as industrial partners). Several points of concern regarding the effect of casting defects' presence in a A357-T6 aluminium alloy have been investigated although the precise role of each partner on the project is not detailed here; the attention is primarily focused on the INSA work.

Apart from this **Introduction**, this manuscript contains three chapters and several appendixes.

[1]Those defects that are placed deep into the bulk material which allows crack nucleation and propagation to essentially occur without interacting with the ambient air

Chapter 1 which introduces the material of study (A357-T6) and the experimental methods is divided into three sections. First, the tomographic techniques required for material characterization and fatigue crack monitoring are presented. The second section describes the manufacturing of the specimens used for the different types of fatigue tests. Special attention is given to the production of fatigue specimen containing internal defect. Finally, the casting process of the studied material, its resulting mechanical properties, and microstructural characteristics are given in a third section.

Chapter 2 is focused on the study of A357-T6 fatigue behaviour when tested under either uniaxial pull-pull (R=0.1) or torsional push-pull (R=-1) loading. The main objective of the tensile crack monitoring is to investigate the effect of the material microstructural parameters upon the fatigue behaviour of small cracks. The fatigue mechanisms controlling crack nucleation and propagation in torsion are also studied at the microstructural level.

A brief literature review on the characteristics of internal failure as well as on the influence of environment on the fatigue behaviour is first introduced in **Chapter 3**. The experiments presented in this chapter intend to study the conditions under which internal defects could be more than or at least as deleterious to fatigue life as surface defects. These internal conditions have been investigated at a macroscopic and microscopic scale. Macroscopic testing was performed using specimens which contained $\varnothing_{\mathrm{eq}} \approx 2$ mm artificial defects, the main objective being to obtain S-N curves as well as to perform systematic fractographic analysis. Synchrotron tomography was used to monitor *in situ* fatigue tests on small specimens in order to study internal crack growth nucleated from either natural or artificial defects. In addition, 3D synchrotron images were used to produce realistic FE simulations for further investigation on the influence of the size and shape of defects on crack nucleation.

Finally, the principal **Conclusions** of this study are presented along with some suggestions for further investigation on the fatigue behaviour of A357-T6 cast aluminium alloy. **Appendixes** give further information on the manufacturing process of synchrotron and torsion fatigue specimens as well as additional results on the fractographic observations of torsion and macroscopic (containing artificial defects) specimens, synchrotron crack monitoring and FE simulations.

Introduction (français)

L'excellente coulabilité, les coûts de production relativement bas, et ratio poids/résistance mécanique élevé des alliages de fonderie Al-Si-Mg en font une des solutions les plus intéressantes dans le secteur automobile ainsi que dans le domaine aérospatial. Toutefois, il est bien connu que la durée de vie de ces composants moulés à grand nombre de cycles ($10^5 < N_f < 10^7$ cycles) est sévèrement réduite lorsque des défauts de fonderie (notamment pores et oxydes) sont débouchants et/ou subsurfaciques sont présents. Ces défauts concentrent les contraintes et peuvent considérablement réduire la période d'amorçage des fissures de fatigue en fonction de leur taille, forme et des caractéristiques microstructurales du matériau.

Des coefficients de sécurité restrictifs doivent être imposés afin de garantir la durée de vie des composants moulés. Ces coefficients conduisent la plupart du temps à un surdimensionnement des pièces de fonderie et à des taux de rejet élevés. Une meilleure connaissance de l'influence réelle des défauts est un facteur clé pour améliorer le rapport coût/performance des solutions moulées et pour favoriser leur utilisation en remplacent de produits forgés, plus chers à produire mais réputés plus sûrs. Une bonne connaissance de l'effet de défauts de fonderie sur les performances en fatigue des composants moulés l'un des objectifs du projet scientifique dans lequel ces travaux de thèse se déroulent.

Plus précisément, ce projet scientifique dénommé IDEFFAAR (Influence des DEfauts de Fonderie sur la Fatigue des Alliages AérRonautiques) était financé par l'Agence Nationale de la Recherche française (ANR). Six partenaires différents y participent (CTIF, l'ENSMA et l'INSA en tant que partenaires académiques et Fonderie Messier, SAFRAN, AIRBUS comme partenaires industriels). Plusieurs aspects de l'influence sur les propriétés en fatigue des défauts de fonderie dans un alliage d'aluminium moulé A357-T6 ont été étudiés dans ce projet, même si le rôle de chaque partenaire n'est pas détaillée dans cette introduction; l'attention est principalement portée sur le travail accompli à l'INSA.

L'application de coefficients de sécurité considère que tous les défauts de fonderie présents dans un composant ont la même nocivité sur la durée de vie en fatigue. Par exemple, aucune distinction n'est faite entre les défauts présents à des distances variables par rapport à la surface. Les résultats expérimentaux portant sur le comportement en fatigue des défauts internes [2] sont assez rares dans la littérature. Ceci est l'une des principales raisons pour lesquelles tous les pores présents au sein d'un composant moulé sont considérés également nocifs. Par conséquent, l'étude de l'amorçage et propagation de fissures internes est parmi les principaux objectifs de ces travaux de thèse.

Outre cette introduction, ce manuscrit contient trois chapitres et plusieurs annexes. Le chapitre 1 qui présente le matériau étudié (A357-T6) ainsi que les méthodes expérimentales est divisé en trois sections. Tout d'abord, les techniques tomographiques nécessaires pour caractériser le matériaux et réaliser le suivi de fissures de fatigue sont présentées. La deuxième partie décrit la fabrication

[2] correspondant au cas où l'emplacement du défaut permettrait les fissures d'amorcer et propager essentiellement sans interaction avec l'air ambiance

des échantillons utilisés pour les différents essais de fatigue. Une attention spéciale est accordée à la production des échantillons de fatigue contenant des défauts internes. Enfin, le procédé de fabrication du matériau étudié, les propriétés mécaniques qui en résultent, et les caractéristiques microstructurales sont présentés dans la troisième section.

Le chapitre 2 est focalisé sur l'étude du comportement en fatigue de l'alliage A357-T6 lorsqu'il est testé en traction uniaxiale (R = 0,1) ou en torsion pure (R = -1). L'effet de la microstructure sur le comportement en fatigue des fissures courtes est étudié. Les mécanismes de fatigue influençant l'amorçage et propagation de fissures en torsion sont également analysées en relation avec la microstructure.

Une brève revue de la littérature concernant la rupture en fatigue depuis des défauts internes ainsi que l'influence de l'environnement sur le comportement en fatigue est d'abord introduite dans le chapitre 3. Les essais de fatigue présentés dans ce chapitre visent à établir dans quelles conditions les défauts internes peuvent être aussi nocifs (ou pas) que les défauts surfaciques. Ces analyses ont été effectuées à l'échelle macroscopique et microscopique. Les essais macroscopiques ont été réalisés en utilisant des échantillons qui contenaient des défauts artificiels de $\varnothing_{\mathsf{eq}} \approx 2$ mm, l'objectif principal étant d'obtenir des courbes S-N et de systématiquement effectuer des analyses fractographiques. La tomographie de synchrotron a permis la réalisation des essais de fatigue *in situ* avec des échantillons microscopiques, l'objectif étant d'étudier l'amorçage et la croissance de fissures internes à partir de défauts naturels ou artificiels. En outre, les images synchrotron ont été utilisées pour générer des simulations EF servant à étudier l'influence que la taille et la forme des défauts de fonderie ont sur l'amorçage de fissures de fatigue.

Les principales conclusions et perspectives d'amélioration du comportement en fatigue de l'alliage d'aluminium A357-T6 sont présentées à la fin de cette étude. Les annexes qui figurent à la fin du rapport donnent des précisons sur l'usinage et la préparation des éprouvettes synchrotron ainsi que celles utilisées pendant les essaie de torsion pure, de même que quelque résultats complémentaires obtenus pendant les observations fractographiques, le suivi des fissures par tomographie synchrotron et la réalisation de simulations EF.

Chapter 1

Experimental Methods and Material

This chapter introduces the material of study (A357-T6) and the experimental methods, and is divided into three sections. First, the tomographic techniques required for material characterization and fatigue crack monitoring are presented. The second section describes the manufacturing of the specimens used for the different types of fatigue tests. Special attention is given to the production of fatigue specimen containing internal defect. Finally, the casting workflow, mechanical properties, and microstructural parameters are given in a third section.

Contents

1.1 Tomographic techniques

Tomography is defined as the quantitative description of a slice of matter contained within an object. Among the different non-invasive methods which allow the imaging of the interior of optically opaque objects, X ray transmission tomography is wildly used in both the medical and industrial fields. Bartholomew and Casagrande produced in 1957 the very first images [BAR 57]. In 1973 Hounsfield obtained the first medical image [HOU 73]. It was not till 1980's that the first industrial images started to appear thanks to the increase of computer capacities (fast CPUs and large RAM capacity) that are required to process the huge amount of data generated with this kind of imaging method. Computed tomography (CT) provides a map of the variation of X ray absorption within

an object offering a wide range of industrial applications as Non-Destructive Testing (NDT) of manufactured components. For example, *Process tomography* is employed to control continuous manufacturing processes. The geometrical inspection of manufactured components as feedback to assist their design is known as *Reverse engineering*. Detection of internal defects or a local characterization of materials (e.g. density measurements) are other examples of these very diverse applications [BUF 14].

High resolution X ray CT, also termed as μ-CT or microtomography, reconstructs samples' interior with the spatial and contrast resolution required for many problems of interest in material science. For example, microtomography offers the possibility to accurately determine the size of internal defects in structural materials. Other more classical surface techniques such as SEM or TEM allow the characterisation of a wide variety of microstructural features at higher spatial resolutions than those available in microtomography. But the surface observations are not always representative of the internal microstructure present in the interior of materials. An illustration of this is given in the work of Buffièere *et al.* [BUF 99]: the initiation and development of damage inside a 6061 Al alloy reinforced with SiC particles were monitored using high resolution synchrotron X ray tomography during *in situ* mechanical tests. Qualitatively, the same damage mechanisms were observed at the surface and in the bulk of the sample; the rupture of SiC particles is the dominant mechanism for the early stages of plastic deformation. However, when the samples are analysed quantitatively it is found that the geometrical characteristics of surface SiC particles differ from those of bulk particles and that the damage growth rate is larger inside the sample.

In addition, the association of μ-CT and *in situ* experiments provides unique data that can be used to prove the validity of existing mechanical models or even allow the development of new ones. This is nowadays favoured by the development of 3D imaging softwares such as Avizo® [AVI 13] that directly transform 3D images into surfaces and 3D meshes. These meshes can then be incorporated into finite elements (FE) calculations (run by softwares such as Abaqus® FEA [ABA 13]) or into other numerical models [BUF 08].

The basics of X ray tomography remain the same regardless of the diverse experimental set ups that can be used. The three elements required to perform X ray tomography are: an X ray source, a rotating sample and a detector (generally a CCD) placed behind the sample. The detector records a series of n radiographs (called a scan) corresponding to n angular positions of the sample in the beam. The number of photons $\mathrm{N_i}$ after transmission through the sample may be written as:

$$ln\left(\frac{N_0}{N_i}\right) = \int_{path} \mu(x,z)dx \tag{1.1}$$

with $\mathrm{N_0}$ being the initial number of photons present in the X ray beam and μ the linear attenuation coefficient and where x and y are the spatial coordinates at a fixed y position. Fig. 1.1 shows the level of attenuation obtained in a sample containing an internal hole for three different angular positions.

A reconstruction software treats the n radiographs in order to obtain a three dimensional distribution of the linear X ray attenuation coefficient μ within the sample. The elementary unit of the resulting 3D map is called a voxel[1]. X-rays interact with the sample though various mechanisms [ALS 11], and in the case of working with X rays photons energies below 200 keV, the photoelectric effect dominates. In this domain, the mass attenuation coefficient, $\mu/\rho \approx (\mathrm{Z^4/E^3})$ (with Z being the atomic number, ρ the density and E the photons energy) is sharply dependent on E and Z [BUF 14]. A drawback of X ray transmission tomography is that it cannot distinguish between phases which have close Z values. This is the case, for example, of small eutectic silicon particles

[1] 3D equivalent to the 2D pixel

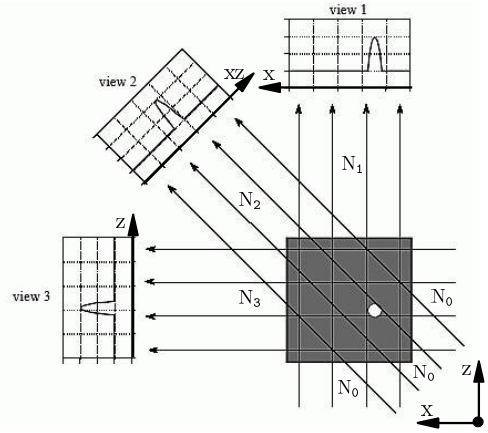

Fig. 1.1: Set of views corresponding to different 3 angular positions of the sample in the beam. The white circle is considered to be a hole embedded in an otherwise homogeneous object. Each profile represents the linear X ray attenuation through the sample for these 3 angular positions. A typical CT scan uses hundreds of views at slightly different angles [SMI 97].

(usually ranging from 1 to 5 μm in size) contained in heat treated Al-Si cast alloys. These particles are undetectable even at high magnifications as aluminium and silicon produce very similar attenuation coefficients.

Algebraic methods and *analytical methods* are the two types of mathematical methods that can be used for the reconstruction of the 3D image. *Analytical methods* are usually faster with the drawback of not being able to deal with missing radiographs. This method reconstructs slices of the sample which are perpendicular to the rotation axis. The stack of reconstructed slices forms the final 3D volume. The viewing and processing of reconstructed 3D images requires appropriate imaging softwares such as ImageJ [SCH 12].

The presence of reconstruction artifacts on tomographic images can introduce erroneous results. These artifacts can come from non-perfect movements of the rotation stage (wobbling[2]) which leads to a degradation in the quality of the reconstructed images. The use of heavy equipments such as *in situ* devices set on the rotation stage tend to increase this phenomenon. The non-linear response of some pixels of the CCD detector can produce *ring artifacts*. The presence of dirt (*e.g.,* dust particles or oil droplets coming from *in situ* devices) on the scintillator[3] surface can create, as well, this kind of ring artifact. Several routines have been proposed to remove *ring artifacts* on either the reconstructed images or the sinograms. However, the use of such routines can alter the contrast between microstructural components of the scanned sample. The severity of *rings artifacts* can be reduced by moving the detector or sample slightly between projections (at the expense of the scan duration).

The artifact called *beam hardening* is specific to laboratory tomography equipment which uses polychromatic X ray sources. The softer X rays of the beam are arrested as they enter the studied specimen. This leads to a shift of the spectrum towards higher energies and the resulting tomographic images seem to be less dense in the centre than in the periphery of the sample. A correction of this artifact while reconstructing images is often available on commercial laboratory tomographs [BUF 14, BUF 10, DAV 06].

1.1.1 Laboratory Tomography

Turnkey μ-CT systems are currently available on the market for routine use in the laboratory. Phoenix X-ray Company is the manufacturer of the laboratory tomograph available at MATEIS.

[2]Non circular movement of the sample during rotation

[3]A scintillator is a thin layer of semi-conductor material which transforms the photons into visible light (see Fig. 1.3)

Fig. 1.2 shows a view of the interior of the hutch where the tomograph main components can be seen. The X ray source is an open transmission nanofocus X ray tube that delivers an X ray cone beam. It can be operated at accelerating voltages ranging from 40 to 160 keV. The source/detector distance is fixed at 60 cm and the voxel size can be adapted by modifying the position of the rotating object placed between the X ray source and the detector. Since the X ray cone bean diverges, a complete rotation of 360° is required to fully capture the sample microstructure. The closest possible position to the source sets the minimum voxel size that can be reached. If small voxel sizes are required, the sample dimensions must be consequently reduced and special care must be taken when mounting the sample on the rotation stage in order to avoid any hitting of the source during rotation.

It must be pointed out that the voxel size is different from the actual *spatial resolution* of the recorded scan. The latter is a complex function that depends on the tomograph set up. As a rule of thumb, however, the spatial resolution is generally close to twice the voxel size. In practice, when using the tomographic setup shown in Fig. 1.2, the minimum spatial resolution obtained is about 1.5 μm with a voxel size of 0.7 μm [BUF 10].

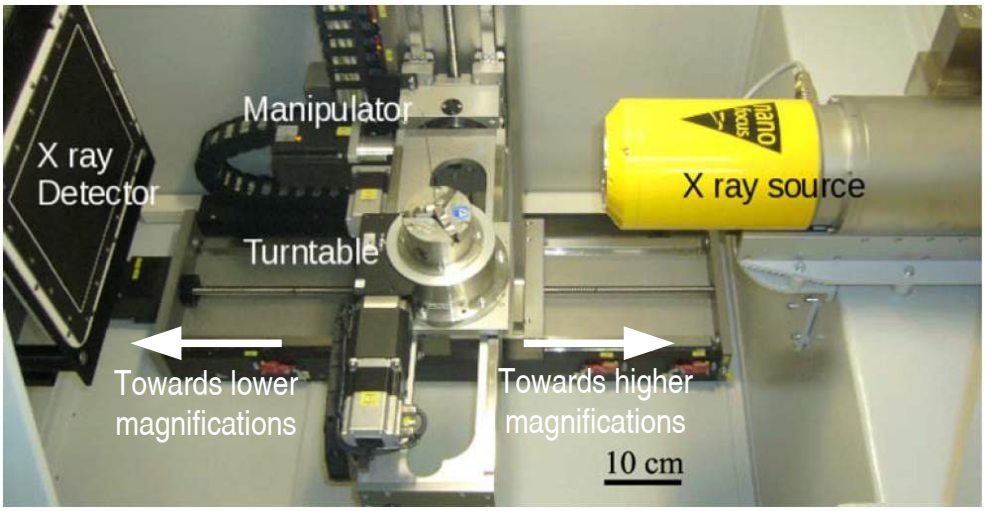

Fig. 1.2: View of MATEIS tomograph interior showing the X ray source, the rotating stage and the detector [BUF 10].

Although Laboratory X ray transmission tomography can deliver voxel sizes of the order of 1 or 2 micrometers, its spatial resolution while working with *in situ* fatigue devices is not high enough to allow a neat imaging of fatigue cracks at their early stages of propagation (small fatigue cracks, *i.e.,* when the cracks opening are very small). As a consequence, in this study, laboratory tomography is mainly used for producing the fatigue specimens (§ 1.2.1) and for characterizing the pore distributions within macroscopic fatigue specimens (§ 1.3.2.4).

1.1.2 Synchrotron Tomography

At synchrotron facilities X ray photons are produced by synchronized magnetic fields which accelerate charged electrons. A third generation synchrotron radiation facility basically consists in: the linear accelerator, the booster and the storage ring. Electrons are produced in the linear accelerator and charged in the booster (*e.g.,* to 6 GeV at the ESRF). Those high energy electrons are then introduced into the storage ring so that they can be accelerated by magnetic fields generated by bending magnets (BM). More electromagnetic radiation can be obtained using insertion devices

(ID) such as wigglers and undulators which can be set in the straight sections between two BMs. Beamlines are located all around the storage ring in order to use the tangential radiation. The high flux of photons delivered to beamlines enables the use of monochromatic X. Another advantage of synchrotron sources is that they produce parallel beams with a large spatial coherence. These features (parallel, coherent and monochromatic) promote the development of various 3D imaging techniques such as phase contrast imaging [WIL 11].

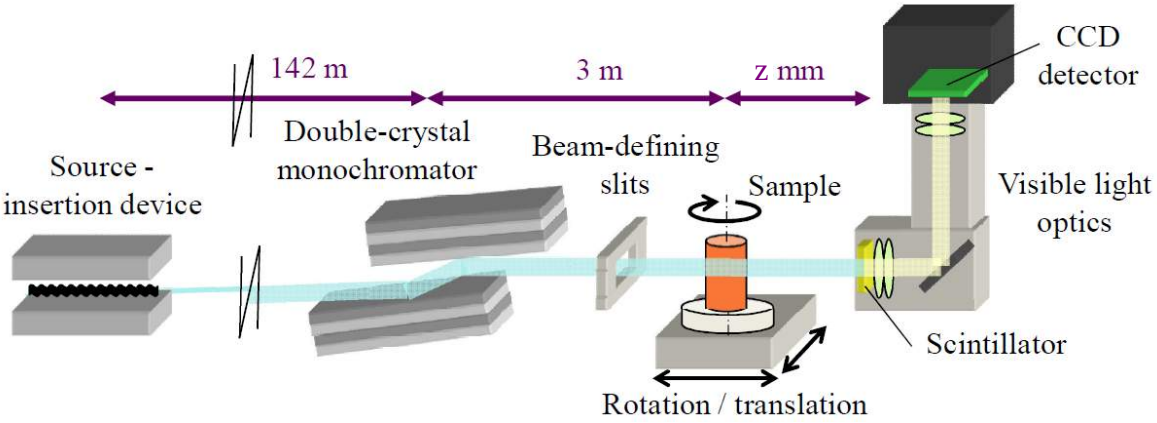

Fig. 1.3: Principal components of the imaging beamline ID19 at the ESRF [ESR 13].

3D imaging experiments with photon energies up to about 30 keV can be performed at various synchrotron facilities (*e.g.,* SLS, Diamond, DESY, SOLEIL, DORIS III). Experiments at higher photon energies can only be performed at a few facilities in the world such as ESRF, APS, SPRing-8 and Petra III. Fig. 1.3 schematically depicts the tomographic set up installed in ID19 beamline at the ESRF[4]. On this beamline, the X ray beam is delivered via one or several insertion devices. Its energy ranges between 8 and 80 keV for high resolution experiments (0.3-2.8 μm), reaching a maximum of 250 keV for observations at average resolution (3.5-50 μm). The detector is a fast read out CCD camera with 2k×2k sensitive elements [ESR 13].

The source/sample distance does not determine the voxel size in synchrotron tomography experiments, as it is the case for laboratory tomography. An exact reconstruction requires a 180° rotation and the sample must remain within the field of view (*fov*). If a N elements detector is used, the voxel size is simply *fov*/N. For example, 1 μm is the minimum voxel size that can be used using a 2 mm sample and a CCD camera with 2000×2000 elements [BUF 10].

1.1.2.1 Phase Contrast Imaging

The interaction of a wave with matter affects both its amplitude and phase. The phase of an X ray beam transmitted by an object is shifted due to the interaction of the incident X ray photons with the electrons in the material. This shift produces interference fringes at the interfaces of heterogeneous materials, and hence contrast. On the contrary to attenuation contrast, the phase contrast method enables the observation of phases with different electron densities which nevertheless produce very similar X ray attenuation values. Moreover, phase contrast imaging deliver images with higher spatial resolutions. For example, for an aluminium sample scanned at 25 keV energy, the minimum diameter of a hole that can be detected by absorption contrast in these conditions is 20 μm. With phase contrast, the minimum detectable hole is reduced to about 0.05 μm [CLO 99].

[4] A pioneering beamline in the field of 3D imaging

Out of the various methods allowing phase sensitive imaging [BUF 14], the propagation technique is the one utilised in this work. It is based on the formation of Fresnel diffraction fringes when the direction of a partially coherent X ray beam is tangential to the interface of the different phases present within a sample. Phase contrast is the consequence of the interference between parts of the wavefront which undergo slightly angular deviations through the crossing of a sample. These angular deviations are associated to different phase gradients; homogeneous variation (such as thickness variations) does not produce any deflection. The overlap of deflected wavefront parts is only possible after a certain propagation distance behind the sample.

The defocusing distance D is function of both the source/sample distance, l, and the sample/detector distance, z: D= (z*l)/(z+l). D and z become practically equal when $l \gg z$ (this is the case of ID19 with $l \geq 145$ m). As shown at Fig. 1.4a, working at $z \approx 0$ means that tomographic images are recorded in the absorption region. A slight increase of z (typically a few centimetres or millimetres depending on the resolution and energy used) leads to a phase contrast effect in the near field region (Fig. 1.4b-c). 3-D reconstruction used for the attenuation contrast can still be used as a first approximation [CLO 97]. As the detector is moved away from the sample (increasing D), the fringes become more pronounced and their number increases. This is the Fraunhofer region, where the width of diffraction fringes becomes so large that 3D images are no longer suitable for a qualitative use. Special methods have to be used for reconstructing the images recorded in this region (holotomography). It must be noted that the Fraunhofer Region is rarely accessible with X rays.

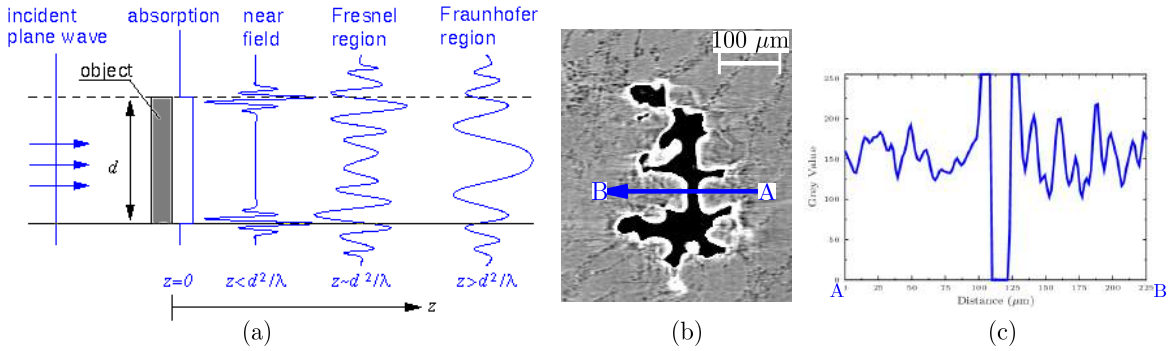

Fig. 1.4: (a) The crossing of a partially coherent X ray beam trough a d dimension object produces four different regions of interference: Absorption Region, Near Field Region, Fresnel Region and Fraunhofer Region[ESR 13]. (b) Synchrotron tomographic image of a porosity embedded in an A357-T6 material. (c) The solid/pore interfaces generate a set of bright (grey value of 255) fringes.

Phase contrast enhances the imaging of weakly attenuating materials (such as polymers), heterogeneous materials where the different phases have close atomic numbers or cracks/defects which opening is smaller than the voxel size (typically, small fatigue cracks). The resulting diffraction fringes of near field region can complicate a quantitative analysis of the crack shape in the latter case [BUF 06]. Consequently, the sample/detector distance has to be carefully chosen knowing that the testing device (§ 1.2.2) used for *in situ* fatigue experiments imposes a distances z larger than 35 mm [BUF 14].

1.2 Fatigue conditions

1.2.1 Synchrotron specimens

As explained in the introduction, one aim of the IDEFFAAR project is to investigate the mechanisms of crack initiation and propagation from casting defects. In the following paragraphs we describe the two methods used to produce millimetre sized fatigue specimens that have been used during synchrotron tomography experiments and which contain a controlled number of internal defects. The first method uses the heat treated material with a random distribution of defects while artificial natural defects are used in the second one.

1.2.1.1 Natural Defects

The machining of synchrotron specimens containing a controlled amount of natural defects comprises several steps illustrated on Fig. 1.5:

1. Slice sectioning of the raw material supplied in the shape of rods (250 mm long, 30 mm diameter; slices: ∼2.5 mm thickness, see Fig. 1.5a).
2. X ray radiographic examination of the central part of the slices which corresponds to an area of ∼10 mm in diameter (pixel size of ∼6 μm, see Fig. 1.5b).
3. Whenever a pore is detected, a sound fatigue specimen (containing no pore) is taped on the slice. It is used as a guide to locate the pore in the gage length during radiographic examinations. This is a sensitive operation which often requires several relocations of the taped specimen used as guide (Fig. 1.5c).
4. Electrical Discharge Machining (EDM) is used to produce the sample from the slice, following the pattern obtained with the guide.
5. Laboratory tomographic scans are recorded in order to screen the machined specimens (voxel size = 4 μm). Only specimens containing internal pores[5] are kept for the following steps (Fig. 1.5d).
6. Final fatigue specimens are obtained by grinding off ∼300 μm of material on all surfaces. This grinding process is necessary to avoid the presence of pitting oxides within the gage induced by EDM (see § 1.3.2.4). The four surfaces of specimen gages are ground up to 2500 grit SiC paper and only occasionally, when surface examinations are required, they are polished with 3 μm oil-based diamond paste and final polished with 0.02 μm colloidal silica. The final section in the specimen gage length obtained after this polishing process is ∼2mm×2mm.

This methodology produces a high number of rule outs: only 25-30 % (98 specimens were machined in total) of machined specimens can be kept, the rest contains pores hitting the free surface. This high rejection rate can be explained by three factors: (a) random location of pores along slice width; (b) lack of accuracy in the marking process and/or (c) deficient machining. Appendix A gives further details on this methodology as well as some examples of the specimens produced for synchrotron experiments.

1.2.1.2 Artificial Defects

Rods containing a nearly spherical (∼1 mm diameter) artificial defect approximately located at the rod centre have been produced by Le Centre Technique des Industries de la Fonderie (CTIF

[5]In this case, the internal pore designation corresponds to a pore located within the specimen gage length, regardless its distance to the specimen free surface.

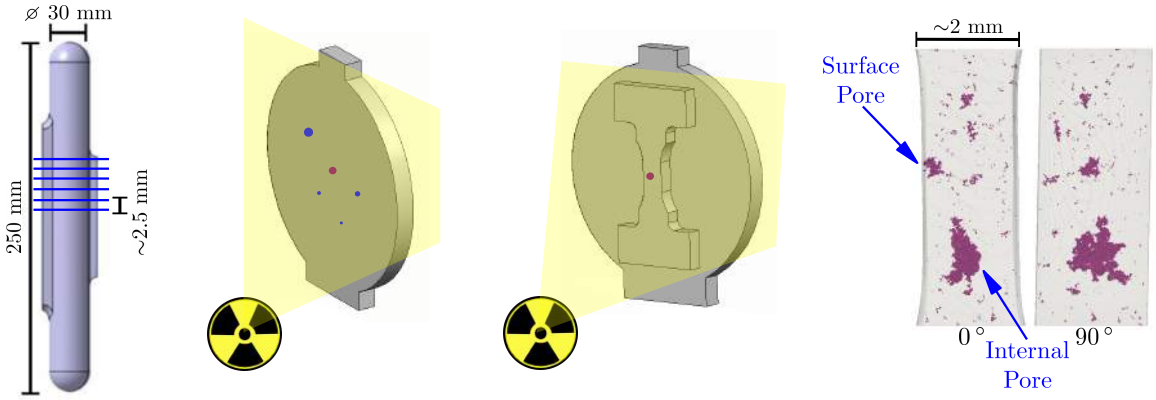

(a) Slicing (b) Detection (c) Marking (d) Screening

Fig. 1.5: Manufacturing process of synchrotron specimens. (a) Sectioning of cast rod into ∼2.5 mm thick slices. (b) Laboratory tomographic inspection in order to detect pore presence. Only pores laying within the central region (10 mm in diameter) are of interest. (c) Marking process. A sound specimens (without any pore that could be detected by radiographic examinations) taped on the slice surface is used as a guide. Once the guide is well in place (this might need several tentative), the specimen profile is drawn on the surface. (d) Sorting out of the specimen using 3D renderings. The example shows a specimen gage containing a *large* internal pore and a *small* surface pore.

[CTI 13]). The production process is confidential and the only point that can be disclosed is that the artificial defect is made out of salt. Tensile tests have shown that the material produced with this method has the same mechanical properties that the material containing only natural defects. From those rods, synchrotron fatigue specimens have been produced following a procedure similar to the one described in the previous §. The final cross section of the sample is however larger (3mm×3mm) because of the size of the artificial defect. The rejection rate for the specimens containing artificial defects is quite low (∼15%) when compared to natural defect specimens. This can be mainly explained by the fact that the location of the defect along the rod length/diameter is no longer random.

1.2.2 Synchrotron *in situ* fatigue testing conditions

Three different experiments of synchrotron *in situ* fatigue testing have been carried out during this work. Two of them took place at the Swiss Light Source (SLS) and the third one at the European Synchrotron Radiation Facility (ESRF). The experiments were conducted using a dedicated fatigue machine at stress ratios of R=0.1 and at frequencies of 10 Hz or 20 Hz, depending on the performance of the rotation stage available at each synchrotron facility. The main features of *in situ* fatigue machine are given in Fig. 1.6. Its most distinctive feature is the PMMA tube employed for the load transmission from the bottom to the top of the machine. This thin tube allows a 180° rotation without hiding the specimen from the beam and gives a constant but negligible attenuation of the X photons. (See Lachambre *et al.* [LAC 12] for a detailed description of the machine).

The testing process (see Fig. 1.7) is divided in two main parts: crack detection and crack propagation. During the first stage, specimens are cycled in intervals of n cycles. The value of n is a function of the stress amplitude used. Specimens are radiographically evaluated at the end of every interval and, occasionally, some scans can be recorded to endorse the radiographic observations. Monitoring of the crack propagation starts once a crack is detected. Usually, the crack is already ∼100 μm long when the first radiographic detection occurs. As the crack grows

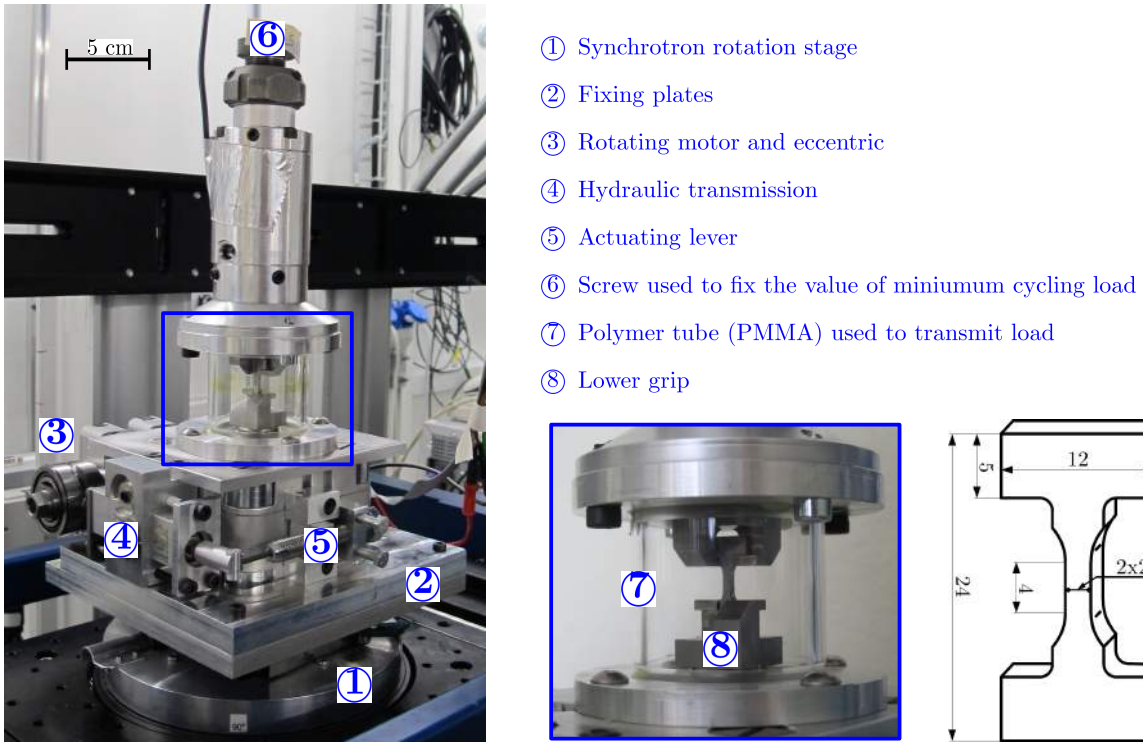

Fig. 1.6: *In situ* fatigue testing. (a) Fatigue machine setup at the SLS [LAC 12]. (b) Zoom of the PMMA tube. (c) Geometry of synchrotron specimens (dimensions in millimetres) containing natural defects.

larger, the number of cycles between the scans becomes smaller.

1.2.3 Macroscopic specimens

1.2.3.1 CTIF and ENSMA fatigue specimens

Fatigue tests on macroscopic specimens took place simultaneously at ENSMA and CTIF. The same model of Vibrophore AMSLER 20 HFP 5100 electromagnetic resonance machine running at a constant frequency of 110 Hz was used at ENSMA [ENS 13] and CTIF. ENSMA was in charge of S-N testing in tension-tension (R=0.1) and compression-tension (R=-1), while CTIF testing established the A357-T6 fatigue limit at 10^7 cycles (staircase method). Additional S-N data at R=0.1 was produced at CTIF. The geometry of the specimens used for those tests is shown in Fig. 1.8.

1.2.3.2 Fatigue specimens for surface crack monitoring at INSA

Specimens with rectangular cross sections were used for crack monitoring of small cracks (surface observations). Their geometry is shown in Fig. 1.9; a large gage volume favours the occurrence of *large* microshrinkage pores, as the aim here is to monitor small crack propagation originated from these microshrinkage pores. After EDM and prior to grinding, fatigue specimens are scanned using laboratory tomography. 3D renderings serve to evaluate the pore population within each specimen gage. A specimen is considered suitable for fatigue testing when its gage contains at least a surface pore outsizing the others. This pore will be monitored throughout fatigue life using microscopical

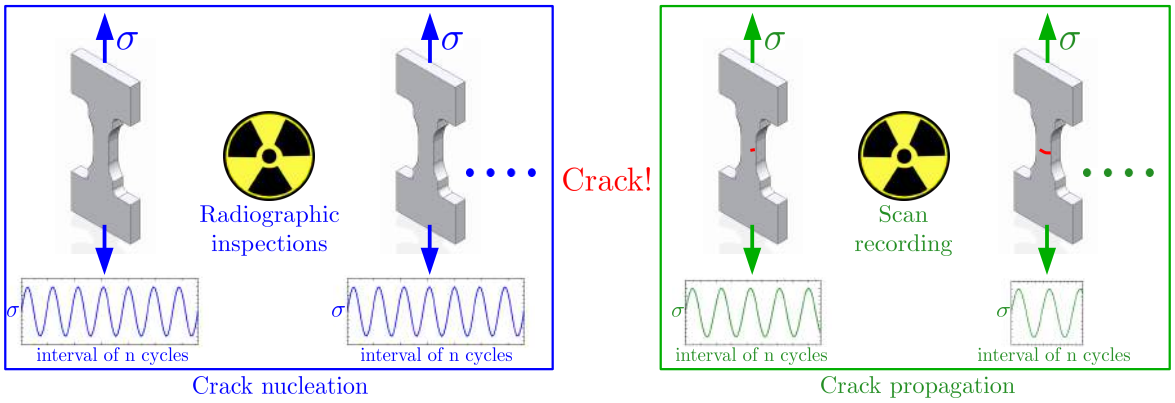

Fig. 1.7: Schematic representation of synchrotron *in situ* fatigue testing.

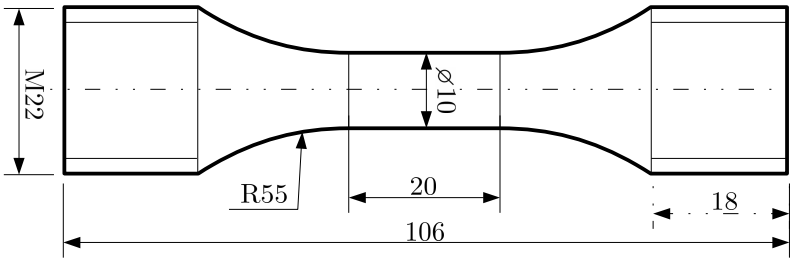

Fig. 1.8: Geometry of CTIF/ENSMA specimens (dimensions in millimetres).

means as it is considered to be the most favourable site for early crack nucleation. Finally, these specimens are tested in a servo-hydraulic Instron 8516 machine under load control using pull-pull (R = 0.1) sinusoidal signals at a frequency of 10 Hz (machine highest possible frequency).

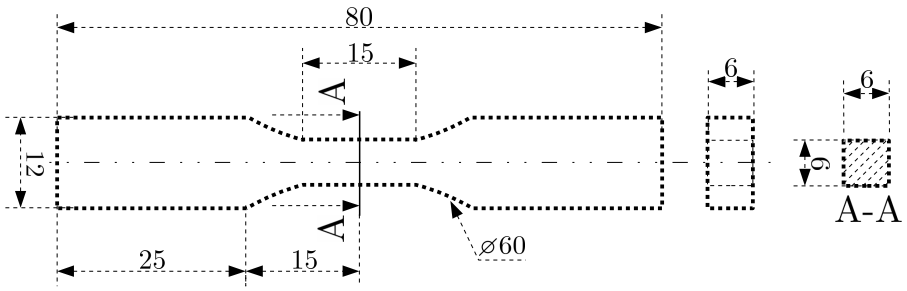

Fig. 1.9: Geometry of fatigue specimens used for 2D surface monitoring of crack initiation and propagation (dimensions in millimetres).

Before the experiments, the specimen surface has to be very carefully prepared. A ∼400 μm surface layer is first ground off in order to eliminate any oxide from EDM. Extra grinding is usually necessary in order to make the tomographically identified pore intersect the free surface of the specimen. Finally, the four surfaces of the gage length are prepared following the EBSD polishing process (§ 1.3.2.3).

1.2.4 Torsion fatigue specimens

Torsion fatigue specimens were machined according to ISO-1352-2011 Standard [ISO 11]. Their geometry is shown in Fig. 1.10. Reversed torsional fatigue tests were carried out using a MTS 809

Axial/Torsional servohydraulic machine at stress ratios of R=-1 and a frequency of 10 Hz.

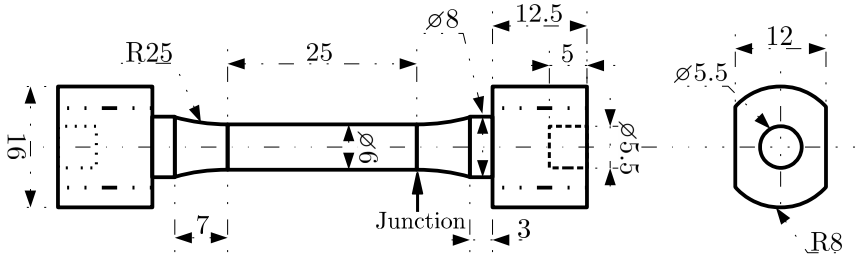

Fig. 1.10: Geometry of torsion specimens (dimensions in millimetres).

A profilometry analysis showed that notches of ∼25 μm were formed at specimen junctions (arrow in Fig. 1.10) as a result of the machining process. FE simulations estimated that this specimen geometry produces 3% of stress concentration at the junctions (see Appendix B). The combination of these two factors induced as-machined specimens to systematically fail at one of the junctions. Very often, cracks were also observed on the other junction. In order to produce defect free specimens, it was decided to grind off a superficial layer of ∼200 μm thick (using a turning machine). After grinding, specimens were polished in the direction parallel to the longitudinal axis up to 4000 grit SiC paper. The final diameter used to obtain the torsion S-N curve (see Fig. 2.39) is therefore ∼5.8 mm. Polished specimens produced failures located within the gage length although sometimes they also failed at one of the junctions. Polished specimens failing at junction were not taken into account when plotting the torsion S-N curve.

The objectives of torsional testing are: (i) as mentioned above, to obtain the torsion S-N curve of A357-T6 material, (ii) to analyse the fatigue mechanisms involved in the nucleation and propagation of fatigue torsion cracks, and (iii) to perform both a tomographic and fractographic study to evaluate the effect of porosity on the fatigue life. For point (ii), *flats* are grounded along one side of the cylindrical gages in order to enable crack monitoring and subsequent examination of the microstructure (see § 2.4.5).

1.2.5 Fractographic examination

Fractographic observations were carried out using a ZEISS SUPRA™ VP55 SEM. Additional X ray energy dispersive spectroscopy (EDS) is used when identifying fatigue crack initiators other than pores. Depending on their distance with respect to the free surface, pores are classified as:

* *Surface* pore when the pore intercepts the free surface (Fig. 1.11a).
* *Subsurface* pore if the pore is located at a distance to the free surface smaller that $\varnothing_{\mathsf{eq}}$[6] (Fig. 1.11b).
* *Internal* pore when the pore is located at a distance d larger than $\varnothing_{\mathsf{eq}}$ (Fig. 1.11c).

1.3 Material of study

1.3.1 Introduction to Al-Si-Mg cast alloys

Al-Si-Mg alloys are known to offer high strength to weight ratio, low production costs as well as good weldability and resistance to corrosion, as described by [POL 05]. They also exhibit a

[6] $\varnothing_{\mathsf{eq}} = \sqrt{\frac{4\times A}{\pi}}$ corresponds to the equivalent diameter of the defect area A measured on the fracture surface.

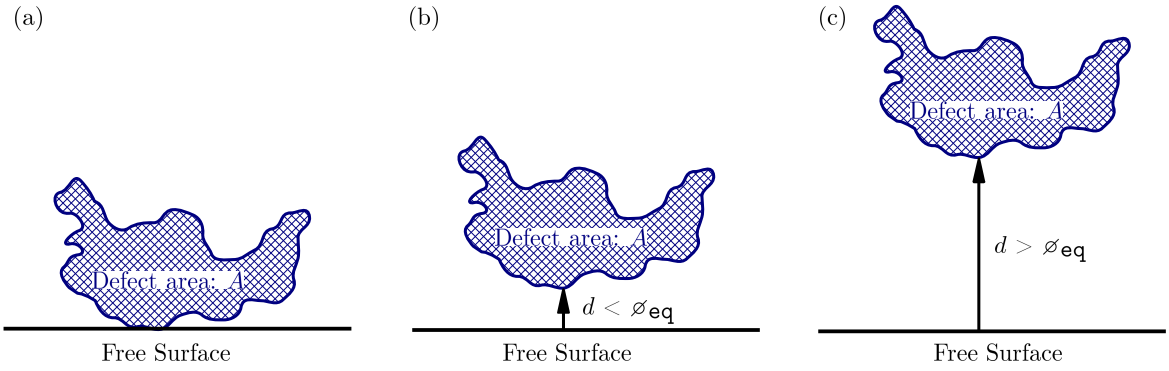

Fig. 1.11: Schematic illustration of (a) *Surface pore*, (b) *Subsurface pore*, and (c) *Internal* pore.

remarkable *fluid life*[7] imparted by the high heat of fusion of silicon (∼1810 kJ/kg compared with ∼395 kJ/kg for aluminium) and the presence of large volumes of Al-Si eutectic phase. Another advantage of the presence of Si phase is that it increases in volume during solidification which leads to reduced volumes of shrinkage. Rapid cooling of the melt, as is the case of permanent mould castings, produces a dendritic microstructure of primary α-Al matrix containing approximately 1% Si in solid solution. For the case of the eutectic phase containing virtually pure silicon particles, the composition has been estimated to be Al-12.6Si. In unmodified alloys, those particles have an interconnected acicular morphology.

Iron is a hard to remove impurity in aluminium. Its content has to be controlled to minimize the formation of large and brittle intermetallic particles which act as stress raisers and lower ductility and fatigue resistance. These particles form because of the very little solubility of iron in solid aluminium, and so Fe tends to combine with other elements present in the melt. In Al-Si-Mg alloys the dominant phases are the Chinese script-like α-Al_8Fe_2Si and π-$Al_8FeMg_3Si_6$ as well as the β-Al_5FeSi with characteristic platelet shape [TAY 12]. Another intermetallic phase that forms within α-Al during solidification is the Mg_2Si phase. As it can be observed in Fig. 1.12, Fe and Mg intermetallic particles are also present in the eutectic region.

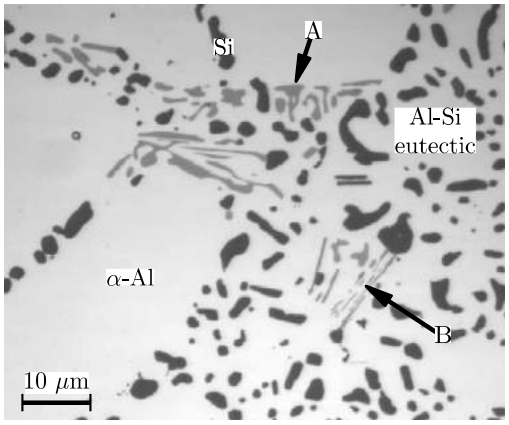

Fig. 1.12: Micrograph of Al-Si-Mg microstructure showing fine *needles* of β phase (arrow B) and Chinese script-like π-phases (arrow A) within the eutectic region. β needles were formed after solution treatment of an Al-7Si-0.4Mg-0.12Fe alloy at 540 °C [TAY 12]

Small additions of magnesium to Al-Si melts increase the yield strength through precipitation hardening mechanisms when the as-cast alloy is heat treated. For the same amount of minuscule Silicon, the value of yield strength of Al-Si-Mg alloys in the T6 condition is twice that of the untreated alloy. Increasing the content of magnesium in A357 increases its tensile properties through

[7]This is the distance the molten alloy can flow in a mould before being too cold to flow further.

age hardening [POL 05]. On the other hand, a higher Mg content promotes the formation of relatively large π-$Al_8FeMg_3Si_6$ intermetallic particles that act as stress concentrators resulting in a reduction of A357-T6 ductility when compared to the A356-T6 alloy. Another disadvantage of forming coarser π intermetallic particles is that it promotes a larger magnesium removal from the α-Al matrix, consequently lowering the expected yield stress of A357-T6 alloys. So, A356-T6 containing ∼0.3 wt% Mg and A357-T6 with ∼0.6 wt% Mg are the most produced members of the Al-7%Si-xMg alloy family.

1.3.1.1 Heat treatment

As mentioned before, as-cast Al-Si-Mg alloys are usually heat treated to obtain a desired combination of strength and ductility. A standard T6 heat treatment involves 3 stages: solution heat treatment, water quenching and artificial ageing.

The solution treatment main objectives are (i) to fragment (by dissolving) and spheroidize eutectic silicon particles, (ii) to partially dissolve Fe and Mg intermetallic particles, and (iii) to homogenize the Mg and Si content through the α-Al matrix. Silicon particles reach their maximum value of roundness[8] ($\alpha = 0.85$) after 5 minutes of heat treatment at a temperature of 540°C in the case of the A356 alloy. In this alloy, heat treatment exceeding 30 minutes only result in an ongoing coarsening of silicon particles [KRU 13]. Out of the four intermetallic phases present in Al-Si-Mg alloys, the platelet-like β-Al_5FeSi phase is the only one that does not undergo dissolution during the solution heat treatment. Moreover, fine needles of β-phase can be formed as the π-phase particles dissolves [YAO 12]. As for the homogenization of Mg and Si content throughout the α-Al matrix, higher solution heat treatment temperatures (*e.g.,* from 500°C to 540°C) can promote the dissolution of higher amounts of Mg_2Si [KRU 13].

The solution heat treatment and quenching stages create a metastable supersaturated solid solution (ssss) suitable for subsequent age-hardening. The precipitation of $\beta(Mg_2Si)$ intermetallic phases in the α-Al matrix is the mechanism responsible of A356/A357 strengthening during artificial ageing.

The β phase precipitation sequence can be described as follows:

$$\alpha_{ssss} \rightarrow GP\ zones \rightarrow \beta'' \rightarrow \beta' \rightarrow \beta \tag{1.2}$$

where GP zones are the Guiner-Preston zones, β'' phase are coherent precipitates, β' phase are semicoherent precipitates and $\beta(Mg_2Si)$ phase are incoherent precipitates. Li *et al.* [LI 06] studied the T6 heat treatment (3h of solution treatment at 550°C, quenching into cold water and 6h of ageing at 175°C) applied to A356 alloy with a nominal composition (wt.%) of 7%Si, 0.47%Mg, 0.01%Cu, 0.12%Fe, 0.09%Ti and balance Al. This work shows that the T6 condition produces shearable needle-shaped β'' precipitates. Even though the mechanical properties are significantly influenced by the presence of β' precipitates and spheroidized silicon particles, the number of cycles to failure of A356 alloys remains essentially unaltered between the as-cast and heat treatment (age hardened) conditions. This is due to the deleterious effect to fatigue properties caused by the presence of casting defects [POL 05].

1.3.1.2 Casting defects

Casting defects (pores and oxides) are inherent to the foundry process and they are of particular interest to this work because the fatigue resistance of casting components is largely influenced by

[8]The roundness is defined as $\alpha = \frac{MinorAxis}{MayorAxis}$. An ideal sphere is equivalent to α=1

their presence, usually resulting in lower fatigue lives when large defects are present at or near the free surface of the specimen. The presence and size of pores can be significantly reduced by faster solidification rates and careful degassing of the melt, while the occurrence of oxide inclusions can be mainly controlled by molten metal filtration before the pouring operation [ASM 09].

• *Oxide type*: Oxide inclusions are categorized as *old* and *young*. Old oxides form early during the melting process, originating from the surface of the melting furnace or transfer ladle. Their chemistry consists of spinel Al_2O_3MgO, and they present higher levels of Mg and O when compared to the spectra taken from the immediately adjacent Al matrix. They also show a number of trace elements like Ti, Fe and S. Other contamination from Ca, K and Cl is likely to originate from fluxes used during the melting or even from the ingot supplier [NAY 01].

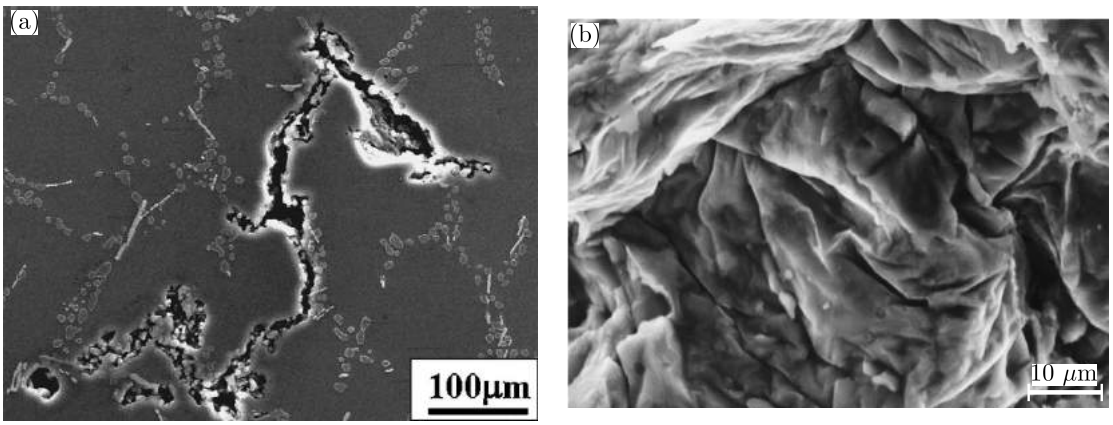

Fig. 1.13: Examples of oxide defects: (a) illustrates the case of an oxide film observed in an A356-T6 alloy casting [YI 06], and (b) Secondary electron micrograph showing an old oxide film defect acting as fatigue crack initiator in a filtered Al-7Si-Mg alloy casting [NAY 01]

Young oxides (also known as oxide films) are folded into the melt during the filling of the mould and their chemistry consists of nearly pure alumina. After the filling and solidification process they end up entangled inside interdendritic regions forming convoluted networks where no bond is developed across the oxide-oxide interface. These films have a variable size, with a thickness that varies between 1 and 10 μm, and are randomly oriented in the cast component. They are a linear discontinuity and an obvious site for crack initiation. The fatigue life of a Al-Si7-Mg cast alloy free from oxides tested in pull-pull sinusoidal loading was found to be larger (one or two orders of magnitude) than when oxides were present [NAY 01]. The surface of the melt is usually covered by an oxide film which is entrained by the turbulence, folding it over to make a double film (or bifilm), as a crack. It was shown by Green [GRE 94] that the mould filling stage plays a major role in influencing the variability of tensile strength of cast Al-7%Si-Mg alloys. If the mould is filled quiescently, the tensile strength is not only higher but also shows lower scatter. On the contrary, a lower average tensile strength with higher variability is observed when the mould filling occurs turbulently.

• *Pore type*: Pores can be divided in two main classes called gas porosity and microshrinkage porosity.

Gas porosity results from the presence of hydrogen in the melt. Because the solubility of hydrogen in Al is an increasing function of temperature, a part of the hydrogen content is rejected during the solidification process forming relatively uniformly distributed gas pores which are mainly trapped in interdendritic regions. Small gas pores formed during relatively high cooling rates tend to have a spherical morphology [MCD 03]. Note that the quantity of porosity increases with hydro-

gen content but is also very dependent on the solidification rate, so larger gas pores can form when the hydrogen content is higher than expected and/or when slow cooling occurs. The growth of these larger pores is geometrically hindered by the solidifying dendrites and this results in convoluted shapes (lower sphericity than for smaller gas pores) [BUF 01].

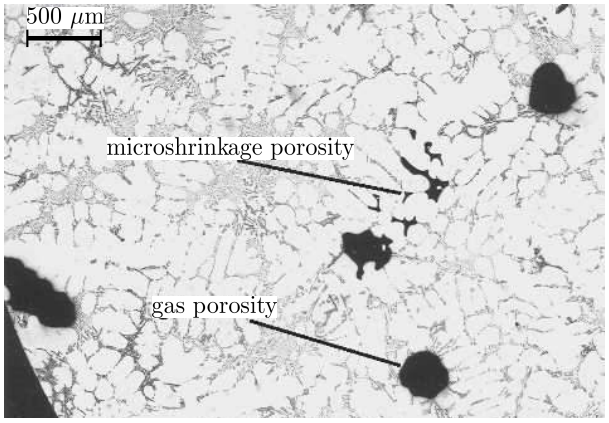

Fig. 1.14: Sr-modified 319 lost-foam casting showing examples of both gas and microshrinkage porosities. The pores labelled as microshrinkage porosity are quite likely connected to a nearby gas pore [WAN 06].

Microshrinkage porosity appears at the final stage of solidification, when the remaining liquid is present between dendrites. They are a consequence of the inability to feed molten metal to reach these interdendritic areas. Microshrinkage pores exhibit a tortuous three dimensional morphology (see Fig. 1.14) and their shape is as important as their size, with elongated pores having a larger detrimental effect than round pores on mechanical properties. Typically, the minimum radius of curvature is of the order of one third to one half the secondary dendrite arm spacing (SDAS, see Fig. 1.16a) for large shrinkages surrounding several dendrite cells [MCD 03]. Since the largest microshrinkage pores in a cast usually form at grain boundaries, grain refinement can influence the size of microshrinkage defects. Pores obtained in a grain-refined A356 alloy are smaller than those formed in an alloy without any grain refiner addition [FAN 89]. Grain refinement also enhances the feeding properties of the melt during solidification [ZOU 89].

The cleanliness of the melt is another parameter influencing shrinkage related defects as their size is increased by at least a factor three when oxide films are present in the melt [MAJ 97]. Campbell [CAM 06] even states that no pore defects seem to occur without the presence of an initiating bifilm.

1.3.2 A357-T6 (Al-7%Si-0.6%Mg) cast aluminium alloy

The A357-T6 alloy used in this work was supplied by CTIF in the form of rods with a diameter of 30 mm and a length of 250 mm. Its processing route is as follow:

1. Primary aluminium ingots are melt in a Nabertherm electric furnace.
2. A rotary lance degasser injecting 5-7 l/min of nitrogen is used during 7 min. for the degassing and cleaning of liquid metal.
3. A commercial Al-5Ti-1B grain refiner is added to reach 0.14 wt% of Ti in the melt.
4. Another degassing is performed before alloying of the melt which is controlled by *Thermatest* samples. The resulting chemical composition of the unmodified alloy is given in Table 1.1.
5. The hydrogen content is monitored *in situ* with an ALSCAN unit, reduced pressure test (RPT) and Ransley sample. The presence of oxides is evaluated by a qualitative fluidity test device (Qualiflash).

6. Prior to mould filling, the permanent mould is preheated to 350°C and the melt temperature in the furnace is held at 730°C. A ladle is used for the extraction and pouring. During this process the melt temperature drops by about 20°C.

Weight%	Si	Mg	Fe	Ti	Cu	Mn	Pb	Ni,Zn,Sn	Al
	6.94	0.56	0.097	0.13	<0.015	<0.03	<0.003	<0.01	Bal.

Table 1.1: Chemical composition of A357-T6, as obtained by Optical Emission Spectroscopy (OES).

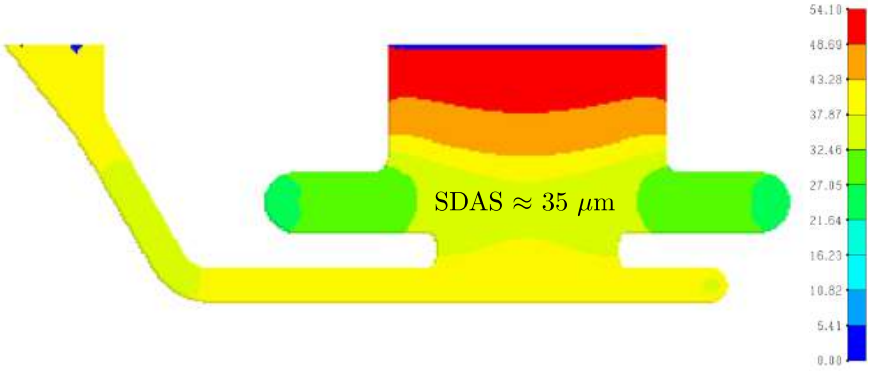

Fig. 1.15: Image of Dans Quikcast® sofware (ESI group) showing the simulation of SDAS values along cast rods. The solidification time (∼28 s) is established to produce a ∼35 μm SDAS size in the centre (light green region).

The solidification time (∼28 s) in the permanent mould was previously established by simulation techniques (using Dans Quikcast® software) in order to produce a SDAS with an average size of ∼35 μm in the centre of the rods (Fig. 1.15).

The T6 heat treatment consists in: (a) solution treatment at 540°C for 10 h in an air circulated furnace; (b) water quenching at room temperature and (c) artificially ageing at 160°C for 8 h.

1.3.2.1 Tensile properties and microhardness

CTIF performed tensile experiments on three specimens (10 mm diameter) following the NF EN ISO 6892-1 [NFE 09] standard. A Zwick BT1 100kN machine with a 25 mm extensometer was used. The Vickers microhardness (100 g) at rod centre has been measured at INSA. The average ultimate tensile strength (σ_{UTS}), yield strength (σ_y), elongation percentage and Vickers microhardness are reported in Table 1.2.

σ_y (0.2%, MPa)	σ_{UTS} (MPa)	Elongation at fracture (%)	Hv (100 g)
275 ± 4	335 ± 3	6 ± 2	116 ± 7

Table 1.2: Average tensile properties and Vickers microhardness (average of 50 values).

Both chemical and mechanical results are in good agreement with the values established in ASM Handbook Vol 2 [COM 10] for an A357-T6 material.

1.3.2.2 Quantitative metallography

Optical examinations were performed in a Zeiss microscope on metallographic samples transversally sliced (∼2 mm) from a cast rod. Sample preparation requires the sectioning of 10 mm square at the central part of every slice. Mirror polishing is achieved after mechanical grinding with 2500 grit SiC paper and polishing with 3 μm diamond suspension. 1 μm polishing is to be avoided as diamond particles usually remains embedded within the soft aluminium matrix. Instead, a 0.02 μm colloidal silica suspension providing chemomechanical polishing is used in the final preparation step.

Measurement of the secondary dendrite arm spacing (SDAS) was carried out following the ARP1947B Standard [ARP 07]. SDAS is obtained by identifying and measuring aligned groups of secondary dendrite cells. The value of the SDAS is then calculated as SDAS = AB/nM, where AB is the length of the line drawn from edge to edge of the measured dendrite. M is the magnification and n the number of dendrite cells crossed by the line (n has to be at least 5 or larger). This measurement method is illustrated in Fig. 1.16a-b.

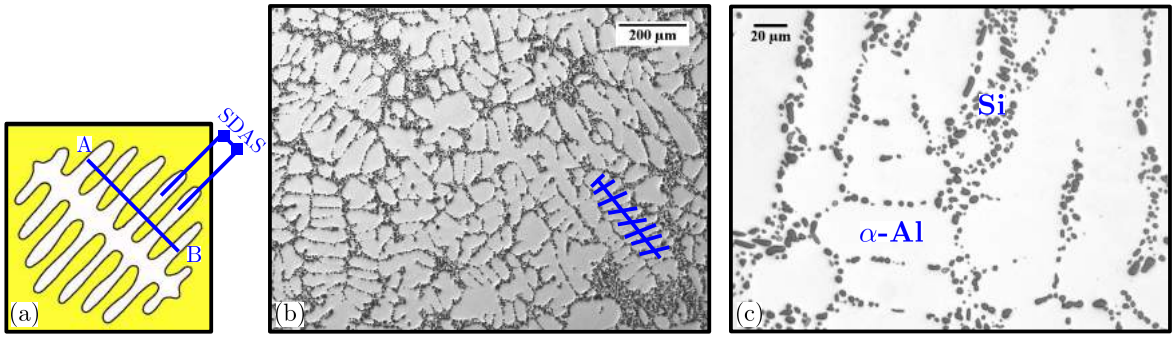

Fig. 1.16: (a) Schematic illustration of SDAS measurement (*e.g.,* SDAS=AB/5). (b) OM images of A357-T6 dendritic microstructure used for SDAS measurements (x4 magnification). (c) OM images used for Si particles quantification (x20 magnification).

The eutectic Si particles (Fig. 1.16c) were quantified (using ImageJ software) in terms of their average surface fraction (f_{Si}), their average aspect ratio[9] (A_R) and their average Feret's diameter[10] size (L_{Si}). All these features along with the average SDAS (155 measurements performed on 57 micrographs) are listed in Table 1.3.

f_{Si} (%)	A_R	L_{Si} (μm)	SDAS (μm)
8.4 ± 0.6	3 ± 4	4 ± 3	38 ± 6

Table 1.3: Microstructural characteristics of A357-T6.

With regard to the intermetallic phases, Fig. 1.17a shows backscatter electron imaging (BEI) along with EDS analysis on a large Chinese script-like π-$Al_8FeMg_3Si_6$ intermetallic while Fig. 1.17b illustrates a case of needle-like β-Al_5FeSi and some π-type intermetallics. Mg_2Si phase cannot be observed when working at this magnification level. Although α-Al_8Fe_2Si particles are not shown is this figure, they could be observed in other metallographic samples that were studied.

[9]The aspect ratio of the particle's fitted ellipse, *i.e.,* $A_R = \frac{MayorAxis}{MinorAxis}$

[10]The longest distance between any two points along particles, representative of the acicular shape of Silicon particles.

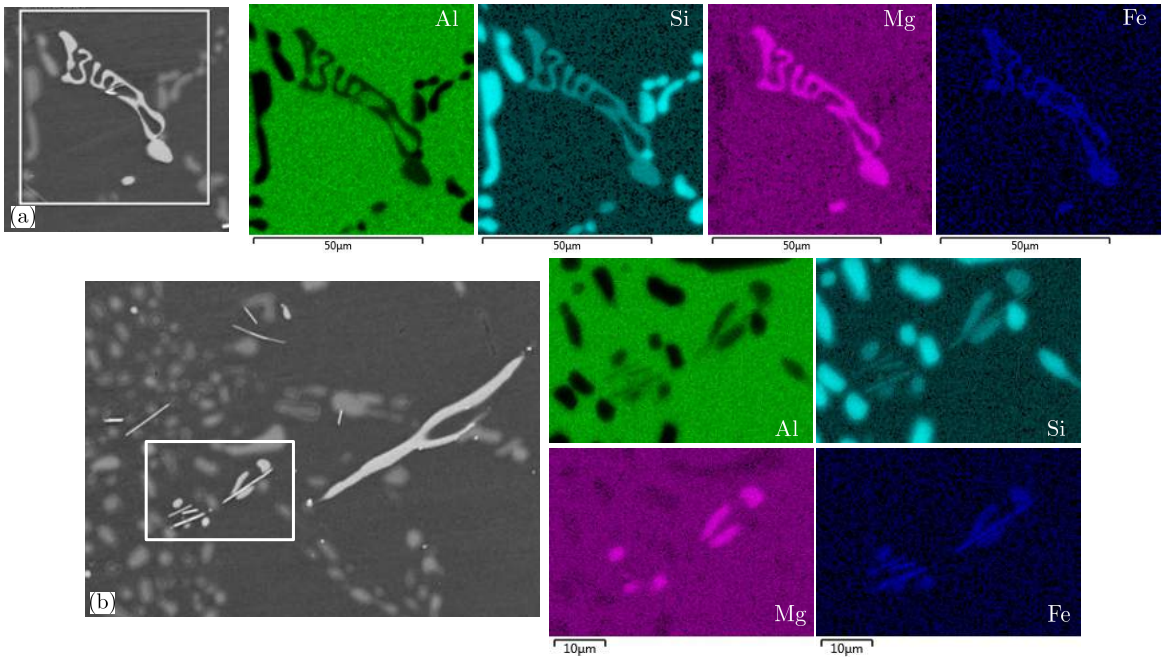

Fig. 1.17: (a) BEI image and EDS analysis on a large Chinese script-like π-$Al_8FeMg_3Si_6$ intermetallic. (b) Needle-like β-Al_5FeSi intermetallic (square insert) close to a large π-type intermetallic shown on the right.

1.3.2.3 Grain size

In this study the average grain size was measured using two different methods. The first one consists in etching for a few seconds a mirror polished sample with ferric chloride ($FeCl_3$). The sample is then visually characterized by comparing the etched surface (Fig. 1.18) to CTIF rating charts for grain sizes. This method was used by technicians at CTIF and gives a grain size in the range of [300-500] μm.

The grain size has also been measured on Electron BackScatter Diffraction (EBSD) images. This technique is based on the acquisition and analysis of Kikuchi diffraction patterns from the surfaces of bulk polycrystals. EBSD allows the measurement of microtexture, microstructure quantification, grain and phase boundary characterization, phase identification and strain determination [SCH 09b]. In addition to this, EBSD also provides a mean to analyse the relationships between fatigue crack paths and local crystallography.

As EBSD diffraction patterns form from the interaction of incident electron with the top few micrometres of the specimen surface, their quality is very sensitive to any deformation present in this layer. Optimum sample preparation is fundamental to obtain an adequate indexing rate. For this reason, smooth sample sectioning and two extra polishing steps are required when preparing samples for an EBSD experiment. The two extra steps are: mechanical polishing with 9 μm diamond suspension for at least 5 minutes and vibratory polishing with 0.02 μm non-crystallizing colloidal silica suspension for no more than 15 minutes. Preparation times must be carefully respected when polishing samples with the colloidal silica suspension. This is due to its etching effect that inevitably damages the surface after long exposure.

The grain size has also been measured on relatively large EBSD maps (Fig. 1.19). The EBSD analyses were carried out on seven samples (always extracted from the central part of slices). Grains parameters were determined using an EBSD system installed in a ZEISS SUPRA™ VP55 SEM equipped with HKL technology Channel 5.0 and AZtecHKL data acquisition, analyses and post-

Fig. 1.18: Grain microstructure was revealed by using a chemical etchant on a mirror polished sample. Comparison between this sample and CTIF rating charts enables determination of the average grain size.

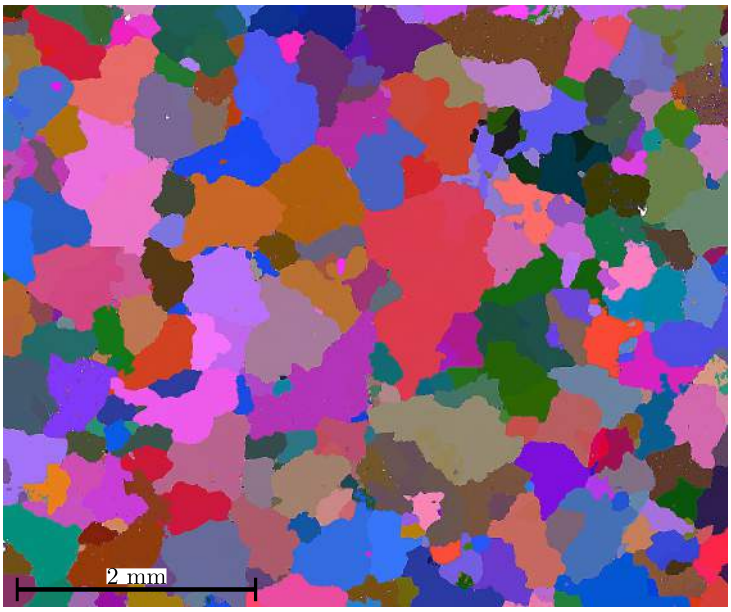

Fig. 1.19: Example of one of the EBSD Euler maps used to calculate the average grain size for the material of study.

processing software package [HKL 01] with fully automatic diffraction pattern indexing capability. EBSD maps were collected with a step size of 5 μm and at 200 magnification. The use of multimapping technique was required in order to produce ∼5mm×5mm maps. The SEM was operated at an accelerating voltage of 20 kV with a working distance of 13 mm. The diffraction patterns were acquired by 4x4 binning and summing 2 frames, with each frame acquired in 48 ms. The grain orientation data were stored as Euler angles (ϕ_1,Φ,ϕ_1), *i.e.,* Bunge's notation.

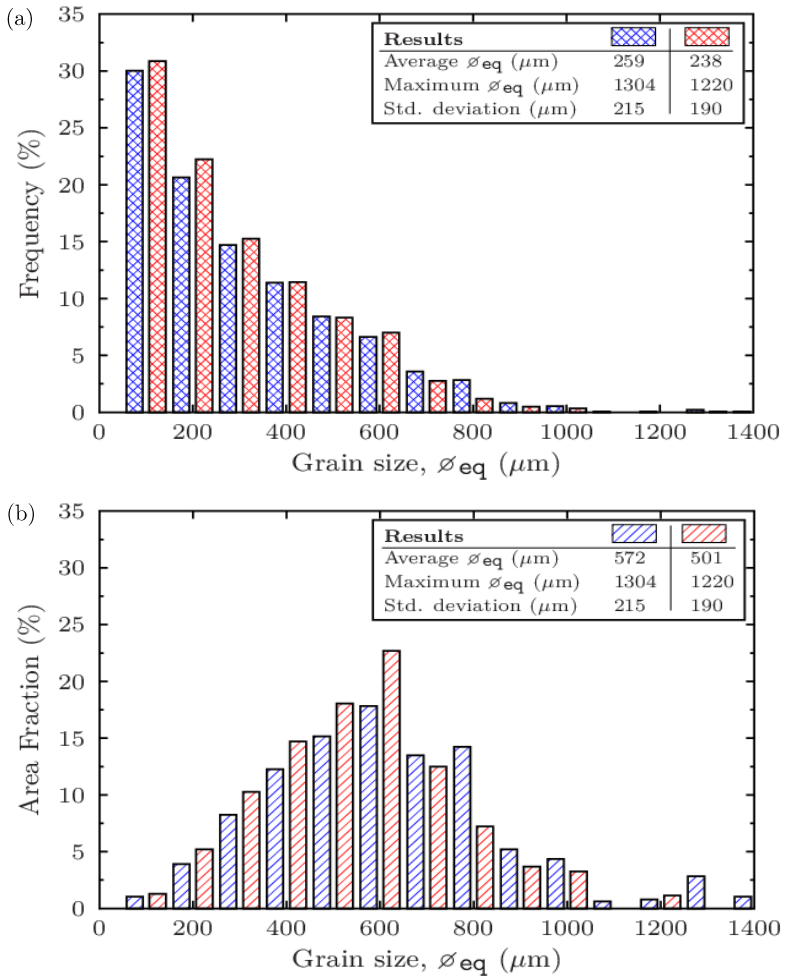

Fig. 1.20: Plots of equivalent grain diameter ($\varnothing_{eq}$) distributions in (a) Frequency of counts and (b) Area fraction. Blue colour indicates that measured grain areas are corrected by multiplying by 2 if a grain touches one map side and by 4 if it touches two map sides. Red colour corresponds to the actual gain area measured without applying any correction.

Grains sizes inferior to 27 pixels are considered as noise and therefore ruled out; neighbouring pixels with misorientations larger than 5° are considered to belong to different grains. The grain size is defined as the diameter $\varnothing_{\mathsf{eq}}$ of a circle having the same area as the measured grain ($\varnothing_{\mathsf{eq}} = \sqrt{\frac{4\times Area}{\pi}}$). The frequency distribution of $\varnothing_{\mathsf{eq}}$ obtained in this work is shown in Fig. 1.20. Two different results are presented here. Blue bars give the frequencies when the border grains are taken into account while red bars present the results without counting the border grains. It is found that these two methods produce similar average grain sizes. The number of counts being close (1449 counts for the blue data against 1416 counts for the red one), it was decided to keep the red values because they only use the actual measured grain size. Thus, an average grain size of

$\varnothing_{eq} = 238 \pm 38$ μm is obtained. Nevertheless, this value underestimates the real average grain size because *small* grains largely outnumber *big* grains on the EBSD Euler maps (see Fig. 1.19). An area fraction analysis enables a more accurate calculation of the average grain size which in this case is 501 ± 38 μm (Fig. 1.20b).

Fig. 1.21 shows an example of *small size* grain clusters ($\varnothing_{eq} \in$ [10-30] μm) that are sometimes observed on EBSD maps. These *small size* grains always appear entrapped between eutectic particle clusters. It is likely that they result from the late solidification occurring in large eutectic regions. In this work, the presence of small grain clusters in the vicinity of microshrinkage pores has never been observed. Nevertheless, the intergranular nature of these cluster indicates that they might also occur around pores. Further EBSD investigation would be required in order to validate this assumption.

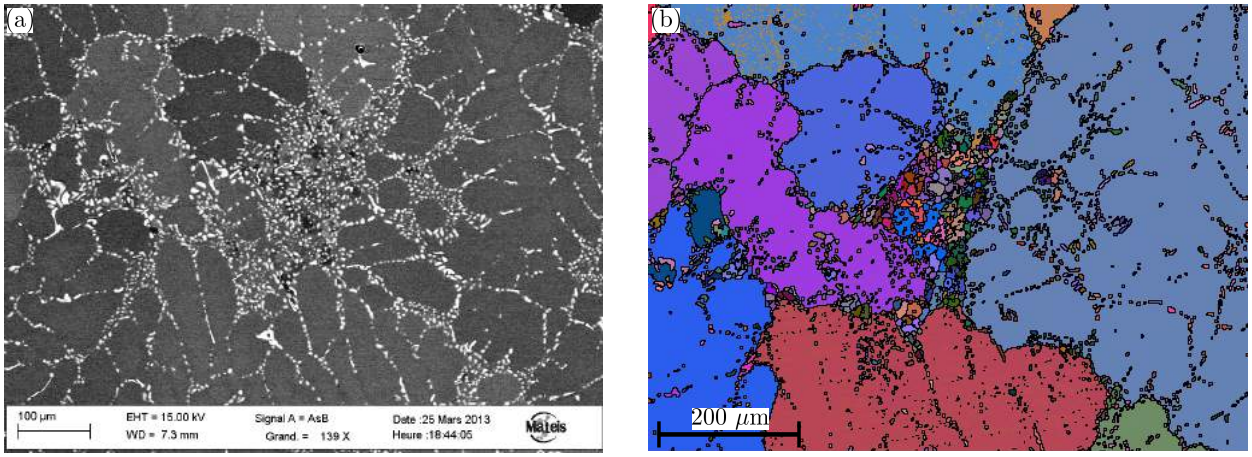

Fig. 1.21: SEM micrograph of the studied alloy showing a cluster of *small size* eutectic grains. (a) BEI image and (b) EBSD Euler map.

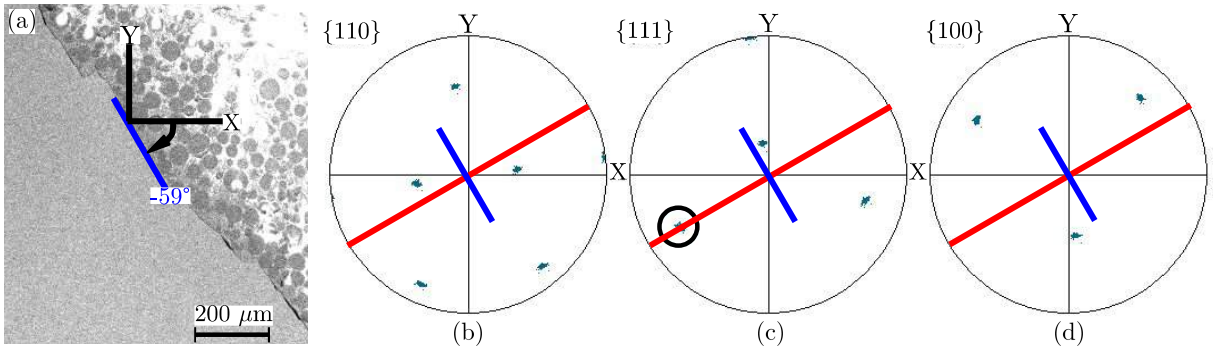

Fig. 1.22: (a) SEM observation on a crystallographic crack showing a trace drawn in parallel to the propagation plane. (b) {110}, (c) {111}, and (d) {100} stereographic projection pole-figures giving local grain orientation relative to the loading direction (Y) where the surface trace of crystallographic crack path (short-line in blue) and the locus of all possible crack plane normals are shown. {111} family is the only one exhibiting a normal interception (black circle). Therefore, it is concluded that crystallographic propagation occurs on {111} planes.

Another advantage of EBSD analysis is that it allows determination of the family of planes on which crystallographic crack propagation occurs. Fig. 1.22 describes the surface trace method used to determine the slip plane family. It must be noted that the literature indicates that crystallographic propagation in Al materials usually occurs on {111} planes.

1.3.2.4 Natural Defect distribution

Prior to the majority of tensile and torsional testing (some fatigue specimens tested at ENSMA were not controlled), dye penetrant inspections (DPI) were carried out at CTIF. Using this method, only fatigue specimens showing non-aligned surface defects smaller than $\varnothing_{\mathsf{eq}} = 500$ μm along the gage length were classified as apt and therefore kept for fatigue testing (Fig 1.23).

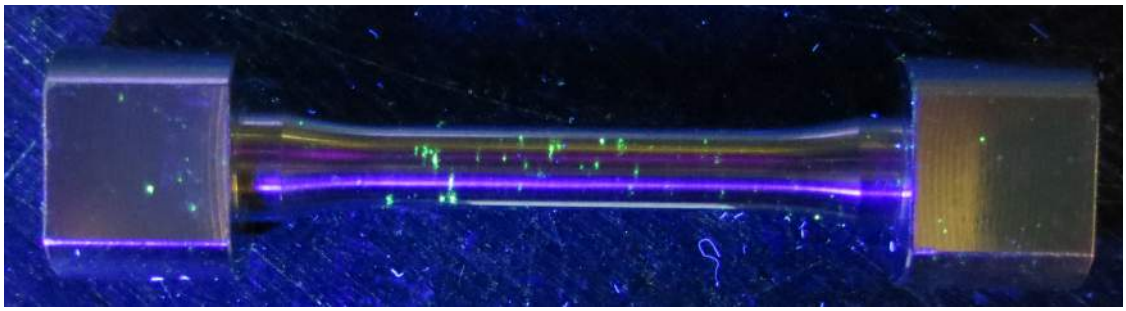

Fig. 1.23: DPI on a torsional fatigue specimen showing some surface defects. This specimen is classified as non-apt.

• *Shrinkage Pores*: Laboratory tomography images of 7 torsion specimens and 6 rectangular fatigue specimens were used to obtain a representative sampling of the pore population (voxel size = 12 μm). The size of each individual pore is defined as the diameter $\varnothing_{\mathsf{eq}}$ of a sphere having the same volume as the measured pore ($\varnothing_{\mathsf{eq}} = (\frac{6 \times Volume}{\pi})^{\frac{1}{3}}$). The size distribution of pores is shown in Fig. 1.24. Pores with sizes larger than $\varnothing_{\mathsf{eq}} = 100$ μm only represents 2-3% of total counts. The average pore volume fraction is 0.002%. Hereafter, this material will be named as the **reference material**.

Reference radiographs for inspection of Aluminium and Magnesium Castings are spelled out in detail in ASTM E155-10 Standard. However, the quantitative use of laboratory tomographic 3D images is not regulated by any standard at the time of writing (2013). Attention must be paid when working with these images as the arbitrary use of image treatments (such as *filters* to get rid of the noise) on raw data and/or the voxel size used can lead to quite different results.

It is assumed that all microshrinkage pores present in the material are intergranular with occasional gas pores occurring intragranularly. Fig. 1.25 shows an example of a microshrinkage pore surrounded by four large grains.

• *Oxides defects*: Some defects have been systematically found at the surface of specimens obtained by EDM. These kind of defects are not observed when the specimens are obtained by mechanical machining (*e.g.,* torsion fatigue specimens). Fig. 1.26 gives an example of such defects. EDS analysis confirmed the defects to be oxides. Literature indicates that the formation of pitting oxides is possible for this kind of material when submitted to aggressive environments. The reason is the nobler electrochemical potential of Si over Al, which causes the latter to be more prone to corrosion. Pitting corrosion is therefore triggered at the interface between Si particles and the surrounding eutectic Al. It was concluded that those defects were created during EDM by interaction with the surrounding environment (tap water).

Laboratory tomographic observations were performed in order to enable 3D characterisation of oxide defects. When the specimens are analysed using laboratory tomography, oxide defects are poorly contrasted (see Fig. 1.27a) and thus they are easily overlooked when inspecting the scans. An optimal 3D characterisation of oxides defects requires synchrotron radiation, as shown in Fig. 1.27.

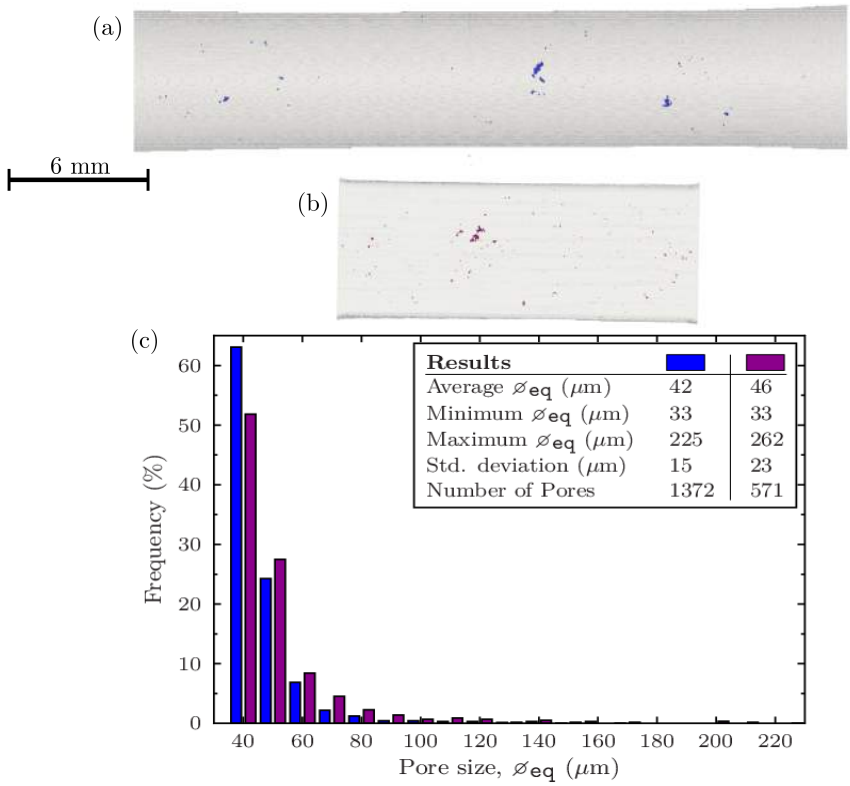

Fig. 1.24: Tomographic analysis of the pore populations within fatigue specimen gages. (a) 3D rendering of the pore distribution within a fatigue torsion specimen gage (b) The same as before but for a fatigue tensile specimen gage (c) Pore Distribution. Torsion specimen pores appear in blue and tensile pores in darkmagenta.

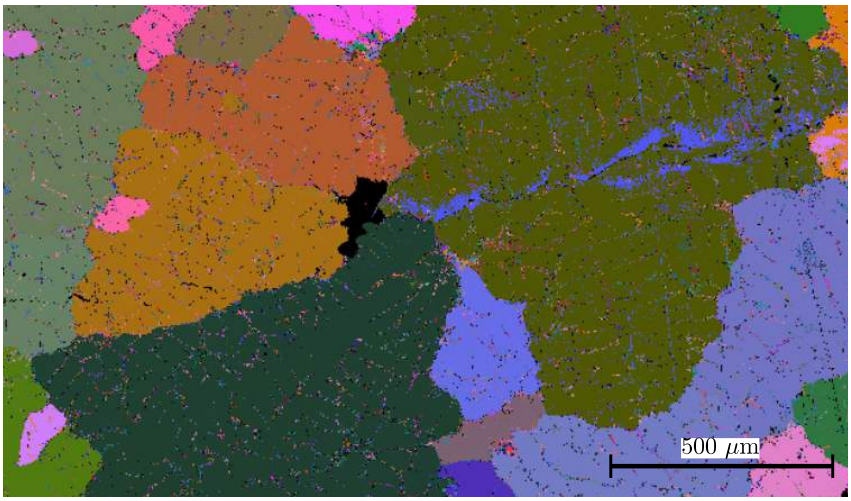

Fig. 1.25: EBSD Euler map showing an intergranular pore (in black) surrounded by four different grains.

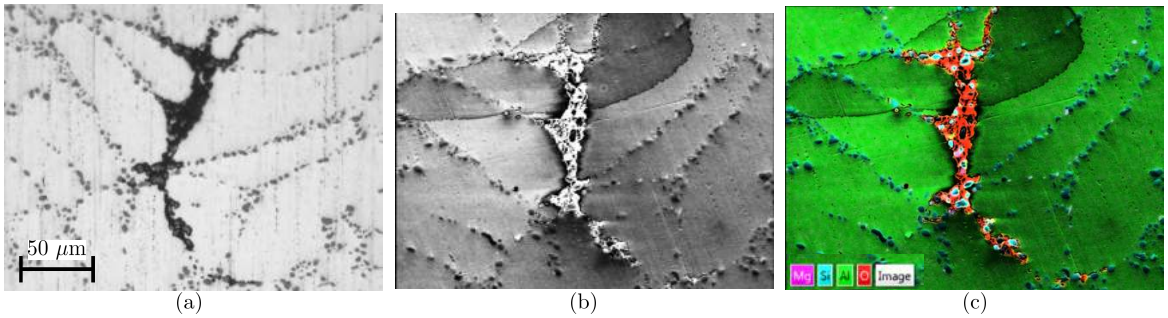

(a) (b) (c)

Fig. 1.26: 2D surface images of a pitting oxide. (a) OM image; (b) SEM image and (c) EDS superposition image showing the presence of Mg, Si, Al, and O.

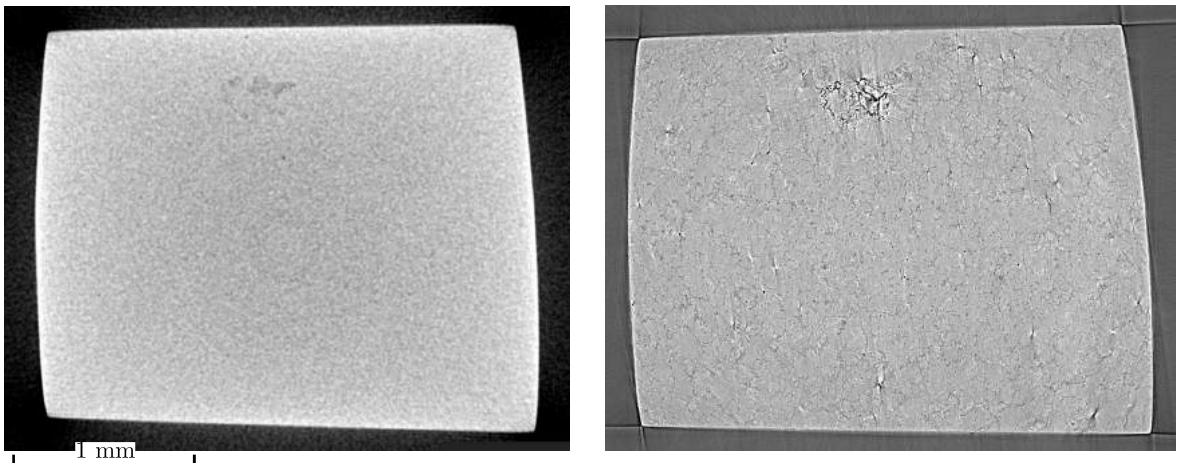

(a) (b)

Fig. 1.27: Tomographic slices of a 2mm×2mm specimen containing an oxide defect. Laboratory tomography did not enable 3D characterisation of this defect. (a) Laboratory tomographic image of the specimen (voxel size = 4 μm) and (b) Synchrotron tomographic image of the previous specimen (voxel size = 1.7 μm). Both slices are taken at the approximate same location.

Fig. 1.28a gives an example of the noxiousness of the EDM process. Seven pitting oxides can be observed at the free surface of a 2mm×2mm fatigue specimen. They are able to reach depths of 250-300 μm (see Fig. 1.28b). Apart from pitting oxides, Fig. 1.28a shows another casting defect (shown in orange, ∼700 μm length, a slice is shown in Fig. 1.28c). By examination of its morphology, this defect was considered to be an oxide film formed during the casting of the melt into the mould.

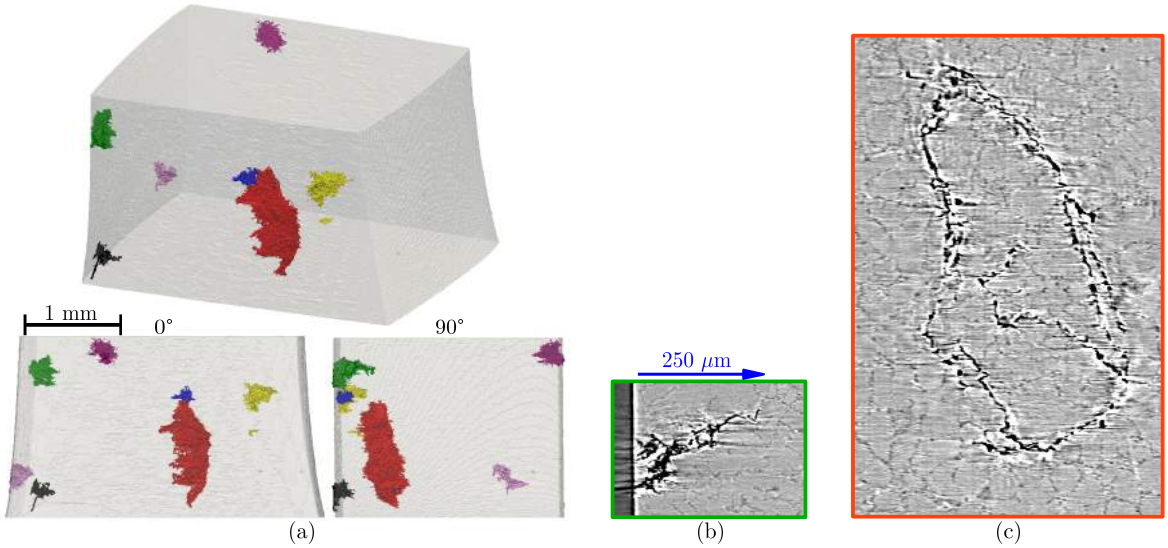

Fig. 1.28: (a) 3D renderings of 2mm×2mm fatigue specimen fabricated by EDM showing all pitting oxides that were formed at the free surface. These images were obtained using synchrotron radiation as these defects can not be clearly identified by laboratory tomography. Orange colour corresponds to an oxide film formed during the casting process. (b) Synchrotron tomographic image of a pitting oxide. (c) Synchrotron tomographic image of an unbounded oxide film.

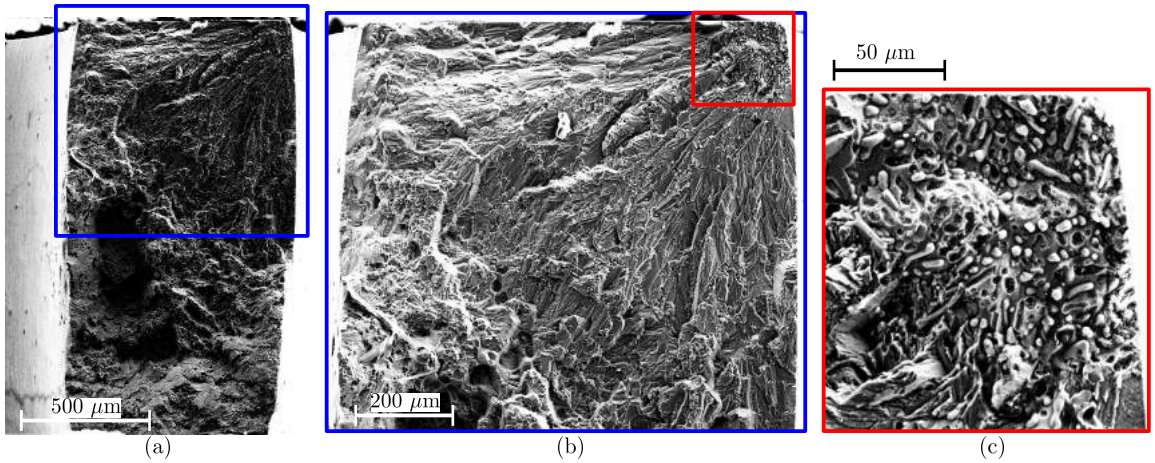

Fig. 1.29: Fracture surface of a small fatigue specimen used for synchrotron tomography which failed after 227 476 cycles (life expectancy ∼700 000 cycles for macroscopic specimens). Crack initiation has occurred on a pitting oxide. (a) General view of the fracture surface, (b) Detail of crack propagation, and (c) Zoom on the oxide nucleating the crack. This oxide was not detected by laboratory tomographic imaging.

When present, pitting oxides can significantly reduce the fatigue life of synchrotron specimens because they are very efficient sites of nucleation for fatigue cracks (see Fig. 1.29). For these

reasons, a superficial layer (∼400 μm thick) was systematically ground off the fatigue samples. This grinding requires a slightly overdimensioning (∼300 μm) of the synchrotron specimens during EDM in order to respect the established 2mm×2mm dimensions.

1.4 Conclusions

Different tomographic techniques have been first introduced in this chapter. They are of major importance to this work because they enable the preparation (laboratory tomography) and monitoring (synchrotron tomography) of 3D small fatigue cracks. The main conclusions of this chapter can be drawn as follows:

1. It has been shown that the preparation of synchrotron specimens containing natural defects has to be carried out very carefully. Nevertheless, it produces a high rejection rate (75-70% of all machined specimens are rejected).
2. Specimens containing $\varnothing_{\mathtt{eq}} \approx 1$ mm artificial defects were produced with a considerably lower rejection rate (∼15%).
3. The microstructure of the A357-T6 material supplied by CTIF (rods of 30 mm diameter and 250 mm length) was characterized using different microscopical techniques which gave an average SDAS of 38 μm and grain size of 501 μm.
4. Microscopical techniques are also used in the study of fracture surfaces (SEM and EDS) and the analysis of the interactions between small fatigue cracks and grain boundaries (EBSD).
5. The EDS technique allowed the identification of the pitting oxides produced during EDM which are very detrimental to fatigue life. It was therefore decided to systematically remove a surface layer of ∼400 μm thick in all EDM specimens prior to fatigue testing.
6. The free surface quality was as well a sensitive issue for the torsion testing where the presence of ∼25 μm notches produced during the mechanical cutting caused as-machined specimens to fail at the junctions.

Différentes techniques de tomographie ont été dècrites premièrement dans ce chapitre. Celles-ci sont d'une grande importance pour ce travail car elles permettent la préparation d'éprouvettes (tomographie de laboratoire) ainsi que le suivi de fissures courtes tridimensionnelles (tomographie de synchrotron). Les principales conclusions de ce chapitre sont résumées de la manière suivante:

1. Il a été montré que la préparation des éprouvettes synchrotron contenant des défauts naturels internes doit être très soigneusement effectuée. Cette méthode produit un taux de rejet élevé (75-70 % de toutes les éprouvettes usinées sont des éprouvettes rejetées).
2. Les échantillons contenant des défauts artificiels internes ($\varnothing_{\mathtt{eq}} \approx 1$ mm) ont été produits avec un taux de rejet beaucoup plus faible (∼15%).
3. La microstructure du matériau A357-T6 fourni par le CTIF a été caractérisée par différentes techniques microscopiques qui ont donné une valeur moyenne de SDAS de 38 μm et une taille de grain moyenne de 500 μm .
4. Des techniques de microscopie sont également utilisées pour l'étude des faciès de rupture (MEB et EDS) et l'analyse des interactions entre les fissures courtes de fatigue et les joints de grains (EBSD).
5. La technique EDS a aussi permis l'identification de piqûres d'oxydes produites au cours de l'usinage par electro-érosion. Ces piqûres réduisent considérablement la durée de vie en

fatigue. Il a donc été décidé de systématiquement supprimer une couche surfacique de ∼400 μm d'épaisseur dans tous les échantillons EDM avant de réaliser des essais de fatigue.

6. L'état de surface était aussi un point clé pour la réalisation d'essais de torsion. La présence de petites entailles de $\sim$ 25 μm de profondeur produites pendant l'usinage mécanique induit une rupture systématique au niveau des congés de raccordement.

Chapter 2

Uniaxial and Torsional Fatigue Behaviour

This chapter is focused on the study of A357-T6 fatigue behaviour when tested under either uniaxial pull-pull (R=0.1) or torsional push-pull (R=-1) loading. The main objective of the tensile crack monitoring is to investigate the effect of the material microstructural parameters upon the fatigue behaviour of small cracks. There is a scarcity of results regarding the fatigue response of this material under multiaxial conditions. Torsional tests intend to elucidate the fatigue mechanisms controlling cracks nucleation and propagation with this less studied type of loading. The influence of defects under torsional loading is briefly addressed. The inclusion of data obtained at CTIF and ENSMA institutions is sometimes required for a better understanding of the results obtained by the author.

Contents

2.1 Background on uniaxial HCF behaviour

2.1.1 Small crack behaviour

There exist situations under high cycle fatigue (HCF) in which cracks exhibit higher growth rates than the extrapolation of linear elastic fracture mechanics (LEFM) solutions would anticipate [MIL 82]. These cracks are named *small cracks*, they normally exhibit a crystallographic propagation and are usually categorized in three different families [CAM 00]:

- *Microstructurally* small cracks correspond to the case where the crack length is of the order of the characteristic microstructural dimension (*e.g.,* the grain size or the interparticle spacing) and so an interaction of the crack front with these microstructural features is expected (see Fig. 2.1a). Easy crack growth can appear when the local microstructure promotes *weak* paths or is favourably oriented. On the other hand, other microstructural features (such as grain boundaries) can act as barriers to crack propagation.
- *Physically* small cracks are those with lengths exceeding at least more than three times the characteristic microstructural dimension (See Fig. 2.1b), in practice, this means that they are long enough to be able to sample the microstructure as a continuum. Nevertheless, the dimensions of these cracks are still insufficient to induce shielding behind the crack tip. This lack of shielding leads to higher propagation rates than LEFM would predict at the same applied K level for the corresponding long crack behaviour .
- *Mechanically* small cracks correspond to the case where the near-tip plasticity is comparable to the crack size itself or where cracks are engulfed within the strain/stress field of a stress concentrating defect (*e.g.,* notch). In this situation the LEFM condition of small scale yielding at the crack-tip is violated (see Fig. 2.1c).

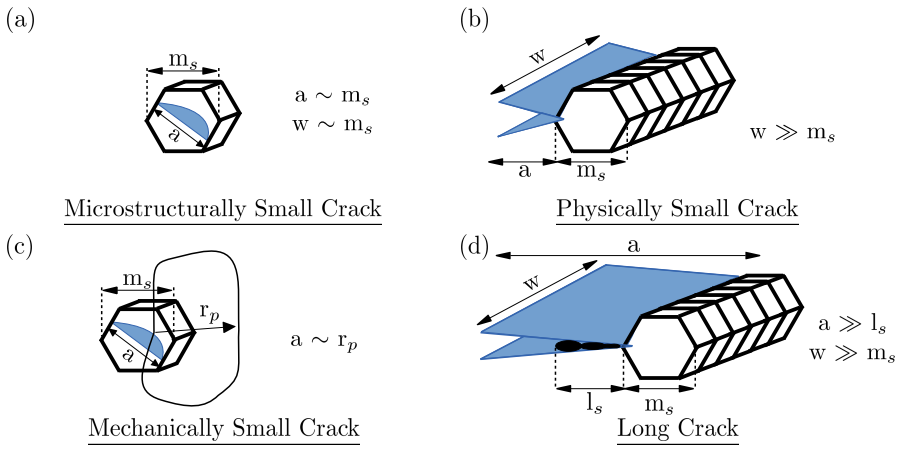

Fig. 2.1: Small fatigue cracks can be categorized based on the relationship between their length (a) and width (w), or the length of the shielding zone (l_s), the characteristic microstructural size (m_s) and the plastic zone radius (r_p). Adapted from [CAM 00].

A small crack contained within a single grain will have to reorientate itself when entering the second grain because none of the slip systems will exactly match the initial crack slip plane. Some plasticity must be induced in the following grain before the crack can enter it [ZHA 92] and two

alternatives are possible to describe the overcoming of grain boundaries: (i) the initial crack induce a local high stress concentration inside the neighbouring grain produce an internal crack which will snap back to meet the first crack, or (ii) the local high stress concentration inside the second grain can cause a new slip band to form in the next grain that will promote the continuing of crack propagation [MIL 93].

Zhai *et al.* [ZHA 00a] proposed a crystallographic model describing the mechanisms which control the passage of small cracks through grain boundaries in Al-Li alloys (Fig. 2.2). In this model, the tilt deflection (β angle) corresponds to the angle that is formed on the free surface between the two crack-planes. The twist deflection (α angle) accounts for the area on the grain-boundary plane that the crack has to fracture before entering the neighbouring grain. This angle is considered to be the parameter which opposes the major resistance to propagation through the boundary. It is therefore expected that the initial crack will preferentially select the slip system within the second grain that would minimise the α angle.

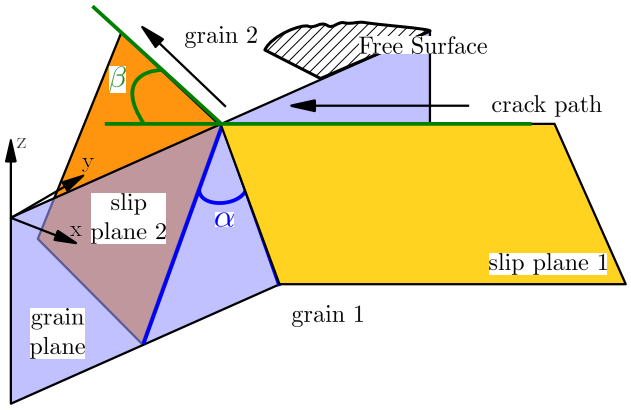

Fig. 2.2: Crystallographic model for stage I crack retardation at a grain boundary proposed by Zhai *et al.* [ZHA 00a] where the twist (α) and tilt (β) angles represent the crack-plane deflection at a grain boundary.

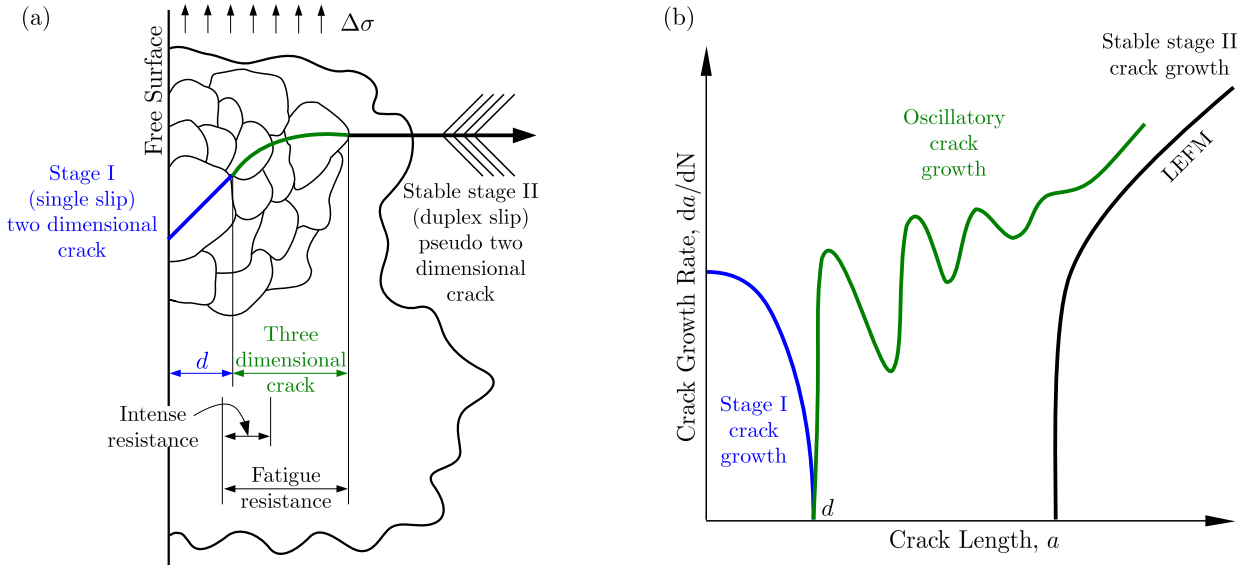

Fig. 2.3: (a) Schematic illustration of the fatigue resistance indicated in terms of difficulty for an initial stage I shear crack to become a stage II, tensile opening mode crack [MIL 93]. (b) Schematic illustration of oscillatory crack growth where d corresponds to the first microstructural barrier (able to arrest the crack) that opposing propagation [MIL 93].

As shown in Fig. 2.3b, a characteristic "oscillatory "crack growth results from the interaction of small cracks with microstructural barriers. This so-called stage I crack growth is typically observed to evolve into stable stage II regime (or long crack regime) for crack lengths of the order of 3-10 grain diameters, depending on the strength of the material, itself a function of grain size and heat treatment. For example, Lankford [LAN 82], who studied the growth of small cracks in a 7075-T6 aluminium alloy, stated that small cracks may become long cracks when their plastic zones begin to exceed in size the maximum grain size dimension.

2.1.2 HCF damage evolution in Al-7%Si alloys

The following two § present some studies which have been carried out on the influence of Al-7%Si alloys microstructure on the propagation of fatigue cracks at different stages of propagation.

2.1.2.1 Small crack propagation

In Al-7%Si alloys, small fatigue cracks predominantly propagates through dendrite cells of α-matrix. The crack avoids Si particles and only follows them if they are in line with the crack plane. In this case, cracks propagate by debonding interface between Al-eutectic matrix and Si particles are left intact. Shiozawa *et al.* [SHI 97] reported that the initiation and propagation of a microcrack up to 1 mm length occupies about 90% of the total fatigue life for a defect-free material (Al-Si-Mg-Cu squeeze-cast alloy) where crack nucleation occurs at Si particles. Evidence of strong da/dN oscillations experienced by small surface cracks when interacting with eutectic areas has been given by several researchers [ZEN 14, KRU 13, JAN 10, GAL 99, PLU 86]. This oscillatory behaviour has been explained through a blockage mechanism that would acts upon the slip bands ahead of the crack tip due to the presence of harder Si particles [PAD 87, FAN 01]. Moreover, the results of Wang *et al.* [WAN 01a] indicate that the number of cycles to failure decreases with increasing SDAS values in both finer (SDAS $<$ 40 μm) and coarser (SDAS $>$ 60 μm) structures (case of a A356-T6 unmodified alloy). The fatigue life seems to remain constant when the material presents intermediate SDAS values (40-60 μm).

Lados *et al.* [LAD 06, LAD 04] studied the fatigue behaviour of a single notched specimens ($\sim$500 μm corner notch within a 10mm$\times$10mm cross section). The sizes of the notches were about 20 times the SDAS size (20-30 μm with an average grain size of 280-320 μm). They stated that the lack of oscillatory behaviour exhibited by cracks nucleated at these notches is most probably due to a microstructurally-to-physically small crack transition occurring at a crack length value a of $\approx$ 5$\times$SDAS to 10$\times$SDAS (*i.e.,* $\sim$125-250 μm, value smaller than the notch size). In a Al-7Si-0.6Mg cast alloy, Jana *et al.* [JAN 10] documented an oscillatory crack growth behaviour which continued up to 450 μm, length corresponding to $\sim$5 times the SDAS value ($\sim$100 μm). In both studies the SDAS is believed to be the microstructural parameter controlling fatigue strength; the possible influence of grain boundaries is considered as a second order parameter.

Evidence of small crack decelerations, or even the occurrence of crack arrest for several thousand of cycles, occurring at both grain boundaries and cluster of Si particles has been observed by Buffière *et al.* [BUF 01]. Using optical microscopy, they were able to monitor the growth rates of a surface small crack initiated at a porosity. The crack path was subsequently analysed by EBSD in order to reveal the underlying grain structure. The highest crack arrest was observed to occur at the first grain boundary during 50 000 cycles. Additional synchrotron radiation X ray microtomography was carried out by Ludwig *et al.* [LUD 03] on the very same sample in order to visualize the intricate 3D shape of the small crack and grains (grains boundaries were imaged using liquid Ga which served as a selective contrast agent). It was showed that the propagation of a crack into the

next grain occurred preferentially from regions on the grain perimeter where the deflection could be accommodated with a tilting of the crack plane (see Fig. 2.4). On the other hand, the crack had difficulties in entering the neighbouring grain from regions where a twisting of the crack plane is required.

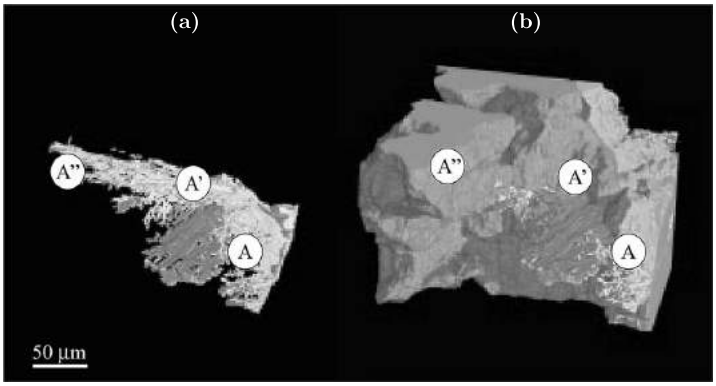

Fig. 2.4: (a) 3D rendering of the crack inside the new grain (set to transparent). (b) Same scene with the surrounding grains. The crack entered the new grain between points A and A' by tilting. Between points A' and A" the crack followed the perimeter of the grain. It is likely that the preferential attack along A-A' is governed by favourable slip mismatches with the neighbouring grain [LUD 03].

Brochu *et al.* [BRO 10, BRO 12] performed surface crack monitoring via replicas on two different kinds of casting materials and reported that a semi-solid molding (SSM) material (with finer eutectic constituents and smaller grain sizes) displayed longer fatigue lives than the same alloy produced using a permanent mold. They also observed small crack arrests occurring at grain boundaries in both materials. Based on these findings, they stated that the fatigue strength of both materials is primarily a function of the grain size when no large casting defects are present in the material. Or in other words, this study considered the grain size to be the most important microstructural barrier encountered by small cracks. As a conclusion, they suggested that a reduction in the average grain size of these two materials would improve their fatigue performances.

In view of works of Lados *et al.* and Jana *et al.* [LAD 06, LAD 04, JAN 10] like those of Brochu *et al.* [BRO 10, BRO 12], to this day, the actual influence of the SDAS and grain size on the fatigue resistance of cast Al alloys remains a debated issue. One of the main objectives of the tensile fatigue testing carried out in this work was to further investigate the actual influence of these two microstructural parameters on small crack propagation.

2.1.2.2 Near-threshold regime and long crack propagation

Stanzl-Tschegg *et al.* [STA 95] obtained higher fatigue lives using a coarse material (SDAS $\approx 50\ \mu$m) instead of a finer material (SDAS $\approx 25\ \mu$m) and concluded that the coarse microstructure increased crack deflection which resulted in enhanced roughness-induced crack closure effects. A similar result was found in the study of Lados *et al.* [LAD 06], where it was stated that larger SDAS values and coarser Si particles (case of unmodified alloys) will result in lower near-threshold growth rates and higher ΔK_{th} (see Fig. 2.5).

It has been shown [LEE 95, GAL 99, CHA 03] that in cast Al-Si alloys small cracks propagate preferentially through the Al-α matrix and by debonding of the Si-matrix interface when passing through eutectic clusters that are directly in line with the crack plane. Only elongated eutectic particles with the major axis perpendicular to the primary crack plane are fractured. Nevertheless, a transition point from interface debonding to propagation through fractured Si particles has been found to occur at $K_{max} \approx$ 6-7 MPa$\sqrt{m}$ (see Fig. 2.6), *i.e.,* close to the mechanical threshold ΔK_{th} (which usually values 3-4 MPa$\sqrt{A}$). This transition occurs when the crack-tip plastic zone is large enough to damage a statistically significant number of eutectic particles ahead of the crack tip. In this regard Gall et al. [GAL 00] estimated that the maximum size of the crack-tip plastic zone had

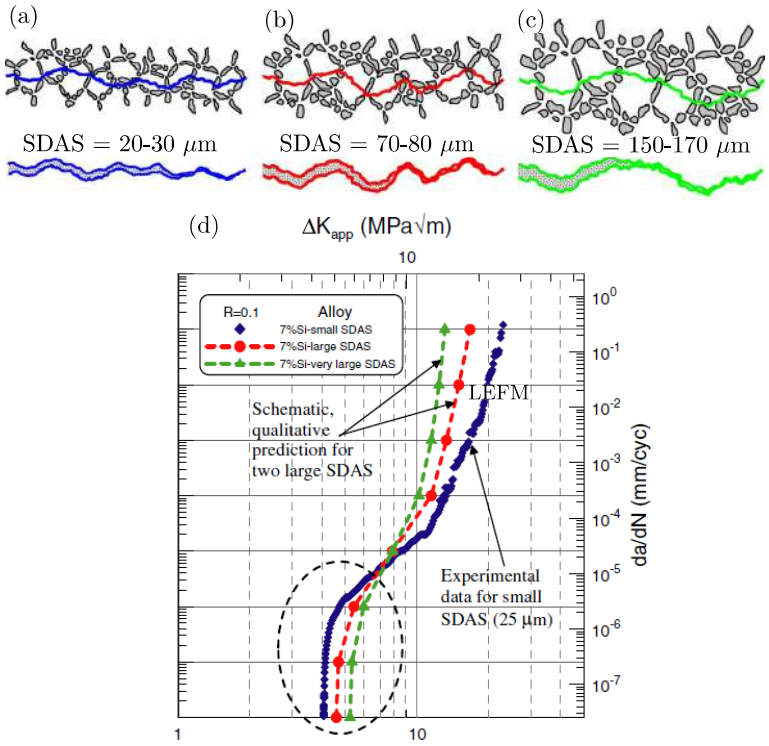

Fig. 2.5: Schematic illustrations of closure mechanisms for 7% Si alloys with different SDAS values: (a) small, 20-30 μm; (b) large, 70-80 μm; and (c) very large, 150-170 μm. (d) Effect of the SDAS on the near-threshold crack behaviour (the encircled part of the graph) and the LEFM behaviour [LAD 06].

to be r_p = 96 μm (this is two-three times the value of the average dendrite cell, ~40 μm) when cycling at R=-1 in a A356-T6 aluminium alloy.

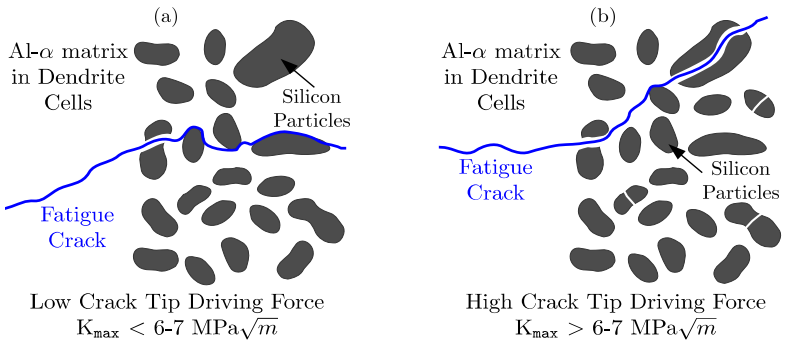

Fig. 2.6: Schematic illustration of the fatigue crack propagation through eutectic region. Depending on the crack-tip driving force: (a) small fatigue cracks avoid and meander around Si particles. Only elongated particles with the major axis perpendicular to the primary crack plane will be fractured. (b) The silicon particles are fractured or debonded ahead of the crack tip in the case of long cracks [GAL 99].

Above this transition point, long cracks propagate almost exclusively through paths of damaged Si particles. As ΔK values further increased, the roughness and area fraction of damaged eutectic particles observed on fracture surfaces also increased. The final failure occurs through ductile static tearing of the eutectic aluminium at Si and intermetallic particles. The formation of dimples is characteristic of final ductile fracture [LAD 07].

All in all, it seems that the eutectic particles are able to influence all stages of crack propagation by: (1) slowing down the growth of microstructurally small cracks, (2) influencing the value of the ΔK_{th} in the near-threshold regime, and (3) offering weak paths of propagation (as they crack when engulfed within the crack plastic zone) in the long crack regime.

2.1.2.3 Effect of casting defects

Casting defects are known to act as preferential crack nucleation sites and therefore to be the main cause of the poor fatigue properties exhibited by Al-7%Si components. They act as local stress raisers which lead to the early development of cracks. Depending on their characteristics (*i.e.,* size, shape, distance to the free surface, type), they can cause a considerable reduction in the nucleation period of small fatigue cracks [ZHA 00b] or even induce an early transition to stage II propagation if they are severe enough.

Microshrinkage pores have been identified as the most damaging among casting defects and significant disparity of results were observed when their size distribution is the only changing parameter. Ødegård *et al.* [ODE 94] obtained approximately 50% reduction in fatigue life when using a defective material (the fatigue strength reduction at 10^7 cycles is of the order of 20%). Jana *et al.* [JAN 10] measured a five times fatigue life improvement in the case of a defect-free casting. For Wang *et al.* [WAN 01b], the reduction caused by the presence of pores is of at least one order of magnitude. Moreover, it has been well established by numerous studies [WAN 01b, COU 90, BRO 10, ATX 01, KUM 10, YI 03, GAO 04, JIA 99] that microshrinkage defects are more dangerous when placed at or near the free surface and that fatigue lives directly decrease with increasing pore sizes and number. For example, Ammar *et al.* [AMM 08] showed that 89% of all tested specimens failed because of pores located at the free surface.

When pore are larger than the critical size mentioned above, it has been observed that increasing pore sizes produces higher reductions on the fatigue life. For example, Kumar *et al.* [KUM 10] found that, below a threshold pore size for a given stress amplitude (case of an AS7GU alloy at R=-1 for equivalent pore diameter of ∼1.0 and ∼0.4 mm and 75 and 100 MPa, respectively), the number of cycles devoted to the initiation of a propagating crack increased with decreasing pore sizes. Roy *et al.* [ROY 11] observed that a A356-T6 material produced life-limiting fatigue cracks only when the projected area $\sqrt{A}$ of nucleating pores was larger than ∼500 μm. They also determined that pores with smaller sizes produced a slight 8% reduction of the expected endurance limit ($\sigma_{\mathtt{D}} \approx 90$ MPa tested at R=-1 and defined as the stress level for fracture at 10^6 cycles).

Ferrié *et al.* [FER 05] used *in situ* X ray microtomography to show crack initiation mechanisms and how grain boundaries can hinder the progression of the growing small crack at the interior of the material. This hindering process results in an increase of the number of cycles required for the crack to surround the nucleating pore (see Fig. 2.7). It was also reported that a substantial part of the lifetime (25% of the estimated fatigue life) was necessary for the crack to surround the pore and assume a semi-elliptical shape.

Finally, there exists a critical size below which pores no longer influence the fatigue life and crack nucleation is transferred to other microstructural features (*e.g.,* Si or intermetallics particles) although the critical size values reported in the literature vary depending on the study and material tested. For instance, Zhang et al. [ZHA 00b] identified that fatigue cracks initiate from surface and subsurface pores when pore size is greater than a critical value of $L_{max} \approx 80$ μm (maximum length of pores). Brochu *et al.* [BRO 10] determined the critical defect size to be $\sqrt{A} = 155$ μm while for Wang *et al.* [WAN 01b] this value is $\sqrt{A} \approx 25$ μm. Buffière *et al.* [BUF 01] found that pores with an equivalent diameter lower than 50 μm did not initiate any crack (see Fig. 2.8a). When pores were larger than the critical size it was noticed that only propagating cracks grew to sizes (L_c) larger than the maximum lateral dimension of the pore below the free surface (L_p) which they measured using tomographic means. They also observed that, in most cases, nucleation at surface pores occurs on Si particles located very close to one convex part of the pores and located nearly perpendicular to the applied stress. As show in Fig. 2.8b, sometimes these Si paths coincide with grain boundaries. However, no reference is made in this study to the influence that these grain

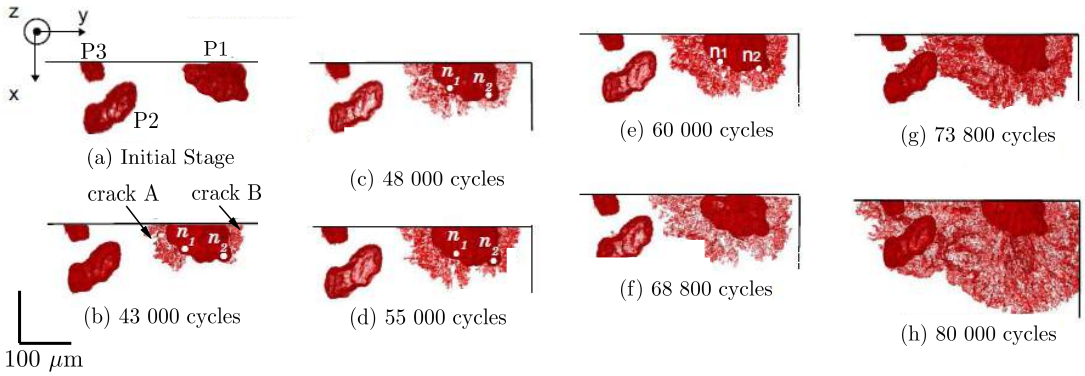

Fig. 2.7: Tomographic projections of the crack on the (xy) plane showing the evolution of the crack shape during the nucleation and propagation process form pore P1. In the first part, from steps (b)-(d), the cracks A and B developed on each side of the pore P1 and joined each other at step (e). In step (b), the two cracks consisted in two *lateral bands* on each side of the pore, whereas the backside of the pore between points n_1 and n_2 remained uncracked. Gallium wetting confirmed that points n_1 and n_2 corresponded to grain boundaries. Although the interval between successive tomographic scans did not allow direct observation of a crack arrest at these points, this coincidence provides strong support to the assumption that the grain boundaries acted as microstructural barriers hindering crack propagation around pore P1 [FER 05].

boundaries might have on the incubation period.

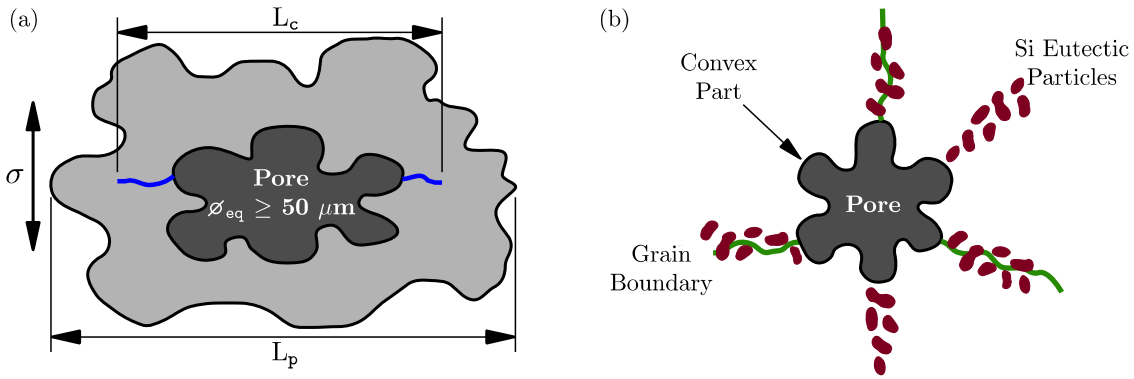

Fig. 2.8: (a) Schematic 2D illustration of the lateral size L_c of the crack at free surface (including the pore), and the maximum lateral dimension of the pore below the surface L_p [BUF 01]. The pore intersection with the sample surface is presented in dark grey and a projection of the 3D shape of the pore below the surface is in light grey. (b) Spatial arrangement of eutectic particles and grain boundaries (in green) in the vicinity of a microshrinkage pore. Crack nucleation at pores occurs on Si particles located very close to one convex part of pore and lying nearly perpendicular to the applied stress. Sometimes the eutectic particle paths coincide with grains boundaries [BUF 01].

2.1.3 Summary on the background of uniaxial HCF behaviour

In order to account for all fatigue nucleation and propagation characteristics described in previous §, McDowell *et al.* [MCD 03] proposed a HCF model which categorizes the severity of a defects according to their impact on fatigue life. Here, the total life is modelled as the sum of numbers of cycles spent in several consecutive stages:

$$N_T = N_{inc} + N_{MSC} + N_{PSC} + N_{LC} = N_{inc} + N_{MSC/PSC} + N_{LC} \tag{2.1}$$

where N_{inc} account for the number of cycles required to incubate an initial crack a_i of the order of the maximum Si particle or pore present in the material. It embodies nucleation and small crack growth through the region of defect influence. $N_{\mathtt{MSC}}$ is the number of cycles required for propagation of a microstructurally small crack ($a_{\mathtt{MSC}}$) larger than a_i but smaller than $k * SDAS$ (k is a nondimensional factor which represents a saturation limit reached when a 3D crack front encounters a Si particle network; typically k is comprised between 3 and 5). $N_{\mathtt{PSC}}$ is the number of cycles required for propagation of a physically small crack (PSC) during the transition from microstructurally small crack (MSC) to the long crack (LC) regime. For $a \ll k{*}SDAS$, a significant portion of the 3D MSC crack front may propagate through the α-Al matrix present within dendrite cells. $N_{\mathtt{LC}}$ corresponds to the long crack propagation as described by LEFM. In the particular case of a AlSi7Mg microstructure, the model postulates that the incubation life ($N_{\mathtt{inc}}$) is about 50-70% of total life in the HCF regime. This is for the case of pores with an equivalent diameter of 50 μm. For 200 to 400 μm pores, only about 20-30% of the total life is devoted to crack nucleation. Finally, in the presence of ~500 μm pores $N_{\mathtt{LC}} \gg N_{\mathtt{inc}} + N_{\mathtt{MSC/PSC}}$.

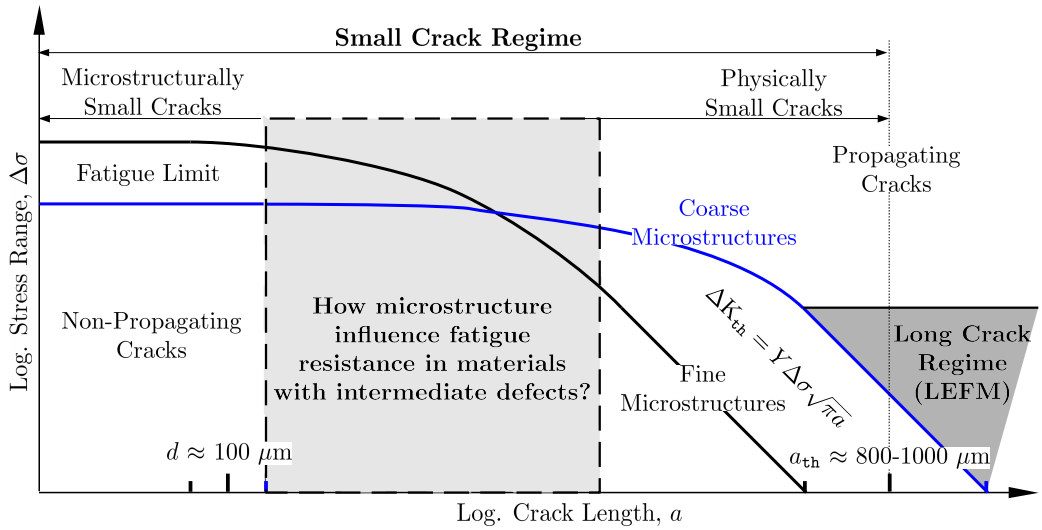

Fig. 2.9: Schematic of the Kitagawa-Takahashi curve showing two fundamentally different fatigue thresholds: microstructural barrier threshold d, and long crack LEFM threshold $a_{\mathtt{th}}$. Considering the fatigue resistance in terms of difficulty for an initial stage I shear crack to become a stage II crack, it is the ability of the microstructure to hinder crack propagation which enhances the fatigue strength of materials [MIL 93].

It follows that, depending on their sizes, the influence of pores on fatigue life can be categorized in three main families (see Fig. 2.9):

1. Large defects ($\sqrt{A} \gtrsim$ 400-600 μm) are the main responsible for the poor fatigue response of casting alloys. They severely reduce $N_{\mathtt{inc}}$ and $N_{\mathtt{MSC/PSC}}$ periods with fatigue life ultimately consisting in long crack propagation.
2. No important reduction in fatigue life is observed when intermediate defects ($\sqrt{A} \approx$ 100-400 μm) are at the origin of final failure. The dominant period seems to be $N_{\mathtt{MSC/PSC}}$ with coarse microstructures favouring surface roughness-induced crack closure in the near-threshold regime.
3. Casting defect with sizes $\sqrt{A} \lesssim 100\ \mu$m are no longer responsible of final failure and crack nucleation is reported to other microstructural parameters (i.e., eutectic particles, matrix strength). In this case, a high fraction of fatigue life is devoted to $N_{\mathtt{inc}}$ period.

As introduced in § 2.1.2.1, the actual influence of the SDAS and grain size values remains an

open question. For components with intermediate size defects, it seems reasonable to decrease the average grain size in order to multiply the number of barriers opposing the small crack propagation. On the other hand, it has been determined that reducing the grain size/defect ratio diminishes ΔK_{th} values and $N_{inc} + N_{MSC/PSC}$ periods. The experimental results presented in what follows intend to bring more insight into this matter along with and a better understanding of the crystallographic mechanisms involved in stage I crack propagation.

2.2 Uniaxial fatigue results

2.2.1 Results obtained at ENSMA and CTIF

2.2.1.1 S-N curves

Fatigue tests were undertaken simultaneously at ENSMA, where Pengfei Mu and Yves Nadot were in charge of Wöhler testing for both tension-tension (R=0.1) and compression-tension (R=-1) cyclic loading, and at CTIF (Amaury Chabod and Yves Gaillard) where Wöhler testing was also carried out and the fatigue limit at 10^7 cycles (σ_D = 115 MPa ± 10) was established using the staircase method. It must be noted that the two S-N curves presented in Fig. 2.10 are important to this work because they were systematically used to choose the stress level whenever an experiment was performed at INSA. As it can be observed in Fig. 2.10b, the ENSMA results are slightly higher than those of CTIF. So far, there is no clear explanation to this behaviour although an influence of the specimen position within the rod is suspected. ENSMA machined two specimens per rod while CTIF only used one (carved out at the centre of each rod). This means that the position of the specimen gages along the rod length was different. Therefore, the SDAS average value varies from CTIF specimens to ENSMA ones which is suspected to be the reason to the observed differences.

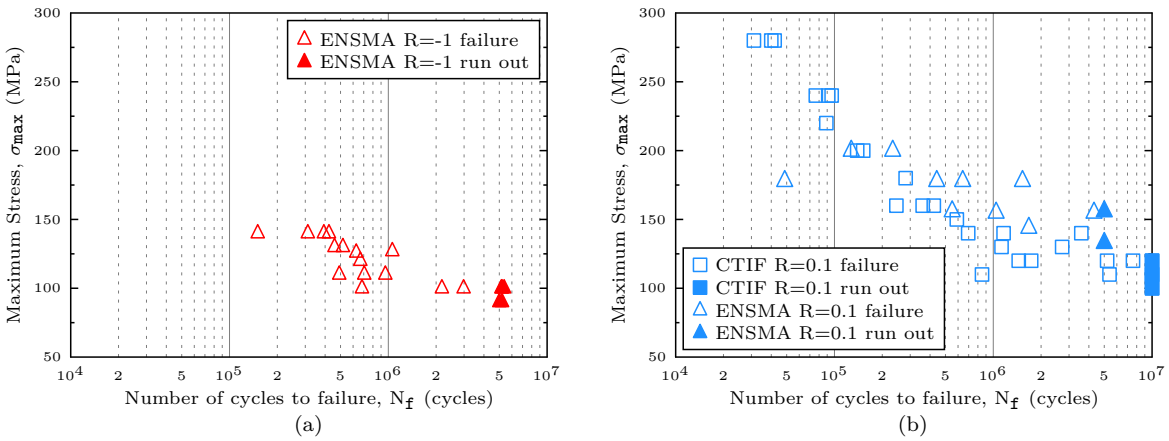

Fig. 2.10: (a) Plot of the maximum stress against the number of cycles to failure for R=-1 testing. (b) The same as before but for R=0.1 testing.

These results are in good agreement with those obtained in [BRO 12] for the same type of A357-T6 material.

2.2.1.2 Kitagawa-Takahashi diagrams

The experimental Kitagawa-Takahashi relationship was obtained at ENSMA (see the work of Mu *et al.* [MU 14] for more details on these experiments). SEM observations on the fracture surfaces were

used to identify and measure the size of the nucleating defects. Tests using specimens containing spherical artificial defects (machined by EDM) with different sizes were also performed. Fig. 2.11 indicates that the critical defect size ($\sqrt{A_c}$) under R=-1 conditions is ∼400 μm while under R=0.1 conditions this value is ∼350 μm. Two extra points are added to Fig. 2.11b. These points correspond to the nucleating pores of the two rectangular specimens (labelled as Sample A and Sample B) that were cycled at INSA during the crack monitoring experiments. It is noteworthy that the Kitagawa-Takahashi predicts propagating cracks for both defects with the difference that Sample B is placed a distance of 23 MPa above the fatigue limit and Sample A is about 43 MPa above the mechanical threshold.

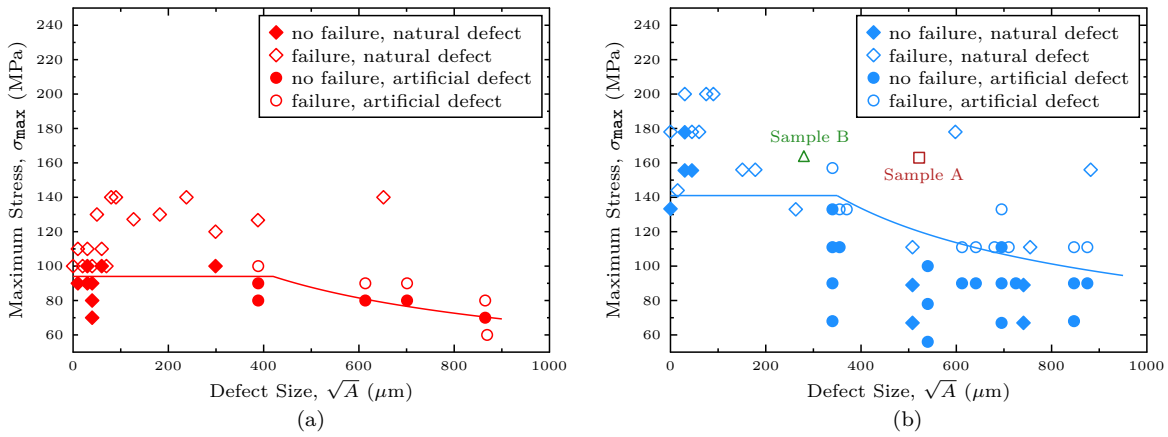

Fig. 2.11: (a) Kitagawa-Takahashi diagram with the maximum stress σ_{max} plotted against the measured defect size $\sqrt{A}$ at fatigue ratio of R=-1. (b) The same as before but for testing at R=0.1; two extra points labelled as Sample A and Sample B corresponding to rectangular specimens have been added.

2.2.2 Surface crack monitoring results

The two rectangular specimens used to carry out these experiments were submitted to a nominal stress level of σ_{max} = 163 MPa for a life expectancy of ∼500 000 cycles (see Fig. 2.10b). Crack nucleation and propagation were monitored using a Zeiss optical microscope on specimens that are systematically removed form the set up. The main objective of this experiment is to study the interactions with the underlying microstructure. Thus, it was decided to favour the quality of optical observations even though there exists the risk of changing loading conditions. Optical images were taken every 50 000 cycles and the intervals were reduced to 20 000-10 000 cycles when the crack grew to a length of ∼1.3 mm. The results of the surface crack monitoring on the two specimens along with tomographic images, EBSD measurements, and Taylor analysis are presented in the following §.

It can be assumed that each individual grain of a FCC polycrystalline ensemble undergoes the same deformation mechanisms as those of a single crystal. But the incompatibility of elastic and plastic deformation between adjacent grains due to the variety of slip orientations imposes a shape change compatibility between grains, predominantly in the form of multislip. Thus, the single slip condition cannot be maintained. Based on this, Taylor developed an analysis to determinate the slip systems in a crystal that can geometrically produce a specified shape change with the least expenditure of energy [HOS 93]. For example, the Taylor factor for randomly textured polycrystalline FCC metals is M_T = 3.06.

Several Taylor analyses are performed in this work using the EBSD grain mean orientations

expressed in Euler's angles in a calculation which is based on an elasto-visco-plastic model performed by imposing an elementary deformation ($\varepsilon = 0.02\%$ equivalent deformation). In this model, each grain of the polycrystal undergoes the same (macroscopic) deformation (or iso-deformation). This is equivalent to consider all grains behaving independently from each other and therefore the effects of neighbouring grains hindering deformation is not considered in the analysis.

2.2.2.1 Crack monitoring results on Sample A

Fig. 2.12 and Fig. 2.13 present all documented stages of Sample A cracking process. The surface pore is ~100 μm long at 0 cycles. It can be observed that three fatigue cracks (named c_{l1}, c_{r1} and c_{r2}) of $c \approx 200$ μm were already formed at $N_f = 50\,000$ cycles with the difference that c_{l2} crack remained arrested throughout the rest of the cycling. The two other cracks continued steady propagation until they were slowed down when bifurcating. For c_{l1} crack, the bifurcation occurred at $N_f = 150\,000$ cycles and $c \approx 691$ μm, with the resulting c_{l3} crack growing to a final length of 1056 μm. In the case of c_{r1} crack, the bifurcation occurred at $N_f = 190\,000$ cycles and $c \approx 877$ μm (see Fig. 2.12i) to create the final c_{r2} crack which propagated up to a length of $c \approx 1147$ μm.

Once the monitoring concluded, the specimen was sectioned to a smaller size in order to perform EBSD analysis and more accurate laboratory tomography on the cracking pore. The latter results are presented in Fig. 2.14 where the projected area of the pore over the Y-axis is $\sqrt{A} = 522$ μm. Here, the ligament between the pore and the free surface is included in the measurement of the projected area. It must be noted that the small fatigue crack is barely distinguished on the tomographic scans and so no information regarding the 3D shape of the crack can be obtained.

• *Crack nucleation*: Fig. 2.15 indicates that all three cracks (c_{r1}, c_{l1}, and c_{l2}) nucleated at convex parts of the pore and followed an intergranular path of eutectic particles. c_{r1} crack propagated for $c \approx 112$ μm before being deflected to intragranular propagation while c_{l1} crack went on for $c \approx 255$ μm. The addition of the underlying pore profile suggests that the intergranular crack propagation approximately corresponds to the cracking of the pore ligament. It would be interesting to investigate whether this behaviour occurs readily at the beginning of the cycling and the crack was therefore slowed down while transitioning to intragranular propagation.

• *Crack propagation*: Fig. 2.16 presents the combination of the EBSD results and crack growth rates and shows that some of the decelerations not always correspond to the cracks interacting with grain boundaries. Moreover, it is observed that cracks propagated for considerable lengths ($c_{l3} \approx$ 691 μm and $c_{r2} \approx 1125$ μm) before meeting any grain boundary.

Fig. 2.17 presents two details of the crack path formed within Grain 1 where two of the three major deflections are shown at 50 000-100 000 and 160 000-180 000 cycles. No crystallographic propagation is observed to occur although a series PSBs at three different {111} directions can be observed surrounding the crack path along its entire length. This observation suggests that propagation within Grain 1 occurred by multiple slip. Interestingly, the Taylor results (see Table 2.1) indicate that the slip system with the highest activity ($8.4{\cdot}10^{-4}$) is placed at θ = -6° (the explanation for the θ and ψ angles is given in Fig. 2.18b) but no evidence of PSBs at this direction was found with the SEM observations.

The evolution of crack growth rates shown in Fig. 2.16c reveals that the branching occurring between 160 000 and 180 000 cycles produced a slightly deceleration on the crack growth rates. Conversely, when entering into Grain 2 the crack did not slow down. Fig. 2.18a shows the progression within Grain 1 and Grain 2. It is observed that the crack propagated along Grain 1/Grain 2 grain boundary for about 40 μm. Some crystallographic propagation within Grain 2 is also observed ($\theta = 40°$ and $\theta = 29°$ which correspond to the planes exhibiting the highest slip activities, *i.e.,* $\sim 7.9{\cdot}10^{-4}$). The most favourable values of the α and β angles described in the Zhai model

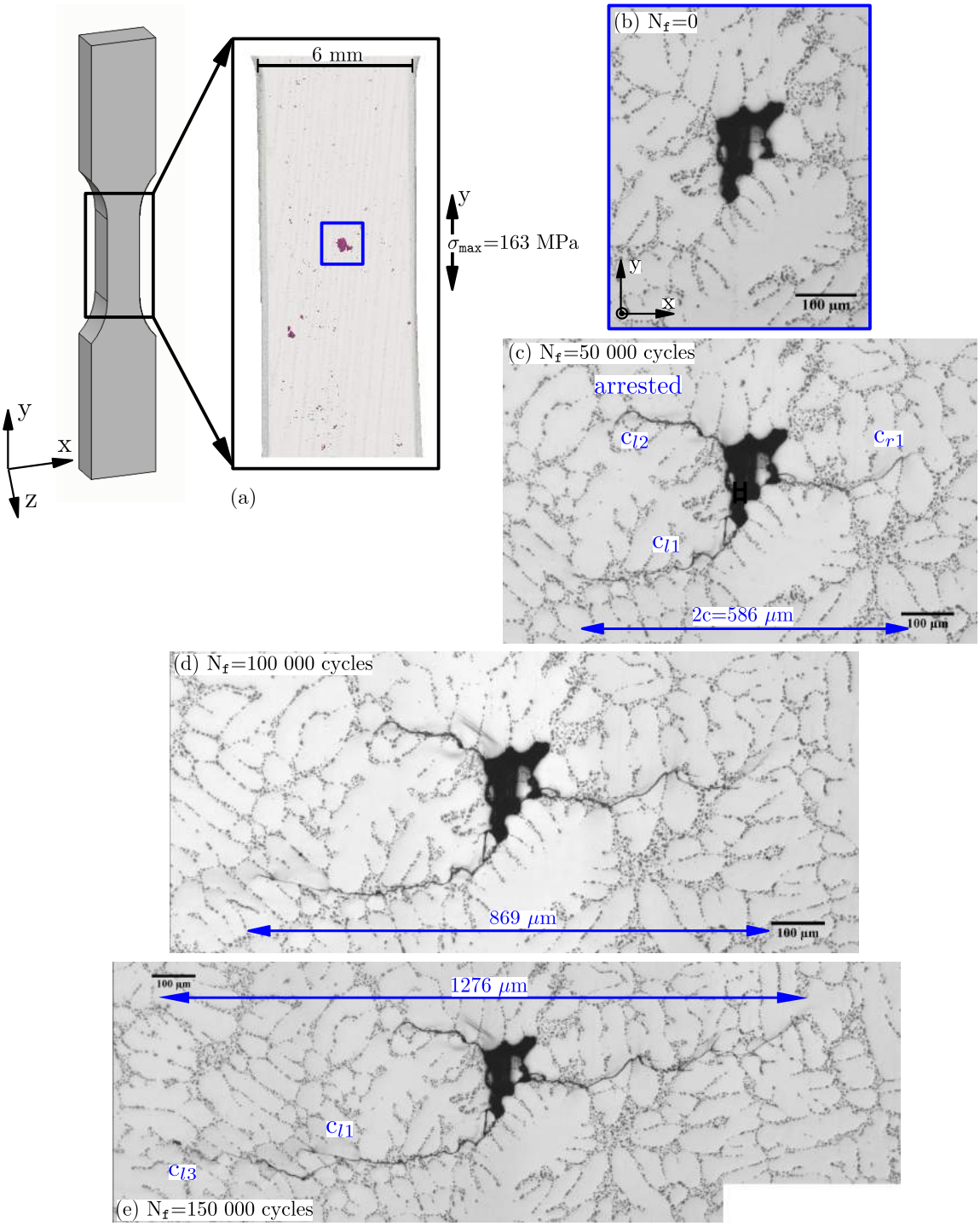

Fig. 2.12: (a) 3D rendering obtained using laboratory tomography (voxel size = 12 μm) prior to uniaxial fatigue testing at σ_{max} = 163 MPa. The pore distribution is shown in magenta and the cracking pore is highlighted with a blue box. (b)-(e) Sequence of optical images presenting crack initiation at N_f = 0 cycles and subsequent propagation stages until N_f = 150 000 cycles.

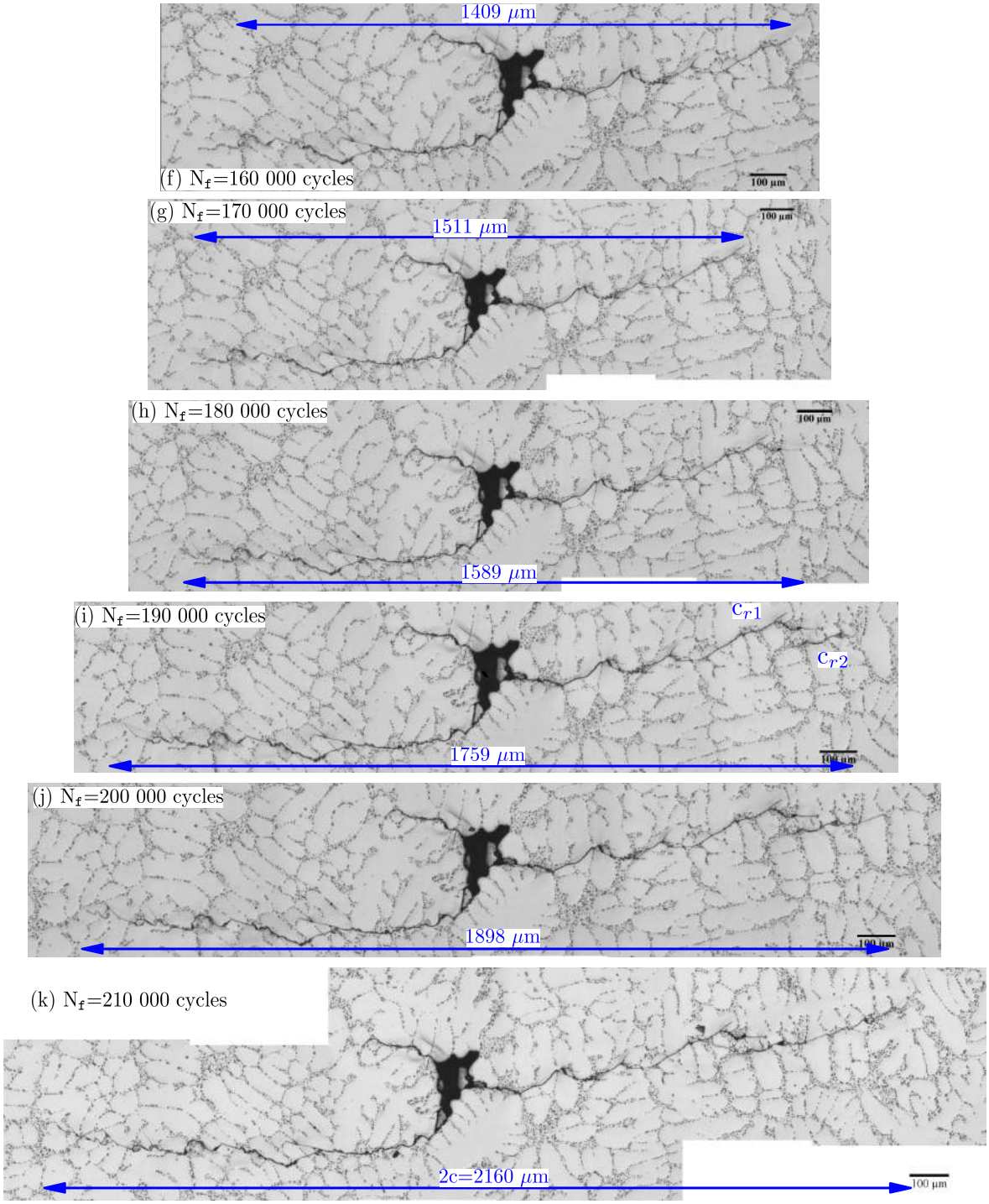

Fig. 2.13: (f)-(k) The same as the previous image but showing the crack progression from 160 000 up to 210 000 cycles where the experiment was stopped.

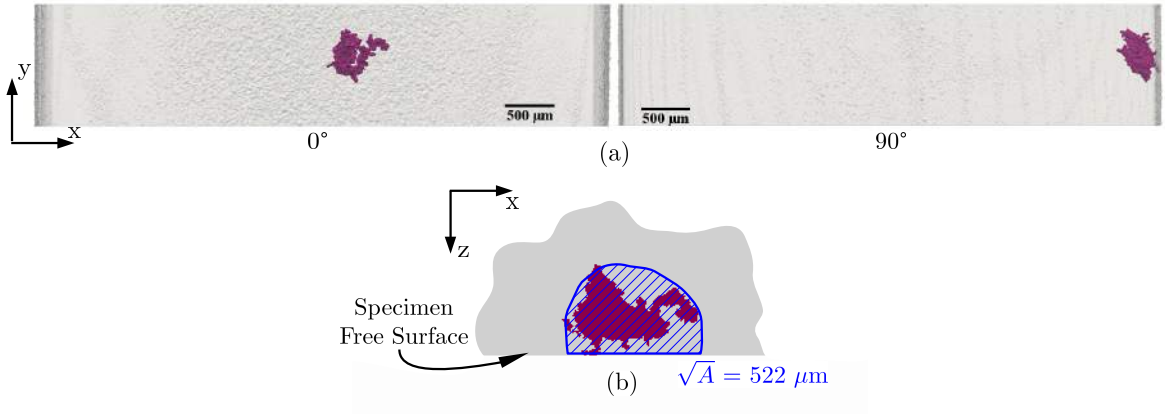

Fig. 2.14: (a) Sample A 3D rendering (voxel size = 6 μm) of the post-mortem specimen gage at 0° and 90°. (b) Detail of the pore corresponding to the Y projection of the pore. An approximate area projection of the pore is shown in blue ($\sqrt{A} = 522\ \mu$m).

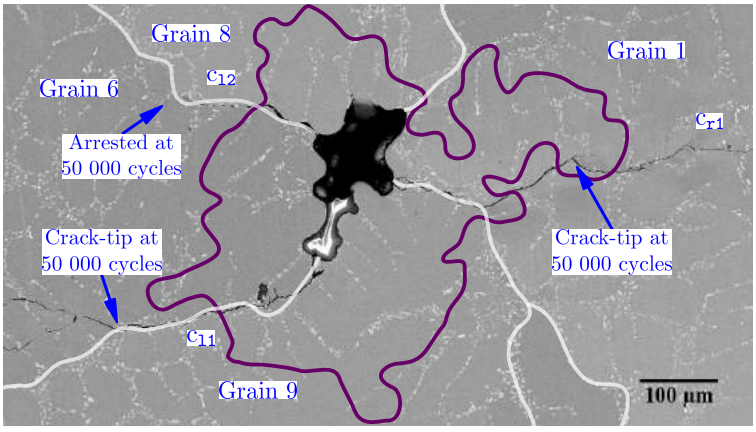

Fig. 2.15: BSE image of the nucleating pore where the grain boundaries are shown with white lines. The outline in magenta corresponds to the approximate location of the underlying pore obtained using the tomographic images.

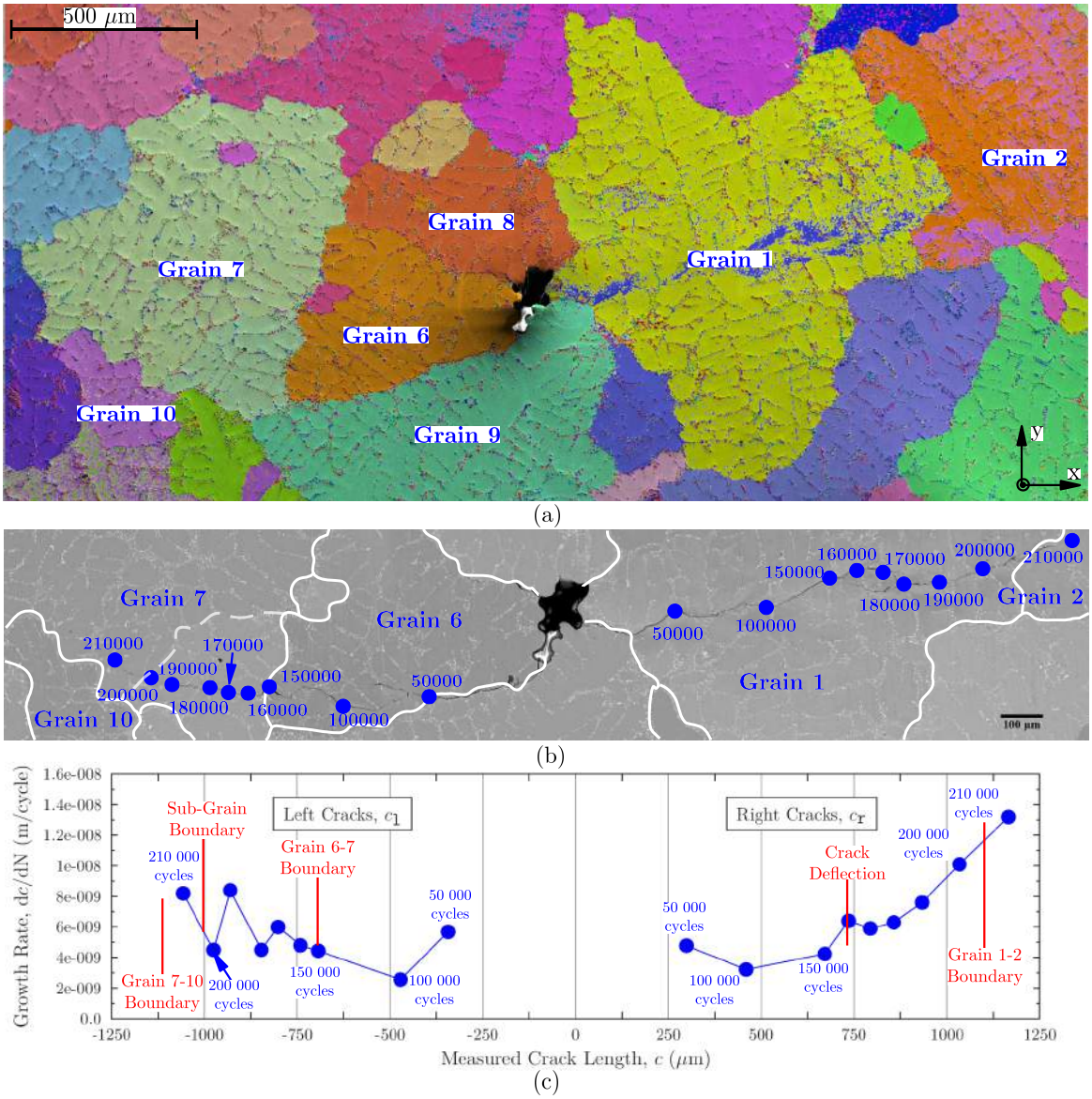

Fig. 2.16: (a) EBSD Euler map of the grain population around the pore and cracks. (b) BSE image of the crack path with blue circles indicating the observed stages of the propagation from 50 000 to 210 000 cycles. The white lines correspond to the approximate location of grain boundaries and the dashed line corresponds to a sub-grain boundary (lattice misorientation lower than 5°). (c) Plot of the crack growth rates (dc/dN) against the measured crack lengths (c).

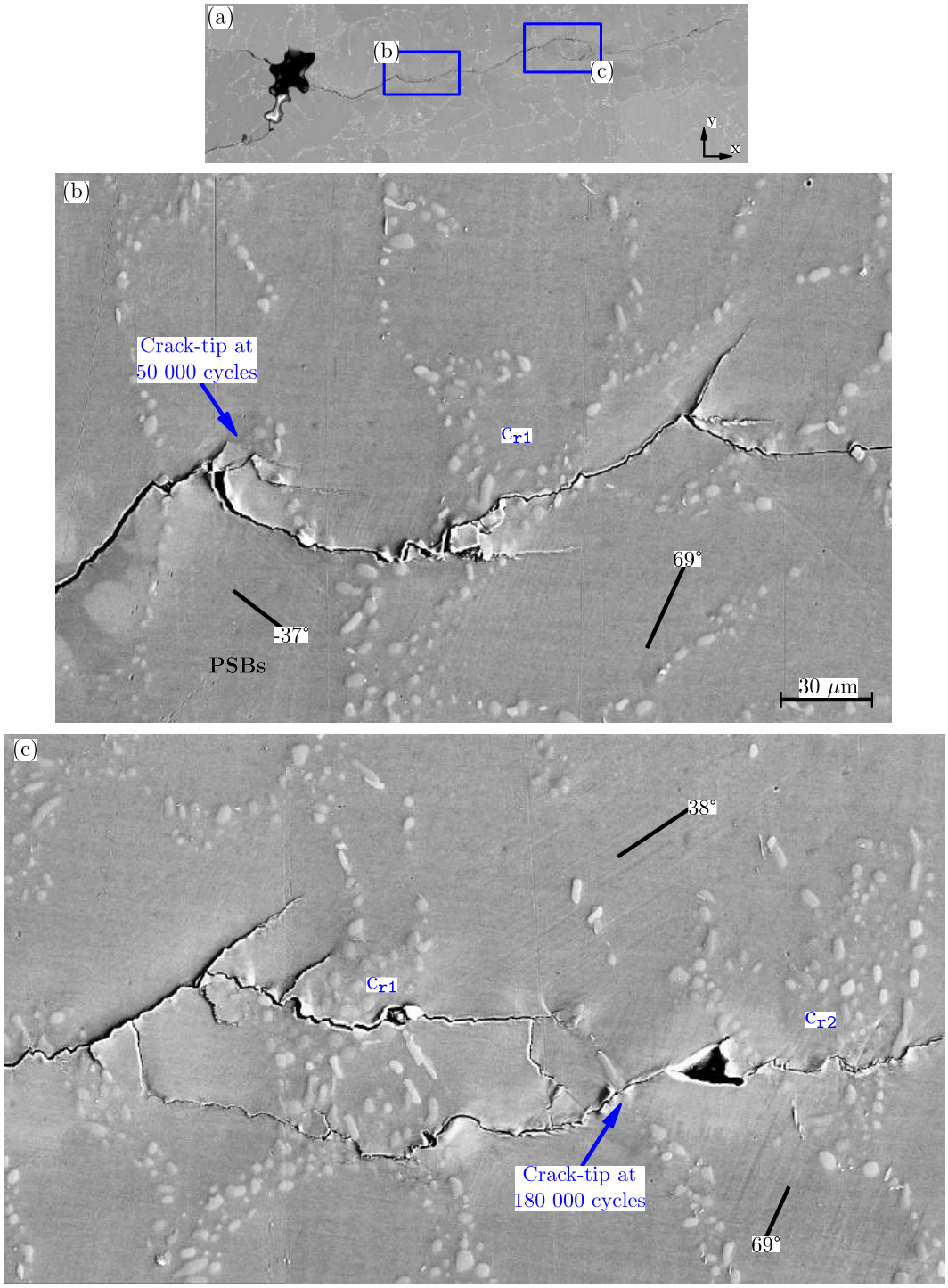

Fig. 2.17: (a) BSE image at low magnification of the right crack indicating the location of the details: (b) SEM image of the crack within Grain 1 where the PSBs observed on the free surface are indicated with black lines, and (c) the same as before but for a location closer to Grain 2.

[ZHA 00a] are 1° and 9° respectively. Such low values might be one of the reasons explaining by this crack did not decelerate when entering Grain 2.

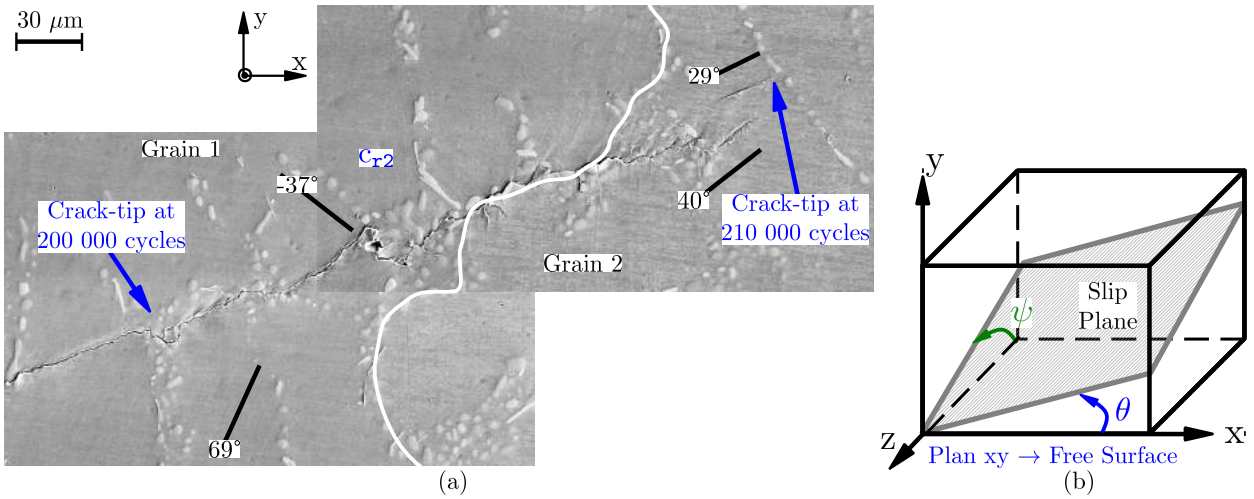

Fig. 2.18: (a) SEM image on the c_{r2} crack showing the passing into Grain 2 and the final location of its tip. (b) Schematic illustration of the θ angle (corresponding to the intersection with the free surface, *i.e.*, the xy plane) and the ψ angle (corresponding to the zy plane) used to calculate the tilt β and the twist α.

	(111) [0$\bar{1}$1]	**(111) [10$\bar{1}$]**	**(111) [$\bar{1}$10]**	**($\bar{1}$11) [0$\bar{1}$1]**	**($\bar{1}$11) [101]**	**($\bar{1}$11) [110]**	**(1$\bar{1}$1) [011]**	**(1$\bar{1}$1) [10$\bar{1}$]**	**(1$\bar{1}$1) [110]**	**(11$\bar{1}$) [011]**	**(11$\bar{1}$) [101]**	**(11$\bar{1}$) [$\bar{1}$10]**
Grain 1	θ = 38°; ψ = -58°			θ = -6°; ψ = 51°			θ = -37°; ψ = -17°			θ = 69°; ψ = 34°		
M_T=2.3	$1.4{\cdot}10^{-4}$	0	$-4.5{\cdot}10^{-4}$	0	$-8.4{\cdot}10^{-4}$	$-1.8{\cdot}10^{-6}$	0	$5.5{\cdot}10^{-4}$	$2.9{\cdot}10^{-4}$	$-4.5{\cdot}10^{-7}$	0	$-1.1{\cdot}10^{-6}$
Grain 2	θ = 29°; ψ = -59°			θ = 89°; ψ = -80°			θ = 40°; ψ = 61°			θ = -20°; ψ = 3°		
M_T=2.99	$-7.7{\cdot}10^{-4}$	$7.7{\cdot}10^{-4}$	0	0	$1.4{\cdot}10^{-8}$	$-8.4{\cdot}10^{-9}$	0	$-8.1{\cdot}10^{-4}$	$5.3{\cdot}10^{-4}$	0	0	0
Grain 6	θ = -24°; ψ = 59°			θ = -43°; ψ = -60°			θ = -89°; ψ = 82°			θ = 20°; ψ = -4°		
M_T=2.98	$-7.8{\cdot}10^{-4}$	$7.5{\cdot}10^{-4}$	0	$7.9{\cdot}10^{-4}$	0	$-5.6{\cdot}10^{-4}$	0	$-4.6{\cdot}10^{-12}$	$-2.9{\cdot}10^{-12}$	0	0	0
Grain 7	θ = -86°; ψ = 89°			θ = 68°; ψ = 62°			θ = 17°; ψ = -17°			θ = -51°; ψ = 9°		
M_T=3.1	0	$1.7{\cdot}10^{-5}$	$-5.8{\cdot}10^{-5}$	0	$-9.6{\cdot}10^{-4}$	$-1.2{\cdot}10^{-5}$	0	$-1.2{\cdot}10^{-5}$	$-2.3{\cdot}10^{-4}$	0	$-7.0{\cdot}10^{-4}$	$9.9{\cdot}10^{-4}$

Table 2.1: Taylor analysis on grains involved in the crack propagation of Sample A.

The crack path within Grain 6 and Grain 7 (Fig. 2.19) also shows a series of PSBs. The particularity for Grain 6 is that some PSBs can be observed occurring at $\theta = 20°$ ($(11\bar{1})$ plane) while there is theoretically a zero activity on this slip plane. This result indicates that the Taylor analysis shown in Table 2.1 is not completely satisfactory to describe the actual slip activity. Finally, it must be noted that no deceleration is observed at 150 000-160 000 cycles when the crack passes into Grain 7 (minimum mismatch of $\alpha = 7°$ and $\beta = 3°$) although a slight retardation is reported at 180 000 cycles. Surprisingly, a major deceleration is observed at 200 000 cycles in what appears to be the result of an interaction with a sub-grain boundary (lattice misorientation lower than 5°).

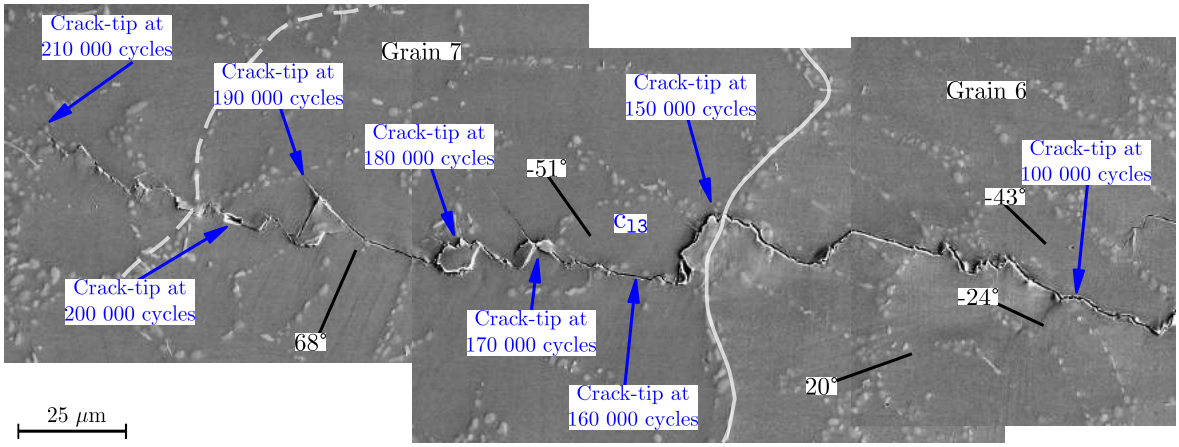

Fig. 2.19: SEM image showing the progression of the c_{13} crack within Grain 6 and Grain 7.

The major results observed with Sample A can be summarised as follows:

- A surface pore of $\sqrt{A} = 522$ μm nucleated and propagated a fatigue crack reaching a length of $2c = 2160$ μm after 210 000 cycles.
- At the nucleation, the crack exhibits intergranular propagation which is most certainly due to the cracking of the pore ligament.
- The rest of the propagation is intragranular and the crack path predominantly exhibits multiple slip behaviour.
- Cracks arrived to the first grain boundary after considerable propagation had occurred ($c \approx$ 700-1100 μm). No marked decelerations of the growth rates were observed when the crack entered the different grains.

2.2.2.2 Crack monitoring results on Sample B

Fig. 2.20a-m presents the nucleation and first stages of propagation observed on Sample B. Two surface pores about 70 μm long are visible on the free surface of this specimens at 0 cycles. Three fatigue cracks (c'$_{l1}$, c'$_{r1}$, c'$_{r2}$; ~30 μm long, see 2.20c) are formed after a first interval of 50 000 cycles. All three nucleated at the convex parts of the pores and followed paths of eutectic particles (case of c'$_{r1}$ and c'$_{r2}$) or propagated through the α-Al matrix (c'$_{l1}$). Propagation went on until c'$_{r2}$ crack was arrested at $N_f = 150\,000$ cycles and $c \approx 70$ μm, and c'$_{l1}$ crack bifurcated to form c'$_{l2}$ crack at $N_f = 300\,000$ cycles and $c \approx 70$ μm. Before, at $N_f = 200\,000$ cycles, c'$_{r3}$ crack had been nucleated at another convex part of the top pore and propagated through the α-Al matrix until it was arrested at $N_f = 400\,000$ cycles with a length of $c \approx 90$ μm (see Fig. 2.21j). From 400 000 to 500 000 cycles, c'$_{l2}$ crack was the only one to continue propagation until c'$_{r4}$ crack readily emerged after $N_f = 550\,000$ cycles on the right side of the pore, growing $c \approx 165$ μm within an interval of 50 000 cycles. Then these two cracks (c'$_{l2}$ and c'$_{r4}$ crack) steadily progressed from 600 000 to 780 000 cycles reaching a final length of $2c = 2030$ μm. Fig. 2.21n shows that these cracks have a relatively smooth profile for almost the entire path, only exhibiting some tortuosity within Grain 19 (a serrated crack path was formed across this grain). Finally, the tomographic results are presented in Fig. 2.22 where the projected area of the upper pore (in darkmagenta) is $\sqrt{A} = 280$ μm.

• *Crack nucleation*: Fig. 2.23 shows that the c'$_{r1}$ and c'$_{r2}$ cracks followed an intergranular propagation with the latter crack being arrested at the triple point between Grain 11, Grain 12,

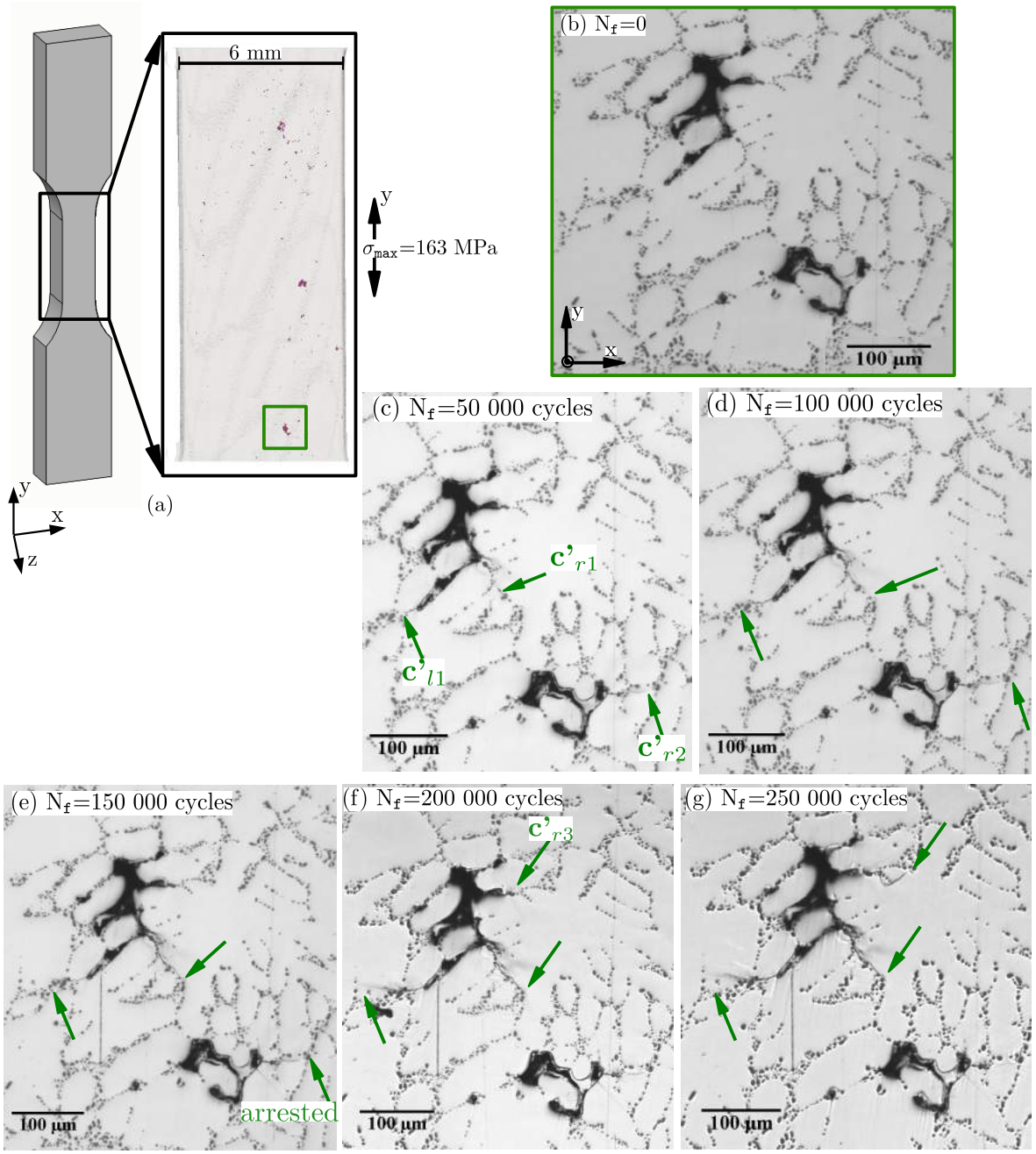

Fig. 2.20: (a) 3D rendering obtained using laboratory tomography (voxel size = 12 μm) prior to uniaxial fatigue testing at σ_{max} = 163 MPa. The pore distribution is shown in magenta and the cracking pore is highlighted with a green box. (b)-(g) Sequence of optical images presenting crack initiation at N_f = 0 cycles and subsequent propagation stages until N_f = 250 000 cycles.

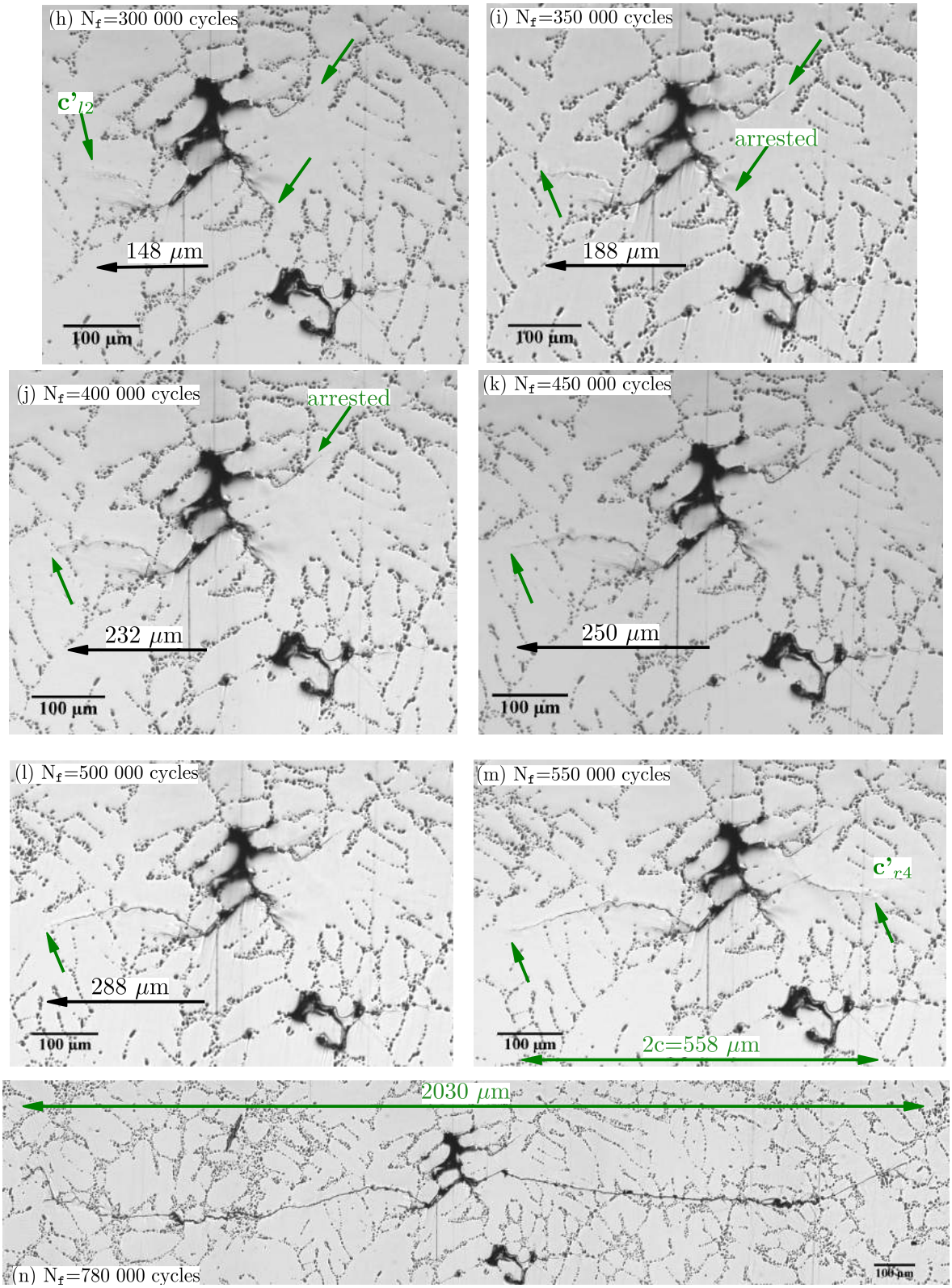

Fig. 2.21: (h)-(m) The same as the previous image but showing the crack progression between 300 000 and 550 000 cycles. This latter stage (m) presents the merging of the crack on the right side of the pore. (n) Optical image of the last stage (780 000 cycles).

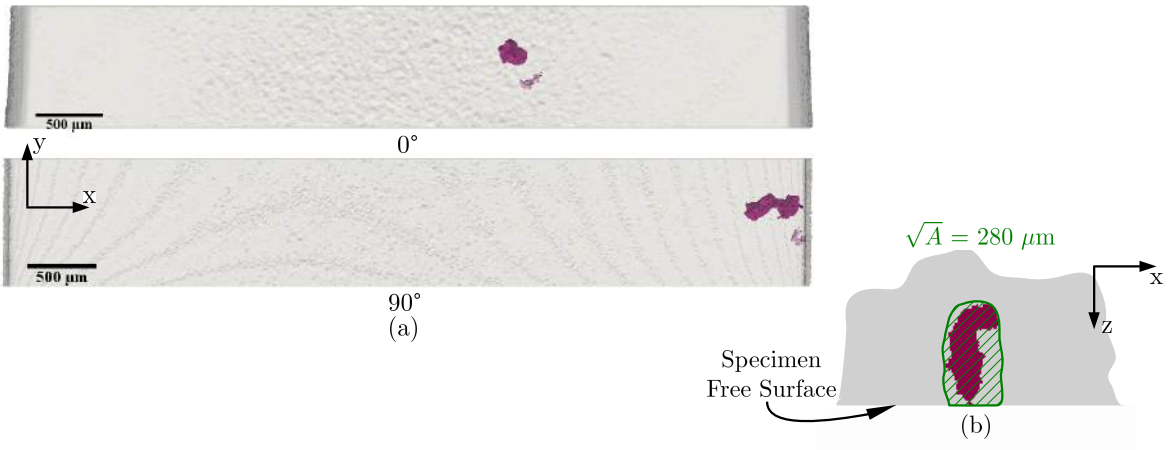

Fig. 2.22: (a) Sample B 3D rendering (voxel size = 6 μm) of the post-mortem specimen gage at 0° and 90° . (b) Detail of the pore corresponding to the Y projection of the pore. An approximate area projection of the pore is shown in green ($\sqrt{A}$ = 280 μm)..

and Grain 20. The addition of the underlying pore profiles indicate that this behaviour might result from the cracking of the ligament as already suggested for Sample A. On the other hand, no evidence of PSBs was found during the SEM observations performed on Grain 11 and Grain 16. Two small crystallographic paths at θ = 34° and θ = 26° are observed within Grain 11. The slip activity of this grain (see Table 2.2) suggests multiple slip propagation. Grain 16 presents the particularity of only four slip systems having any activity. Moreover, the activity on the slip systems at -10° ($\sim 10^{-3}$) exceed by at least a factor two that of the other two active systems which suggests that a stage I crack should theoretically have propagated by duplex slip in this grain. This result seems to be in good agreement with the EBS observations showing a smooth crack path that grew almost perpendicular to the loading direction.

• *Crack propagation*: Fig. 2.24a-b shows that, as it was the case for Sample A, the two cracks progressed for considerable lengths ($c'_{12} \approx 432$ μm and $c_{r4} \approx 596$ μm) before arriving to the first grain boundaries. The difference in Sample B is that the cracks passed across another five grain boundaries before reaching the final stage at 780 000 cycles. It is also observed in this sample that crack decelerations are easier to correlate with the presence of grain boundaries.

Fig. 2.25 presents the crack progression from Grain 11 to Grain 15. The study of the crack path within Grain 13 reveals a micro-serrated profile. In this grain, a series of crystallographic microcracks are observed to alternate propagation between {111} directions at θ = -61° and θ = 66°, with several PSBs visible in the vicinity of the grain boundary with Grain 14. The {111} planes corresponding to these two θ angles exhibit the highest slip activities ($\sim 10^{-3}$) within Grain 13, exceeding by at least a factor of two the activity registered on the other slip systems. It is noteworthy that when entering into Grain 13, the crack decelerated (see Fig. 2.24c). As for the Grain 13/Grain 14 crossing, the crack exhibits a relatively small deceleration. Finally, it must be noted that the crystallographic orientation within Grain 13 seems detrimental to crack propagation.

With regard to Grain 14, the crack followed a crystallographic path at θ = 28° across the entire grain length; this seems to be the result of the high slip activity ($\sim 2 \cdot 10^{-3}$) predicted on this $(1\bar{1}1)$ plane with the activity on the rest of slip systems being lower by at least a factor two (Table 2.2). The plastic activity seem to be highly concentrated on a single slip system. When approaching Grain 15, the crack is deflected and slows down (but does not stop) within Grain 14.

Fig. 2.26 shows the differences on the crack path formed within Grain 18 and Grain 19. A

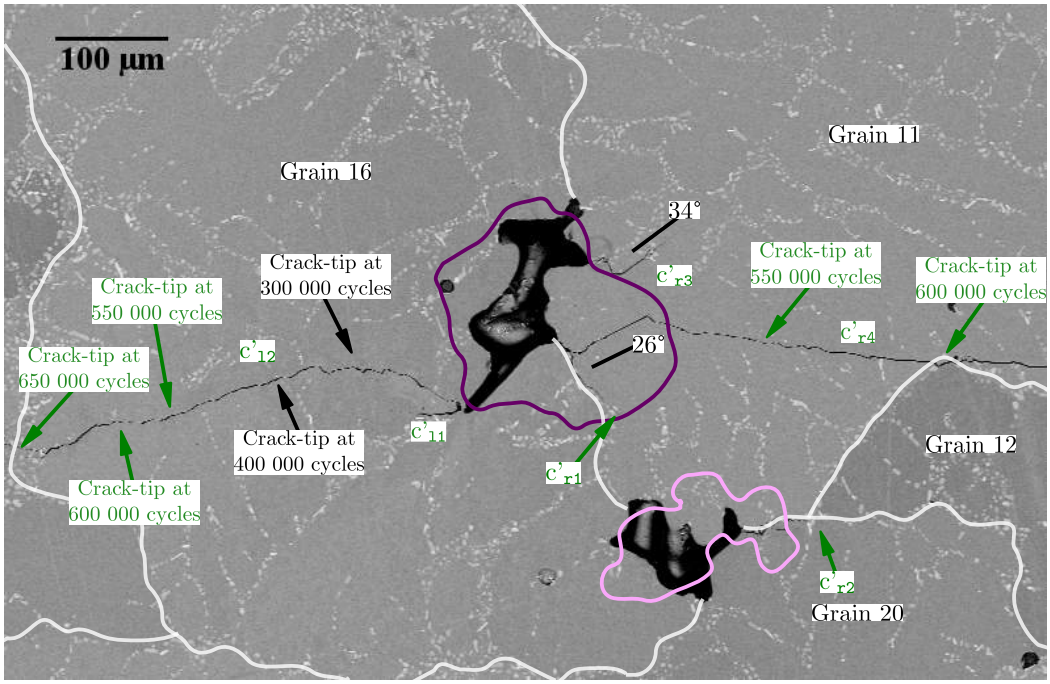

Fig. 2.23: EBS image of the nucleating pores where the grain boundaries are shown with white lines. The outlines in magenta and pink correspond to the approximate location of the underlying pores obtained using the tomographic images.

	(111) $[0\bar{1}1]$	(111) $[10\bar{1}]$	(111) $[\bar{1}10]$	$(\bar{1}11)$ $[0\bar{1}1]$	$(\bar{1}11)$ $[101]$	$(\bar{1}11)$ $[110]$	$(1\bar{1}1)$ $[011]$	$(1\bar{1}1)$ $[10\bar{1}]$	$(1\bar{1}1)$ $[110]$	$(11\bar{1})$ $[011]$	$(11\bar{1})$ $[101]$	$(11\bar{1})$ $[\bar{1}10]$
Grain 11	θ = 34°; ψ = 56°			θ = -52°; ψ = -42°			θ = -75°; ψ = 72°			θ = 26°; ψ = -20°		
M_T=2.67	$-8.3\cdot10^{-4}$	$4.0\cdot10^{-4}$	0	$3.6\cdot10^{-8}$	0	$-8.9\cdot10^{-4}$	0	0	0	0	$1.7\cdot10^{-4}$	$-3.8\cdot10^{-4}$
Grain 13	θ = 53°; ψ = -79°			θ = -61°; ψ = 26°			θ = 66°; ψ = 62°			θ = 7°; ψ = -7°		
M_T=3.37	$-3.9\cdot10^{-4}$	$1.7\cdot10^{-6}$	0	$6.4\cdot10^{-4}$	0	$-1.1\cdot10^{-3}$	0	$-3.1\cdot10^{-6}$	$-1.2\cdot10^{-3}$	0	0	0
Grain 14	θ = 16°; ψ = 70°			θ = 80°; ψ = 50°			θ = 28°; ψ = -43°			θ = -31°; ψ = 7°		
M_T=2.59	0	$5.9\cdot10^{-4}$	$-3.4\cdot10^{-6}$	0	$-1.3\cdot10^{-4}$	$-3.9\cdot10^{-5}$	0	$-5.1\cdot10^{-5}$	$-1.6\cdot10^{-3}$	0	$-1.0\cdot10^{-5}$	$-1.7\cdot10^{-4}$
Grain 15	θ = -74°; ψ = -78°			θ = 59°; ψ = -43°			θ = 13°; ψ = 30°			θ = -54°; ψ = -4°		
M_T=2.93	0	0	0	$-1.6\cdot10^{-4}$	$-9.1\cdot10^{-4}$	0	$-2.3\cdot10^{-4}$	0	$-7.8\cdot10^{-4}$	0	$-3.0\cdot10^{-4}$	$5.4\cdot10^{-4}$
Grain 16	θ = -10°; ψ = 48°			θ = -88°; ψ = -88°			θ = 73°; ψ = -66°			θ = -7°; ψ = -23°		
M_T=2.68	$-1.1\cdot10^{-3}$	$9.4\cdot10^{-4}$	0	0	0	0	0	$-5.6\cdot10^{-4}$	0	$3.9\cdot10^{-6}$	0	0
Grain 17	θ = 59°; ψ = -63°			θ = -19°; ψ = 40°			θ = -35°; ψ = -36°			θ = 65°; ψ = 47°		
M_T=2.09	$1.4\cdot10^{-10}$	0	$-2.6\cdot10^{-5}$	0	$-1.0\cdot10^{-3}$	$-2.1\cdot10^{-4}$	0	$7.2\cdot10^{-4}$	$1.8\cdot10^{-5}$	$-2.2\cdot10^{-9}$	0	$-1.5\cdot10^{-4}$
Grain 18	θ = 38°; ψ = -54°			θ = -45°; ψ = 42°			θ = -63°; ψ = -58°			θ = 35°; ψ = 27°		
M_T=2.58	$-3.0\cdot10^{-4}$	$5.2\cdot10^{-4}$	0	0	$-1.7\cdot10^{-4}$	$-6.2\cdot10^{-4}$	$9.9\cdot10^{-5}$	$1.1\cdot10^{-4}$	0	0	$3.4\cdot10^{-4}$	$-4.1\cdot10^{-4}$
Grain 19	θ = 51°; ψ = -68°			θ = -72°; ψ = 8°			θ = 55°; ψ = 66°			θ = -2°; ψ = 0°		
M_T=3.52	$-9.7\cdot10^{-4}$	3.2×10^{-4}	0	6.1×10^{-4}	0	-5.9×10^{-4}	0	-2.5×10^{-4}	-7.3×10^{-4}	0	0	0

Table 2.2: Taylor analysis on grains involved in the crack propagation of Sample B.

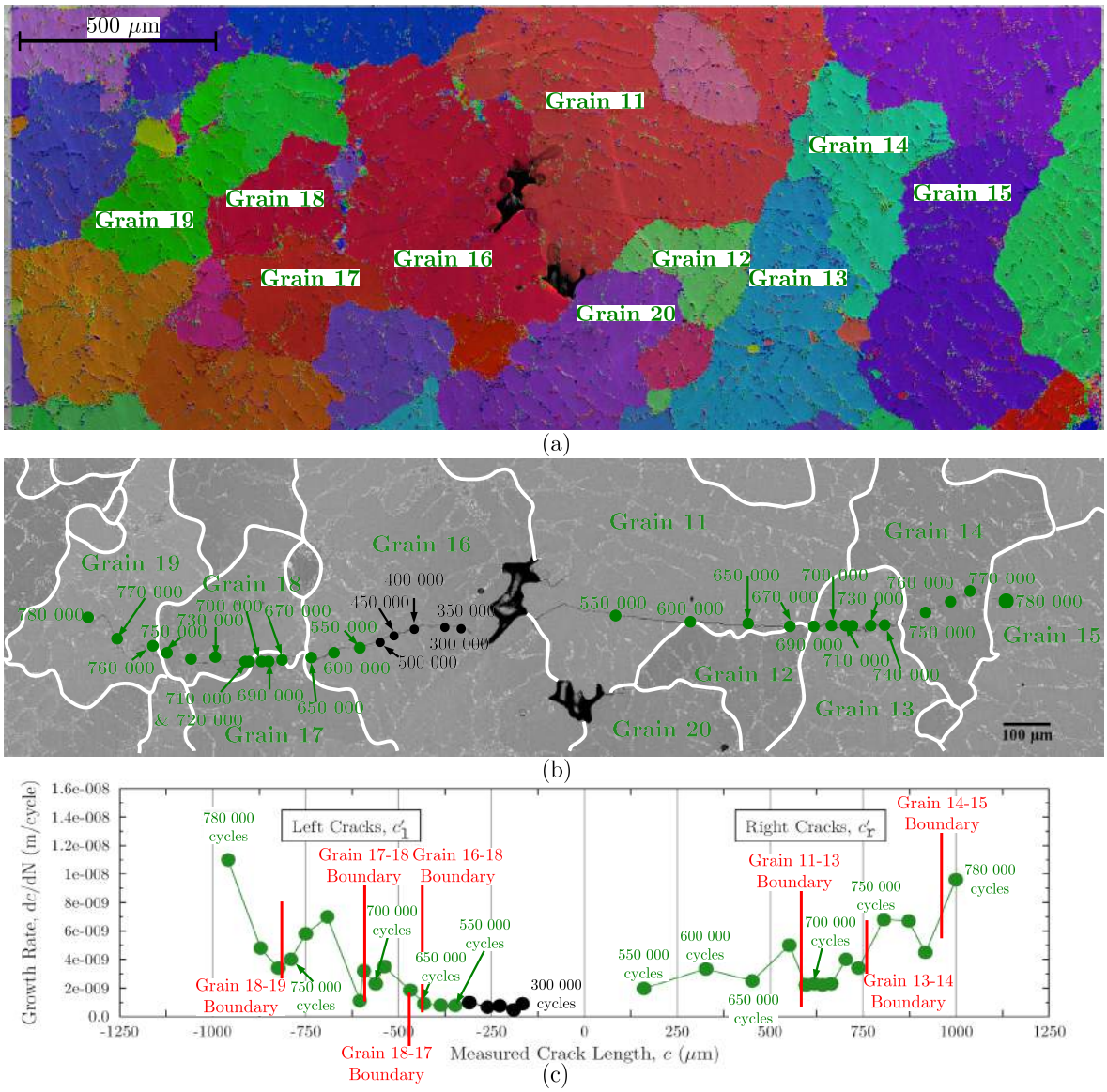

Fig. 2.24: (a) EBSD Euler map of the grain population around the pores and cracks. (b) BSE image of the crack path with green circles indicating the different stages of the propagation from 50 000 to 780 000 cycles. The white lines correspond to the approximative location of grain boundaries. (c) Plot of the crack growth rates (dc'/dN) against the measured crack lengths (c').

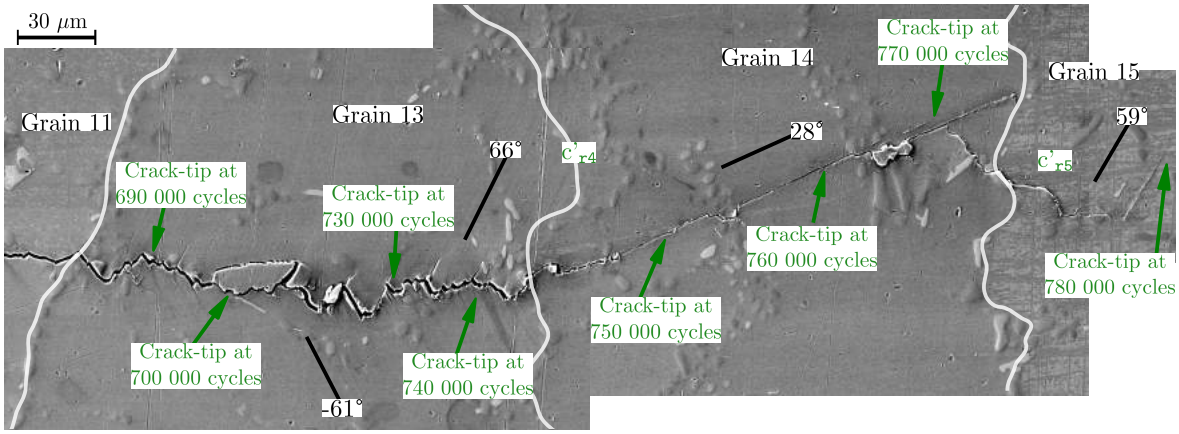

Fig. 2.25: SEM image showing the progression of the c'_{r4} crack from Grain 11 to Grain 14 and the final deflection when passing into Grain 15.

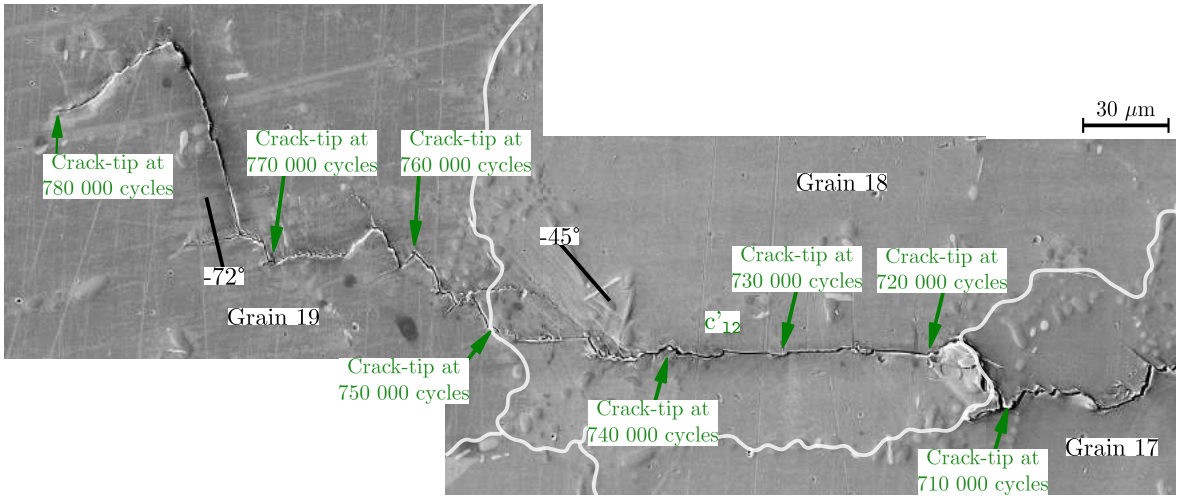

Fig. 2.26: SEM image showing the progression of the c'_{12} crack within Grain 17, Grain 18 and Grain19.

smooth crack path is observed in Grain 18 while a tortuous one is observed in Grain 19. The Taylor analysis does not help to clarify the cause of these two distinct behaviours. Grain 18 exhibits an evenly distributed activity through all {111} planes with a rather low values ($\geq 6{\cdot}10^{-4}$). Regarding Grain 19, it is observed the crack the predominantly propagated on the $(\bar{1}11)$ plane at -72° although this slip system only exhibits the third highest activity. Finally, a relatively important deceleration is registered during the Grain 18/Grain 19 crossing, with a series of PSBs occurring at 45° being observed within Grain 18, just before the grain boundary with Grain 19.

The major results observed with Sample B can be summarised as follows:

* A surface pore of $\sqrt{A} = 280$ μm nucleated and propagated a fatigue crack approximately 2 mm long after 780 000 cycles for an expected fatigue life of 500 000 cycles.
* In total, the observed cracks encountered seven grain boundaries which generated deflections and/or decelerations. Crack propagation was observed to occur by single, duplex or multiple slip and the local crystallography is suspected to influence on the crack growth rates (for example, the case of Grain 13).

A schematic illustration of the major observations on the propagation behaviour of both Sample A and Sample B is given in Fig. 2.27. The cracks primarily propagated through the α-Al matrix and the occasional eutectic propagation mainly corresponds to the intergranular crack nucleation at pores; some occasional eutectic propagation though grain boundaries has also been observed (*e.g.*, the crossing into Grain 2).

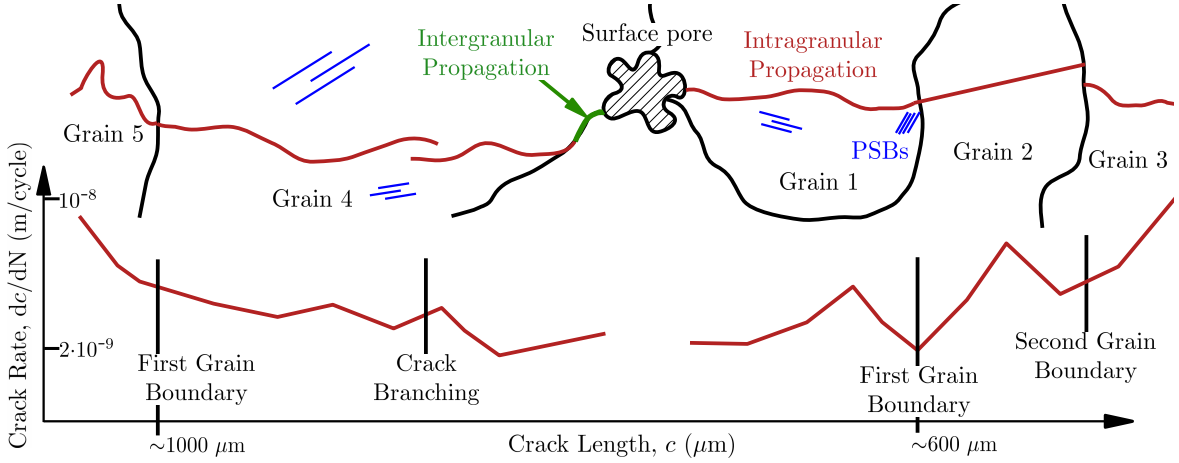

Fig. 2.27: Schematic illustration summarizing crack nucleation at a surface pore and the subsequent possible interactions of the propagating crack with grain boundaries.

In addition, it must be noted that no cracking of Si particles was observed (they appear to be only debonded) although the occasional cracking of Fe-rich intermetallic particles is observed all along the crack paths (see Fig. 2.28).

2.2.2.3 Differences between Sample A and Sample B fatigue behaviour

A graph showing the evolution of the surface crack size ($2c$) as a function of the number of cycles (N_f) is shown in Fig. 2.29. It can be observed on this figure that the pore in Sample A readily nucleated a crack 586 μm long between 0 and 50 000 cycles. From this point to 210 000 cycles, the Sample A crack propagated through two grain boundaries, one on the left side, c_{13}, between 150 000 and 160 000 cycles, and the other one on the right side, c_{r2}, between 200 000 and 210 000 cycles.

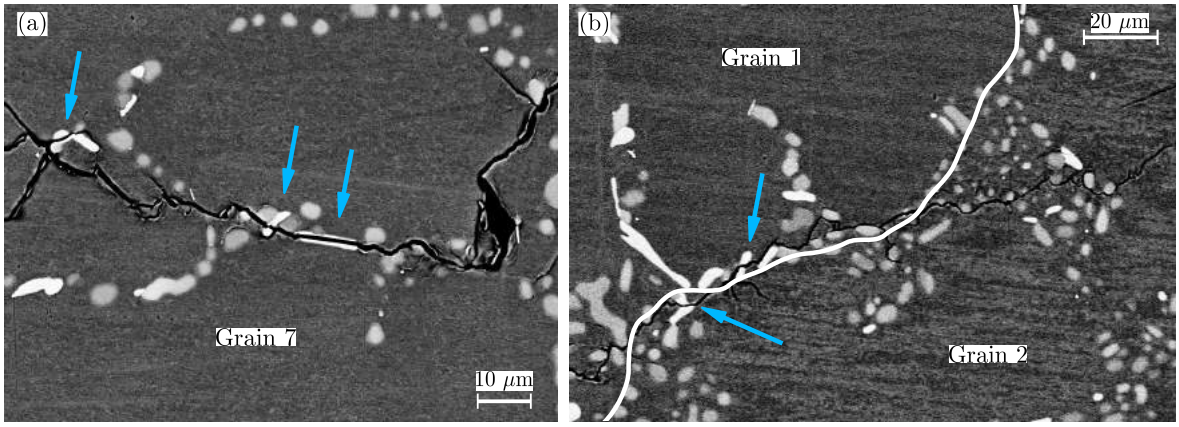

Fig. 2.28: BSE images showing the cracking of Fe-rich particles (blue arrows) in Sample A (a) when the crack just entered Grain 7 and (b) when crossing into Grain 2.

The presence of those two grain boundaries barely influences the crack growth (see blue arrow). It is noteworthy that the crack in Sample A only needed 50 000 cycles to reach a length of 586 μm while the Sample B crack needed 550 000 cycles to reach a nearly equivalent length (558 μm). A clear acceleration of the Sample B crack is observed between 550 000 and 650 000 cycles. Two small fluctuations due to the interaction with grain boundaries are observed (Sample B passed across seven grain boundaries) from 650 000 to 780 000 cycles with the final crack length being 2030 μm.

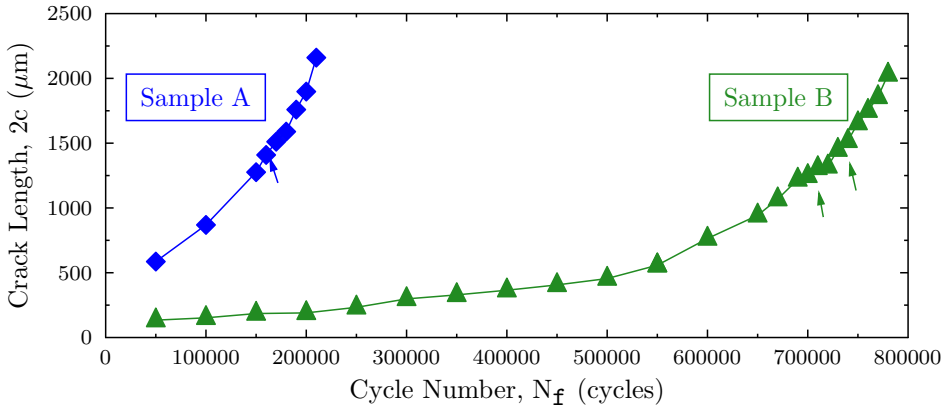

Fig. 2.29: Plot of the surface crack size (2c) as a function of the number of cycles (N_f), Sample A data appears in blue diamonds and Sample B data is drawn in green triangles. For Sample A the cycling ended at 210 000 cycles and for Sample B at 780 000 cycles. Arrows indicate the interaction of the cracks with the grain boundaries.

The maximum size of the plastic zone at the different cycling stages can be estimated using an Irwin-based approach [AND 95]. For the crack geometry, specimen shape, and loading conditions given above, the maximum plastic zone size under plane stress conditions is estimated as:

$$r_y = \frac{1}{2\pi}\left(\frac{K_{max}}{\sigma_y}\right)^2 \tag{2.2}$$

where σ_y is the yield strength of A357-T6 aluminium alloy employed in this work, whose value is 275 MPa.

The general solution for the maximum crack-tip driving force during tensile fatigue testing is:

$$K_{max} = \beta \sigma_{max} \sqrt{\pi a} \tag{2.3}$$

where β is a function of the specimen geometry and the loading configuration, σ_{max} is the maximum applied stress during the fatigue test, and a is the crack length towards the interior of the specimen. For the samples studied here, the stress intensity solution is obtained by considering the fatigue specimen as a flat plate containing a semielliptical centred flaw which forms a curvilinear crack front with a ratio of $a/c = 1.1$. This ratio is obtained using the synchrotron results on small crack propagation (Chapter 3). The numerical solutions for β can be found in [NEW 81].

The results of the estimation of r_y using Eq. 2.2 are shown in Table 2.3. As introduced in § 2.1, the validity of this calculation depends on several assumptions that can break down for small fatigue cracks. Keeping this limitation in mind, the results of the calculation are used for comparison purposes.

Table 2.3 shows that the maximum values of K_{max} for the two studied cracks ($K_{max} = 6.42$ MPa$\sqrt{m}$ for Sample A at 210 000 cycles and $K_{max} = 6.22$ MPa$\sqrt{m}$ for Sample B at 780 000 cycles) are close to the $K^{tr}_{max} \approx 6$ MPa$\sqrt{m}$ value which corresponds to the transition from the debonding to the Si fracture mentioned in the literature (for an A356-T6 alloy with $\sigma_y = 240$ MPa and an average dendrite cell size of ~40 μm [GAL 99]). Thus, this result is consistent with the SEM and BSE observations where no cracking of Si particles was observed at any point of the fatigue crack paths. Conversely and as shown in Fig. 2.28, the Fe-rich intermetallics can appear cracked all along the crack paths even in the case of elongated intermetallics with their major axis parallel to the primary crack plane.

Sample A, N_f (cycles)	50 000	—	100 000	150 000	200 000	210 000
Sample A, r_y (μm)	23.2	—	34.5	50.9	76.0	86.7
Sample A, K_{max} (MPa$\sqrt{m}$)	3.32	—	4.05	4.92	6.01	6.42
Sample A, $2c$ (μm)	586	—	869	1276	1898	2160
Sample B, N_f (cycles)	550 000	600 000	650 000	700 000	750 000	780 000
Sample B, r_y (μm)	22.1	30.4	37.5	49.7	66.2	81.4
Sample B, K_{max} (MPa$\sqrt{m}$)	3.24	3.8	4.22	4.86	5.61	6.22
Sample B, $2c$ (μm)	558	764	943	1248	1655	2030

Table 2.3: Evolution of the crack-tip plastic zone size for Sample A and Sample B cracks for different number of cycles.

The results given in Table 2.3 show that the points where the crack-tip plastic zone r_y reaches the size of the SDAS (38 μm) correspond to ~100 000 cycles for Sample A ($r_y = 34.5$ μm) and ~650 000 cycles for Sample B ($r_y = 37.5$ μm). Moreover, the point at ~650 000 cycles in Sample B corresponds to the change in the slope observed in Fig. 2.29. Thus, this point can be considered as the transition from microstructurally small crack behaviour to physically small crack behaviour. This transition is not observed in Sample A even though the first observed point exhibits a r_y value (23.2 μm) lower than the SDAS. It is thought that this behaviour (no transition observed) is due to the influence of the Sample A pore (twice the size of the pore observed in Sample B) on the first stages of propagation. The SDAS seems to be the controlling microstructural parameter. Nevertheless, it must be noted that no slowing of small cracks was observed when they approached a cluster of Si particles. This is a controversial point and further investigation (by performing

observations at very reduced intervals, for example every 100 cycles) have to be carried out in order to verify the interaction between microstructurally small cracks and the SDAS.

In order to improve the comparison between the crack growth curves of Sample A and B, the data of Fig. 2.29 is shown in in Fig. 2.30 with a common origin corresponding to the beginning of the transition to a steeper slope, *i.e.,* 550 000 cycles for a length of 558 μm in Sample B and, 50 000 cycles and 586 μm in Sample A. It can be observed that Sample B needed an extra 70 000 cycles to propagate and reach a final length similar to that of Sample A (1472 μm against 1574 μm). This difference is most probably due to the retardation effect of the grain boundaries encountered by the crack in Sample B (seven grain boundaries compared to two in Sample A) but the precise influence of the crystallographic orientation of each grain cannot be elucidated.

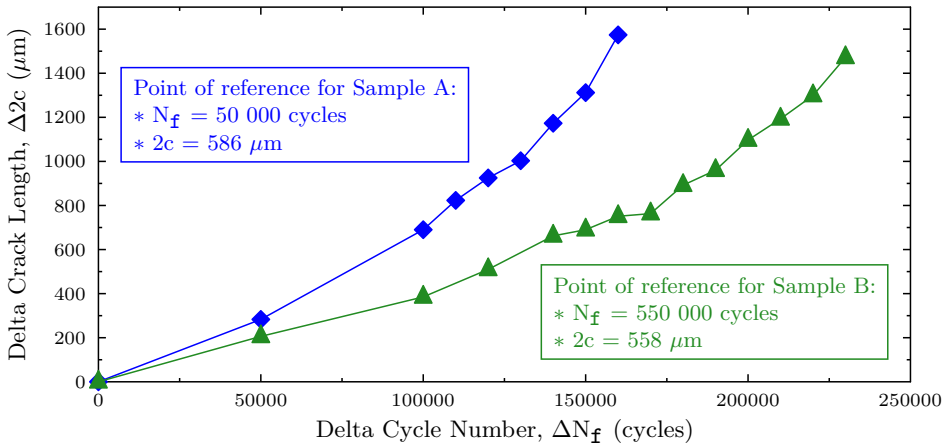

Fig. 2.30: (a) Plot of the differential of crack size (Δ2c) as a function of cycle number (ΔN_f). Sample A crack grew 690 μm in 100 000 cycles while Sample B crack needed 150 000 cycles to grow 690 μm. (b) Sample A crack grew 884 μm in 60 000 cycles while Sample B crack needed 80 000 cycles to grow 782 μm.

Fig. 2.31 presents the crack growth rates, dc/dN, for Sample A and Sample B specimens along with some literature results [BRO 12] obtained using a similar material (A357-T6 alloy with SDAS [22-62] μm and grain size [400-1500] μm). The scatter in crack growth rates is higher for Sample B. This is in good agreement with the higher number of grain boundaries observed on the EBSD analysis of Sample B. Finally, it can be observed that the small cracks of both samples exhibit slightly higher crack growth rates than those documented in literature. The literature results indicate a slowing down occurring at ~ 3 MPa$\sqrt{m}$. It seems likely that a grain boundary was the responsible for this deceleration. Therefore, a grain boundary encountered earlier in the crack path could explain the lowest crack growth rates observed for the literature results.

2.2.3 Analysis of the uniaxial fatigue results

It has been shown in Fig. 2.15 that the first crack propagation stages in Sample A corresponds to intergranular propagation paths. Lack of recorded images on Sample A crack before 50 000 cycles does not allow to know the exact sequence of events. Nevertheless, it seems likely that the presence of horizontal grain boundaries within the pore ligament acted as weak paths which led to intergranular propagation occurring in a relatively low number of cycles.

The difference in the number of cycles required to nucleate and propagate a crack of $2c \approx 570$ μm (see second column in Table 2.3) is most certainly a direct consequence of the difference in size of the nucleating pores. The Sample B pore is almost half smaller than that of Sample A. It is also

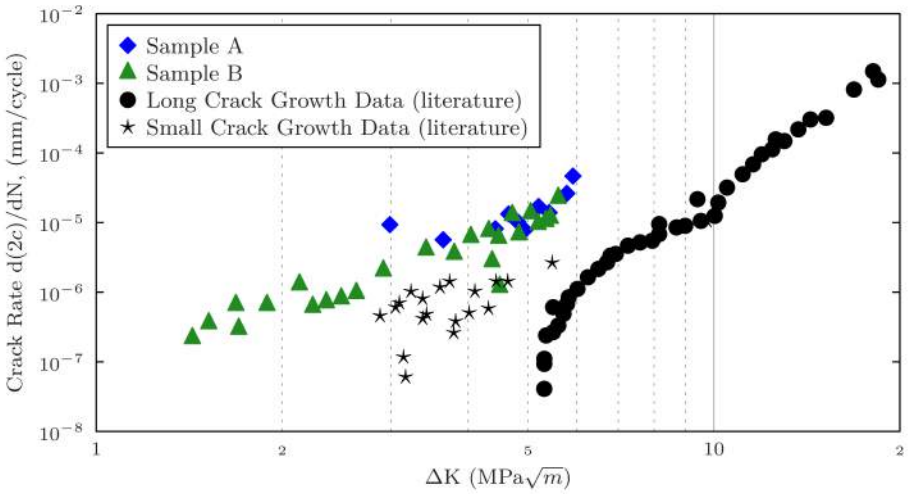

Fig. 2.31: Fatigue crack growth rate diagram for Sample A and Sample B along with the long and small (σ_{max} = 138 MPa) crack growth data for the A357-T6 alloy obtained in Ref. [BRO 12] where the SDAS value ranges [22-62] μm and the grain size [400-1500] μm.

likely that the presence of grain boundaries arranged perpendicularly to the loading direction in Sample A (as shown in Fig. 2.15) has a non negligible influence on the faster nucleation observed in this specimen. Another factor that can explain this important difference in nucleation behaviour is the presence of a grain boundary arranged parallel to the loading direction around Sample B pore. It has been shown by Ferrié *et al.* [FER 05] that the presence of grain boundaries at a pore blocks the propagation of cracks around the pore perimeter. This can be the case of the first stages of crack propagation within Sample B, where the growth of cracks around the pore could be hindered by a grain boundary placed perpendicular to the crack front.

Fig. 2.16 and Fig. 2.24 show that grains boundaries can act as barriers that hinder and retard crack propagation into neighbouring grains. Nevertheless, the case of cracks stopping completely and finally crossing the grain boundaries after a several thousand cycles of arrest was not observed in this work. The relatively high stress level at which the specimens were cycled, and the fact that the first grain boundaries are distant of about 700 μm from the nucleating pores, could explain this observation. As a matter of fact, when the crack fronts reach the grain boundaries, their estimated crack-tip plastic zone have already reach a considerably size (of $\sim$37 μm).

Both Sample A and Sample B display a relatively smooth crack paths resulting from multi-slip propagation and corresponding to low Taylor factors ($M_T \approx$ 2.5-3). On the other hand, it seems that high Taylor factors ($M_T \gtrsim 3$) constrain the major fraction of the strain activity on few slip systems leading to a multi-slip propagation that tends to form serrated (and rather crystallographic) crack paths (in particular, the case of Grain 19). It is noteworthy that even with a low Taylor factor (M_T = 2.59), Grain 14 exhibits a crystallographic crack path at $\theta = 28°$. This crystallographic behaviour seems the result of the strain activity being primarily focused on $(1\bar{1}1)[110]$ slip system; this slip system overriding the rest of the slip systems that are active within Grain 14.

From the observations presented above, it would seem that reducing the average grain size (while keeping a constant SDAS value) can be an interesting solution to improve the fatigue strength of cast aluminium alloys, mainly by introducing more grain boundaries in the region where cracks still exhibits microstructurally small crack behaviour. But it must be born in mind that negative effects can be introduced by reducing the grain size. For example, an increased number of grain boundaries around a nucleating pore could reduce the material fatigue resistance to crack initiation.

2.2.4 Summary of the uniaxial fatigue results

The uniaxial fatigue behaviour of two A375-T6 specimens was investigated. Each specimen contained a surface microshrinkage pore; the pore sizes and the local microstructure in their vicinity were different. The following results have been obtained:

1. The Sample A pore ($\sqrt{A} = 522$ μm) nucleated and propagated a crack (2160 μm long) during 210 000 cycles while the Sample B pore ($\sqrt{A} = 280$ μm) nucleated and propagated a crack (2030 μm long) during 780 000 cycles. Based on the CTIF Wöhler curve of the material, the expected fatigue life was of 500 000 cycles at $\sigma_{\mathtt{max}} = 163$ MPa.
2. The important difference in these two fatigue lives is due to both the presence of a larger pore size (almost two times bigger) in Sample A and the spatial arrangement of the grain boundaries which surround the pores.
3. Grain boundaries oriented perpendicularly to the loading direction can act as weak paths that favour crack nucleation.
4. Crack growth in Sample B accelerated at about 650 000 cycles when the size of the crack-tip plastic zone reached the value of the SDAS (38 μm). This transition was not observed in Sample A.
5. The cracks propagated preferentially through the α-Al matrix and only occasionally through the eutectic. This eutectic growth mainly corresponds to intergranular propagation.
6. In this study, grain boundaries act as microstructural barriers that slightly hinder crack propagation without completely stopping it. The relatively high remote stress level and the large lengths ($\sim$ 700 μm) that the cracks have to grow before meeting the first grain boundaries are suspected to be responsible for this behaviour.
7. Both Sample A and Sample B cracks exhibit relatively smooth profiles favoured by the multi-slip character of crack propagation. The local crystallography seems to play a role in controlling the roughness of the crack path.

Le comportement en traction cyclique de deux éprouvettes macroscopiques a été étudié. Chaque échantillon contenait un pore situé à la surface; la taille de ces pores ainsi que la microstructure locale étaient différentes. Les résultats suivants ont été obtenus:

1. Le pore présent dans l'Eprouvette A ($\sqrt{A} = 522$ μm) a amorcé et propagé une fissure (2160 μm de long) pendant 210 000 cycles. Le pore de l'éprouvette B ($\sqrt{A} = 280$ μm) a amorcé et propagé une fissure (2030 μm de long) pendant 780 000 cycles. Sur la base de la courbe Wöhler du matériau obtenue par le CTIF , la durée de vie attendue était de 500 000 cycles pour une contrainte de $\sigma_{\mathtt{max}} = 163$ MPa.
2. Les nombres de cycles nécessaires pour obtenir une fissure de taille comparable ($\sim$2 mm) différent considérablement. Ceci est dû à la taille du pore amorçant plus grande (près de deux fois plus grande) pour l'Eprouvette A et aussi à l'arrangement spatial des joints de grains autour des pores.
3. Les joints de grains orientés perpendiculairement à la direction de chargement peuvent agir comme des chaînons faibles favorisant l'amorçage de fissures de fatigue.
4. La propagation de fissures dans l'Eprouvette B a accéléré à partir d'environ 650 000 cycles lorsque la taille de la zone plastique en pointe de fissure a atteint la valeur de la SDAS ($\sim$40 μm). Cette transition n'a pas été observée dans l'Eprouvette A.

5. Les fissures se sont propagées préférentiellement à travers la matrice α-Al et très occasionnellement à travers l'eutectique. La croissance à travers l'eutectique correspond principalement à une propagation intergranulaire.
6. Dans cette étude, les joints de grains agissent comme des barrières microstructurales entravant légèrement la propagation de fissures courtes sans pour autant complètement les arrêter. Le niveau de contrainte relativement élevé et les grandes longueurs ($\sim$700 μm) que les fissures ont dû parcourir avant de rencontrer les premiers joints de grains sont soupçonnés d'être les responsables de ce comportement.
7. Les deux fissures présentes dans l'Eprouvette A et l'Eprouvette B montrent des profils relativement plats qui sont favorisés par le glissement multiple en pointe de fissure lors de la propagation. La cristallographie locale semble contrôler la formation de chemins de fissures plus ou moins tortueux.

2.3 Background on torsional fatigue behaviour

2.3.1 Torsion fatigue mechanisms

Under remote cyclic tension (σ_∞), the maximum shear stresses ($\tau_{\mathtt{max}}$) are found on planes placed at $\pm 45°$ with respect to the loading axis and act in combination with opening tensile stresses (σ_2), see Fig. 2.32a). Under cyclic pure torsion (τ_∞), however, the maximum shear stresses are found along the transverse (0°) and longitudinal (90°) directions, with maximum tensile stresses ($\sigma_{\mathtt{max}}$) acting on planes at $\pm 45°$ with respect to the loading axis. The most remarkable difference between these two loading modes is that the opening tensile component is missing on maximum shear planes when cycling under pure torsion. This characteristic leads to the presence of mushy debris and marks of abrasion on torsion fracture surfaces and also to retarded crack propagation compared to uniaxial tensile fatigue.

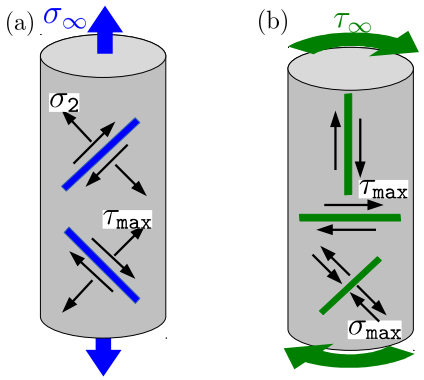

Fig. 2.32: Slip planes with maximum shear stress: (a) for a cylindrical rod subjected to cyclic tension and (b) for cyclic torsion [SCH 09a].

Torsion fatigue cracks initiate at the specimen free surfaces where the remote torque gives the highest shear stress level. Microcracks are first formed on longitudinal and/or transverse planes where the shear stresses are maximum. At the intersection with the surface, the crack tips are subjected to mode II displacements (points B and C in Fig. 2.33). Mode III displacements are induced as the cracks grow and penetrate toward the interior of the specimen (point A), [HUR 82] and so, such cracks tend to be shallow and have large aspect ratios with the crack depth a being shorter than the surface length c.

Because the maximum shear occurring in tension is equal to half the remote tensile stress one could expect the torsion fatigue limit ($\tau_{\mathtt{f}}$) to be equal to half the uniaxial tensile fatigue limit $\sigma_{\mathtt{f}}$.

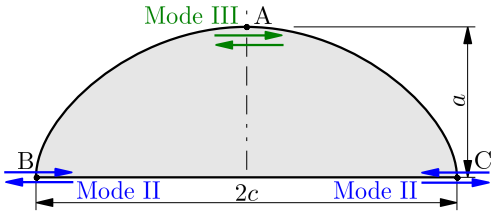

Fig. 2.33: Schematic illustration of the internal shape of a surface crack nucleated under torsion loading. The stress condition is of pure Mode III at the deepest point of the surface crack, point A and mode II at points B and C [MUR 02b].

However, the lack of crack opening in torsional loading leads to slightly higher values. Some fatigue limit examples are given in Table 2.4 where it can be observed that Titanium alloys are the only exception. It is noteworthy that the cast materials display fatigue limit ratios close to 1.

Table 2.4: Mean values of τ_f/σ_f for different kinds of materials and fabrication processes [SCH 09a].

Material	Mean value of τ_f/σ_f
steel	0.60
Al alloys	0.55
Cu and Cu alloys	0.56
Mg alloys	0.54
Ti	0.48
Cast iron	0.90
Cast Al and Mg alloys	0.85

In the case of smooth specimens of an Inconel 718 alloy, Socie [SOC 93] observed that crack propagation essentially occurred on planes of maximum shear for most portion of the fatigue life. Even at the lowest strain amplitude cracks nucleated and continued propagation on shear planes throughout the life. Moreover, the fraction of life (N/N_f) spent for initiating a dominant shear crack was less than 0.1; the remaining 90% of life was spent in propagating this shear crack ($Nf < 10^6$ cycles). For $Nf \approx 10^7$ cycles,the N/N_f ratio increased to 0.2. The low incubation period characteristic of torsion loading contrasts with the high values reported in uniaxial tensile testing. For example, Shiozawa *et al.* [SHI 97] observed under tensile loading that the initiation and propagation period of a small crack up to 1 mm in length represents about 90% of fatigue life in a defect-free Al-Si-Mg-Cu material.

Tscheeg [TSC 82] adopted an experimental method allowing the assessment of the effective mode III propagation rate for an AISI 4340 steel tempered at 650°C (cylindrical V-notched specimens). These experiments were conducted with stress intensity control, which means that the stress intensity value ΔK_{IIInom} at the crack tip was held constant during the whole test (see Fig. 2.34a). Crack growth rates were calculated by applying a finite difference procedure allowing the measurement of the intermediate crack advance (Δc) after a given number of cycles (ΔN). The crack propagation rates curves are then plotted as a function of the crack depth c emanating from the notch root. The resulting curves are extrapolated to zero crack length (c→0) to obtain the crack growth rate in the absence of any fracture surface interference (*i.e.,* $\Delta K_{IIInom} = \Delta K_{IIIeff}$). These (c→0) points correspond to a constant level of the remote loading (*i.e.,* ΔK_{IIInom}). As schematically shown in Fig. 2.34b, the crack growth rates tend to decrease as the crack sizes increase due to the increasing fracture surface interference. This means that the measurement of the effective (intrinsic) mode III crack growth rate would require the exclusion of the crack closure effect.

Fig. 2.34a also shows different propagation behaviour depending on the specimen diameter (12.7 mm and 25.4 mm) when testing at $\Delta K_{III} = 30$ MPa$\sqrt{m}$. Although the extrapolated (c→0) crack growth rates fall at the same points from 0 to 0.4 mm, the curves start to diverge at 0.4 mm crack depths. Thus, the influence of sliding crack closure diminishes with decreasing specimen diameters. In addition to these parameter, there are many other factors, such as materials microstruc-

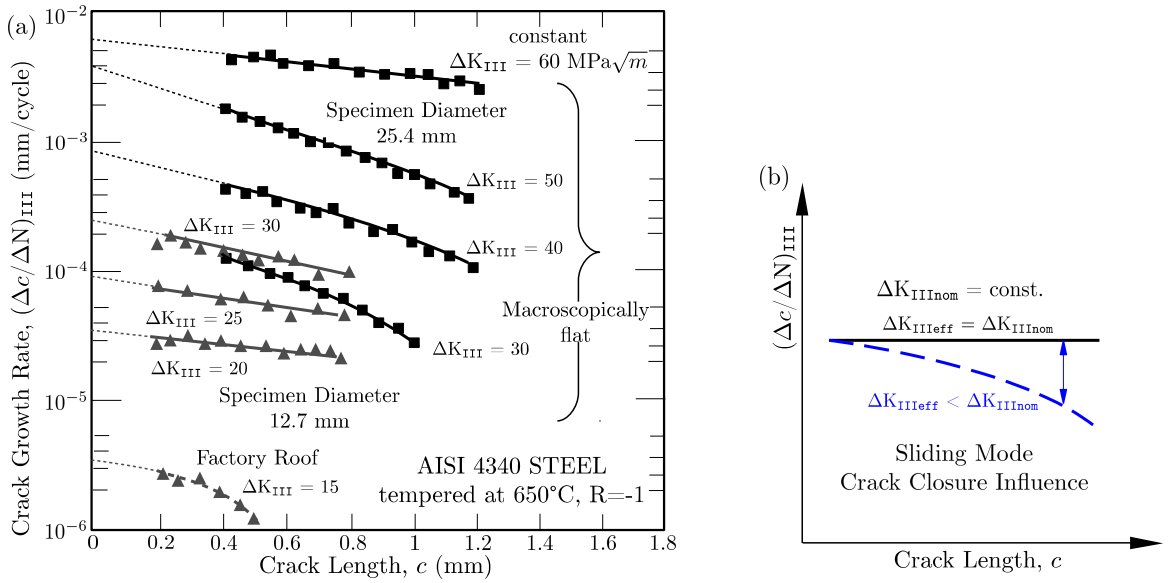

Fig. 2.34: (a) Comparison of fatigue crack growth rates in mode III as a function of crack length c (emanating from the notch root) for 12.7 and 25.4 mm diameter specimens stressed at constant ΔK_{IIInom} values [TSC 82, TSC 85]. (b) Schematic representation of the sliding mode crack closure influence on the crack growth rates depending on crack depth c measured under stress intensity control. The separation between the solid and dashed lines gives a measure of the influence of sliding mode crack closure on fatigue crack growth rates [TSC 85].

ture, loading amplitude, cyclic ratio, loading frequency or environment, that might influence mode III propagation [TSC 85].

In order to compare crack growth rates resulting from propagation in mode III with those of mode I, Tscheeg [TSC 83, TSC 85] plotted the extrapolated $(\Delta c/\Delta N)_{III}$ values and the fatigue crack growth rates $(\Delta c/\Delta N)_{I}$ as a function of $\Delta K_{I,IIIeff}$ (see Fig. 2.35). The comparison shows that the crack growth curve for the mode III is higher and steeper than that of mode I for the case of ΔK_{IIIeff} values ranging from 60 MPa$\sqrt{m}$ down to 20 MPa$\sqrt{m}$. An intersection point occurs between the two curves when ΔK_{IIIeff} values are slightly inferior to 20 MPa$\sqrt{m}$. This point indicates the existence of a mode III threshold, or in other words, a transition from shear mode III to tensile mode I crack propagation. This transition corresponds to crack branching and in some cases to the formation of the so-called *factory-roof*[1] morphologies. The remarkable surface roughness of these morphologies leads to increased crack closure effects and so, reductions in crack growth rates with increasing crack lengths (c) are more severe in factory-roof morphologies than in macroscopically flat ones (see Fig. 2.34a).

An example of the mode II-to-mode I transition (or branching) of a surface crack is shown in Fig. 2.36a. In this study, Murakami [MUR 02a] used a 0.47% carbon steel (S45C) material containing an artificial small hole of 40 μm diameter/depth in order to introduce an initial small crack (of 400 μm length) by preliminary fatigue push-pull testing. The loading of the sample was changed to reverse torsion (under a stress level higher than the fatigue limit) to monitor the change in crack morphology. The surface observations indicate that both mode I and mode II cracks started from the initial crack tips and that those in Mode II stopped propagation after ~10 μm. However, mode I cracks went on propagating and led to the final specimen failure. The Mode II cracks propagated in the transverse direction (0°) while the branched cracks grew in directions perpendicular to the

[1] A characteristic fracture surface where cracks essentially propagate on tensile mode I planes at ±45° forming a particularly rough topography

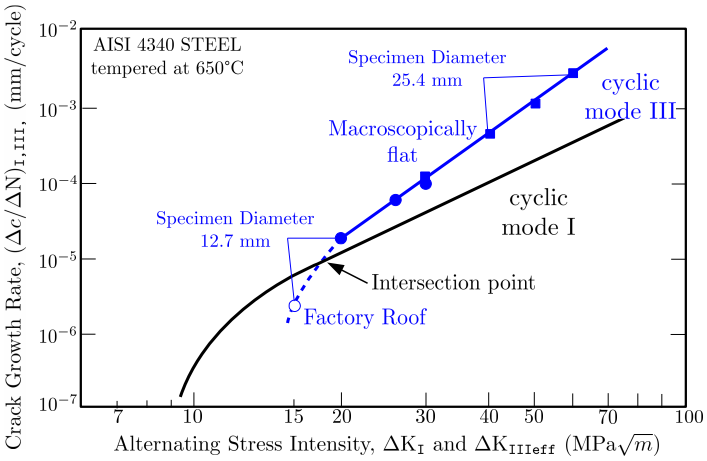

Fig. 2.35: Comparison of fatigue crack growth rates in mode I and mode III as a function of ΔK_{Ieff} and ΔK_{IIIeff}. Mode III values obtained through the extrapolation procedure that was introduced in Fig. 2.34b [TSC 85].

principal stresses (±45°). As schematically illustrated in Fig. 2.36b, the branching from mode II-to-mode I propagation consists in a tilt deflection where branched crack-planes intersects the initial crack-plane along a line (or curve). On the other hand, mode III cracks (found in the interior along the crack front) can only branch around a plane perpendicular to the initial crack-plane (see Fig. 2.36c) which means that the twist deflections is constraint to occur at microscopic ledges along the internal crack front.

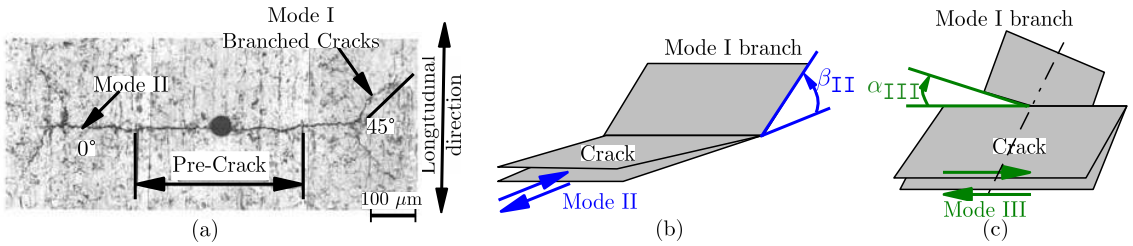

Fig. 2.36: (a) Example of the branching of torsion cracks formed at an initial semi-elliptical crack induced by prior push-pull fatigue loading [MUR 03]. (b) Schematic illustration of the tilt deflection which causes mode I branching from initial mode II crack propagation. (c) Schematic illustration of the twist deflection which causes mode I branching from initial mode III crack propagation.

2.3.2 Torsion fatigue behaviour in cast aluminium alloys

Very few results have been published on the torsional fatigue behaviour of aluminium cast alloys, to the best of our knowledge, only a few papers deal with this subject.

Kouitiri *et al.* [KOU 13] performed interrupted testing at varying number of cycles (R=-1 and τ_{max} = 80 MPa) on a AlSi7Cu05Mg03-T7 material in order to identify crack initiation mechanisms. After 150 000 cycles, surface observations showed multicracking nucleation occurring at eutectic Si particles, on planes of maximum shear stress (0°, see Fig. 2.37a). The second interruption at 250 000 cycles allowed detection of several newly formed small cracks with the difference that at that stage some of the microcraks nucleated at surface pores whose sizes are inferior to 100 μm. All these cracks became non-propagating and the final failure occurred at 1.2×10^6 cycles due to an undetected crack which nucleated at a surface pore visible with the naked eye. Macroscopic

propagation of this fatal crack was perpendicular to the loading axis.

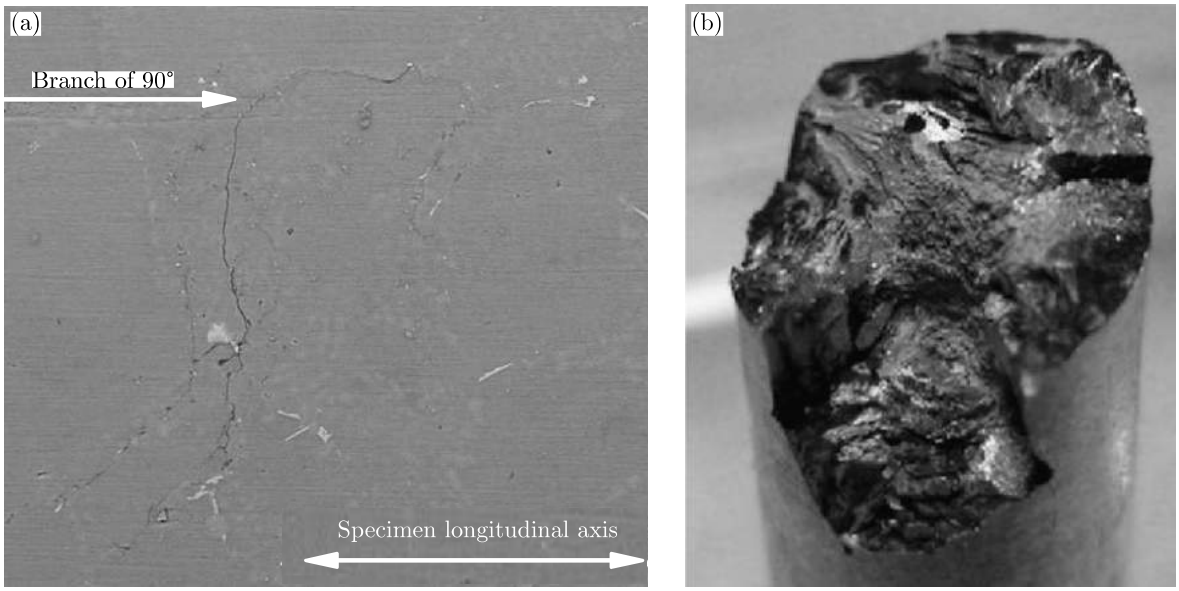

Fig. 2.37: (a) Crack initiation site occurred at 0° within an eutectic cluster after 150 000 cycles in a AlSi7Cu05Mg03-T7 material. A 90° branch was observed to occur when the microcrack was still evolving through the cluster. The testing parameter are: τ_{amp} = 80 MPa and R=-1 [KOU 13]. (b) Optical observation of a tortuous fracture surface obtained after 300 000 cycles at τ_a = 85 MPa and R=-1 using a A356-T6 aluminium alloy. Cracks predominantly propagated in mode III across transverse and longitudinal planes [ROY 11].

Roy *et al.* [ROY 11, ROY 12] also observed multiple initiation sites on a A356-T6 aluminium alloy cycled using the step technique[2]. Very tortuous fracture surfaces were formed due to the linkage of some individual crack planes propagating at different levels across specimen gages (see Fig. 2.37b). It is noteworthy that no evidence of macroscopic mode I propagation was found. Because of the rubbing between crack sides, fracture surfaces were severely reshaped and the identification of microstructural parameters responsible of crack nucleation was not possible for most of the cases. Despite this nucleation site masking, the authors noticed a definite decrease in endurance limit (τ_f) when defects larger than $\sqrt{A}$ = 300 μm were observed on fracture surfaces. Mode III crack propagation (on both transverse and longitudinal planes) was dominant with some microscopic mode I branching also being observed. Moreover, it seems that branching acted as a mechanism interconnecting the multiple nucleation sites. Another particularity of this material is that the pre-bifurcation crack length was on the order of millimetres which contrasts with the relatively short length (100-300 μm) observed in steel materials (see Fig. 2.38).

2.3.3 Summary on the background of torsional fatigue behaviour

The major points regarding the torsional fatigue behaviour can be summarised as follows:

1. Maximum shear stresses occur at transverse (0°) and longitudinal (0°) planes in torsion while they occur on planes at ±45° in tensile fatigue testing with no mode I stresses being present.
2. The nucleation period was observed to be smaller in torsional fatigue testing than in tension-compression.

[2]This technique consists in cycling each specimen at a given stress amplitude which is assumed to be below the expected endurance limit. When samples did not fail after 10^6 cycles, they are cycled again at a stress amplitude one step higher

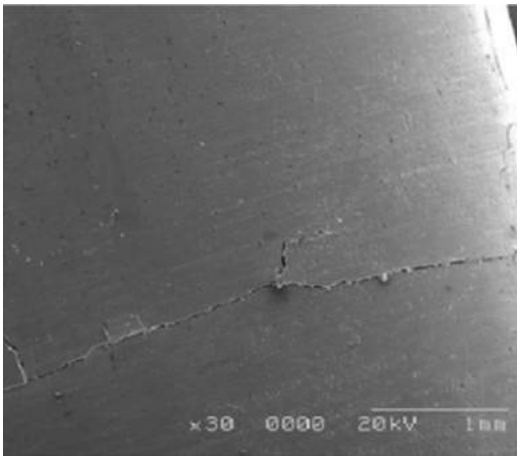

Fig. 2.38: Shear crack exhibiting some bifurcations on the gage of a torsion specimen occurred far from the fracture surface [ROY 12].

3. The lack of crack opening in torsion mode III propagation leads to sliding closure effects. As a consequence, fracture surfaces exhibit abrasion and rubbing marks.
4. For steel, the existence a mode III propagation threshold was observed. Once this threshold is reached, cracks bifurcate and continue propagation in mode I on planes at ±45°.
5. There exists a lack of experimental data with regard to aluminium cast alloys tested under torsional loading and the results to date do not relate the microstructural parameters (*e.g.,* porosity, SDAS, grain size) to nucleation and propagation of torsion cracks.

2.4 Torsional fatigue testing results

2.4.1 Torsional S-N curves and macro-analysis of fracture surfaces

Torsional fatigue testing parameters and specimen geometry was already introduced in § 1.2.4. The resulting S-N curve is shown in Fig. 2.39 along with the ENSMA tension-compression curve. These two curves tend to converge at 10^7 cycles giving a fatigue limit ratio of $\tau_f/\sigma_f = 0.95$, which is in good agreement with the values found in the literature for the case of cast materials. The non-valid results obtained using as-machined specimens with ∼25 μm notches at junctions are given in Appendix B.

Depending on fracture surface morphologies, the S-N curves can be divided into three regions along the vertical axis (τ_{max}) on Fig. 2.39. Here, Zone 1 (high stress level, τ_{max} = 110-105 MPa) corresponds to macroscopically flat fracture surfaces where cracks predominantly propagated on transverse planes (see Fig. 2.40a-c). Zone 2 (intermediate stress level, τ_{max} = 105-85 MPa) corresponds to tortuous fracture surfaces where cracks mainly alternate between transverse and longitudinal planes. Finally, the spiral-like crack profile at ∼45° presented in Fig. 2.40j corresponds to Zone 3 (low stress level, $\tau_{max} < 80$ MPa).

2.4.2 Micro-analysis of torsional fracture surfaces

2.4.2.1 Fractographic study in Zone 1

Fig. 2.41a presents fracture surface observations on one of the three specimens ascribed to Zone 1. All three fracture surfaces show several nucleation sites (never more than three were observed) in association with some murky debris (see Fig. 2.41b). Nucleation sites are easily identified because they exhibit crystallographic facets (Fig. 2.41c). No large casting defects were observed at the

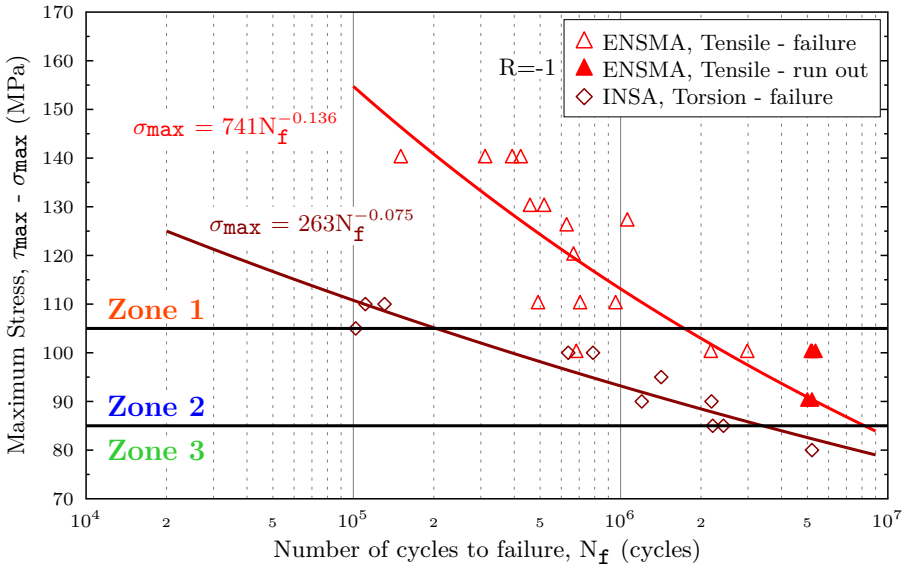

Fig. 2.39: Torsion and uniaxial tension S-N curves. The two horizontal lines indicate the limits of the three zones that were established depending on fracture surface morphologies (see Fig. 2.40 and the main text for details).

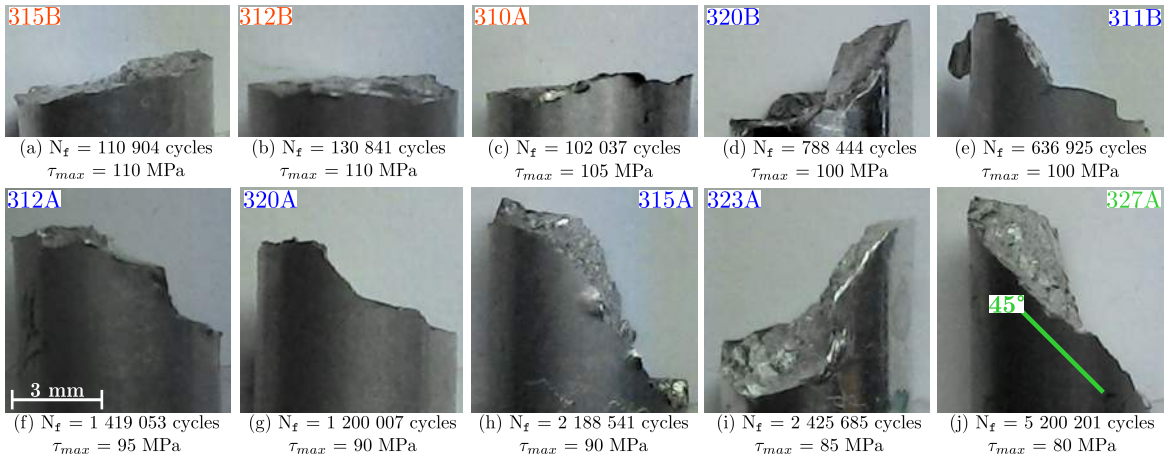

(a) N_f = 110 904 cycles, τ_{max} = 110 MPa
(b) N_f = 130 841 cycles, τ_{max} = 110 MPa
(c) N_f = 102 037 cycles, τ_{max} = 105 MPa
(d) N_f = 788 444 cycles, τ_{max} = 100 MPa
(e) N_f = 636 925 cycles, τ_{max} = 100 MPa
(f) N_f = 1 419 053 cycles, τ_{max} = 95 MPa
(g) N_f = 1 200 007 cycles, τ_{max} = 90 MPa
(h) N_f = 2 188 541 cycles, τ_{max} = 90 MPa
(i) N_f = 2 425 685 cycles, τ_{max} = 85 MPa
(j) N_f = 5 200 201 cycles, τ_{max} = 80 MPa

Fig. 2.40: (a)-(c) Zone 1: flat profiles formed at high stress levels perpendicular to the longitudinal axis. (d)-(i) Zone 2: tortuous crack profiles formed at intermediate stress levels. (j) Zone 3: spiral-like crack profile.

nucleation sites. As for crack propagation, the presence of some microsteps can be observed. It seems that local mode III propagation along longitudinal planes occurred to form the microstep observed on the left side of Fig. 2.41b. Some river patterns can be observed on the microstep formed at the right lower side of this figure which suggests local crack propagation in mode I. Fig. 2.41d shows some circumferential patterns which sometimes are formed on mode III fracture surfaces.

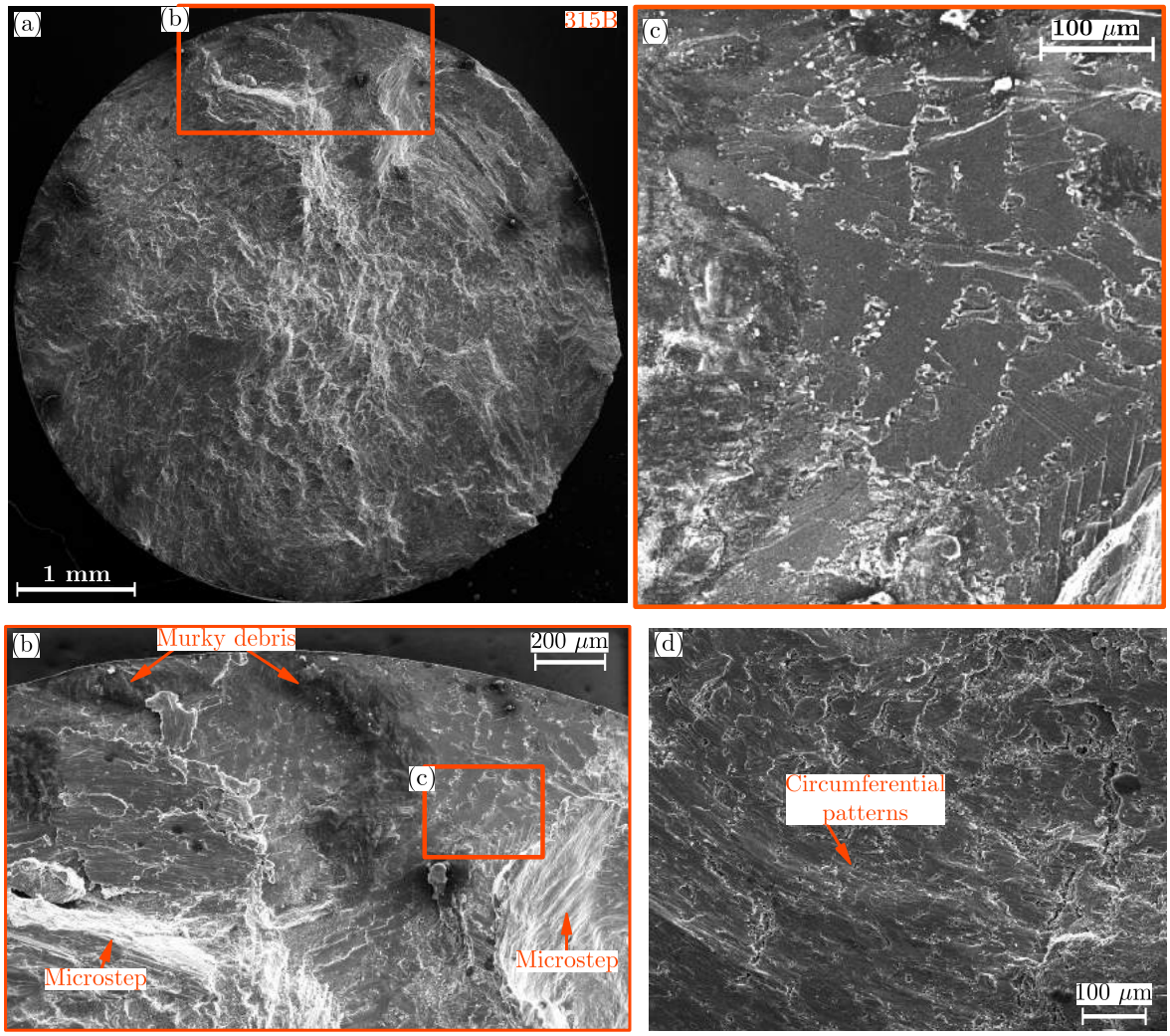

Fig. 2.41: (a) SEM observation at low magnification on the fracture surface of 315B specimen. The testing parameters are: $\tau_{max} = 110$ MPa, $N_f = 110\,904$ cycles. (b) Higher magnification on one of the nucleation sites observed. Some murky debris and two microsteps can be observed. (c) Detail on the crystallographic facets formed at nucleation sites. (d) Higher magnification on a mode III fracture surface showing some circumferential patterns (also known as rubbing marks).

2.4.2.2 Fractographic study in Zone 2

Fig. 2.42 presents two of the fracture surfaces ascribed to Zone 2 (six in total, the other four fracture surfaces which correspond to this zone are given in Appendix C). Their study reveals the dominance of mode III crack growth with the particularity that propagation on longitudinal planes is larger and more obvious than in Zone 1. Several nucleation sites can be observed per specimen

(between 1 and 4). They exhibit large and thick murky debris that foul and mask the fracture surface and sometimes even produce charging effects in the SEM. Fig. 2.43 gives two examples of nucleation sites where the presence of crystallographic facets can be barely observed below the murky debris. It is thought that no important casting defect is present beneath this debris for all six specimens of Zone 2.

Regions exhibiting river patterns are also found on fracture surfaces of Zone 2 and they are also larger and more obvious than in Zone 1. Fig. 2.44a shows an example of the patterns observed on the fracture surface of 312A specimen. The presence of fatigue striations was found when studying this surface at higher magnification (see Fig. 2.44b) which indicates that, locally, propagation occurred in a tensile opening mode I. Some mode III circumferential patterns can be observed on the upper transverse plane.

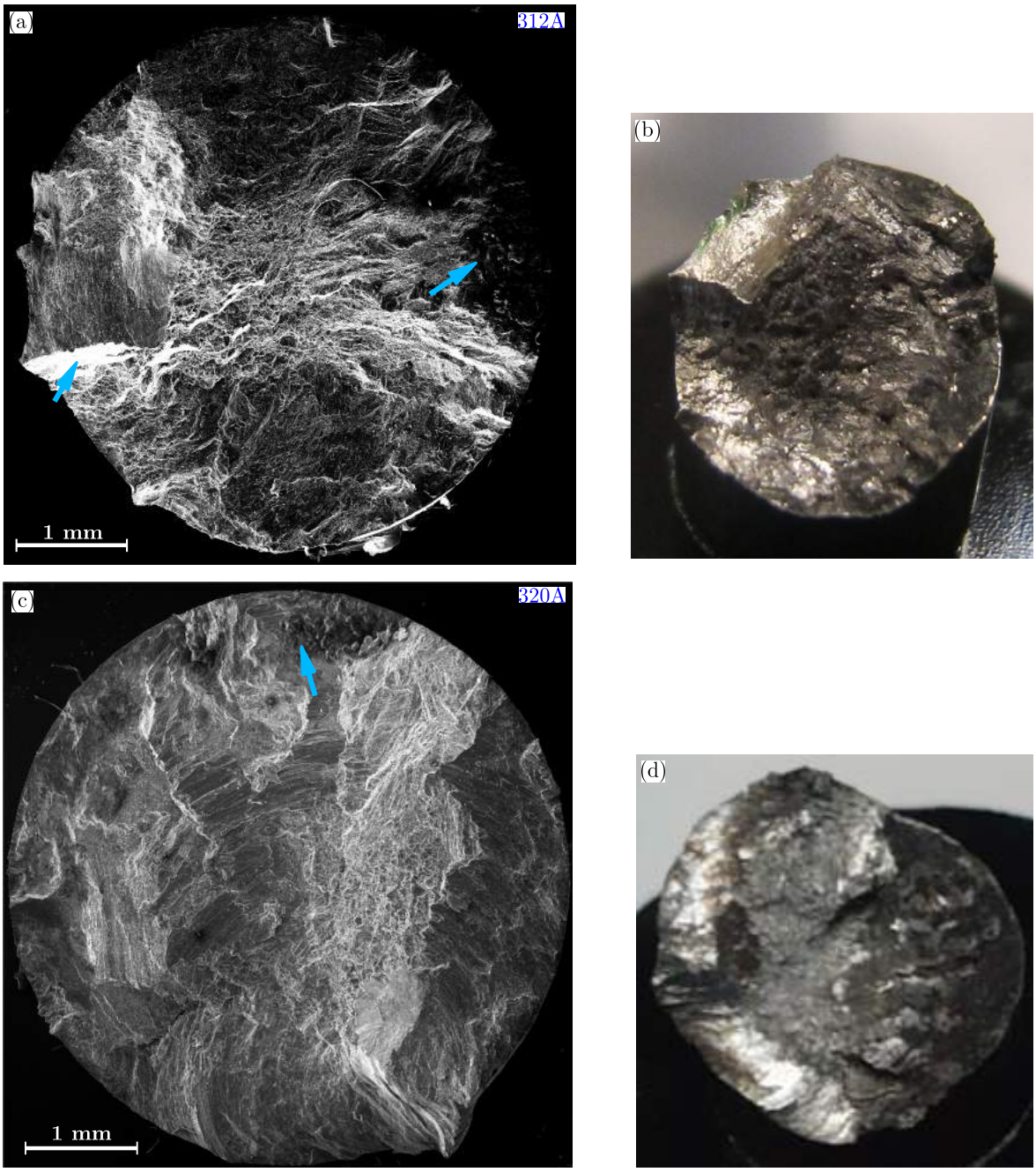

Fig. 2.42: (a) SEM observation at low magnification on the fracture surface of 312A specimen. The fatigue testing parameters are: $N_f = 1\,419\,053$ cycles, $\tau_{max} = 95$ MPa. (b) 3D optical observation on the fracture surface of 312A specimen. (c) SEM observation at low magnification on the fracture surface of 320A specimen. The fatigue testing parameters are: $N_f = 1\,419\,053$ cycles, $\tau_{max} = 95$ MPa. (d) 3D optical observation on the fracture surface of 320A specimen. The right blue arrow on image (a) and the one on image (c) indicate nucleation sites. Higher magnification of these sites is given in Fig. 2.43. Left blue arrow on image (a) indicates a region of mode I propagation (see Fig. 2.44).

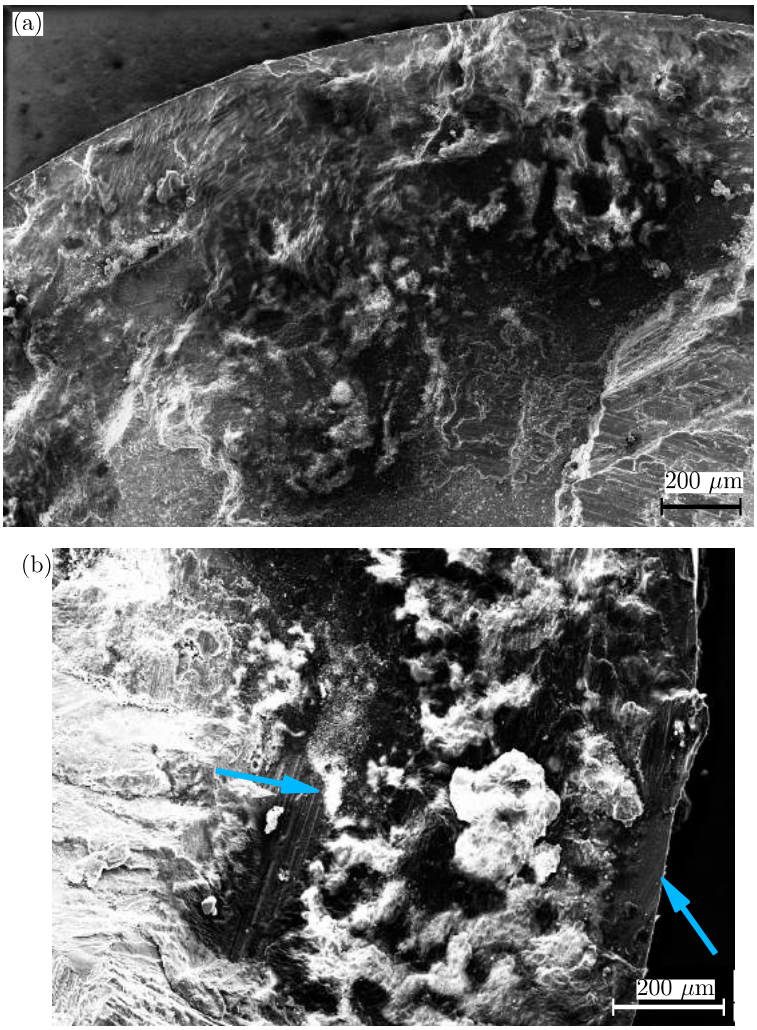

Fig. 2.43: (a) Higher magnification on 320A fracture surface where a thick murky layer fouls and mask the nucleation site. (b) The same as before but for 312A specimen. Here, some crystallographic facets (blue arrows) can be observed.

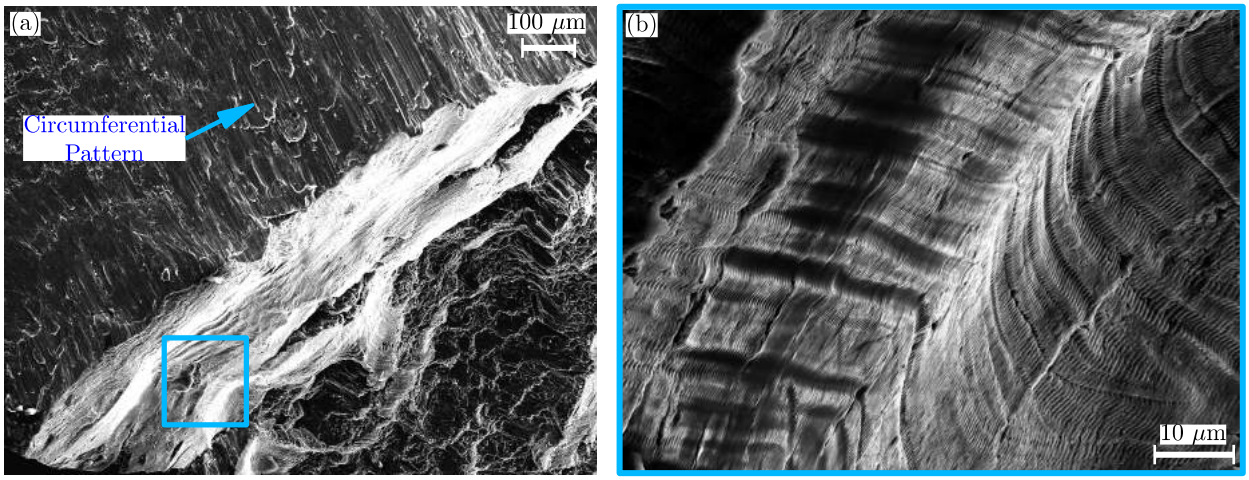

Fig. 2.44: (a) Higher magnification of 312A fracture surface showing evidence of mode I crack propagation. (b) Higher magnification of the previous image showing the presence of mode I fatigue striations.

2.4.2.3 Fractographic study in Zone 3

Only one specimen was cycled at low stress levels. SEM observations on the fracture surface (see Fig. 2.45a) reveals the presence of two different nucleation sites which exhibit layers of murky debris similar to those observed in Zone 2. No presence of casting defects is suspected. Macroscopic mode I propagation is dominant although some local mode III microstepping (small amounts of crack propagation alternatively occurring on transverse and longitudinal planes) is observed. Two small mode III flat regions with some circumferential patterns are also observed at both the top and the bottom of the spiral profile.

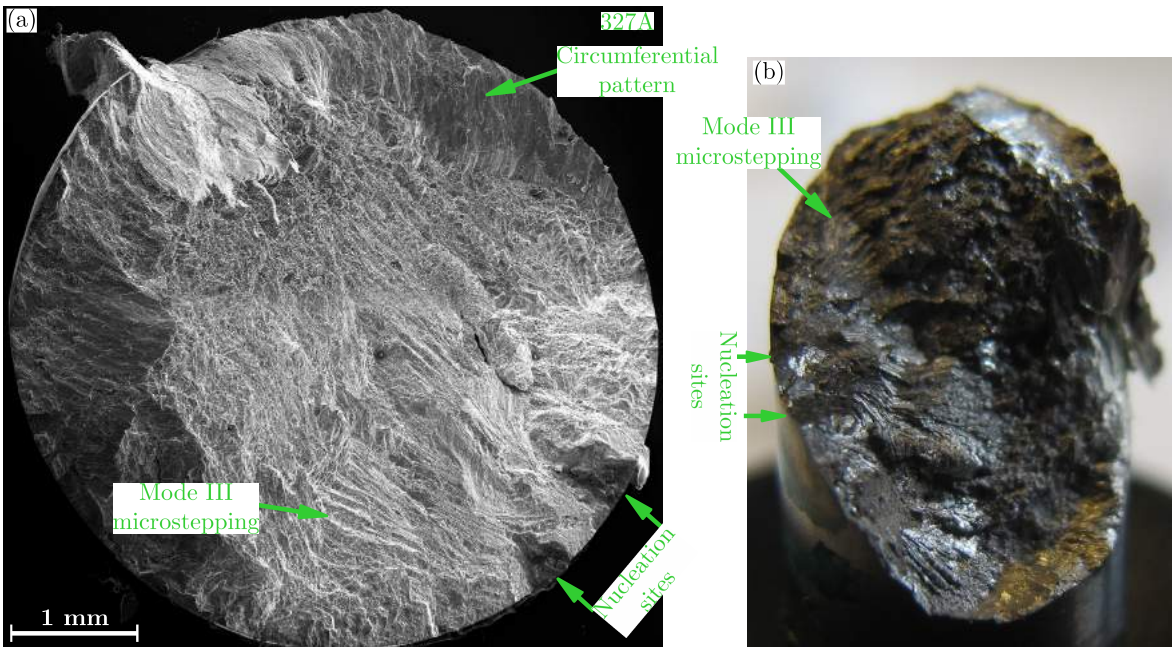

Fig. 2.45: (a) SEM observation at low magnification on the fracture surface of 327A specimen. The fatigue testing parameters are: $N_f = 5\ 200\ 201$ cycles, $\tau_{max} = 80$ MPa. (b) 3D optical observation on the fracture surface of 327A specimen.

Two main points must be kept in mind from this fractographic study:

- Crack nucleation (mode II and III). Crack lips contact produces murky debris at the various nucleation sites that can be observed on torsion fracture surfaces. In this study, ten fracture surfaces have been carefully studied and, even though the presence of debris obstructed a detailed analysis of nucleation sites, it was concluded that no important casting defect was present at the nucleation sites.
- Propagation mode. Transverse mode III is dominant in Zone 1. Mode III is also dominant in Zone 2 although propagation alternates on transverse and longitudinal planes, and occasional propagation in mode I has been observed. For stress levels close to the fatigue limit, fractographic observations indicate that mode I propagation at ∼45° is dominant.

2.4.3 Secondary crack observations on the free surface of fractured specimens

Apart from the fatal crack, the cycled specimens showed extensive damage accumulation (around 4 to 8 secondary cracks were observed for each specimen) randomly distributed over the entire gage length. Secondary cracks are observed in the three zones defined previously on the S-N curves.

They are however larger and more obvious within Zone 2 where some of them can even be observed with the naked-eye. Some of the most remarkable findings are presented in what follows.

Two long secondary cracks (which extend more than one half of the specimen diameter) along with five others crack (with lengths[3] ranging between ∼1.5 and 5 mm) were noticed on the free surface of 311B specimen. Fig. 2.46 presents the secondary crack termed as 311B-1. Even though the sequence of cracking events is unknown, it seems likely that this crack is the result of the linkage of two different cracks. The blue arrows indicate the presumed nucleation sites. These sites are identified based on the fact that torsion cracks predominantly nucleate in shear mode on planes close to 0°. The presence of some abrasion debris can also help to identify nucleation sites. Therefore and starting from the bottom arrow and following right, it can be thought that this crack grew a distance of ∼850 μm at about 0° until it was deflected. The crack path is smooth and some debris can be observed between the lips of the crack, just behind the deflection. The deflected crack macroscopically grew at 36° for ∼500 μm creating a mode I crack path where two microsteps at about 0° and 90° can be observed. This deflection is followed by a sequence of four more deflections showing smooth paths at 80°, 83° and 89°. Small crack deflections are observed at 29° and 0°. The crack grew in this manner for ∼1 mm before linking with the upper one. The crack morphology and direction indicate that the shear mode is dominant with possible mode I growth occurring in the deflection at 36 °. It must be pointed out that, with the exception of the nucleation, none of the observed crack planes correspond to planes of maximum shear and normal stresses.

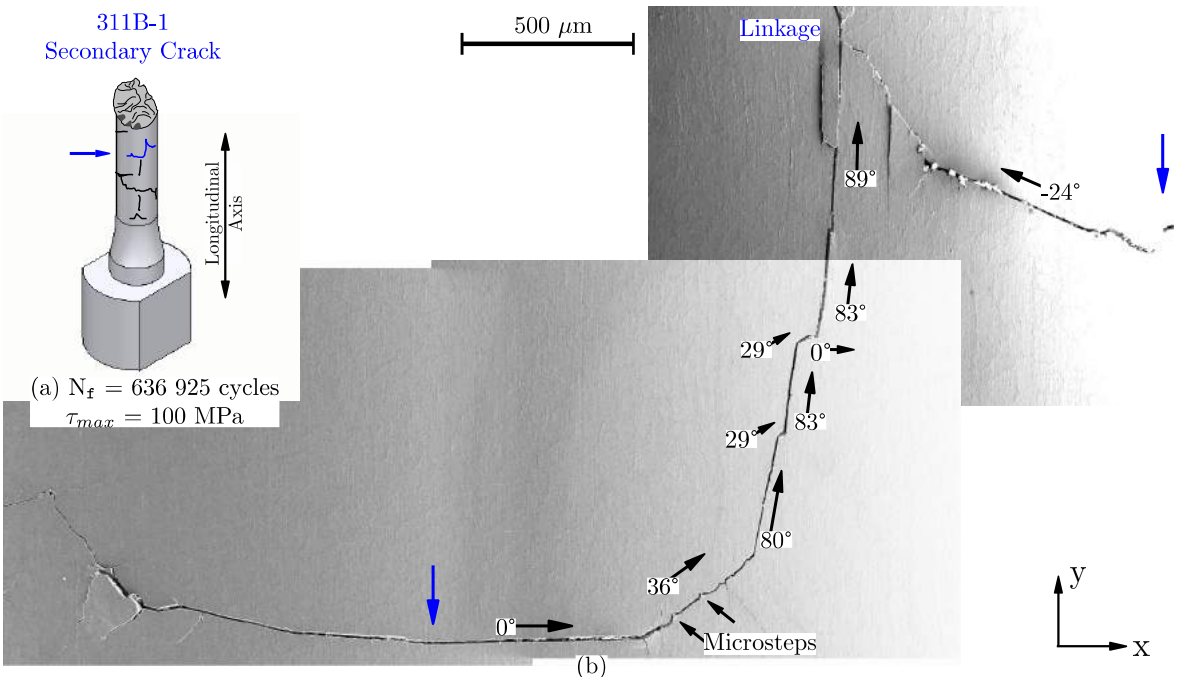

Fig. 2.46: (a) Schematic illustration of one half of the fractured gage showing the location of 311B-1 secondary crack. (b) SEM image of this crack where the two blue arrows indicate the presumed locations of the nucleation sites.

With regard to the 311B-1 top crack, it is thought that its nucleation site was not observed in this image. Starting from the top right (blue arrow) and following left, this crack presents first a

[3]These lengths were directly measured on SEM images and corrected by taking into account the specimen curvature. This correction is not applied to longitudinal cracks. This is true for all measurements performed on the free surface.

wavy path and then a smooth path developed at -24° for ∼600 μm. Some abrasion debris are also observed behind the deflection that linked the top and bottom cracks. During this deflection, the crack seems to have propagated alternatively on planes at -54°, -33° and 90°. Mode III also seems to dominate.

Fig. 2.47b shows another example of the linking phenomenon which resulted in a much more extensive crack. This crack exhibits four points which are suspected to be possible nucleation sites and which are located relatively close to each other (from 1.5 to 3 mm). Fig. 2.47c presents one of the linkage points where three scenarii are possible: (i) the top left crack was deflected and reached the right one; (ii) the other way round, the bottom right crack was deflected to reach the left one or; (iii) both cracks were deflected and they met at some point in between. It would be interesting to know whether the linkage occurs because the presence of the other crack leads to a local stress concentration which induces the deflection or if the deflection is induced by the propagation mechanisms themselves (*e.g.,* the mode III threshold is reached). Several PSBs occurring at 0° and 90° are also observed.

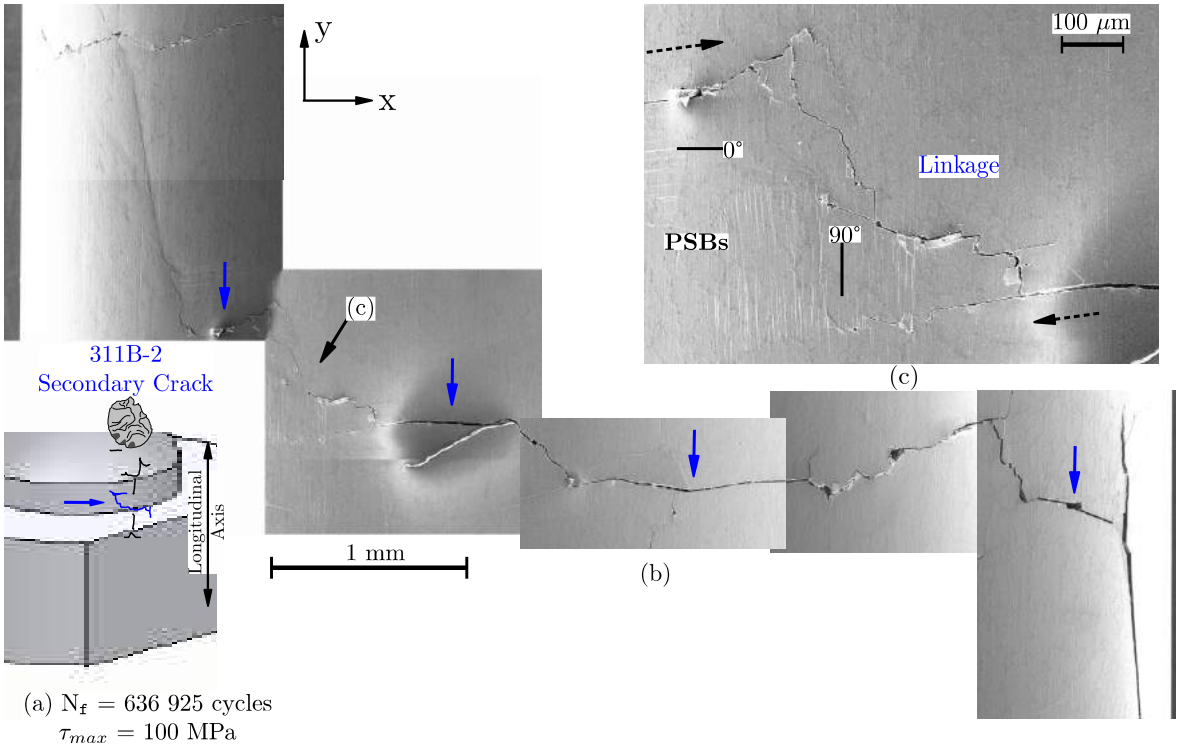

Fig. 2.47: (a) Schematic illustration of one half of the fractured gage showing the location of 311B-2 secondary crack. (b) SEM image of this extensive crack which is presumed to be the result of several linkages. (c) Higher magnification of a linking point where some PSBs at 0° and 90° can be observed.

BSE and EDS observations were also performed in order to investigate the influence of the microstructure on crack propagation. The 311B-2 secondary crack is an example of such analysis and it is presented in Fig. 2.48a-b. A mode III longitudinal crack showing smooth paths at 81° and 76° with branches at the top and the bottom is observed. Fig. 2.48c shows the top branching where the crack bifurcated to the left at -45° while meandering through eutectic particles. The path of the right branch is more complex, with the crack propagating first at 42° before being deflected after 50 μm and starting a meandering through eutectic particles. The propagation here is thought to occur in tensile mode I as both crack paths are close to 45°.

Fig. 2.48d shows the point where this vertical crack changed propagation from 81° to 76° (blue arrow). It occurred at a cluster of eutectic particles that may correspond to a grain boundary. It is noteworthy that the crack propagating at 81° was deflected and meandered through a big cluster of eutectic particles just a dendrite cell before the deflection. Considering the shape and total length of this crack (∼2.5 mm), nucleation most certainly occurred at some point near this location.

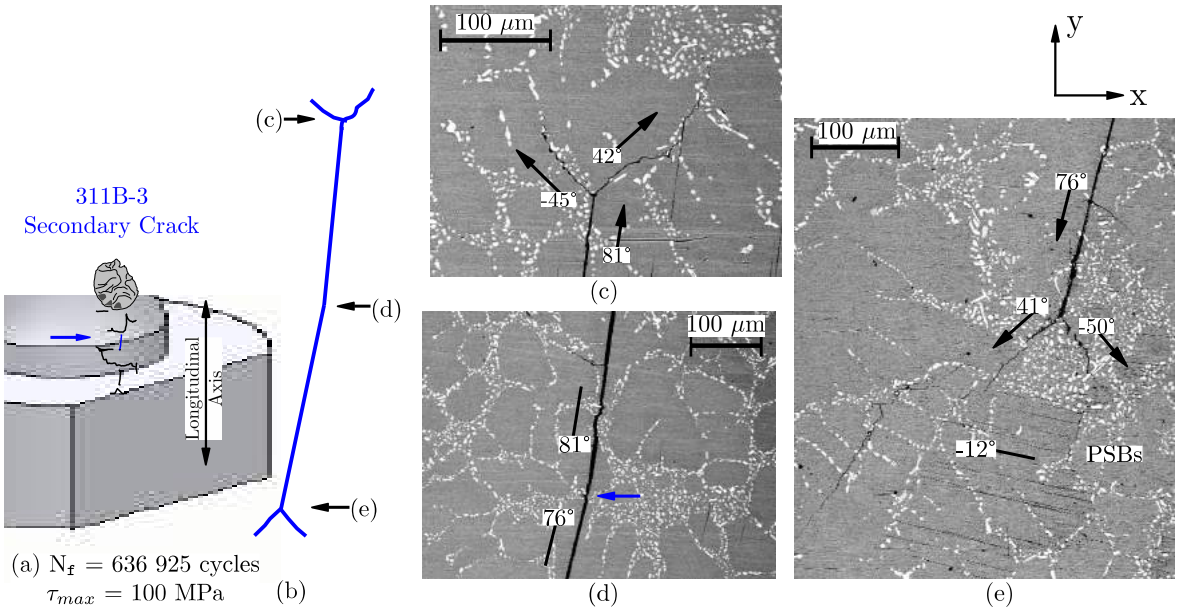

Fig. 2.48: (a) Schematic illustration of one half of the fractured gage showing the location of 311B-3 secondary crack. (b) Schematic drawing of this longitudinal crack where the arrows indicate the points of crack branching and deflection. (c) BSE image of the crack branching occurring at the top. (d) BSE image of the crack deflection at the middle. (e) BSE image of the crack branching at the bottom.

Fig. 2.48e corresponds to the bottom branching where the crack propagated at 76° before deflecting in two directions at 41° and -50° at the beginning of a large cluster of eutectic particles. After only ∼30 μm of growth both branches followed an erratic behaviour. In addition, PSBs at -12° can also be observed confined between the branched cracks. Finally, it was noticed that, for the whole length of this crack, the Si particles were debonded and remained unbroken.

Fig. 2.49b shows a small shear crack whose three deflections occurred at the encounter of Si particles. It is unknown if the crack changed its propagation direction because the presence of Si produced a deflection or because these Si particles could correspond to grain boundaries and the crack is therefore following different crystallographic paths within each grain.

312A-1 secondary crack (see Fig. 2.50b) is another example of a transverse torsional crack which was deflected after some propagation. The difference in this case is that after deflection (Fig. 2.50c) the crack started to grow by alternating shear propagation on longitudinal and transverse planes which led to the formation of microsteps. This characteristic was also found on the other crack that was observed on this specimen gage and might indicate that with increasing crack length and for lower stress levels this material develops other propagation mechanisms than mode I growth.

Post-mortem microscopic observations performed on the free surface revealed several secondary cracks of different lengths occurring within the specimen gages. The crack morphology study indicates that crack propagation can occur on planes other than the planes of maximum shear and normal stresses. Moreover, propagation paths seem to be highly influenced by the underlying microstructure.

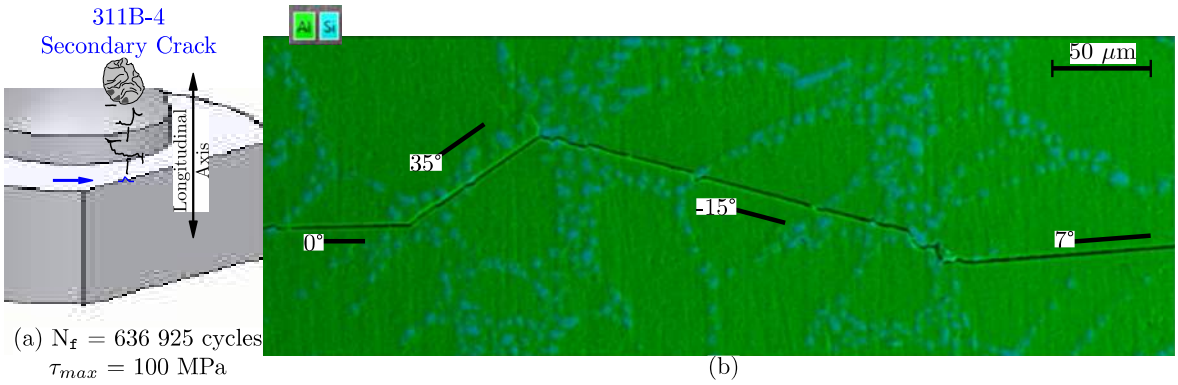

Fig. 2.49: (a) Schematic illustration of one half of the fractured gage showing the location of 311B-4 secondary crack. (b) EDS image showing the crystallographic path formed by this crack.

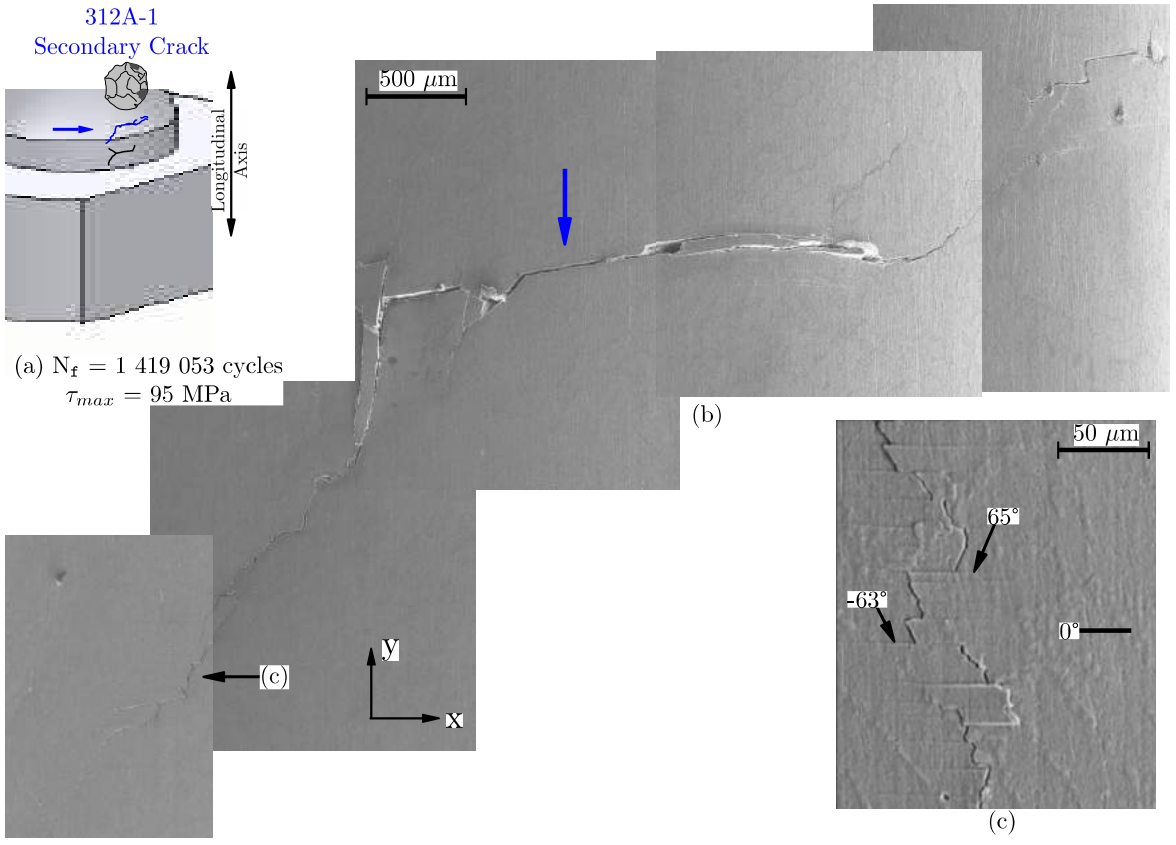

Fig. 2.50: (a) Schematic illustration of one half of the fractured gage showing the location of 312A-1 secondary crack. Two cracks were observed on this gage. (b) SEM image of the crack path. The blue arrow indicates the presumed location of the nucleation site. (c) Higher magnification of the bottom left part of the crack.

2.4.4 Observations on longitudinal cuts of torsion specimens

In order to further investigate the influence of the microstructure on crack propagation, longitudinal cuts were performed on specimens showing significant secondary crack damage and so this type of observation has been limited to specimens ascribed to Zone 2. After longitudinal sectioning, the cuts were polished following the EBSD protocol described in § 1.3.2.3.

Fig. 2.51c shows the path followed by 312A-1a_1 crack when progressing towards the interior of the specimen. This crack is 2 mm long and first grew in Grain 1 on two parallel crystallographic paths at -18°. The EBSD analysis confirmed that this direction corresponds to a {111} plane. A branched crack (termed as 312A-1a_2) was formed near behind the free surface. After branching (which produced considerable abrasion damage), 312A-1a_2 crack continued propagation though Grain 9, Grain 10, and Grain 11, with the particularity that this propagation was discontinued every time the crack passed into the next grain (discontinuities are indicated with two white arrows on Fig. 2.51). It is also observed that 312A-1a_2 crack partially grew on a {111} plane at -76° when propagating through Grain 9.

The study of the remaining 312A-1a_2 crack path is difficult to analyse. Some portions of the crack path either has been altered by frictional contact or exhibits a non-crystallographic propagation. In addition, the propagation direction does not correspond to the planes of maximum shear and normal stresses. This same conclusion can be extended to 312A-1a_1 crack, from Grain 2 to Grain 8. In any case, the propagation behaviour seems to be highly dependent on the crystallographic orientation of each grain as both crack morphology and/or direction are observed to change from one grain to the next.

Fig. 2.52 presents the progression of 312A-1a_1 within Grain 2 where some branches were formed on {111} planes at 90°. These longitudinal and crystallographic branches are only found in Grain 2 which means that they are favoured by this particular crystallographic orientation. It is noteworthy that the top crystallographic crack observed in Grain 1 (the one with the branch) remained arrested at the grain boundary and formed a series of PSBs within Grain 2. The bottom crack of Grain 1 is the one which managed to cross into Grain 2. Interestingly, this crack must have been formed within the interior of the sample because its presence is not observed on the free surface.

Apart from 312A-1a_2 branch, another crack branch (termed as 312A-1a_3) is distinguished in Fig. 2.51c. An explanation to the formation of this latter branch could be that it was originated within Grain 5 and then followed a backward propagation through Grain 4, assuming that a backwards progression could actually occur. A higher magnification image of this branch is given in Fig. 2.53a where a darker zone of ∼5 μm width was formed just before the branching. EDS analysis (see Fig. 2.53b) indicates that this darker zone contains oxygen which is most likely caused by thermal oxidation resulting from the crack lips contact.

Another example of how the crack paths are influenced by the microstructure is given in Fig. 2.54. In this case, 320A-1a_1 crack evolved differently through each one of the ten observed grains. Along this crack path, the three first grains exhibit {111} crystallographic propagation (Grain 1 at 7°, Grain 2 at 8° and Grain 3 at 25°) and a crack branching occurs at a triple point between Grain 7, Grain 8, and Grain 10. The inferior branch progressed at -47° in Grain 10, a direction which corresponds to a {111} crystallographic plane. The bifurcation occurring just at the grain boundary suggests that the microstructure is another factor that can produce crack branching. Nevertheless, it is unclear whether the microstructure can by itself produce the branching or is acting in combination with other factors such as the decreasing remote shear stress τ and the increasing crack length.

Fig. 2.55b shows a 750 μm long crack of 750 μm length which was formed at 26° and created extensive abrasion debris. The width of the worn area reaches a thickness of ∼45 μm across the

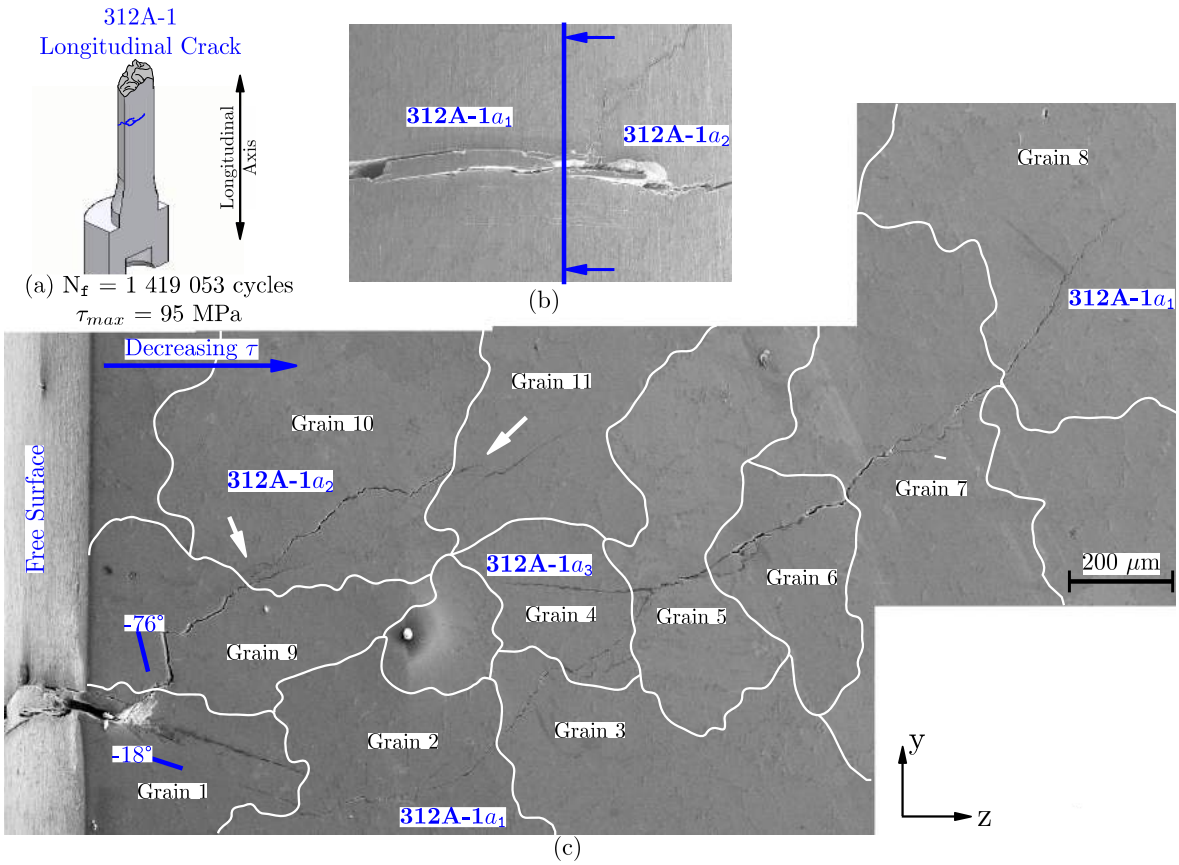

Fig. 2.51: (a) Schematic illustration of the longitudinal cut performed on 312A-1 secondary crack. (b) SEM image showing the approximate location of the cut on the free surface. (c) SEM image on the cut showing the crack path formed towards the interior of the specimen. 312A-1a_1 crack reached a 2 mm length. White lines indicate the approximate location of the grain boundaries obtained by EBSD. The two white arrows indicated the crack discontinuities observed when 312A-1a_2 crack crosses the grain boundaries of Grain 10 and Grain 11.

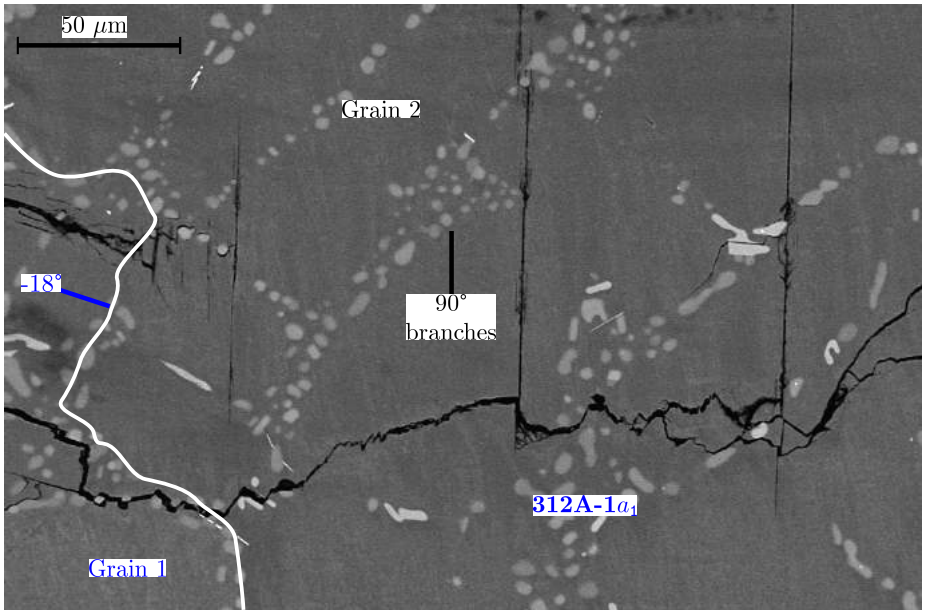

Fig. 2.52: BSE image of 312A-1a_1 crack path within Grain 2 where some PSBs at 90° are observed.

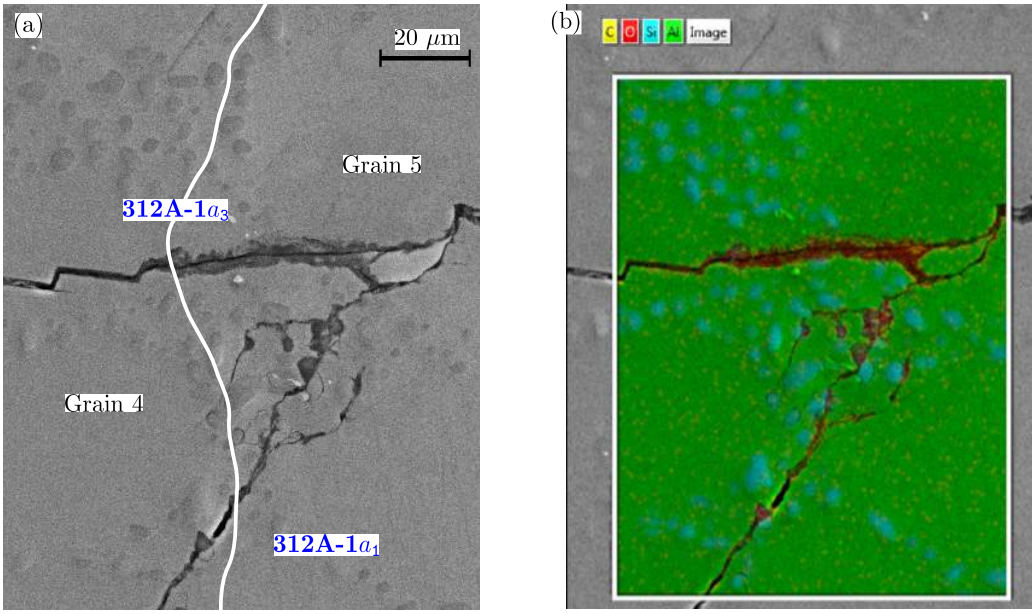

Fig. 2.53: (a) SEM image of the branch which occurred within Grain 5 and formed 312A-1a_3 crack. The white line indicates the approximate location of the grain boundary. (b) EDS analysis performed on the same zone as before and where the red colour indicates the presence of oxygen.

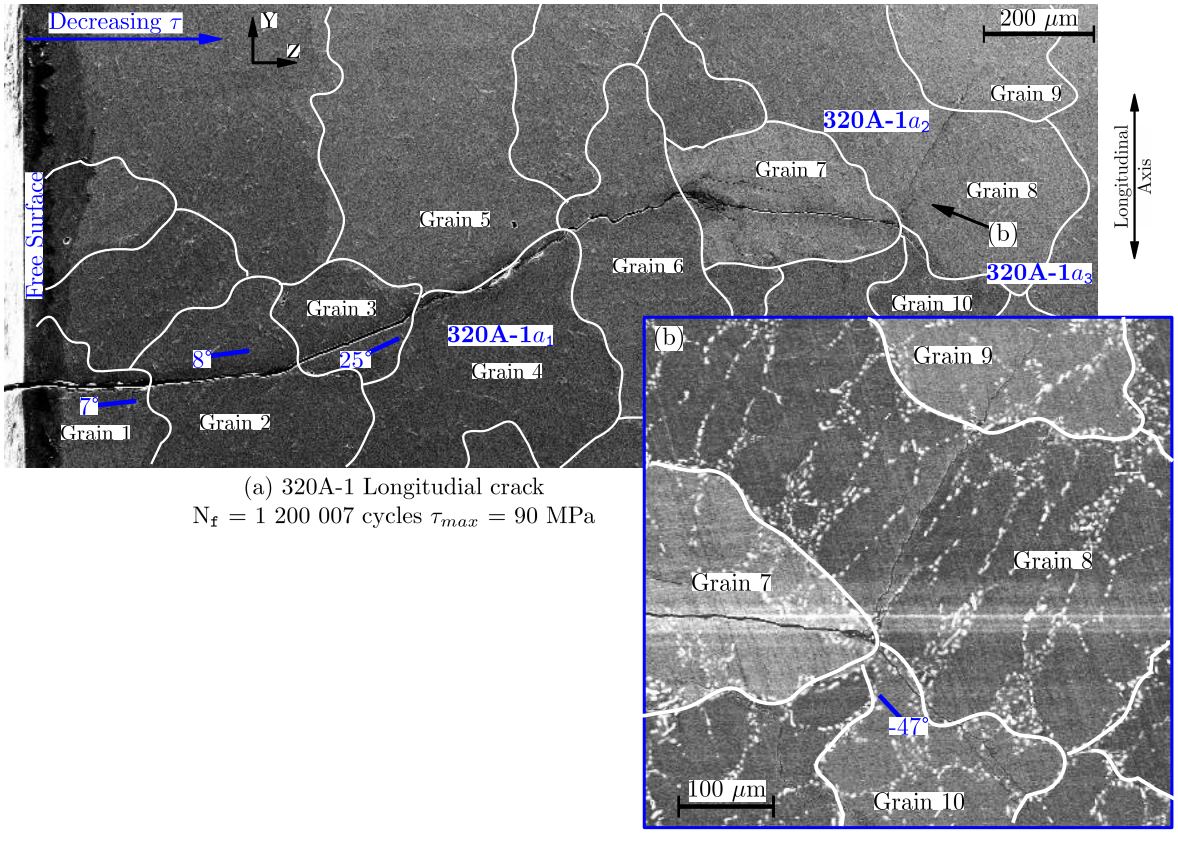

(a) 320A-1 Longitudial crack
N_f = 1 200 007 cycles τ_{max} = 90 MPa

Fig. 2.54: (a) SEM image on the cut of 320A-1 specimen presenting the crack path formed towards the interior of the specimen. The white lines indicate the approximate location of the grain boundaries obtained by EBSD. (b) Higher magnification (BSE image) at the end of the crack where a very pronounced bifurcation occurred at a triple point. The total length of this crack from the free surface is 1740 μm.

two crack faces (white arrow) and is responsible for the opening of the crack at the free surface (see Fig. 2.55b). The presence of the branch (Fig. 2.55d) might be induced by the microstructure (*e.g.* by a grain boundary, as the contrast of the image seems to indicate – no EBSD analysis was performed on this crack). As a result, the frictional contact was increased by a clamping effect that closed the crack enhancing the abrasion damage. Another possibility is that crack propagation was severely hindered by the abrasion, and this in combination with the decreasing remote τ could be responsible of the subsequent crack branching.

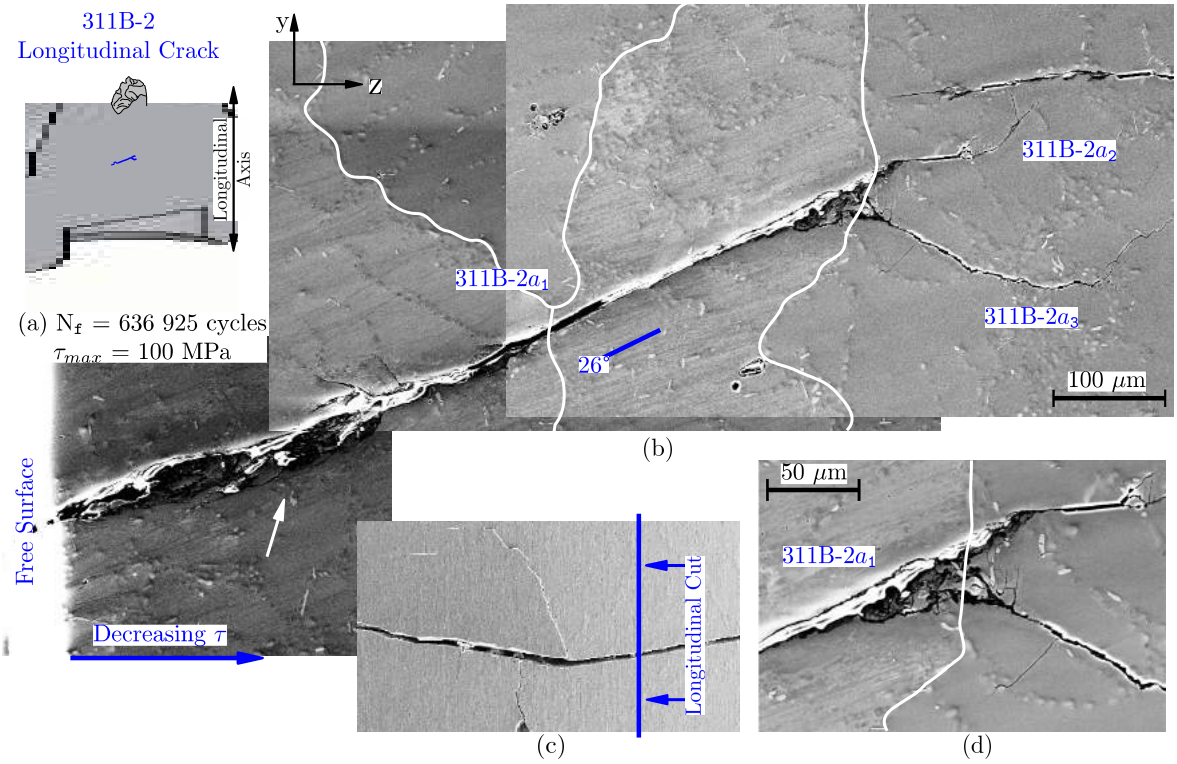

Fig. 2.55: (a) Schematic illustration of the longitudinal cut performed on 311B-2 secondary crack. (b) SEM image on the cut showing the crack path formed towards the interior of the specimen. The white lines indicate the presumed location of some grain boundaries (no EBSD analysis was performed on this sample). (c) SEM image showing the approximate location of the cut on the free surface. (d) Higher magnification of the branch. The white arrow indicates the extensive abrasion debris formed under the free surface.

- SEM observations on the longitudinal cuts confirmed that below the surface the observed cracks strongly interact with the microstructure (grains). The crack paths are complex, crack discontinuities and bifurcations are observed, usually between grain boundaries, and the chronology of events is hard to read.
- Three reasons, other than the decreasing remote shear stress could explain the frequent occurrence of branches:
  (i) a change in orientation at grain boundaries,
  (ii) the increasing surface of contact between crack lips,
  (iii) a combination of both.

2.4.5 Crack monitoring results

329B specimen was mechanically ground and polished in order to obtain a flat surface where *in situ* optical observations of crack growth could be performed. The stress level was fixed at 95 MPa (Zone 2) which gives an expected fatigue life of 800 000 cycles. The first observations were performed after 100 000 cycles without any crack being reported. After another interval of 100 000 cycles, the optical observations revealed a multisite nucleation where three different microcracks were observed. The specimen failed outside of the gage length after additional 40 000 cycles due to a technical problem, the total life being 240 000 cycles.

The progression of 329B-Crack 1 is given in Fig. 2.56b-c. After 200 000 cycles, this crack was 753 μm long following the same direction at $\sim$12° and only a small deflection located at the left end was observed. The length after 240 000 cycles was 1360 μm with the crack showing deflection at both ends. The two other cracks exhibit the same pattern as Crack 1, *i.e.,* nucleation following the same direction and a deflection after some propagation. 329B-Crack 2 reached a final length of 543 μm while 329B-Crack 3 was 1073 μm long. Assuming a fatigue life of 800 000 cycles, this means that under torsional loading 30% of expected fatigue life was devoted to nucleate and propagate millimetric cracks ($\sim$1000 μm long).

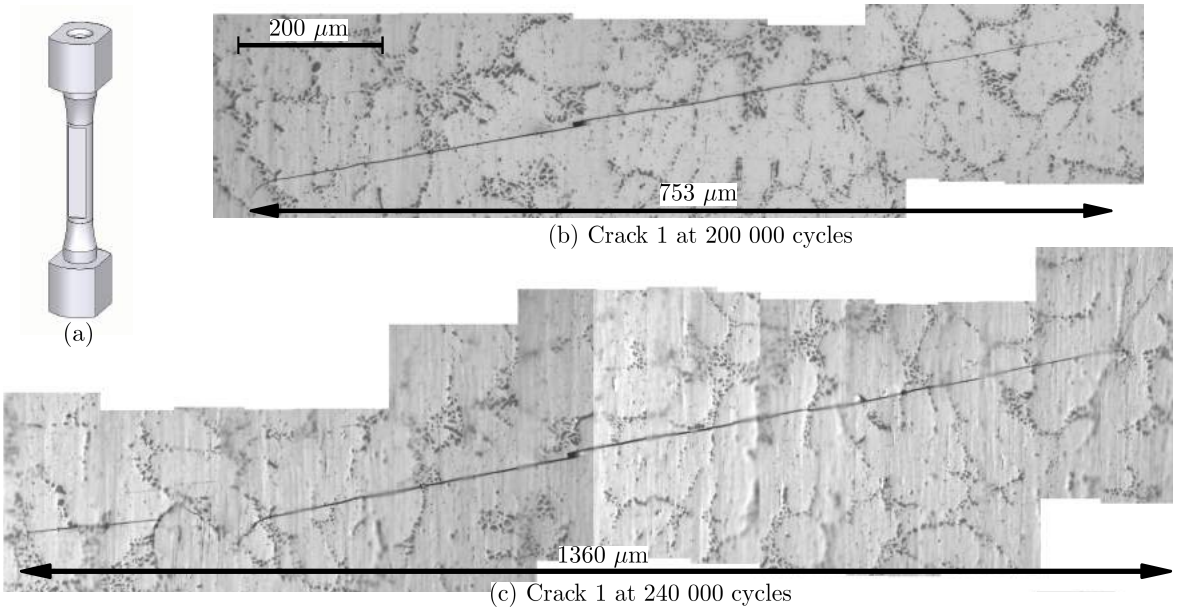

(a)

(b) Crack 1 at 200 000 cycles

(c) Crack 1 at 240 000 cycles

Fig. 2.56: (a) 3D rendering of a torsion specimen showing a flat along the gage length. (b) MO image of 329B-Crack 1 progression after 200 000 cycles. (b) The same as before but for 240 000 cycles.

2.4.5.1 SEM observations and EBSD analysis

The flat surface was repolished with 3 μm oil-based diamond paste and, eventually, with 0.02 μm colloidal silica in order to ensure an optimum surface preparation to obtain an adequate indexing rate in EBSD. Fig. 2.57a presents the results for Crack 1 within Grain 1 and Grain 2. Those two grains share a nearly common $\{11\bar{1}\}$ plane which exhibits almost the same θ (12° and 11°) and ψ (11° and 9°) angles so Crack 1 could propagate about 750 μm in approximately the same direction (see Fig. 2.57a and Fig. 2.57c). On the left side, the crack was reorientated towards 0° when passing into Grain 3 (Fig. 2.57b). On the right side, Fig. 2.57d shows that the crack meandered though eutectic particles forming a non-crystallographic path at an overall crack direction of 59°.

The propagation directions of both Grain 3 and Grain 4 do not correspond to any {111} plane although for Grain 3 it matches a plane of maximum shear stress. Finally, the comparison of both EBSD and monitoring results reveals that the first 200 000 cycles were devoted to nucleate and propagate a crystallographic crack along Grain 1 and Grain 2. In the remaining 40 000 cycles, 329B-Crack 1 was able to cross and propagate about ∼100 μm through the neighbouring grains.

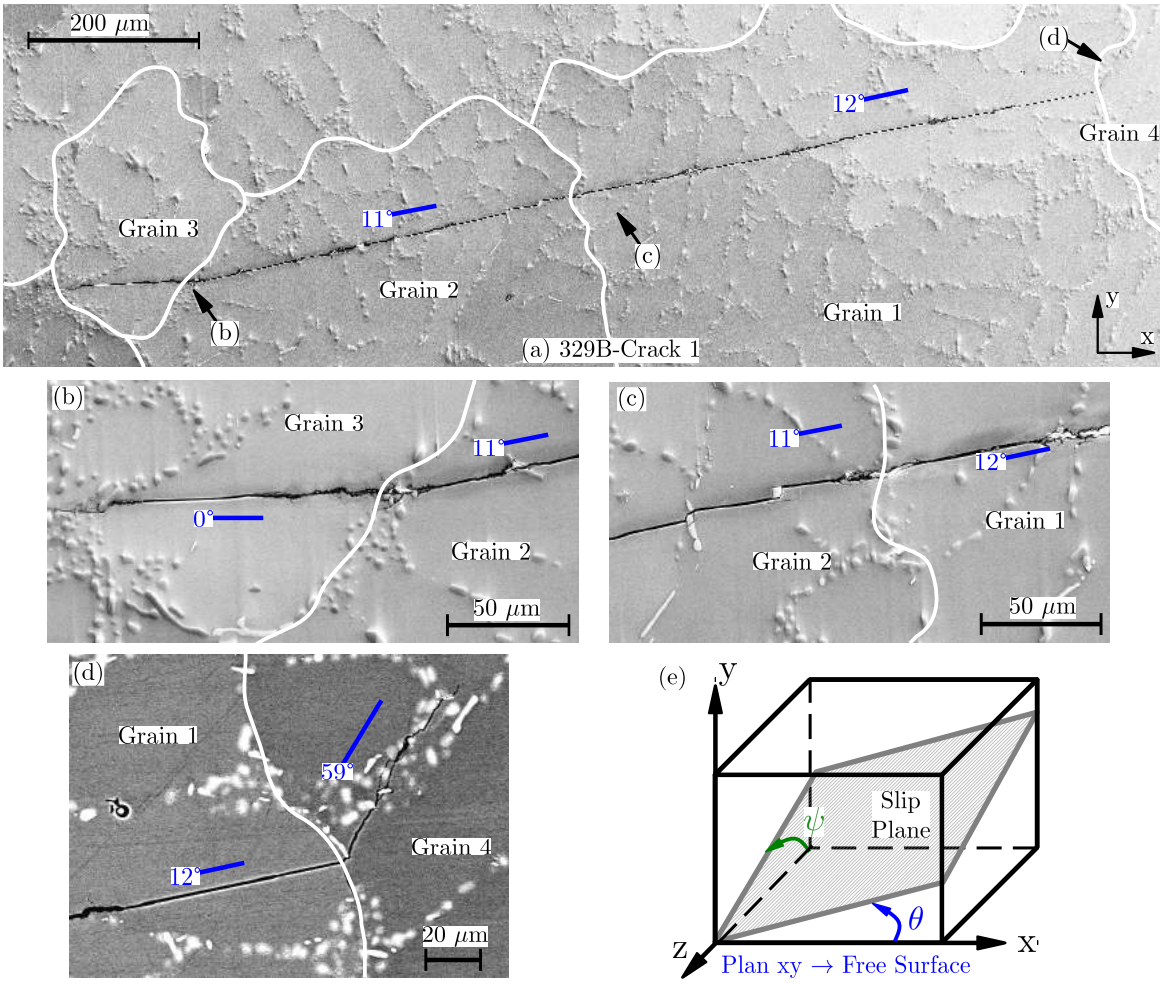

Fig. 2.57: (a) SEM observation showing propagation of 329B-Crack 1 through four different grains. The white lines indicate the approximate location of the grain boundaries. (b) Higher magnification of the crack crossing between Grain 2 and Grain 3. (c) The same as before but for Grain 1 and Grain 2. (d) BSE image of the crossing between Grain 1 and Grain 4. (e) Schematic illustration of the θ and ψ angle.

Similar crack behaviour is also observed in 329B-Crack 2 (see Fig. 2.58a) and 329B-Crack 3 (Fig. 2.58b), where the nucleation and first propagation stages occurred on crystallographic planes (at 20° in Grain 5 for 329B-Crack 2 and -17° in Grain 8 for 329B-Crack 3) with subsequent non-crystallographic propagation after deflection at the grain boundaries.

Finally, SEM observations also revealed a fourth crack that was overlooked during monitoring of the surface. This crack was the only one observed nucleating at a pore (surface diameter ∼30 μm). This crack propagated on a crystallographic plane at -7° up to a length of $2c = 260$ μm. Another crack with the same orientation (100 μm length) can be observed isolated at the left bottom of Grain 11. This last crack remained entrapped between Grain 12 and Grain 16.

(a) Crack 2

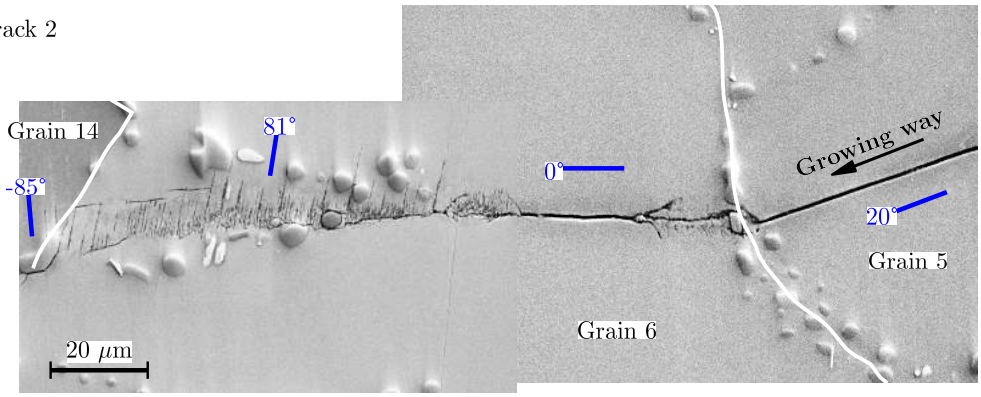

(b) Crack 3

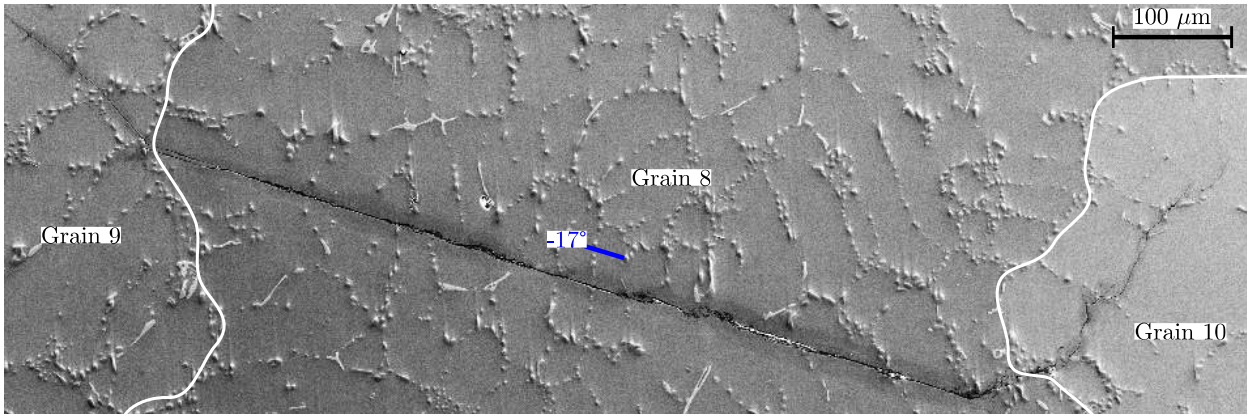

Fig. 2.58: (a) SEM observation focused on the propagation path of 329B-Crack 2 when evolving within Grain 6. (b) SEM observation of the entire 329B-Crack 3.

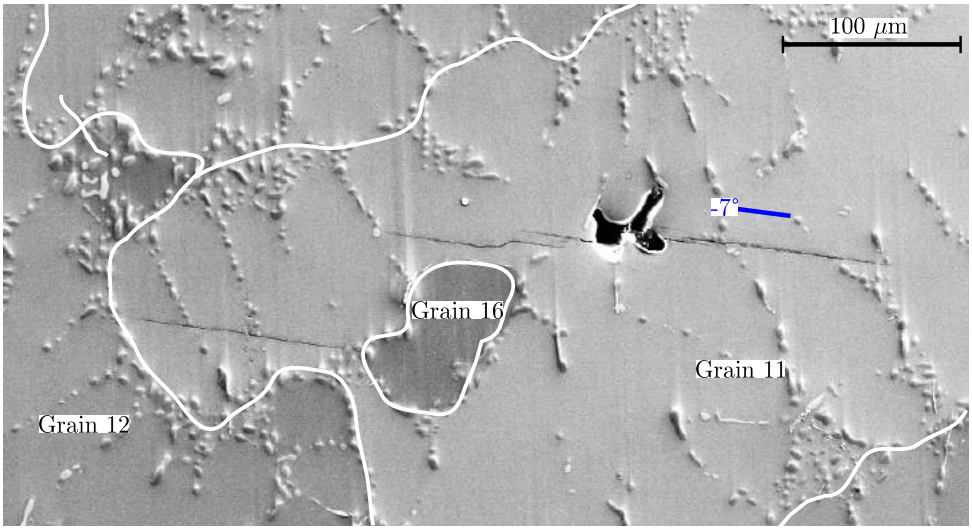

Fig. 2.59: SEM observation showing the progression of 329B-Crack 4 within Grain 11.

2.4.5.2 Taylor analysis

A Taylor analysis was performed using the EBSD data obtained on the flat surface with the objective of further investigating the mechanisms leading to torsional crack nucleation (see Fig. 2.60). The comparison of the strain activity between the four {111} planes of a grain (see Table 2.5) reveals that the nucleating planes are those nearly perpendicular to the stress axis (-20° $< \theta <$ 20°) exhibiting a high strain activity ($\sim 10^{-3}$).

The only exception to this tendency is Grain 8. In this grain, the highest strain activity ($1.2 \cdot 10^{-3}$) is observed to occur on the $(\bar{1}11)[0\bar{1}1]$ slip system at $\theta = 81°$ while the activity on the crack nucleating plane $((11\bar{1})[\bar{1}10]$ at θ = -17°) is $-7.9 \cdot 10^{-4}$. This result might indicate that torsion cracks are more easily nucleated on transverse planes even when they exhibit lower (but closer) strain activities. The cause explaining the tendency towards transverse crack nucleation is so far unclear.

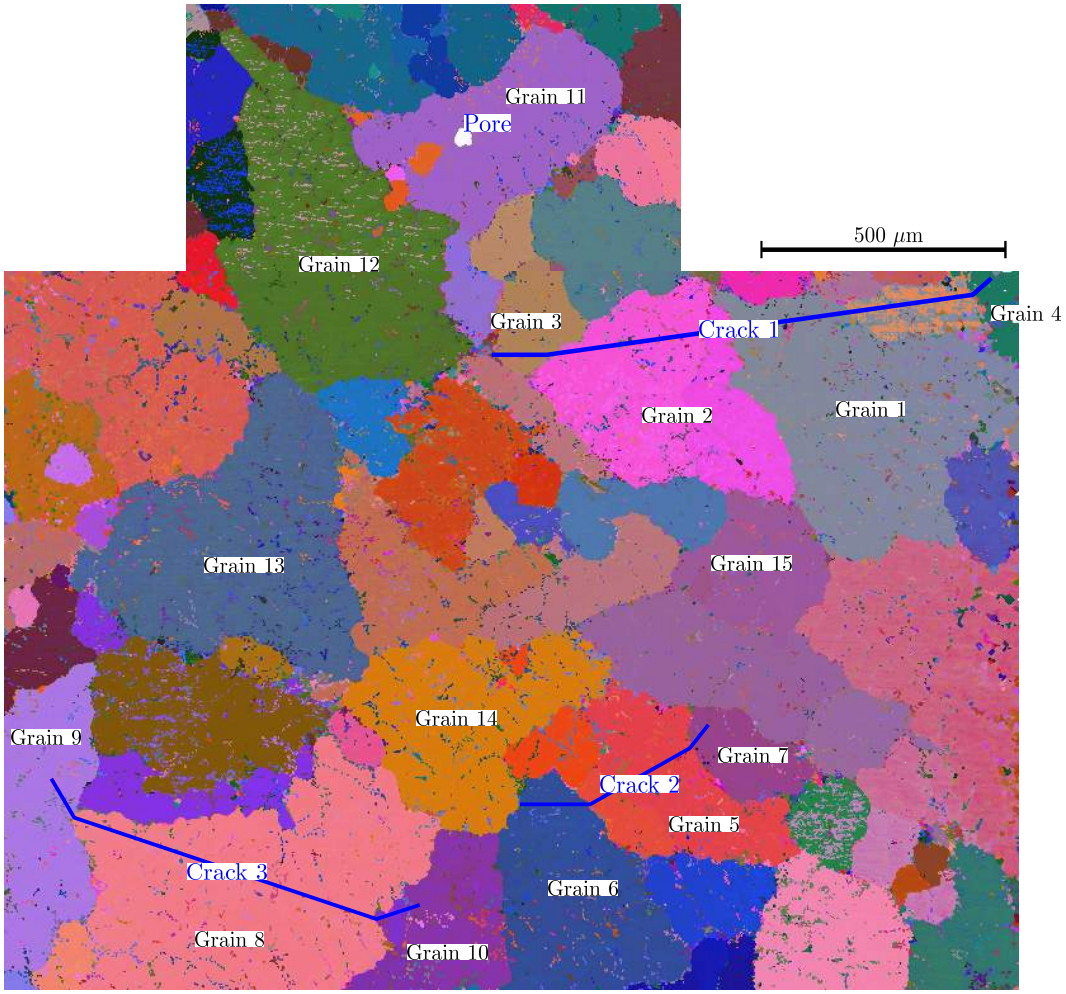

Fig. 2.60: EBSD Euler map showing the grain population of the 329B filleted surface with a schematic representation of the cracks. The labelled grains were used as input for a Taylor analysis.

One commonly accepted idea in fatigue is that cracks are more easily nucleated within large grains because early stages of propagation are less obstructed by the neighbouring grain boundaries. Nevertheless, it can be observed from the data of Table 2.5 that the size of the grain is not the unique factor which leads to crack nucleation as there are non-nucleating grains that have sizes similar to those of nucleating grains. It seems therefore that the ability of a grain to initiate a crack

	(111) $[0\bar{1}1]$	(111) $[10\bar{1}]$	(111) $[\bar{1}10]$	$(\bar{1}11)$ $[0\bar{1}1]$	$(\bar{1}11)$ $[101]$	$(\bar{1}11)$ $[110]$	$(1\bar{1}1)$ $[011]$	$(1\bar{1}1)$ $[10\bar{1}]$	$(1\bar{1}1)$ $[110]$	$(11\bar{1})$ $[011]$	$(11\bar{1})$ $[101]$	$(11\bar{1})$ $[\bar{1}10]$	**Size (mm^2)**
Grain 1	θ = 63°; ψ = 84°			θ = -55°; ψ = -23°			θ = 69°; ψ = -61°			**θ = 12°; ψ = 12°**			0.28
M_T=3.9	0	$-5.7\cdot10^{-4}$	$1.1\cdot10^{-4}$	0	0	0	$-3.8\cdot10^{-6}$	$6.6\cdot10^{-4}$	0	$4.8\cdot10^{-5}$	0	$-1.3\cdot10^{-3}$	Crack
Grain 2	θ = 39°; ψ = -64°			θ = -61°; ψ = 32°			θ = 82°; ψ = 82°			**θ = 11°; ψ = 9°**			0.17
M_T=3.7	$1.2\cdot10^{-4}$	$-2.7\cdot10^{-6}$	0	0	0	0	0	$8.8\cdot10^{-4}$	$6.6\cdot10^{-5}$	$9.5\cdot10^{-4}$	0	$-5.1\cdot10^{-4}$	Crack
Grain 5	θ = -67°; ψ = -76°			θ = 51°; ψ = -52°			**θ = 20°; ψ = 27°**			θ = -54°; ψ = 20°			0.11
M_T=5.0	$-9.0\cdot10^{-4}$	$-3.6\cdot10^{-4}$	0	$4.3\cdot10^{-4}$	$2.3\cdot10^{-4}$	0	$8.7\cdot10^{-5}$	$-1.1\cdot10^{-3}$	0	$1.9\cdot10^{-4}$	$6.9\cdot10^{-5}$	0	Crack
Grain 6	θ = 87°; ψ = -88°			**θ = 7°; ψ = 29°**			θ = -26°; ψ = -38°			θ = 81°; ψ = 49°			0.16
M_T=3.4	0	$-1.3\cdot10^{-4}$	$2.7\cdot10^{-5}$	$-6.0\cdot10^{-4}$	0	$3.6\cdot10^{-4}$	$-4.6\cdot10^{-5}$	0	$-6.5\cdot10^{-5}$	0	$-3.0\cdot10^{-4}$	$8.6\cdot10^{-4}$	No Crack
Grain 8	θ = -6°; ψ = -79°			θ = 81°; ψ = 70°			θ = 47°; ψ =36 °			**θ = -17°; ψ = -9°**			0.37
M_T=3.7	$-4.1\cdot10^{-4}$	$7.5\cdot10^{-6}$	0	$1.2\cdot10^{-3}$	0	$-7.0\cdot10^{-5}$	0	0	0	0	$9.7\cdot10^{-5}$	$-7.9\cdot10^{-4}$	Crack
Grain 11	θ = -86°; ψ = -87°			**θ = -7°; ψ = -16°**			θ = -49°; ψ = 54°			θ = 64°; ψ = -7°			0.16
M_T=3.6	$1.2\cdot10^{-7}$	$-7.2\cdot10^{-4}$	0	$-1.5\cdot10^{-3}$	0	$1.4\cdot10^{-4}$	0	0	0	0	$-9.8\cdot10^{-5}$	$1.8\cdot10^{-5}$	Crack
Grain 12	θ = 46°; ψ = -70°			**θ = 26°; ψ = 49°**			**θ = -21°; ψ = -11°**			θ = 89°; ψ = -14°			0.26
M_T=2.8	0	$-7.4\cdot10^{-9}$	0	$-5.9\cdot10^{-5}$	0	$1.8\cdot10^{-8}$	0	0	0	0	$-6.6\cdot10^{-4}$	$1.3\cdot10^{-3}$	No Crack
Grain 13	θ = -55°; ψ = -77°			θ = 46°; ψ = 34°			**θ = 2°; ψ = -32°**			θ = -65°; ψ =-3°			0.25
M_T=4.1	$2.7\cdot10^{-4}$	$4.3\cdot10^{-4}$	0	0	0	0	0	$-1.6\cdot10^{-3}$	$-5.4\cdot10^{-5}$	$4.3\cdot10^{-4}$	0	$8.8\cdot10^{-5}$	No Crack
Grain 14	θ = 41°; ψ = 64°			θ = 39°; ψ = -59°			**θ = -15°; ψ = 2°**			θ = -85°; ψ = -19°			0.16
M_T=2.9	0	0	0	0	0	0	0	$-2.8\cdot10^{-4}$	$-2.0\cdot10^{-4}$	0	$-7.0\cdot10^{-4}$	$8.7\cdot10^{-4}$	No Crack
Grain 15	θ = 59°; ψ = 77°			**θ = -26°; ψ = -26°**			θ = -66°; ψ = 61°			θ = 45°; ψ = -5°			0.23
M_T=5.1	$4.8\cdot10^{-4}$	$-8.1\cdot10^{-4}$	0	$-8.2\cdot10^{-4}$	$-8.4\cdot10^{-5}$	0	$-1.5\cdot10^{-4}$	$9.5\cdot10^{-4}$	0	$-8.4\cdot10^{-5}$	$-7.2\cdot10^{-5}$	0	No Crack

Table 2.5: Taylor results on the grains which nucleated a torsion crack. The angles in red refer to planes where the crack was formed. The angles written in green refer to the planes with the lowest absolute θ in the case of grains that did not nucleate any crack. The area of the grains as measured at the surface is also given.

increases when highly activated slip planes nearly perpendicular to the specimen axis are present. More systematic analysis should be performed to strengthen this conclusion.

Crack monitoring revealed that {111} crystallographic cracks of about 1000 μm length were formed after 240 000 cycles ($\sim$30% of the expected fatigue life) when cycled at 95 MPa. These cracks were able to cross into the first neighbouring grains; strong crack bifurcations were observed at the grain boundaries. The observed values of θ angles (when crack nucleation occurred) range between -17° and 20°. A Taylor analysis confirmed that these directions corresponds to the planes exhibiting the highest strain activity ($\sim 10^{-3}$) over the twelve slip systems. Crack nucleation on planes with $\theta \approx 90°$ seems to be more difficult even when a high strain activity is predicted on those planes.

2.4.6 Scenario for the cracking mechanisms in torsion

The observations performed on fracture surfaces, secondary and longitudinal cracks, indicate that the crack nucleation mechanisms are the same regardless the remote stress level. Several mode II-mode III crystallographic microcracks are simultaneously nucleated along the specimen gage. They are preferentially formed on planes close to the transverse plane ($\theta \approx 0°$). The presence of abrasion debris (murky debris) is characteristic of nucleation sites although the amount of debris does depend on the remote stress level. Higher stress levels lead to the formation of thinner layers of abrasion debris.

As nucleated microcracks continue propagation, the surface contact between crack lips increases and the value of $\Delta K_{\mathtt{eff}}$ decreases. For high stress levels, it is considered that the crack driving force remains larger than the mode III propagation threshold (observed by Tschegg in steels [TSC 83]), and therefore, torsion cracks can propagate in mode III through the entire cross section; this leads to the formation of the so-called macroscopic flat fracture surfaces (Zone 1).

When the stress level is lower ($85 < \tau_{\mathtt{max}} < 105$ MPa), the crack driving force is reduced and its value tend towards the mode III propagation threshold. Therefore, the crystallographic orientation tends to control the propagation mode. It seems that if the local crystallography is favourable, cracks are able to propagate in mode III. If not, cracks change to mode I propagation. The local crystallography leads to numerous crack deflections and branching. Several millimetric cracks can evolve simultaneously across the specimen gage and the final failure occurs by the linkage of some of these cracks. Tortuous fracture surfaces exhibiting local mode III and mode I crack propagation are formed under these conditions (Zone 2).

When the remote stress level is low enough, crack driving forces are lower that the mode III propagation threshold. Under these conditions, mode I propagation becomes dominant (mode III propagation rarely occurs) leading to the formation of spiral-like fracture surfaces (Zone 3) which have been reported in the literature [SCH 09a].

2.4.7 Summary on torsion results

The most important findings regarding torsion testing are summarised as follows:

1. S-N curves showed that the fatigue life ratio (at 10^7 cycles) in both tension and torsion is close to 1 which is in good agreement with the results given in the literature for cast materials containing defects.
2. Three distinct zones of crack propagation were established depending on the characteristics of fracture surfaces. Flat mode III surfaces are observed under load levels higher than 105 MPa

while tortuous fracture surfaces are observed for load levels ranging between 100 and 85 MPa. Finally, a spiral-like fracture surface is formed at 80 MPa (see Fig. 2.61).

3. The nucleation of cracks in torsion occurs simultaneously at different sites. This characteristic was observed to be more pronounced in Zone 2.
4. The fracture surfaces of Zone 2 resulted from the linkage of different propagating cracks. In this region the crack deflection is induced by variation of the local crystallographic orientations. It was not possible to establish a single mode dominating propagation; both mode III and mode I tend to occur on planes that do not correspond to the planes of maximum shear and normal stress.
5. The fracture surface of Zone 3 is the result of a unique crack that preferentially propagated in mode I (some local mode III microstepping was also observed). The crack was initiated from two different nucleation sites close to each other.
6. In contrast with what was observed with uniaxial tensile fatigue, the monitoring results showed that only 30% of the estimated fatigue life in torsion is devoted to the nucleation of crystallographic cracks (result for a single sample). The fatigue life seems to consist mainly in crack propagation.
7. The four monitored cracks nucleated on {111} planes that have directions ranging from θ = -17° to θ = 20° ($\sim 10^{-3}$, Taylor calculation). All nucleating planes exhibited the highest slip activities among the different slip systems.
8. The influence of SDAS could not be measured during the monitoring experiment (observation intervals are too big). As for the case of uniaxial testing, further investigation is require on the subject.
9. Both fracture surfaces and monitoring observation revealed a negligible presence of pores at the nucleation sites. It seems that other microstrucutral parameters (large grains at the free surface) are able to produce earlier crack nucleation.

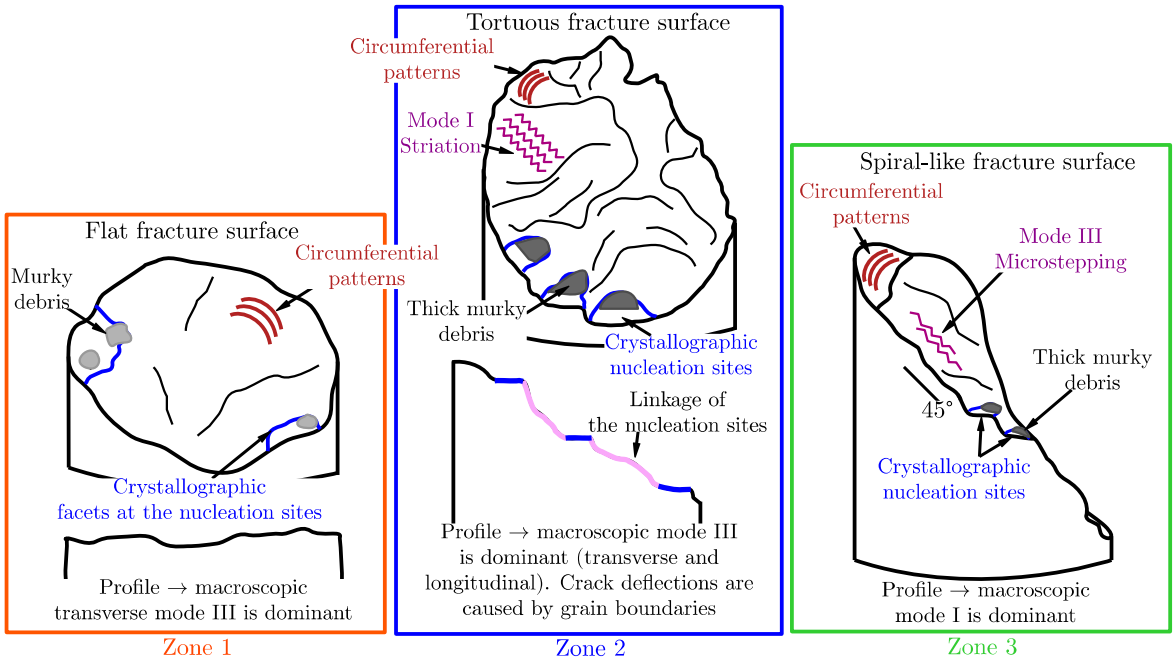

Fig. 2.61: Schematic illustration of the most remarkable features that have been observed in Zone 1, Zone 2 and Zone 3

Les conclusions les plus importantes concernant les tests de torsion se résument comme suit:

1. Les courbes S-N ont montré que le ratio pour la limite de fatigue en traction et en torsion est proche de 1, ce qui est en bon accord avec les résultats expérimentaux trouvés dans la littérature pour le cas de matériaux moulés contenant des défauts.
2. Trois zones de propagation dénommées Zones 1, 2 et 3 peuvent être distinguées en fonction de la morphologie des faciès de rupture. Des surfaces relativement planes et perpendiculaires aux fûts des éprouvettes qui résultent d'une propagation en mode III sont observées à des niveaux de contrainte supérieurs à 105 MPa (Zone 1) tandis que des faciès de rupture tortueuses sont observées pour des niveaux de contrainte entre 100 et 85 MPa (Zone 2). Enfin, une faciès de rupture en forme d'héice est formée à 80 MPa (Zone 3).
3. L'amorçage de fissures en torsion se produit simultanément à différents endroits. Cette caractéristique est plus prononcée dans la Zone 2.
4. Les faciès de rupture dans la Zone 2 résultent de la jonction de fissures se propageant simultanément à des endroits différents le long du fût. Dans cette zone, la déviation des fissures est induite par la variation des orientations cristallographiques locales. Il n'a pas été possible d'établir quel mode domine la propagation. Le mode III et le mode I ont tendance à se produire sur des plans qui ne correspondent pas aux plans maximums de cisaillement et contrainte normale.
5. Le faciès de rupture dans la Zone 3 est le résultat d'une seule fissure se propageant préférentiellement en mode I (certains micro-marches localement formées en mode III ont également été observées). La fissure a été amorcée à partir de deux sites d'amorçage différents mais proches.
6. Contrairement à ce qui a été observé en traction, les résultats de suivi de fissure ont montré que seulement le 30 % de la durée de vie attendue en torsion est dédiée à l'amorçage de fissures. La période de propagation de fissures semble donc dominer la durée de vie en torsion.
7. L'amorçage des quatre fissures observées en surface s'est produit sur des plans {111} ayant des orientations comprises entre θ = -17° et θ = 20° (facteur de Taylor élevé, $\sim 10^{-3}$). Tous le plans amorçant des fissures sont ceux pour lesquels un calcul Taylor prédit une activité plastique élevée.
8. Les faciès de rupture et le suivi de fissures ont montré une présence négligeable de pores dans les sites d'amorçage.

Chapter 3

3D fatigue mechanisms: surface v.s. interior

A brief literature review on the characteristics of internal failure as well as on the influence of environment on the fatigue behaviour is first introduced in this chapter. The experiments presented here intend to study the conditions under which internal defects could be more or at least as deleterious to fatigue life as surface defects. These internal conditions have been investigated at a macroscopic and microscopic scale. Macroscopic testing was performed using specimens which contained $\varnothing_{\text{eq}} \approx 2$ mm artificial defects, the main objective being to obtain S-N curves as well as to perform systematic fractographic analysis. Synchrotron tomography was used to monitor *in situ* fatigue tests on small specimens in order to study internal crack growth nucleated from either natural or artificial defects. In addition, 3D synchrotron images were used to produce realistic FE simulations for further investigation on the influence of the size and shape of defects on crack nucleation.

Contents

3.1 Background on internal failure mechanisms

It has been shown in Chapter 2 that fatigue failure is most usually initiated at specimen free surfaces. Crack initiation is essentially caused by: (i) the formation of slip bands on favoured oriented grains, for the case of defect-free materials, or (ii) surface or subsurface defects (*e.g.,* notches or pores) which act as stress raisers and favour an early crack nucleation. Internal failure is rarely observed under HCF conditions ($10^5 < N_f < 10^7$ cycles). As a matter of fact, of the most documented cases of internal failure are those of high strength steels cycled under Very High Cycle Fatigue (VHCF, $N_f > 10^7$ cycles) conditions [MUR 98, MUR 00, NIS 99]. This material produces a twofold S-N curve where the step indicates the transition from surface to bulk failure. Fractographic observation of this type of material failure showed that internal crack initiation occurred at non-metallic inclusions which led to the formation of characteristic fracture surfaces termed as *fish-eye*.

3.1.1 Conditions for internal failure in VHCF

As mentioned above, internal fatigue failure has been mainly observed under VHCF conditions. However, it seems that some requirements have to be fulfilled for internal failure to occur; otherwise the final failure is prone to occur from the free surface.

3.1.1.1 Case of high strength steels

It seems that the mechanisms responsible for surface nucleation must be delayed or even suppressed for the internal failure to occur. In practice, this means that the volume density of the non-metallic inclusions must be lower than a critical value where the possibility of an inclusion being located at the free surface is almost non-existent [CHA 10, MUG 02]. Some of these materials can also present a surface strengthening effect (*e.g.,* carburized layers) that can also favour the transfer to the bulk [NIS 99]. In addition, Murakami *et al.* [MUR 00] suggested that the hydrogen trapped by inclusions may cause a fatigue embrittlement where the first stages of the internal propagation would be accelerated.

3.1.1.2 Case of aluminium castings

No surface-to bulk transition is observed on the S-N curve of these alloys although the existence of an endurance limit above $\sim 10^8$ cycles has been reported by several authors [STA 95, CAT 03, MAY 03, ZHU 06]. This flattening of the S-N curves is thought to be a consequence of the presence of casting defects in the material [CAT 03].

With regard to the differences between surface and internal cracking, it is generally assumed that internal crack propagation occurs in an inert environment (similar to vacuum conditions) while surface cracks evolve in more harmful environments such as ambient air.

3.1.2 Influence of the environment on the fatigue behaviour

Decades of experimental work (the first study on this subject dates back to 1917) have brought evidences that non-inert atmospheres have a deleterious influence on the fatigue lives of metals. Meyn [MEY 68] was the first to observe the absence of striation marks in a vacuum environment for wrought aluminium alloys which otherwise formed well defined striations. Pelloux [PEL 69] reported similar results and suggested that the alternating shear process is reversible unless an

oxide layer is formed on the freshly created surfaces at the crack tip. This oxide layer hinders slip activity at the loading reversal and so an enhanced slip irreversibility would be responsible for the higher fatigue crack growth rates reported in air environment.

3.1.2.1 Fatigue behaviour in high vacuum

Based on the experimental results obtained for a wide selection of metallic materials, Petit *et al.* [PET 91, PET 99, PET 00, PET 10] identified three main intrinsic propagation regimes (Fig. 3.1a):

(i) **The intrinsic stage I** corresponds to microstrucutrally small cracks propagating at about 45° with respect to the loading axis (see Fig. 3.1b). This stage is considered the fastest regime for a given loading condition but can also be the slowest at a grain boundary.

(ii) **The intrinsic stage I-like** propagation occurs in polycrystals and corresponds to stage I propagation at the scale of each individual grain all along the crack front. At the macroscopic scale, the crack remains as a stage II crack which propagates in the direction perpendicular to the loading axis (see Fig. 3.1c). This stage can be related to the near-threshold regime where physically small cracks still interact with the microstructure. The crack growth in this region are generally the slowest of the three stages presented here.

(iii) **The intrinsic stage II** propagation corresponds to the case where duplex slip is activated and cracks propagate in the direction perpendicular to the loading axis (see Fig. 3.1d). An intrinsic fatigue crack propagation law based on Paris law and allowing consideration of environmental conditions was proposed by Petit *et al.* [PET 06]:

$$da/dN = A/D_0^*[\Delta K_{\mathtt{eff}}/E]^4 \tag{3.1}$$

where A is a dimensionless parameter, D_0^* is a critical cumulated displacement at the crack tip and $\Delta K_{\mathtt{eff}}$ and E are the effective (*i.e.,* closure corrected) stress intensity factor and the Young modulus, receptively.

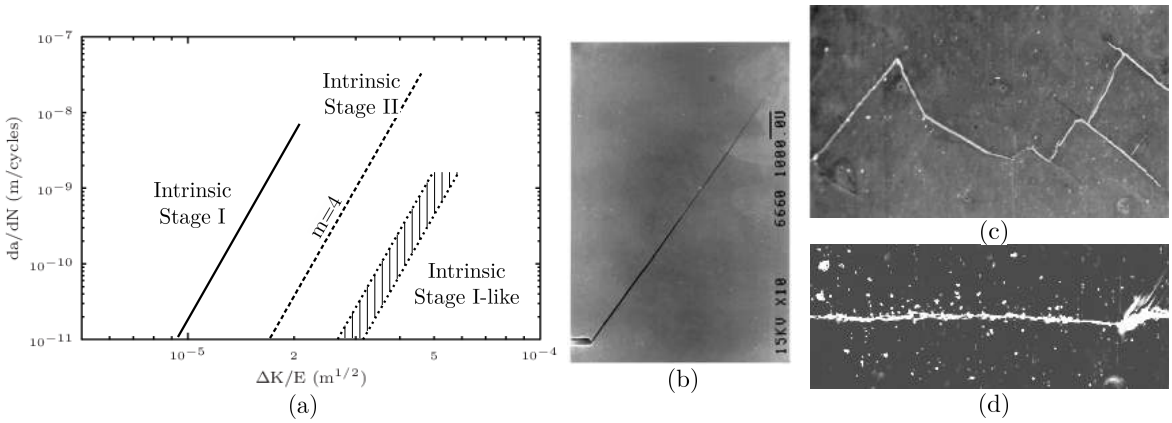

Fig. 3.1: (a) Schematic illustration of the three intrinsic fatigue crack growth regimes for polycrystalline alloys in high vacuum. (b) Stage I crack in a peak-aged single crystal of Al-4.5% wt Zn-1.25% wt Mg alloy oriented for (111) slip. (c) Intrinsic stage I-like crack path in a peak-aged polycrystal of the same material. (d) Stage II crack in the overaged condition of the same material [PET 10].

It must be noted that the crack profiles formed under vacuum conditions are highly dependent on the microstructural features. It was shown by Carter *et al.* [CAR 84] that underaged precipitation states in a 7475 aluminium alloy resulted in rough crack profiles due to a planar slip

propagation (and corresponding to the intrinsic stage I-like propagation) while an overaged state produced smooth profiles (intrinsic stage II propagation). In addition, a coarser microstructure in the underaged state (average grain size of 80 μm) increased the roughness of the crack profile when compared to the crack profile resulting from a finer microstructure (18 μm) [CAR 84].

3.1.2.2 Environmentally assisted propagation

Because of the complex nature of gaseous-assisted cracking, a sound physical explanation being able to account for all phenomena occurring at the crack-tip is still elusive. One of the models obtaining more consensus is that of Wei *et al.* [WEI 81] who proposed a sequential process to describe the hydrogen-assisted cracking in metals (Fig. 3.2). In this model, hydrogen is generated by the reaction of environmental species, such as water vapour, with newly fractured material at the crack tip. This hydrogen is absorbed, dissociated and finally dragged by mobile dislocations or diffusion mechanisms into the highly stressed zone (plastic zone) where an embrittling reaction takes place causing increased fatigue crack growth rates.

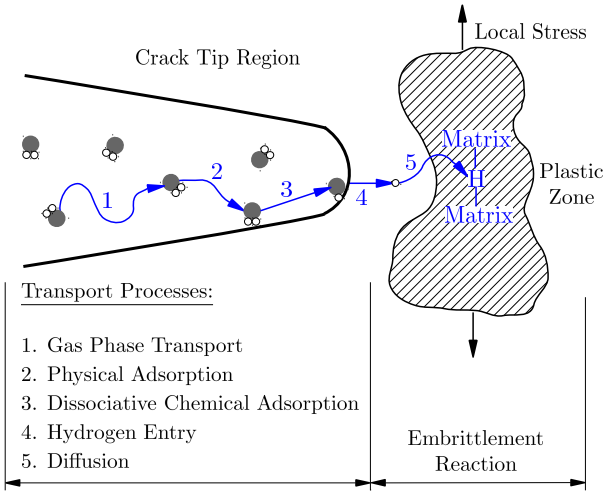

Fig. 3.2: Schematic illustration of the sequential mechanism proposed by Wei [WEI 81] to describe environmentally-assisted cracking occurring in a hydrogenous atmosphere. The embrittlement is showed by a matrix-hydrogen-matrix reaction within the plastic zone.

Several models have been proposed to describe the embrittlement reaction itself. Among them, the hydrogen-enhanced localised plasticity (HELP) model proposes that the plastic activity at the crack tip is facilitated by the presence of hydrogen molecules which are dragged into this region by dislocations [BEA 72, BIR 94]. The effect of hydrogen consists in unlocking the dislocations so their movement is possible even at lower stresses. Hence, this model considers that the embrittling reactions are caused by a hydrogen localisation ahead of crack-tips with hydrostatic stress fields promoting this hydrogen diffusion. The model proposed by Lynch [LYN 88] (known as the adsorption-induced dislocation emission AIDE model) is based on the same idea of plastic localisation with the difference that this model considers that the physical adsorption step can by itself alter the fatigue resistance of the material. Therefore, this approach considers that the species adsorbed on a few atomic layers of the crack-tip surfaces would be sufficient to accelerate fatigue crack propagation by facilitating the dislocation emission on suitably inclined slip planes. The term *dislocation emission* embodies both nucleation and subsequent movement of the dislocations, where the nucleation stage is the one facilitated by the adsorption process.

As for the influence of moist air on the fatigue crack propagation, Petit and co-authors [HEN 95, HEN 96, PET 06, PET 10] observed two types of behaviours depending on the controlling adsorption mechanisms acting at the crack-tip (see Fig. 3.3):

- *Hydrogen-assisted crack propagation*: some critical conditions have to be fulfilled for the

growing process to be assisted by hydrogen. These are: (1) Cracks must propagate at sufficiently low stress intensity factors so the plastic zone remains smaller than the grain size and the slip activity is localized within few dislocation systems. (2) Following Wei's model, the number of molecules of active species reaching the crack tip must be high enough to enable the creation of an instantaneous absorbed mono-layer. Also, the growth rate must be low enough to allow the hydrogen to diffuse by dislocation dragging into the plastic zone. (3) Embrittlement reaction at the crack-tip occurs according to the HELP model.

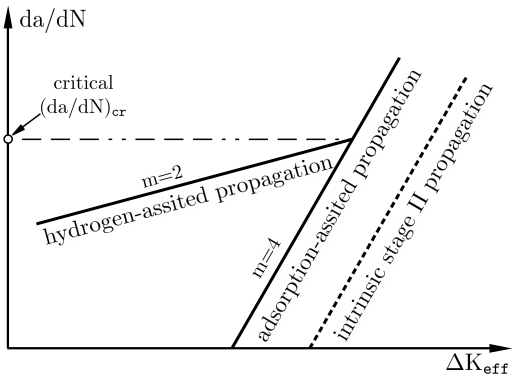

Fig. 3.3: Schematic illustration of the two steps model of fatigue crack growth assisted by water vapour (as in ambient air) in comparison to the intrinsic crack growth behaviour observed in vacuum. The critical $(da/dN)_{cr}$ indicates the transition point between the two steps of the environment-assisted propagation [PET 06].

• *Adsorption-assisted crack propagation*: there is a well-defined change in the slope of the propagation curves when a critical crack growth rate $(da/dN)_{cr}$ is attained. This $(da/dN)_{cr}$ rate depends upon several factors such as the surrounding partial pressure of water vapour, the load ratio, the test frequency, the chemical composition, the microstructure, and so forth. Above this critical value, the growth rates are considered high enough to only enable the adsorption of water vapour molecules. In this case, the embrittlement reaction leading to the enhancement of stage II crack growth rates could correspond to the AIDE model. A model for fatigue crack propagation assisted by water vapour molecules adsorption at the crack tip was developed [PET 06]. In this model, the involved mechanisms are assumed to be identical to those occurring in vacuum and so equation 3.1 is considered also valid for ambient air, with the difference that the parameter D^* is replacing D_0^*. The D^* parameter accounts for the cumulated displacement at the crack tip in any environment; it is assumed that water adsorption diminishes its value.

Fig. 3.4a shows the propagation curve of a 2024-T351 aluminium alloy cycled at ultrasonic frequency in ambient air, dry air and in vacuum environment [STA 91, STA 01], and where the hydrogen-assisted crack growth plateau (between 10^{-9} and 10^{-10} m/cycle) in air environment appears well differentiated from the vacuum results. The largest influence of air is considered to be the reduction of the mechanical threshold from 3.3 MPa$\sqrt{m}$ for vacuum testing to 2.1 MPa$\sqrt{m}$ in both ambient and dry air. Above the 2.1 MPa$\sqrt{m}$ threshold, however, a significant difference (about one order of magnitude lower) in crack growth rates between ambient air and vacuum is observed. It seems that the key factor in this region is the level of exposure to atmosphere water vapour at the crack tip.

Richard *et al.* [RIC 10] investigated the influence of the environment (Fig. 3.4b) on the crack morphology of a naturally aged 2024A-T351 aluminium alloy. It was observed that the crack path is strongly modified when the atmosphere is changed from laboratory air to cold dry air at 223 K. A crystallographic growth (characteristic of an intrinsic stage I-like propagation) occurs in a cold environment while conventional stage II propagation is observed at room temperature. Triangular etch pits on the crystallographic facets of the fracture surfaces allowed to identify a propagation of the crack along {111} planes.

Finally, this literature review reveals that considerable efforts have been made to characterize

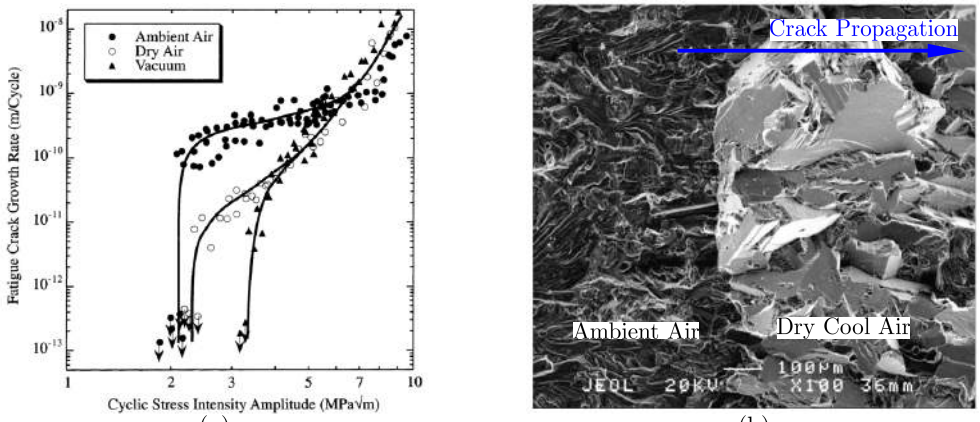

(a) (b)

Fig. 3.4: (a) Fatigue crack growth rates for constant stress amplitude cycling of a 2024-T351 aluminium at ultrasonic frequency (20 kHZ) and R=-1 in ambient air, dry air, and in vacuum [STA 01]. (b) Change induced in the fracture surface morphology of a 2024A-T351 aluminium alloy when the environmental conditions changed from laboratory air to dry cooled air [RIC 10].

the fatigue crack growth rates of wrought aluminium alloys under vacuum conditions [CAR 84, STA 91, HOL 03, HOL 04, GAS 05, RIC 10, STA 06] although very little attention has been paid, so far, to the effect of vacuum on S-N curves. To the author's knowledge, there are no reported studies on the fatigue properties of cast aluminium alloys cycled in a vacuum environment.

3.1.3 Summary on the internal failure background

The main ideas that must be kept in mind with regard to fatigue failure from internal defects are as follows:

1. The stepwise S-N curves reported for high strength steels correspond to a surface-interior transition. It is suggested that surface crack initiation mechanisms must be suspended or delayed for the internal failure to occur.
2. Cast aluminium alloys show an endurance limit for fatigue lives higher than 10^8 cycles. This fatigue limit seems related to the occurrence of non-propagating crack at casting defects.
3. Internal crack propagation is considered to occur in an inert environment similar to vacuum conditions.
4. Propagation in vacuum environment is classified in three different regions : intrinsic stage I, stage I-like and intrinsic stage II which corresponds to three different crack morphologies.
5. Environmentally assisted crack propagation is described by a two-step model accounting for the hydrogen-assisted and adsorption-assisted crack propagation.
6. No result can be found in the literature on the fatigue mechanisms of cast aluminium alloys tested under vacuum conditions.

The experiments presented in what follows intend to investigate the conditions under which internal defects could be more or at least as deleterious to the fatigue life as surface defects. As it not possible to produce series of natural defects having similar size and shape, it was decided to produce casting with artificial defects. These defects can be produced at two sizes: $\varnothing_{eq} \approx 2$ mm and $\varnothing_{eq} \approx 1$ mm, always with a quasi-spherical shape. In addition, the controlled position of these defects within the cast rods facilitates the machining process. Therefore, two sets (internal and surface) of $\varnothing_{eq} \approx 2$ mm artificial defects were produced for the macroscopic testing. The interest of

surface artificial defects is to compare their fatigue behaviour to that of internal artificial defects. Specimens containing internal natural defects (microshrinkages) were produced for the microscopic (synchrotron) testing. Specimens with smaller ($\varnothing_{\mathtt{eq}} \approx 1$ mm) internal artificial defects were also cycled in the synchrotron.

3.2 Uniaxial fatigue testing on cylindrical macroscopic specimens

Fig. 3.5 presents a summary of all macroscopic fatigue results. It shows the curve obtained on the reference material (square symbols, no artificial defects)[1] as well as the fatigue testing results of macroscopic specimens that were cycled under four different conditions:

- Thirty specimens containing **internal artificial quasi-spherical defects of $\varnothing_{\mathtt{eq}} \approx$ 2 mm** (diamond symbols) were cycled at CTIF after being screened by DPI. The artificial defect was centred and the specimens cycled under ambient air (see § 3.2.1).
- Three specimens containing **ex-centred surface artificial defects of $\varnothing_{\mathtt{eq}} \approx$ 2 mm** (triangle symbols) were cycled at ENSMA **under ambient air**. In this case, one half of the artificial defect is intercepting the free surface (see § 3.2.2.1).
- Four specimens also containing **ex-centric surface artificial defects** but cycled in **vacuum** environment (circle symbols, see § 3.2.2.2).
- Five specimens of those produced using the **reference material** were cycled in **vacuum** environment at ENSMA (star symbols). It must be noted that these specimens were neither screened by DPI nor controlled by laboratory tomography (star symbol, see § 3.2.3).

3.2.1 Fatigue results on specimens with internal artificial defects ($\varnothing_{\mathtt{eq}} \approx$ 2 mm)

Fifteen specimens were tested to obtain a Wöhler curve. Only two of the failed from surface natural defects. Another fifteen specimens were used for the staircase method, eight of which exhibited internal failure and the rest were run-outs. The fatigue limit was found equal to 103 MPa. **It can be seen from Fig. 3.5 that the presence of internal defects barely influences the fatigue lifetimes in the HCF regime (from 10^5-10^7 cycles with $\sigma_{\mathtt{max}}$ ranging between 200 and 100 MPa)**. The S-N curve obtained in these conditions is practically identical to the reference curve although the fatigue limit is slightly lower (103 MPa against 115 MPa for the reference).

Fig. 3.6a shows an example of the fracture surfaces features observed on specimens failing from internal defects (other examples are given in appendix D). Three distinct regions of fracture topography (named Region I, II and III) are observed. Region I extends over a quarter of the defect perimeter and about 1 mm towards the exterior of the sample with the red line indicating the approximate boundary between Region I and Region II. This latter region (outlined with a dashed blue line) involves the major portion of crack growth and expands from the artificial defect and Region I towards the free surface exhibiting a distinct faceted topography. Finally, Region III (line in green) extends along the free surface, between Region II and the final ductile failure. Fig. 3.6b presents and alternative case where Region I was formed over the entire perimeter of the artificial defect and no Region III is observed. The characteristic features corresponding to those three different regions are described in more details in what follows.

[1] The reference material (or curve) corresponds to the fatigue tests performed using a material containing a defect distribution similar to that showed in § 1.3.2.4. These specimens underwent mechanical machining and DPI (only apt specimens were kept) prior to the cycling.

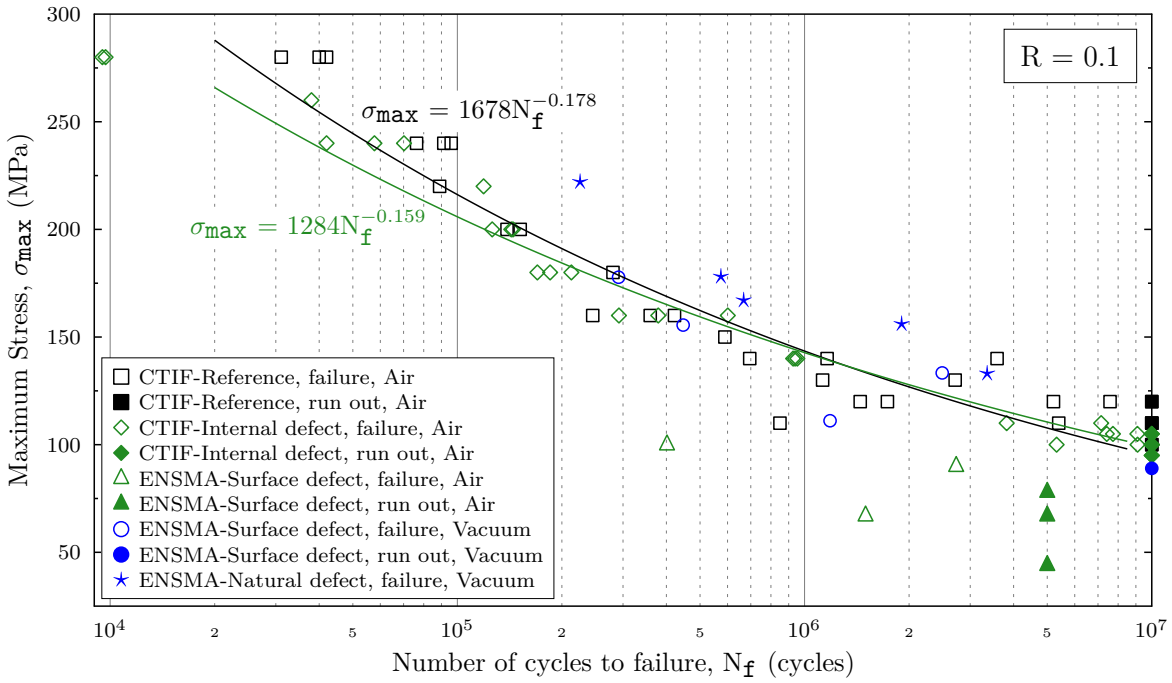

Fig. 3.5: S-N curves for both reference material and specimens containing internal artificial defects of $\varnothing_{eq} \approx 2$ mm cycled in ambient air. The graph also shows results obtained with specimens where one half of the artificial defect intercepts the free surface (cycled in air or vacuum environment) and to the reference material cycled in vacuum.

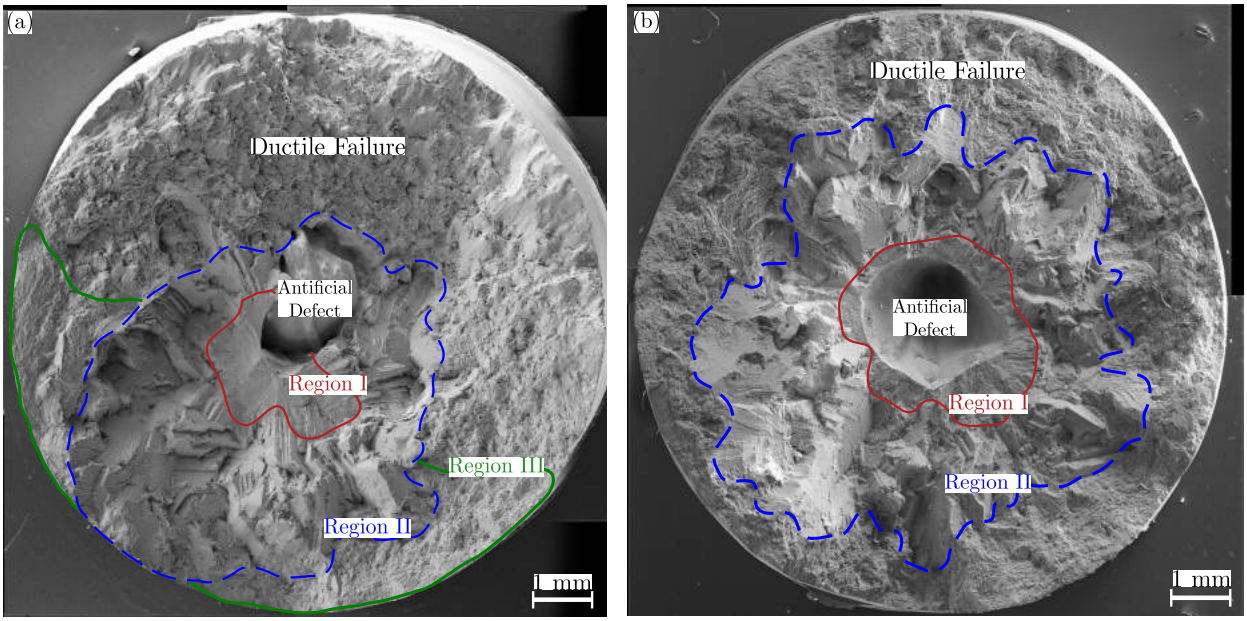

Fig. 3.6: (a) SEM observations at low magnification on the fracture surface of CTIF-131.104 specimen (ambient air) where three distinct regions of fracture topography are reported (see the main text for details). The rest of the surface corresponds to the final ductile failure. The fatigue testing parameters are: $N_f = 9\ 089\ 100$ cycles, $\sigma_{max} = 105$ MPa, Artificial Defect $\sqrt{A} = 1872$ μm and Region I surface and A = 2.9 mm^2. (b) SEM observations on the fracture surface of CTIF-131.114 specimen (ambient air) which only presents propagation in Region I and Region II before final failure. The testing parameters are: $N_f = 600\ 800$ cycles, $\sigma_{max} = 160$ MPa, Artificial Defect $\sqrt{A} = 2116$ μm and Region I surface and A = 3.4 mm^2.

3.2.1.1 Region I

Fig. 3.7 shows a magnified view of Region I where the surface is predominantly flat and a series of radial ridges, characteristic of stage II crack growth, were formed. The cause of this fracture behaviour is unclear. One possibility is that crack growth occurs in an intrinsic stage II regime due to locally high stress intensity values induced by the size and morphology of defects. Such a mechanical explanation would imply that the values of Region I areas increase with an increasing stress level and/or increasing defect size. However, all specimens exhibit Region I areas ranging from 2.5 to 4.5 mm^2 (CTIF-131.105 specimen is the only exception, see Table 3.1). In other words, there is no correlation between the size of Region I and the stress level. The actual environmental conditions at the internal defect are unknown. So the most likely possibility is that Region I is the result of an environment assisted stage II propagation caused by a detrimental (but unknown) environment which enhances the irreversibility of dislocations slip. Therefore, the varying extension of Region I could be explained by a varying number of deleterious molecules somehow trapped or produced by the artificial defect.

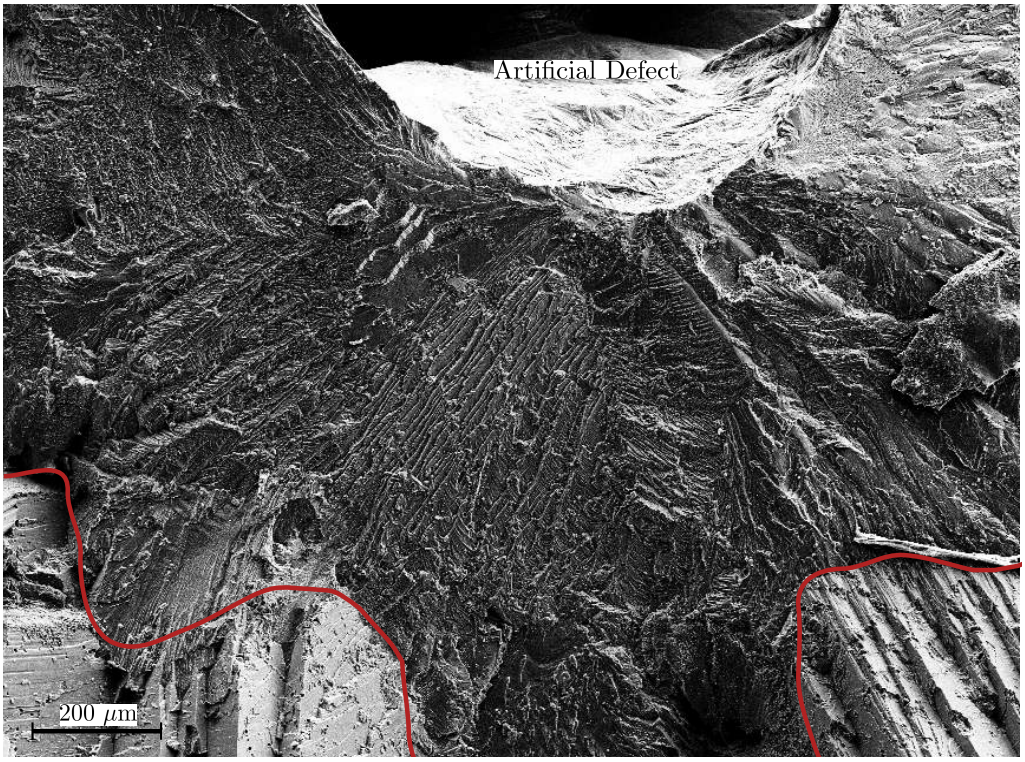

Fig. 3.7: Higher magnification on the Region I of CTIF-131.104 fracture surface. This surface is predominantly flat and shows a series of radial ridges.

As mentioned before, a few of the samples containing artificial defects exhibited surface failure. Fig. 3.8a presents one of them (CTIF-101.57 specimen) which was cycled at $\sigma_{\mathtt{max}} = 140$ MPa and failed after 938 500 cycles from a surface microshrinkage porosity. Tomographic inspection of this sample shows that crack propagation had also occurred from the internal artificial defect proving that, as expected, the formation of Region I is the first event occurring during internal propagation (see Fig. 3.8b).

The CTIF-101.57 specimen was cautiously ground and polished in order to observe its internal crack in SEM and characterise the local microstructure using EBSD. Fig. 3.9a indicates the ap-

Specimen	σ_{max} (MPa)	Region I A (mm^2)	Defect Size $\sqrt{A}$ (μm)	Nf (cycles)
CTIF-131.120	100	4.5	1934	9 099 000
CTIF-131.104	105	2.8	1872	9 089 100
CTIF-131.100	105	2.6	1911	7 770 100
CTIF-131.124	105	2.4	1748	7 423 900
CTIF-131.113	110	1.6	1637	7 151 900
CTIF-131.105	110	6.2	1956	3 823 000
CTIF-131.114	160	3.4	2116	600 800

Table 3.1: Region I area measurements on the inspected fracture surfaces along with the stress level, defect size, and fatigue life. No correlation between the extent of Region I and the stress level can be observed.

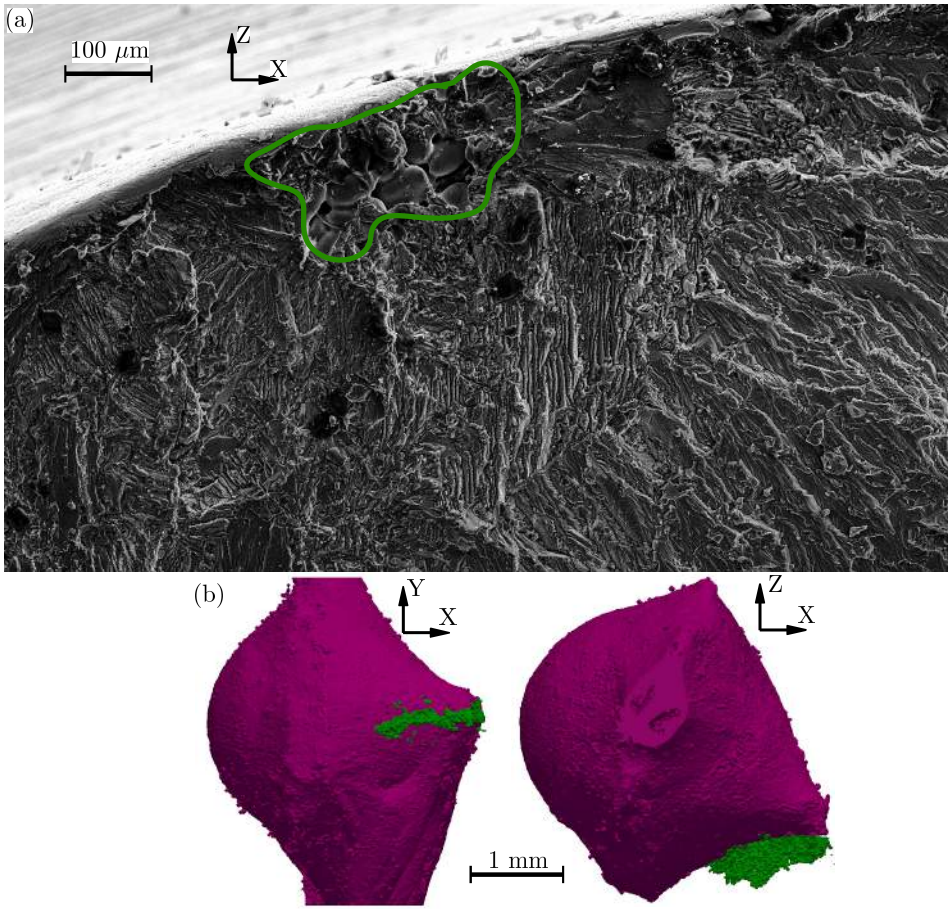

Fig. 3.8: (a) SEM observation at high magnification on the fracture surface of CTIF-101.57 specimen (ambient air, N_f = 938 500 cycles, σ_{max} = 140 MPa) where a surface natural defect of $\sqrt{A}$ = 195 μm was the cause of the fatal failure. (b) 3D renderings obtained by synchrotron tomography of the internal artificial defect ($\sqrt{A}$ = 2064 μm) present in the specimen gage. The crack (which did not lead to failure) is shown in green while the artificial defect appears in magenta.

proximate location of this cut. Fig. 3.9c shows that the internal crack propagated perpendicularly to the loading axis for ∼900 μm showing a bifurcation which, as shown Fig. 3.9b, corresponds to the crack passing into Grain 3. This result indicates that internal crack growth in Region I can be influenced by the underlying microstructure.

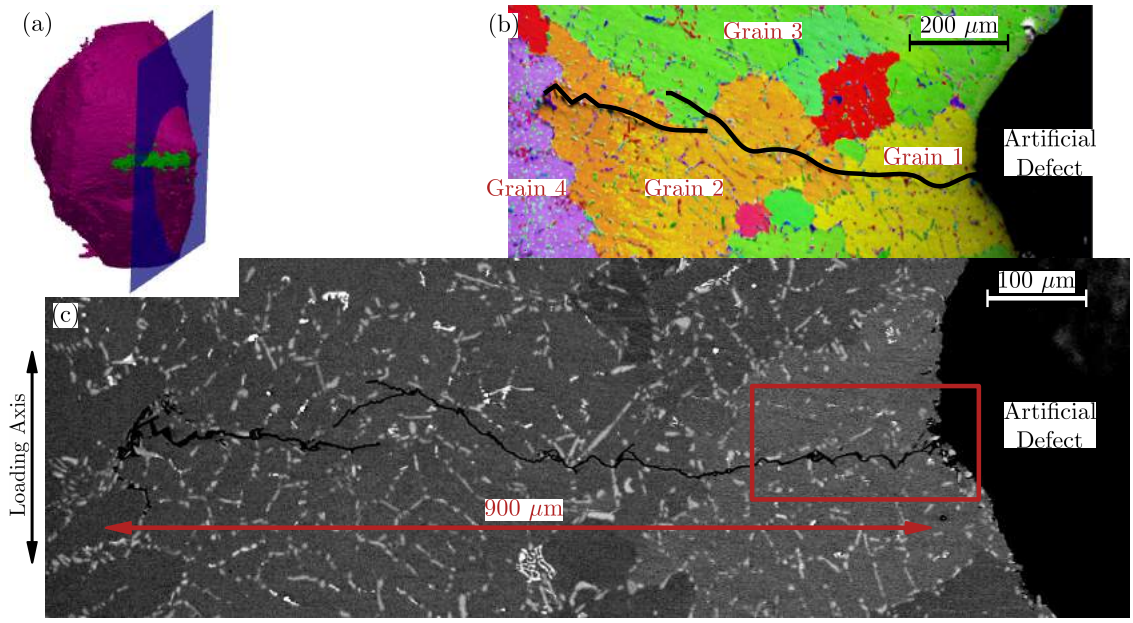

Fig. 3.9: (a) 3D rendering showing the approximate location of the longitudinal cut on CTIF-101.57 specimen (ambient air). (b) EBSD Euler map showing grain distribution around the artificial defect. (c) Backscattered electron image on the non-crystallographic crack. The red rectangle indicates a zone of clear stage II propagation.

3.2.1.2 Region II

Fig. 3.10 shows a magnified view of the *large* crystallographic facets formed in Region II which are characteristic of intrinsic stage I-like regime. Another distinct aspect of this region is that the crack fronts are highly irregular (see, for example, the crack front obtained on Fig. 3.6b).

In order to study the crystallographic orientation of the facets observed within Region II, the lower half of CTIF-131.104 specimen was cold mounted in epoxy resin and longitudinally sectioned. Fig. 3.11a indicates the approximate location of the longitudinal cut on the fracture surface of the upper half. The surface trace analysis (see § 1.3.2.3) shown in Fig. 3.11b-h indicates that Region II fracture surfaces result from crystallographic propagation on {111} planes.

The results of a Taylor analysis performed on these three grains are listed in Table 3.2. It can be observed that crack propagation in Grain 3 primarily occurs on a $(\bar{1}11)$ plane at -59° which corresponds to the system exhibiting the highest slip activity ($\sim 10^{-3}$). The strain activity in Grain 1 is slightly inferior ($\sim 9{\cdot}10^{-4}$). This grain also presents some bifurcations on a different plane which is inclined at 62°. This plane is the second most active one ($\sim 5{\cdot}10^{-4}$). Finally, propagation within Grain 2 occurred at 59°, on a plane exhibiting the third highest slip activity. The activity in this grain is more evenly distributed over the four {111} planes: in this case the crack can therefore propagate on any of the four planes. Other factors (*e.g.,* the slip mismatch between neighbouring grains) could explain this behaviour and further research would be required. Suffices to say here that the crystallographic facets appear preferentially in regions where single slip is possible.

Fig. 3.10: Higher magnification on the Region II of CTIF-131.104 fracture surface where a zigzag topography can be observed due to large crystallographic facets.

	(111) $[0\bar{1}1]$	(111) $[10\bar{1}]$	(111) $[\bar{1}10]$	$(\bar{1}11)$ $[0\bar{1}1]$	$(\bar{1}11)$ $[101]$	$(\bar{1}11)$ $[110]$	$(1\bar{1}1)$ $[011]$	$(1\bar{1}1)$ $[10\bar{1}]$	$(1\bar{1}1)$ $[110]$	$(11\bar{1})$ $[011]$	$(11\bar{1})$ $[101]$	$(11\bar{1})$ $[\bar{1}10]$
Grain 1	θ = 76°; ψ = -84°			θ = 62°; ψ = 63°			θ = 11°; ψ =-11°			θ = -59°; ψ = 6°		
M_T=3.25	$-1.8\cdot10^{-4}$	0	$-2.2\cdot10^{-4}$	$-4.9\cdot10^{-4}$	$-5.7\cdot10^{-4}$	0	0	0	0	0	$-8.2\cdot10^{-4}$	$\mathbf{8.6\cdot10^{-4}}$
Grain 2	θ = -30°; ψ = -60°			θ = 59°; ψ = -39°			θ = 26°; ψ = 45°			θ = -48°; ψ = 17°		
M_T=2.33	$-1.6\cdot10^{-4}$	0	$6.2\cdot10^{-5}$	$-2.9\cdot10^{-4}$	0	$9.6\cdot10^{-5}$	$-1.9\cdot10^{-4}$	0	$-4.9\cdot10^{-4}$	$2.5\cdot10^{-4}$	0	$\mathbf{7.5\cdot10^{-4}}$
Grain 3	θ = 14°; ψ = -73°			θ = -59°; ψ = 43°			θ = 75°; ψ = 65°			θ = 8°; ψ = -2°		
M_T=3.52	$-6.8\cdot10^{-4}$	$4.6\cdot10^{-4}$	0	$\mathbf{1.0\cdot10^{-3}}$	0	$-5.3\cdot10^{-4}$	0	$-4.0\cdot10^{-4}$	$-3.1\cdot10^{-4}$	0	0	0

Table 3.2: Taylor analysis of the grains exhibiting crystallographic propagation on the longitudinal cut of CTIF-131.104 specimen. The slip systems with the highest activities are shown in red.

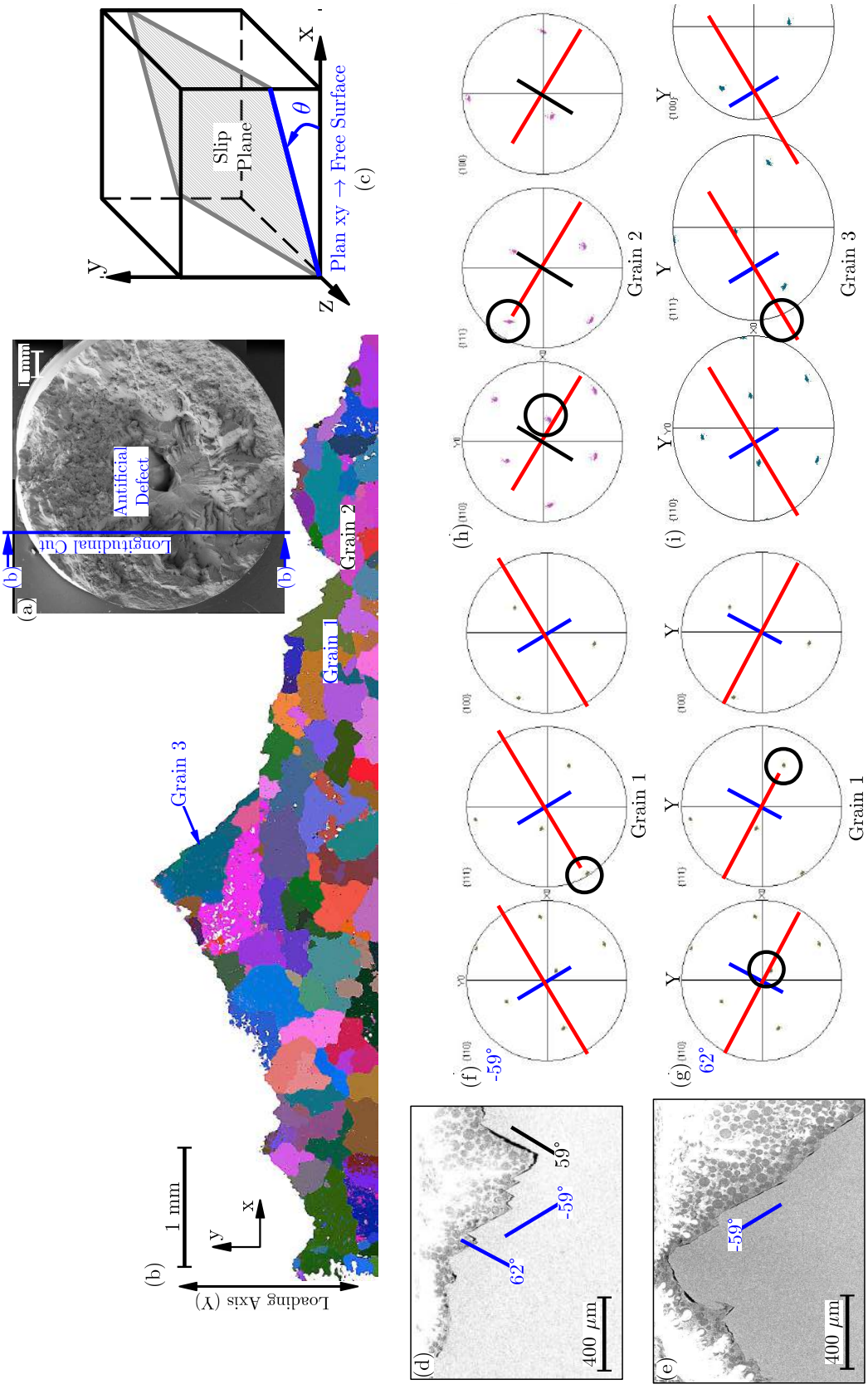

Fig. 3.11: (a) Fracture surface of the upper half of CTIF-131.104 specimen (cycled in ambient air) indicating the approximate location of the longitudinal cut. (b) EBSD Euler map of the longitudinal cut performed on the lower half which shows grain distribution along the internal crack. Only the grains exhibiting crystallographic propagation are labelled. (c) Schematic illustration of the θ angle which indicates the trace orientation. (d) SEM image showing the direction of crack propagation within Grain 1 and Grain 2. (e) Same as before but for the case of Grain 3. (f)-(i) Surface trace analysis on {111}, {110}, {100} stereographic projection pole-figures. {111} family is the only one that always shows interceptions with the normals.

3.2.1.3 Region III

Fig. 3.12 is a typical illustration of the fracture topography observed in Region III where the surface is also predominantly flat and shows features similar to those of Region I. It is thought that the crack was propagating in a vacuum-like environment up to the moment it reached the free surface, entered in contact with the ambient air and starting propagation in an adsorption assisted stage II regime.

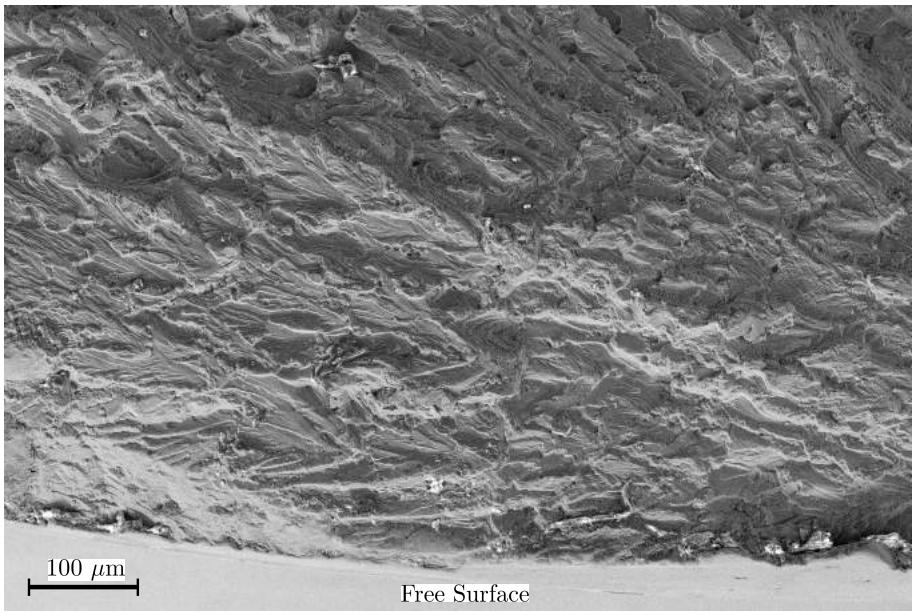

Fig. 3.12: Higher magnification on the Region II of CTIF-131.104 fracture surface. This surface is predominantly flat but a bit rougher than that of Region I. It also shows some ridges.

SEM observations performed on other specimens failing from internal defects present the same propagation regions and fractographic features as the one described so far. They are shown as **additional results in appendix D**. All in all, the main results obtained so far can be summarised as follows:

The macroscopic experiments performed using specimens which contained internal artificial defects are schematically summarised in Fig. 3.13. Four main ideas must be kept in mind:

- In the HCF range (200 MPa $> \sigma_{\texttt{max}} >$ 100 MPa), the S-N curve obtained using these specimens is quite similar to the curve obtained for the reference material (ambient air).
- Cracks nucleate in the majority of cases at the artificial defect and propagate in an environment assisted stage II regime which results in flat surfaces that show a series of radial ridges (Region I).
- After almost one millimetre of propagation, the crack propagation behaviour changes to an intrinsic stage I-like regime forming zigzagged fracture surfaces where large {111} crystallographic facets are observed (Region II). This region corresponds to the main portion of the internal propagation and highly irregular crack fronts characteristic of vacuum environment are formed.
- Additionally, and depending on the geometry of Region II, the internal crack can reach the free surface. In this case, a Region III is formed and crack propagation is thought to occur in an adsorption assisted stage II regime.

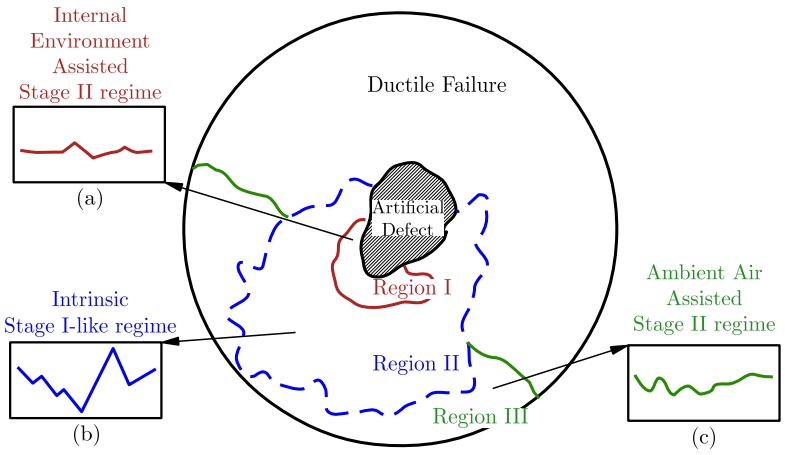

Fig. 3.13: Schematic illustration of the fracture surface produced by failure at internal defects showing the crack propagation features of: (a) Region I, (b) Region II and, (c) Region III.

3.2.2 Fatigue results on specimens with surface artificial defects ($\varnothing_{eq} \approx 2$ mm)

The objective of these tests was to study whether large artificial defects produce the same fatigue results when placed at the specimen free surface. To do so, two types of experiments were carried out under: (i) ambient air conditions and (ii) under high vacuum conditions. It must be noted that in this work the internal and surface artificial defects are considered to cause an equivalent stress state in the surrounding material. This statement is based in the work of Xu *et al.* [XU 12] who has performed FE simulations on spherical pores located at different positions in depth with respect to the free surface. By studying the evolution of the principal stress component σ_{zz}^{max} (which is parallel to the remote loading *direction*, σ_0) he concluded that the stress concentration generated by a pore intercepting the free surface in its middle can be considered identical to that created by an internal spherical pore. Moreover, Borbély *et al.* [BOR 02] obtained similar FE computation results and concluded that the most severe stress concentration state is expected to occur in the ligament, just when a subsurface pore touches the free surface.

3.2.2.1 Testing in Air Environment

The S-N curve shown in Fig. 3.5 indicates that when cycled in an air environment the artificial defects induce a reduction in fatigue life. Specimens always failed from the surface defects and the resulting fracture surfaces show the characteristic features of the adsorption assisted stage II regime from the nucleation site to the border with the final ductile failure (see Fig. 3.14).

3.2.2.2 Testing in Vacuum Environment

Surface artificial defects produce similar fatigue lives to those of specimen containing internal defects when cycled in vacuum environment. Fig. 3.15a shows a typical fracture surface formed under these conditions where crystallographic facets create a zigzagged topography characteristic of the intrinsic stage I-like regime. These features are similar to those of the previously described Region II with a highly irregular crack front. Interestingly, Fig. 3.15b indicates that no Region I was formed around the perimeter of the initiating defect. The same result was observed on the other three specimens and also endorses the possibility that deleterious molecules entrapped within the internal defect are the actual cause of the creation of Region I. Additional SEM observations

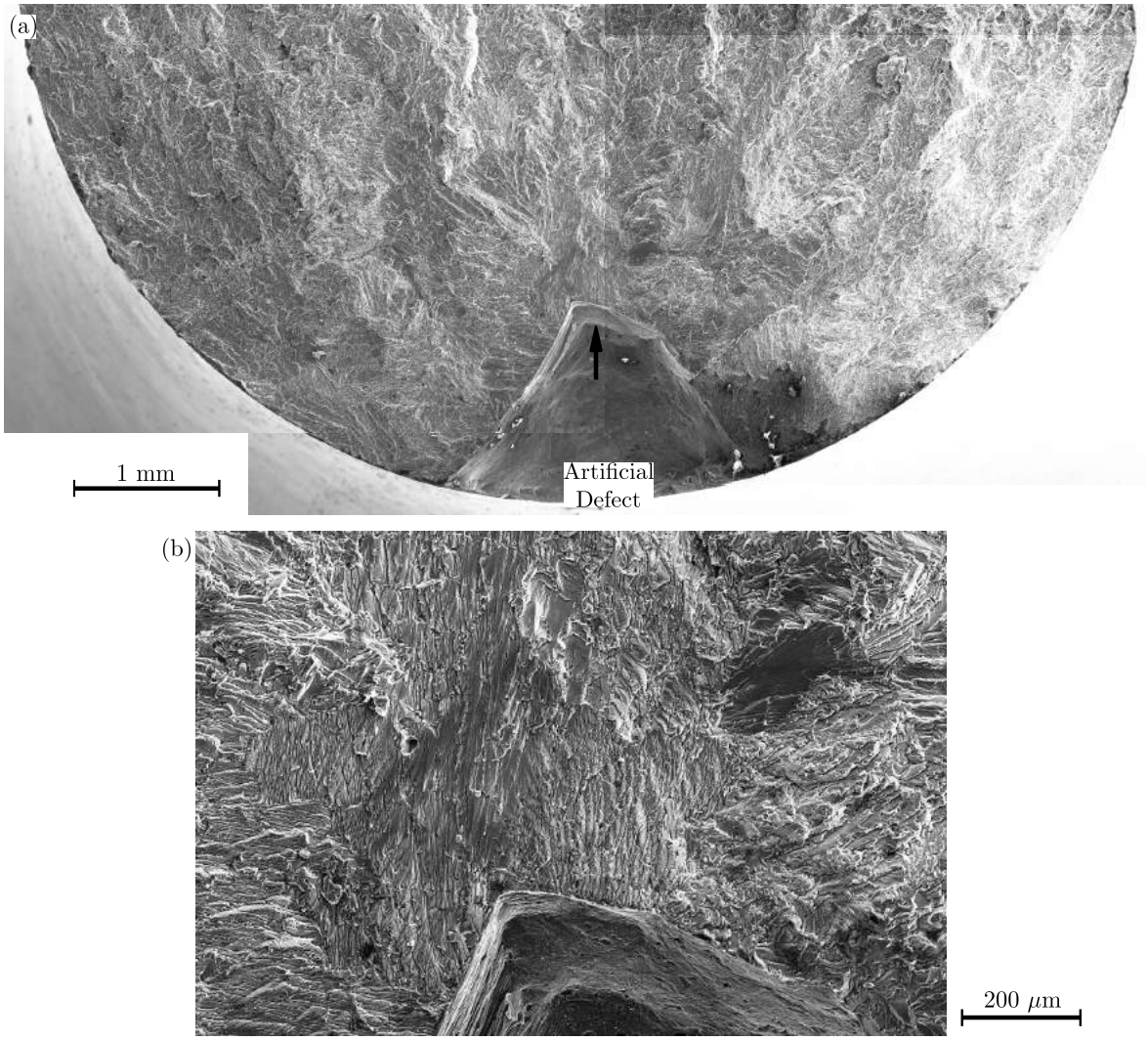

Fig. 3.14: (a) SEM observations on the fracture surface of ENSMA-SDA-03 specimen (ambient air, N_f = 1 498 500 cycles, σ_{max} = 67 MPa, Artificial Defect $\sqrt{A}$ = 1377 μm). Only Region III propagation is observed. (b) Higher magnification on the first propagation stages from the surface defect, close to the region indicated by the black arrow.

on this type of fracture surface are given in appendix E.

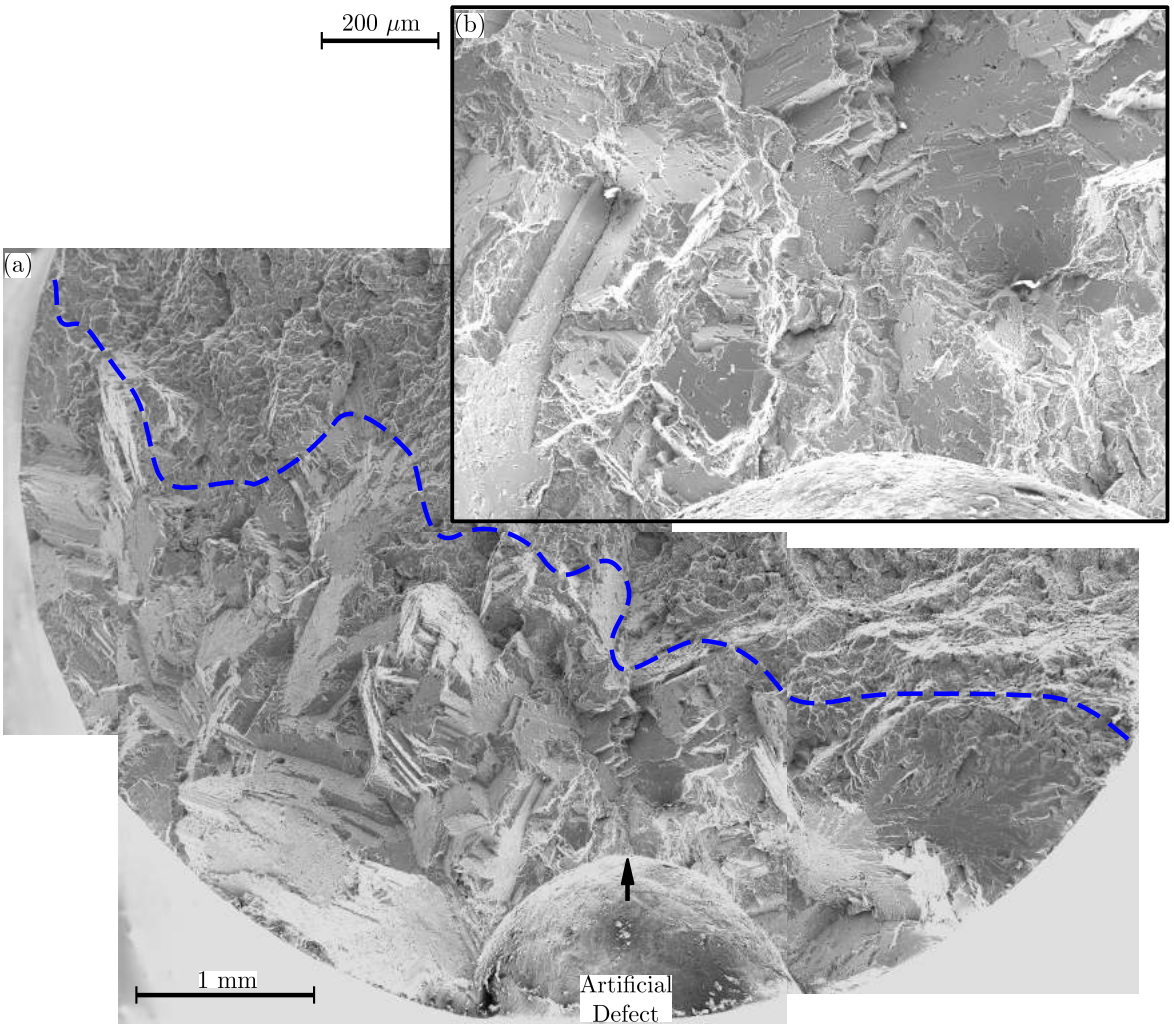

Fig. 3.15: (a) SEM observations on the fracture surface of ENSMA-SDV-01 specimen (vacuum, N_f = 2 491 343 cycles, σ_{max} = 133 MPa, Artificial Defect $\sqrt{A}$ = 1215 μm). Only Region II propagation is observed. (b) Higher magnification on the first propagation stages from the surface defect, close to the region indicated by the black arrow.

3.2.3 Fatigue results on specimens with natural defects cycled in Vacuum Environment

Specimens made out of the reference material and cycled in vacuum show a better fatigue resistance than similar specimens cycled in air as shown in Fig. 3.5 where it can be observed that the corresponding points fall above the S-N reference curve. The characteristic features observed on the fracture surfaces of these specimens are shown in Fig. 3.16: it can be observed that the whole fracture surface consists in a Region II type. Again, crack nucleation around the pore is also crystallographic and does not exhibit any feature of the Region I. Interestingly, the fractographic study revealed that four out of five specimens failed from either surface or subsurface defects. The ENSMA-SNV-04 specimen (N_f = 1 903 551 cycles and σ_{max} = 156 MPa) was the only specimen failing from a *large* internal microshrinkage porosity of $\sqrt{A}$ = 1191 μm, and yet its fracture surface

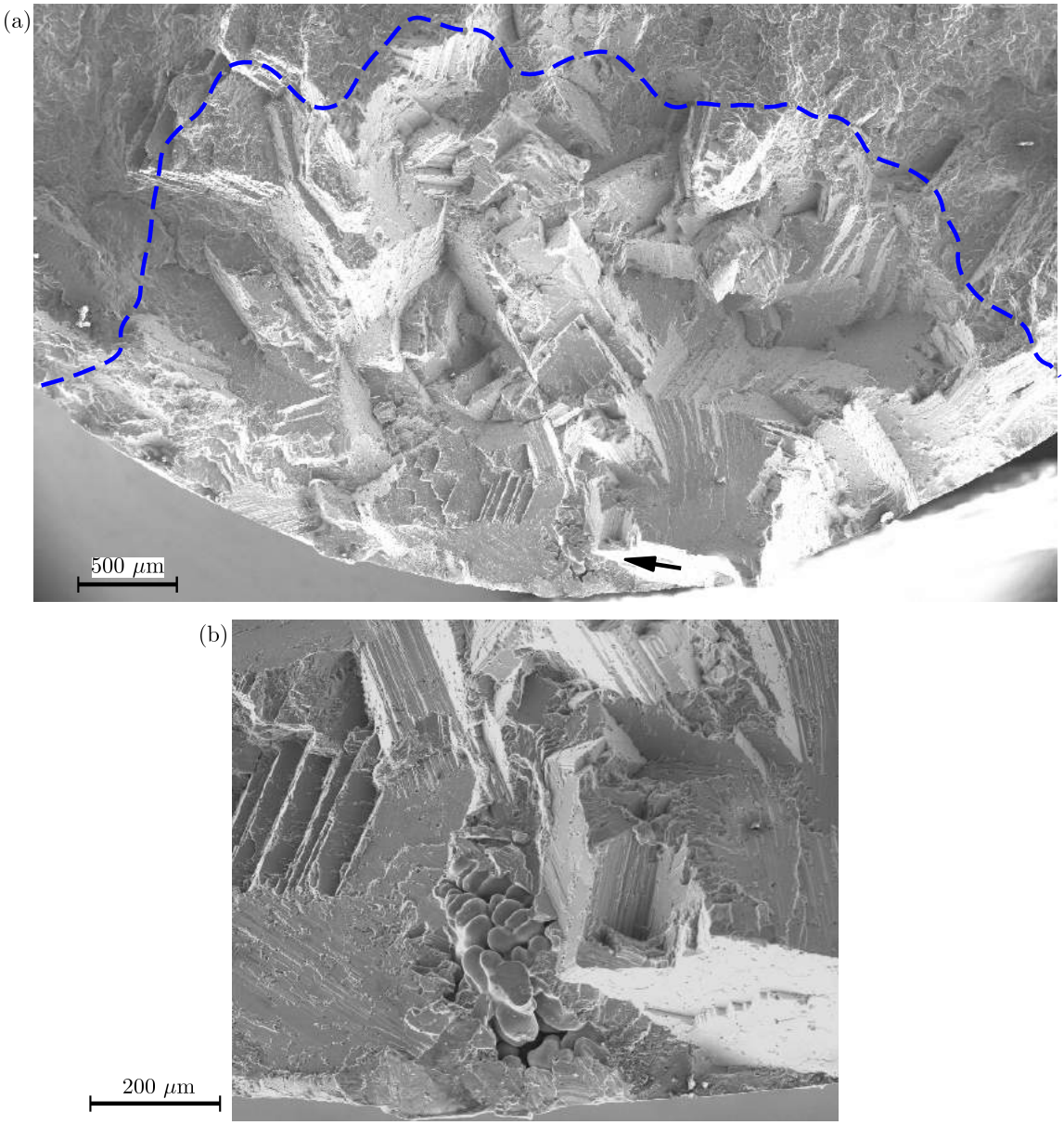

Fig. 3.16: (a) SEM observations on the fracture surface of ENSMA-SNV-03 specimen (vacuum, $N_f = 3\ 356\ 341$ cycles, $\sigma_{max} = 133$ MPa, Artificial Defect $\sqrt{A} = 278$ μm). Only Region II propagation is observed. (b) Higher magnification on the first propagation stages from a surface microshrinkage, close to the region indicated by the black arrow.

exhibits a *surface* microshrinkage of $\sqrt{A} = 505$ μm which propagated a microcrack. SEM observations on this specimen and three others of the same kind are given in appendix F. It must be noted that the pore population within this type of specimen was unknown and so the microshrinkages nucleating the fatal cracks might be the largest ones present within the gage. Nevertheless, results indicate dominance of surface nucleation even when cycling in vacuum environment.

The main findings of the fractographic analysis performed on macroscopic specimens containing surface defects and cycled under ambient air or vacuum conditions are schematically summarised in Fig. 3.17. The ideas that must be kept in mind are as follows:

- The results on specimens containing surface artificial defects indicate that they are highly detrimental to fatigue life when cycled in ambient air.
- When cycled in vacuum environment, surface defects produce similar fatigue results as those of specimens with internal artificial defects. The local stress state is considered equivalent for both types of defects although the affected volume is twice that of a surface defect.
- Crack propagation occurred in an adsorption assisted stage II regime for specimens cycled in air environment and in an intrinsic stage I-like regime for specimens cycled in vacuum environment.
- With regard to the specimens containing natural defects and cycled in vacuum environment, crack nucleation occurs predominantly at surface/subsurface microshrinkage pores and their fracture surfaces show the features of a propagation in an intrinsic stage I-like regime.

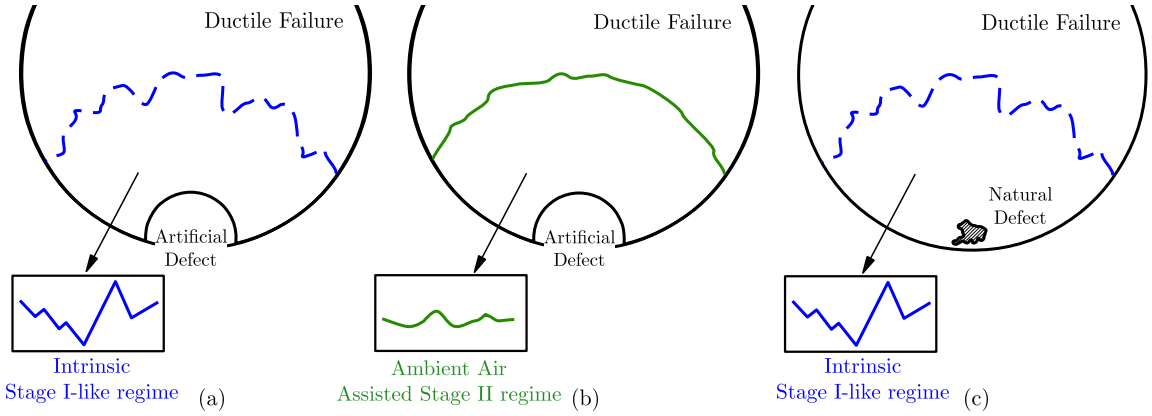

Fig. 3.17: Schematic illustration of the fracture surfaces produced by: (a) failure at surface artificial defects cycled in vacuum, (b) failure at surface artificial defects cycled in air environment and, (c) failure at surface/subsurface microshrinkage pores cycled in vacuum.

3.3 Uniaxial fatigue testing on synchrotron specimens

3.3.1 Synchrotron specimens containing internal natural defects

Small fatigue specimens (cross section 2mm×2mm) containing natural internal defects have been produced using the (time consuming) procedure described in § 1.2.1.1. Appendix A gives more details on selected and rejected specimens and illustrates the amount of work required to produce a few suitable samples. Table 3.3 summarizes the results obtained for the specimens cycled *in situ*

at the SLS synchrotron facility. **None** of the six specimens tested failed because of a fatal crack nucleated at an internal defect. The causes of final failure are: (i) a fatal crack which was nucleated at smaller surface defect (these pores/oxides are about three times smaller than the internal ones), or (ii) a fatal crack caused by fretting of the specimen head with the grips. It must be noted that the presence of *small* surface defects was unintended and that when such defects were not present, the final failure was transferred to the grips.

Specimen	σ_{max} (MPa)	N_f (cycles)	Internal Defect	Cause of Failure
SLS-40	240	>82 000	$\sqrt{A}$ = 350 μm; Nc	Surface Defect; $\sqrt{A}$ = 80 μm
SLS-14	230	>73 000	$\sqrt{A}$ = 340 μm; Pc	Surface Defect; $\sqrt{A}$ = 120 μm
SLS-17	200	190 000	$\sqrt{A}$ = 386 μm; Pc	Failure at the grips
SLS-22	200	355 000	$\sqrt{A}$ = 314 μm; Jnc	Failure at the grips
SLS-06	200	82 000	$\sqrt{A}$ = 341 μm; Nc	Surface oxide; $\sqrt{A}$ = 154 μm
SLS-11	172	>90 000	No internal defect	Surface pore; $\sqrt{A}$ = 435 μm

Table 3.3: Summary of fatigue results obtained with specimens containing natural defects. The symbol > placed in front of some number of cycles (N_f) indicates that the experiment was terminated before the occurrence of final failure, usually when the presence of a fatal surface crack was evident. Pc means *propagated a crack*, Nc means *No crack* and Jnc is for *Just nucleated a crack*.

Internal crack initiation and propagation did occur in a few specimens; from those specimens, interesting comparisons between internal and surface cracking could be obtained. For example, in specimen SLS-14 both Pore 1 (surface pore) and Pore 3 (internal pore) nucleated a crack after 40 000 cycles (see Fig. 3.18a) but with obvious differences in the propagation behaviour. The surface crack (Fig. 3.18b) propagated in a direction almost perpendicular to the loading axis with a slightly rough path characteristic of propagation in ambient air (absorption assisted stage II). The path of the internal crack was strongly inclined with respect to the loading axis creating facets on the fracture surface (Fig. 3.18c). As previously shown, this crystallographic behaviour corresponds to intrinsic stage I-like crack propagation under vacuum conditions.

Fig. 3.19a-b shows the crack front positions of the two cracks along the fatigue life. Those fronts were obtained by projecting the 3D crack shape along the loading axis. It can be observed that the surface crack formed a relatively regular front in the shape of an ellipsoid (with a a/c ratio of 1.1 measured at 71 000 cycles[2] while the front of the internal crack has a more irregular shape and shows a preferential growth on one side of the pore.

As for the crack growth rates, the curve presented in Fig. 3.19c indicates that the growth rate of the internal crack is lower than that of the surface crack which is about five times longer at 73 000 cycles (770 μm against 146 μm) than the internal one. It must be noted that in order to take into account the oblique growth of the internal crack, its projected area was corrected using an average orientation of the crack of 45° with respect to the loading direction.

The crack growth rate was also obtained by measuring the crack length along lines originating from the initiation site and making different angles with the sample surface (see appendix G).The results obtained with this method show similar fatigue behaviour, with lower crack growth rates also being observed for the internal crack. With both methods, the crack growth rate of the internal crack was found lower than that of the surface one.

[2]After 73 000 cycles, this crack had propagated through the specimen corner and its projected area was double the size of that obtained at 71 000 cycles. Therefore and for the sake of clarity, it was decided not to show this last stage although the corresponding value is included in Fig. 3.19

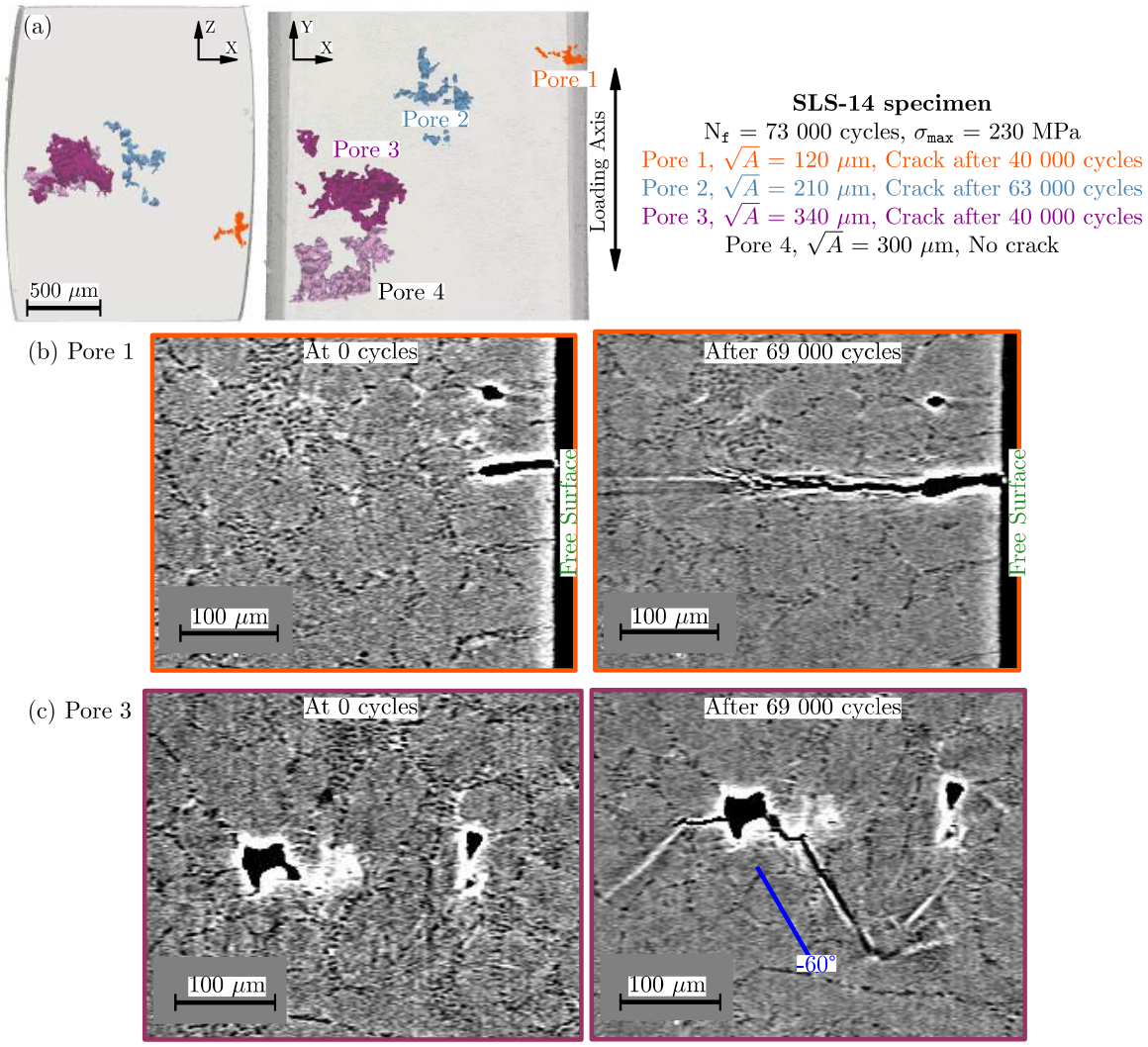

Fig. 3.18: (a) Pore distribution within the gage of SLS-14 specimen. (b) Synchrotron tomographic images showing surface Pore 1 fatigue progression at 0 and 69 000 cycles. (c) The same as before but for the case of internal Pore 3.

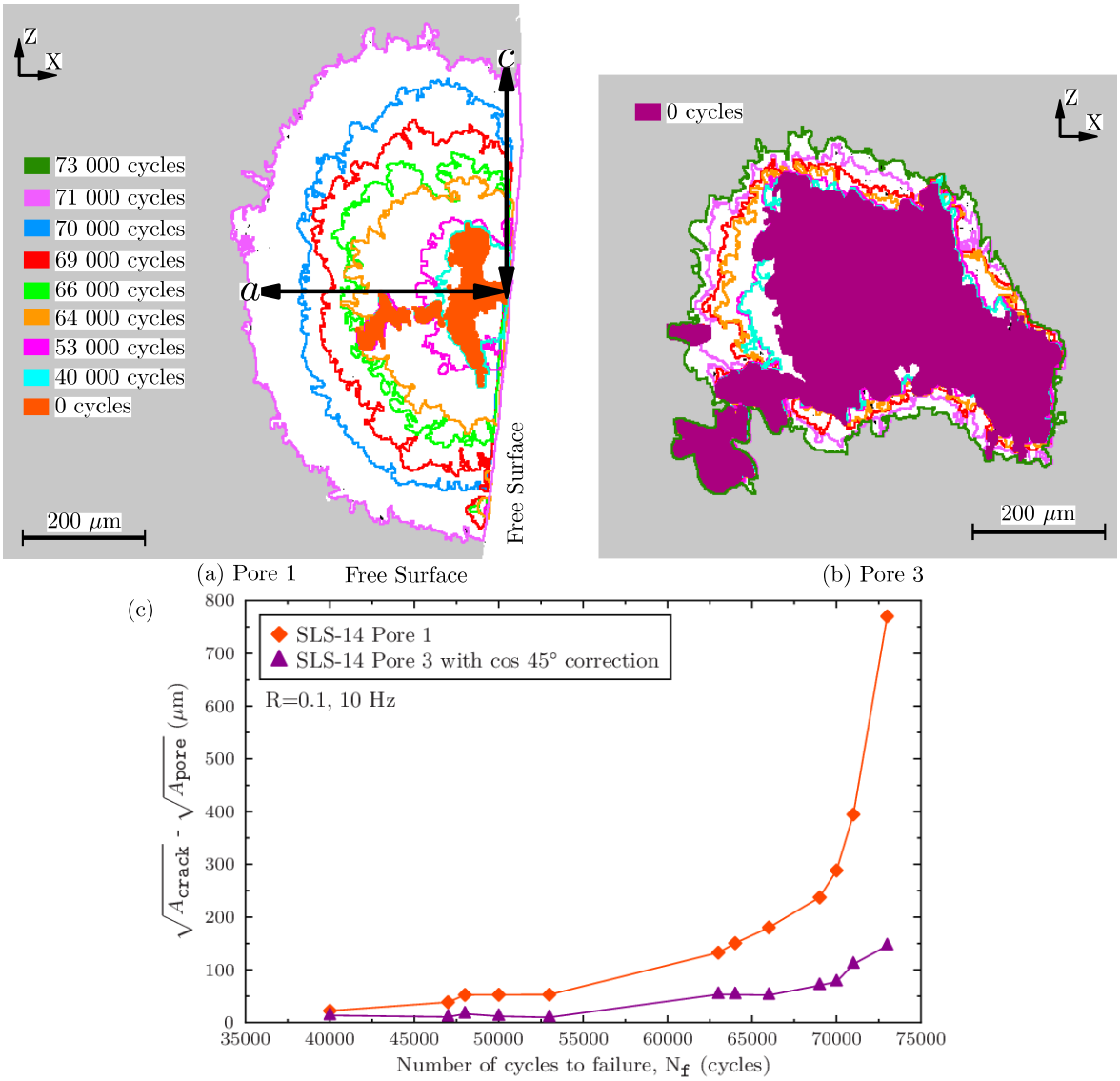

Fig. 3.19: SLS-14 specimen cycled at $\sigma_{max} = 230$ MPa. (a) Y (loading direction) projection of the main growth stages for the crack nucleated at Pore 1 (some stages omitted for clarity). (b) Same as before but for the case of the internal Pore 3. (c) Plot of the crack propagation ($\sqrt{A_{crack}}$ - $\sqrt{A_{pore}}$) against the number of cycles (N_f) for these two pores.

In spite of the time consuming experimental effort deployed to produce and cycle synchrotron specimens containing well controlled internal defects (see appendix A), **we have failed to obtain fatigue failure from the interior of these specimens**. This tend to indicate that, for the conditions investigated, crack initiation and propagation at the free surface were always much easier. It must be noted that internal cracks were observed in two other synchrotron specimens (see Table 3.3 and appendix H). Those cracks exhibited smaller cracked surfaces that the one described previously (∼150 μm long) but the same specific features (slow growth rate and apparently crystallographic paths) could be observed.

3.3.2 Synchrotron specimens containing internal artificial defects ($\varnothing_{eq} \approx 1$ mm)

Based on the observations made for macroscopic specimens containing artificial defects, it was decided to produce and cycle *small* synchrotron specimens containing *artificial* defects. Because the size of the cross section of the synchrotron specimens cannot exceed 3 mm (compared to $\varnothing = 10$ mm for macroscopic specimens), the casting process had to be adapted to produce much smaller internal defects (targeted value for the defect diameter: 1mm).

The first casting (termed 4xx) produced together with the internal defects a high volume fraction (∼0.19%) of un-desired micropores (average $\varnothing_{eq} = 81$ μm) randomly distributed within the specimen gage. The internal defect as well as the parasitic pores are shown in Fig. 3.20a for one sample (SLS-445). Some of these micropores occurred to be at the free surface (12 out of 71) and, as shown in Fig. 3.20b-c, when cycled, five of them nucleated fatigue cracks at different stages of the cycling (with Pore 4 of $\sqrt{A} = 100$ μm nucleating a crack at 130 000 cycles and Pore 5 $\sqrt{A} = 125$ μm at 170 000 cycles). Pore 1 was the one responsible for the failure at $N_f = 190\,000$ cycles and **no cracks were observed at the internal artificial defect** ($\sqrt{A} = 875$ μm). This result is in good agreement with that of CTIF-101.57 specimen (see Fig. 3.8 and Fig. 3.9) where an artificial defect of $\sqrt{A} = 2064$ μm had propagated an internal crack of 900 μm length after 938 500 cycles. It seems likely that the final failure of this specimen occurred way too early for the artificial defect to be able to nucleate an internal crack.

A second casting (termed 6xx) was produced in order obtain a sounder material. The pore volume fraction was successfully reduced to 0.04% (average $\varnothing_{eq} = 90$ μm) however the results of the subsequent fatigue tests remained essentially the same. This is illustrated in Fig. 3.21 in the case of one specimen (ESRF-636) where a surface pore of $\sqrt{A} = 105$ μm (one of the four detected along the whole gage) nucleated a fatal crack between 200 000 and 300 000 cycles. It is noteworthy that the stress level of this specimen ($\sigma_{max} = 105$ MPa) is slightly lower than the fatigue limit of the material ($\sigma_D = 115$ MPa). It must also be noted that the macroscopic specimens cycled at 105 MPa were able to endure 7 500 000-9 000 000 cycles (see Fig. 3.6a) before the occurrence of internal failure. In spite of being about eight times smaller than the internal defects, the surface microporosities seem to be highly deleterious to the fatigue life of synchrotron specimens.

Similar results as those described for specimen SLS-445 and ESRF-636 have been obtained with other synchrotron specimens (see appendix I) for which crack initiation did not occur or occurred at surface defects without any nucleation being observed at the (much larger) internal defects.

Finally, Table 3.4 lists the results obtained with synchrotron specimens containing centred internal defects. It can be observed, as mentioned previously, that for all those specimens failure occurred from surface defects in spite of the presence of a (comparatively) larger internal defects.

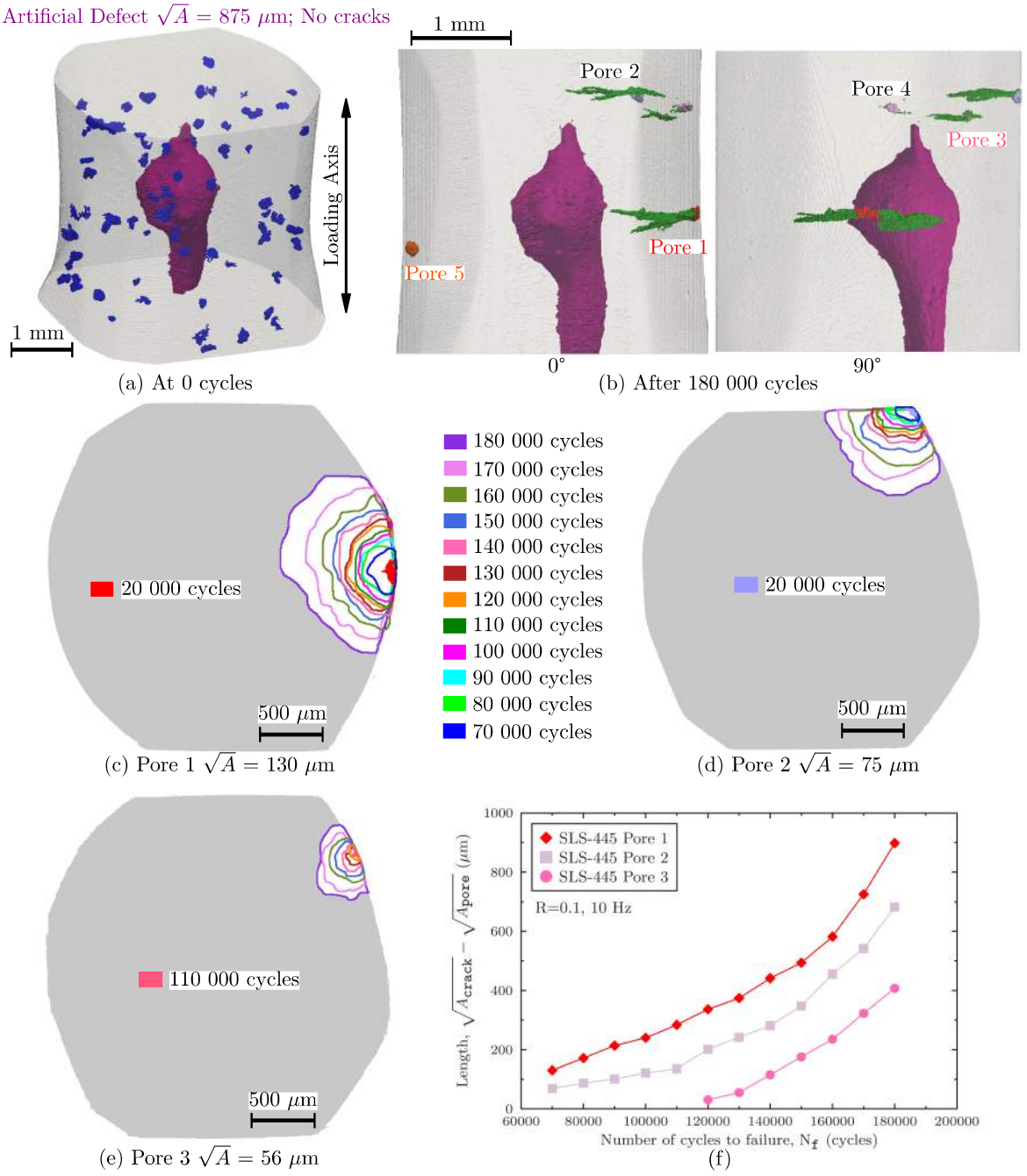

(a) At 0 cycles (b) After 180 000 cycles

(c) Pore 1 $\sqrt{A}$ = 130 μm (d) Pore 2 $\sqrt{A}$ = 75 μm

(e) Pore 3 $\sqrt{A}$ = 56 μm (f)

Fig. 3.20: (a) Defect distribution at 0 cycles within SLS-445 specimen gage. The artificial defect is presented in dark magenta and the microporosities in blue. The fatigue testing parameters are N_f = 190 000 cycles and σ_{max} = 140 MPa. (b) 3D rendering after 180 000 cycles at 0° and 90° only showing the five pores which nucleated a surface crack. (c) Y projection of the main growth stages for the crack nucleated at Pore 1. (d) For the case of Pore 2 and (e) for Pore 3. (f) Plot of the crack propagation ($\sqrt{A_{crack}}$ - $\sqrt{A_{pore}}$) against the number of cycles (N_f) for these three pores.

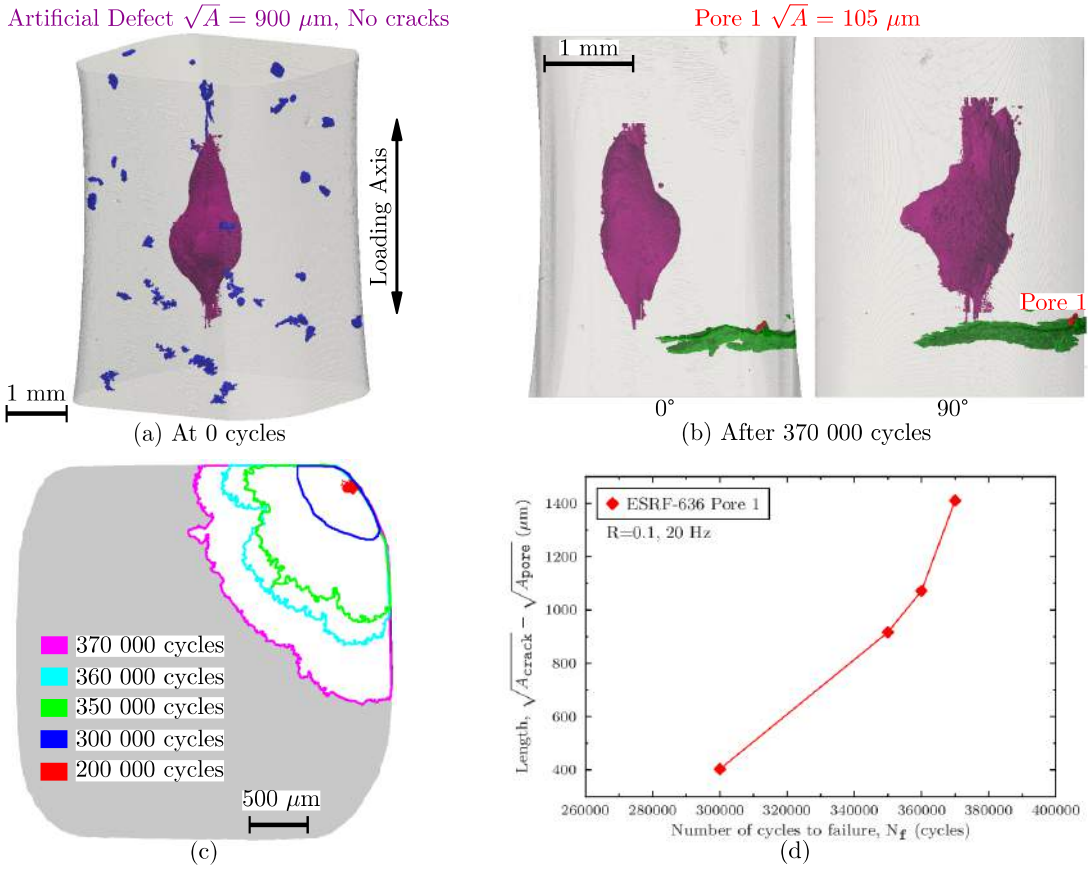

Fig. 3.21: (a) 3D rendering at 0 cycles of the defect population within the gage of ESRF-636 specimen. (b) 3D renderings at 0° and 90° after 370 000 cycles showing the surface crack (in green) formed at Pore 1. The fatigue testing parameters are N_f = 370 000 cycles and σ_{max} = 105 MPa. (c) Y projection of the main growth stages for this crack. (d) Plot of the crack propagation ($\sqrt{A_{crack}}$ - $\sqrt{A_{pore}}$) against the number of cycles (N_f) for Pore 1.

Specimen	σ_{max} (MPa)	N_f (cycles)	Internal Defect	Cause of Failure
SLS-445	140	190 000	$\sqrt{A}$ = 875 μm; Nc	Surface Defect; $\sqrt{A}$ = 130 μm
SLS-449	140	140 000	$\sqrt{A}$ = 830 μm; Nc	No surface cracks; Machine breakdown
ESRF-451	95	>1 700 000	$\sqrt{A}$ = 940 μm; Nc	Surface Defect; $\sqrt{A}$ = 164 μm
ESRF-636	105	>370 000	$\sqrt{A}$ = 900 μm; Nc	Corner Defect; $\sqrt{A}$ = 105 μm
ESRF-641	90	3 000 000	$\sqrt{A}$ = 790 μm; Nc	No surface cracks; Failure at the grips

Table 3.4: Summary of the results obtained with synchrotron specimens containing centred artificial defects. The symbol > placed in front of some number of cycles (N_f) indicates that the experiment was terminated before the occurrence of the final failure, usually when the presence of a fatal surface crack was evident. Nc means *No crack*

The findings of the synchrotron experiments are schematically summarised in Fig. 3.22. Four main ideas must be kept in mind:

* Only internal natural defects of $\sqrt{A} \approx 300$ μm were able to nucleate internal cracks which propagated under vacuum conditions.
* When observed, internal cracks propagated with smaller crack growth rates than surface cracks and the crack path corresponded to (apparently) crystallographic facets.
* Crack initiation at artificial internal defects ($\varnothing_{\text{eq}} \approx 1$ mm) was never observed.
* Instead, crack nucleation occurred at surface pores with a size almost ten times smaller than the internal artificial defect.

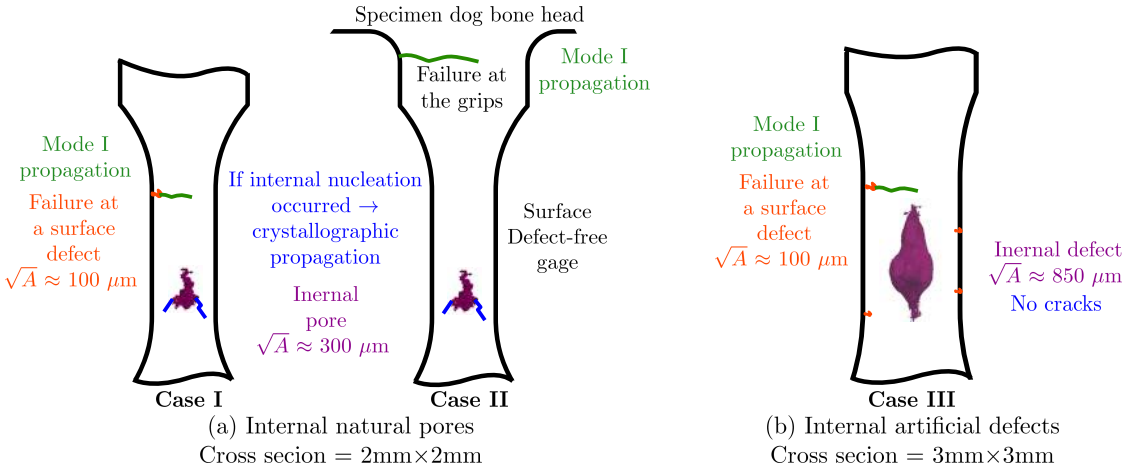

Fig. 3.22: Schematic illustration of (a) the cracking of synchrotron specimens containing internal pores (Case I represents the specimens whose failure was caused by surface defects and Case II is for the specimens failing at the grips) and (b) the cracking of synchrotron specimens containing internal artificial defects (Case III).

The 3D images obtained using synchrotron radiation can offer accurate descriptions of the convoluted morphology of casting defects and so these images were used to perform realistic finite element simulations. The objective of those simulations is the calculation of the local stress levels induced by the different kinds of pores that can be present within specimen gages. The findings of this study are summarised in the following paragraphs after a brief bibliographic introduction on the effects of casting defects.

3.4 Background on the effects of stress concentrations on fatigue strength

Because of their complex geometries, engineering structures invariably contain stress raisers (e.g., holes, changes of cross section, or weld toes) where fatigue cracks are prompt to an early nucleation, strongly influencing the fatigue response of such components. One of the most successful methods for quantitative evaluation of various defects is that of Murakami [MUR 02b] which consists in assessing the fatigue behaviour of materials through empirical relations based on applied stress, hardness and size of the defect. To do so, Murakami introduced a geometrical parameter named $\sqrt{area}$ which corresponds to the square root of the area obtained by projecting the shape of a defect onto the plane perpendicular to the maximum tensile stress. This proposition enables the evaluation of fatigue lives for all kinds of defects since no consideration is made about the complex morphologies that defects usually present. Murakami supported this simplification by arguing

that experimental results on drilled specimens show that fatigue strength depends on the defect size. Nowadays, the efforts are mainly focused on the stress and deformation fields formed in the immediate vicinity of notches since these stress-based approaches allows a better description of the local response of the material [SUS 08, NAD 06].

3.4.1 Effects of porosity on the fatigue life of AlSiMg cast aluminium alloys

As it was introduced first in this chapter, the most damaging localisation of a defect is that of a cavity which lies just beneath the free surface, touching it [BOR 02]. Gao *et al.* [GAO 04] also performed FE simulations on idealized spherical micro-defects located at different distances s with respect to the free surface. Those authors obtained the highest values for K_t when the defect just intersects the free surface (s becomes negative). For a defect of $\varnothing_{eq}$ = 200 μm, K_t is 2.07 when s = 500 μm (internal pore), raising to 2.54 when s = 10 μm (subsurface pore) and to 3.80 when s = -20 μm (intercepting the free surface). These K_t values increase with increasing sizes of the idealized spherical defect, especially for the intersecting cases and, to a lower extent, for the subsurface ones (*e.g.,* $\varnothing_{eq}$ = 600 μm, K_t is 2.42 when s = 100 μm, raising to 3.61 when s = 10 μm and to 5.23 when s = -20 μm). The size effect can be considered as negligible if the defect is located far in the specimen bulk. Moreover, the K_t values observed at the free surface diminish when the distance between the pore and the surface is equivalent to the pore diameter.

Some other FE studies on the influence of pore parameters can be summarised as follows:

* *Defect distribution.* When two pores lay more than one radius apart in the direction perpendicular to the loading direction and at the same level, the stress concentration around them is just the same as that of one individual pore [XU 12].
* *Defect shape.* When a subsurface pore is changed from a prolate (r_y/r_x = 1/4) to oblate (r_y/r_x = 4) ellipsoid, both the highly stressed field around the defect and the projected area in the transverse (xy) plane will decrease, while the local radius of curvature ρ of the pore will increase [LI 09] (Fig. 3.23a).
* *Defect orientation.* For a subsurface pore and if the orientation of the major axis of a prolate ellipsoidal defect (r_y/r_x = 1/2) is rotated from the transverse ($\phi = 0°$) to longitudinal ($\phi = 90°$) plane, both the highly stressed field and the projected area on the transverse plane (xy) will decrease while the projected area on the longitudinal (xz) plane will remain constant [LI 09] (Fig. 3.23b).

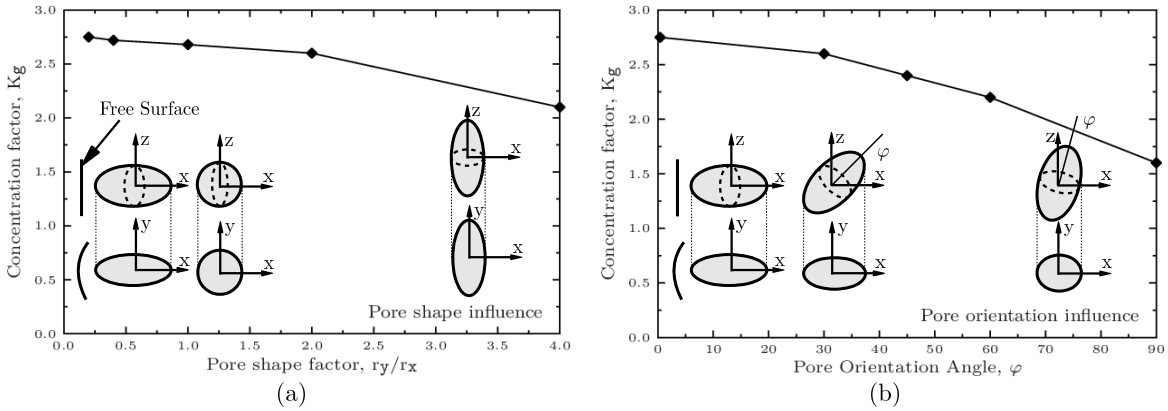

Fig. 3.23: (a)-(b) Plots of the variation of K_g against the shape and orientation of idealized pores [LI 09]. The stress-strain concentration factor, $K_g = \sqrt{k_t k_\varepsilon}$, accounts for the average effect of both local concentrated stress (k_t=$\sigma_{max}/\sigma_\infty$) and strain ($k_\varepsilon = \varepsilon_{max}/\varepsilon_\infty$) in the region of the pore.

All those studies deal with defects having ideal shape which can be quite different from real defect shapes such as the case, for example, of micro-shrinkage cavities. Nicoletto *et al.* [NIC 10] employed X ray microtomography combined with FE simulations to study the complex 3D stress fields around microshrinkages and gas pores in a AlSi7Mg cast alloy. They observed that the K_t values of this two types of defects are quite alike as the local minimum radius of pore surfaces are similar in both cases. In addition, a variation of the K_t values was found when the gas pore morphology was simulated using different far-field load directions. The maximum K_t value, which corresponds to the most unfavourable load direction is 3.5 and the average obtained using the values of all simulated directions (seven in total) is $K_t = 3$. These results differs from those of Yi *et al.* [YI 03]. In this study, 2D FE analyses were performed using random micrographs of shrinkage pores. They found that stress concentrations around the concave tips of the pore can be larger than 3.0, with maximum values of 6.2.

Finally, Vanderesse *et al.* [VAN 11] carried out image analysis on X ray microtomography data obtained, prior to fatigue testing, from five specimens of AlSi9Cu3 material. The evaluation of specimen pore distribution combined with the resulting fatigue lives indicates that the fatal pores have sizes located at the high end-tail of the size distribution. Pore-rich regions are also favourable sites of nucleation. Subsequent FE simulations on 3D meshes generated from the microtomography data suggest that the volume affected by stress concentration at the vicinity of the pores is a valuable indicator of their propensity to initiate cracks.

The major points regarding the fatigue response of components affected by the presence of stress raisers can be outlined as follows:

1. The presence of defects in engineering structures results in reduced fatigue lives of such components.
2. The defects act as stress raisers, causing an early initiation of fatigue damage.
3. 3D pores with complex, tortuous morphologies are often idealized using a sphere of equal projected area in the plane perpendicular to the loading direction (Murakami's approach).
4. FE simulations predict that the highest stress concentrations around a defect occur when it just intersects the free surface.
5. The shape and orientation of real defects have an influence on the K_t values.

3.5 FE results on the effect of casting defects

3.5.1 Meshing process

Due to computation limitations, the FE analysis is restricted to a limited number of 3D elements (tetrahedra) which must not be larger than 500 000. The number of 2D elements generated from surfaces extracted from the 3D tomographic images considerably impacts the number of 3D elements present in the final volume meshes, hence increasing the complexity of the subsequent simulation. To reduce such a number, every tomographic scan recorded prior to fatigue testing is first cropped to a sub-block with a ∼2 mm length along the loading direction and then re-scaled from 1.7 μm to 3.4 μm voxel size. Fig. 3.24 illustrates the re-scaling process, where the overall shape of the pores is respected with the limitation that some particularities (indicated by arrows on the figure) of pore morphology are inevitably lost.

The Avizo [AVI 13] software is used to generate 2D meshes (triangles) from the free surfaces of specimens and the solid/air interface of pores (see Fig. 3.25a). These two 2D meshes are separately exported to two STL files (text-type format files). It is important to mesh the interfaces with a

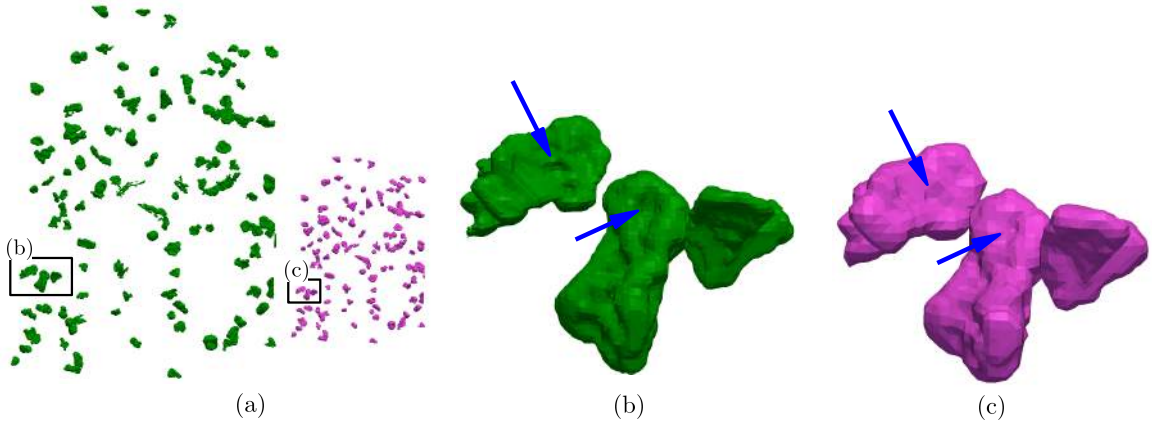

Fig. 3.24: (a) 3D rendering of pore population within and specimen recorded at 1.7 μm of voxel size (in green) and then downsized to 3.4 μm (in pink). (b) Detail of pores appearance at 1.7 μm voxel size. (c) Detail of pores appearance at 3.4 μm voxel size. Arrows indicate some details of the morphology of pores that are lost when performing the re-scaling method.

number of triangles large enough to accurately describe their geometry. In the present case, the pores are far more complex and smaller than the specimen surface. But the resulting STL files contain an unreasonably quantity of triangles (between 300 000 and 400 000 in the case of pores) that must be reduced in order to minimize the computation time. Such a reduction is carried out using the open-source mesh generator Gmsh which allows mesh reduction while producing high-quality meshes [MAR 10]. The remeshed surfaces of pores (30 000-50 000 triangles, see Fig. 3.25b) and free surfaces (2 000 triangles) for each specimen are then concatenated into a single file that enables the generation of 3D meshes. These meshes still contains a high number of elements (800 000-1 000 000 tetrahedra), which is reduced using a Gmsh distance plugin that imposes a size gradient from the pore surface to the free surface (see Fig. 3.25c). This final reduction delivers 3D meshes with approximately 300 000-500 000 elements.

While an accurate simulation of the mechanical behaviour of the material should take the cyclic plasticity into account, a simpler approach is used here to evaluate the influence of pore parameters (*e.g.,* size, shape, orientation) on the propensity of the pores to initiate fatigue cracks assuming that high local stress level will promote cyclic plasticity which will in turn generate a crack. Thus, elastic simulations are performed for the evaluation of the stress concentration factor K_t. Elasto-plastic simulations are also carried out in order to evaluate the characteristics of the volume that is affected by the presence of pores. This volume is hereafter termed as *affected* volume. The maximum principal stress σ_{22}^{max} (where $_{22}$ corresponds to the loading direction) was chosen to perform these types of volume evaluations. The terminology used to describe the affected volume is as follows: (i) the *plastically strained volume* corresponds to the region where microplasticity is formed around the pore ($\sigma_{22}^{max} > 275$ MPa), (ii) the *stress-concentration volume* corresponds to the region where 1.1-1.4$\times\sigma_0^{max} < \sigma_{22}^{max} \leqslant 275$ MPa and, (iii) the term *affected volume* stands for the union of both plastically-strained and stress-concentration volumes. The reader is reminded that $\sigma_y = 275$ MPa and $\sigma_{UTS} = 335$ MPa.

With regard to the computation parameters, it must be noted that the computation is static and was performed using ABAQUS™ [ABA 13]; the material Young's modulus is taken equal to 73.5 GPa and the Poisson ratio to 0.3. A monotonic, uniaxial displacement is imposed to the upper extremity of the mesh, while the lower one is kept at a constant height (the nodes are nevertheless free to move laterally in the plane). The value of the displacement is established

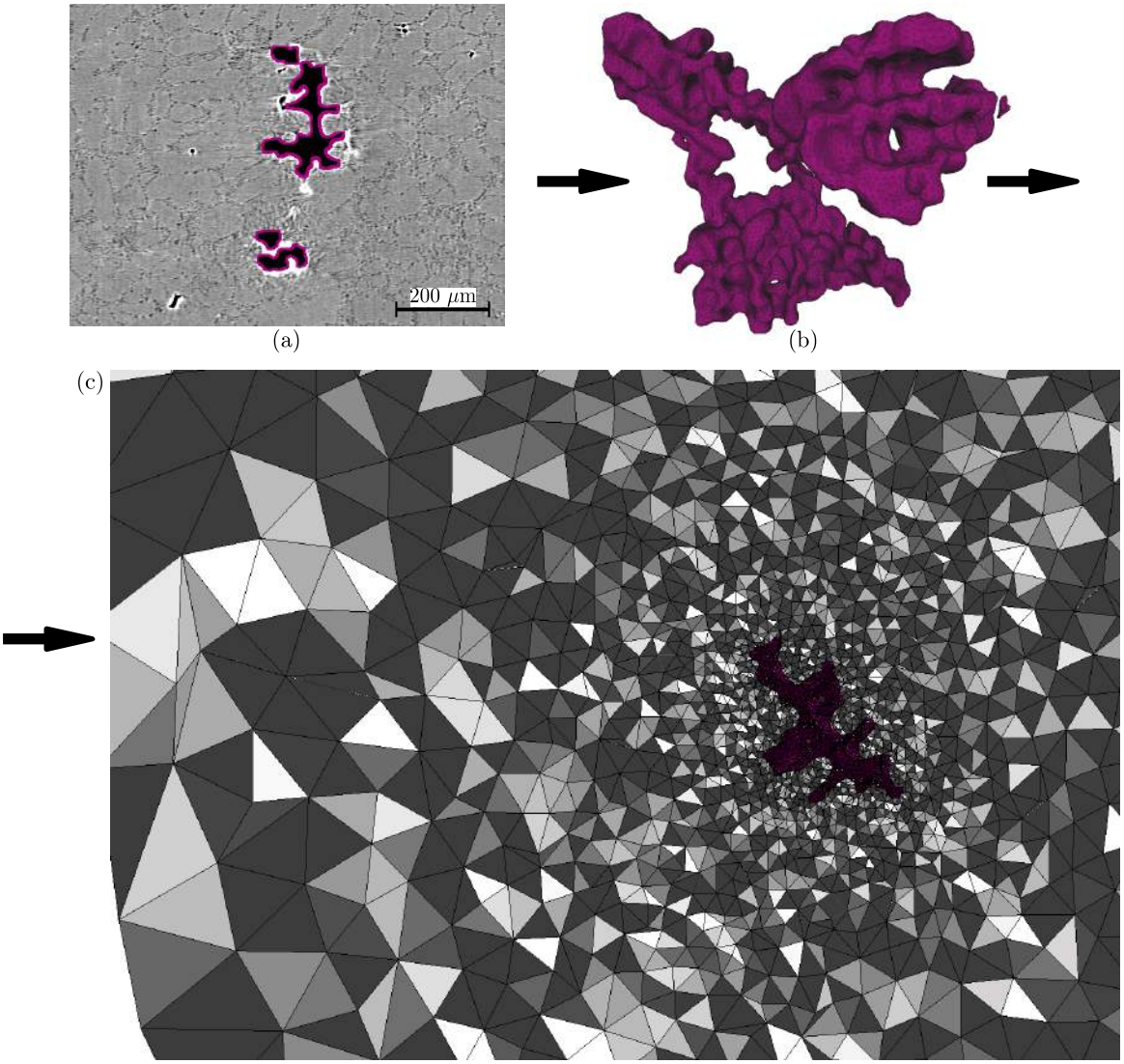

Fig. 3.25: (a) Synchrotron tomographic 2D image of a microshrinkage pore (voxel size = 1.7 μm). (b) 3D rendering of the surface mesh (34 214 triangles) of this pore generated using Avizo + Gmsh. (c) Gmsh rendering of a volume mesh showing fine tetrahedra around the pore surface and rough tetrahedra near the free surface.

through the Young's law such as to match the maximal stress imposed during fatigue tests. For the plastic behaviour, macroscopic monotonic tension tests were performed in order to obtain the material's stress strain curve. A Voce plastic law [PHI 98] was used to model the material elasto-plastic behaviour and subsequently introduced into the ABAQUS™ code for every elasto-plastic simulation that was performed.

3.5.1.1 Meshing process for small surface defects

Fig. 3.26a-b presents a comparison between the K_t values obtained for a subsurface and a surface simulation. The meshing process of surface pores is a heavy and time consuming task because the 3D mesh has to be carefully redefined at the intersection between the pore and the free surface. Meshing the surface pores as subsurface pores, separated by a distance of $\sim$50 μm from the free surface, greatly facilitates the meshing process. Nevertheless, the drawback of subsurface simulations is that attention must be paid to the post-treatment of FE results to avoid taking into account the values obtained within the ligament (see red arrows on Fig.3.26) because such values do not occur in reality. Fig. 3.26c shows that compared to a subsurface simulation, surface simulation slightly increases the K_t counts at the K_t bins between 3 and 5.5, although the frequency increases from six to eight percent at $K_t = 2$. In view of these results, **subsurface simulations were considered a valid approach and systematically performed in synchrotron specimens containing *small* surface defects.**

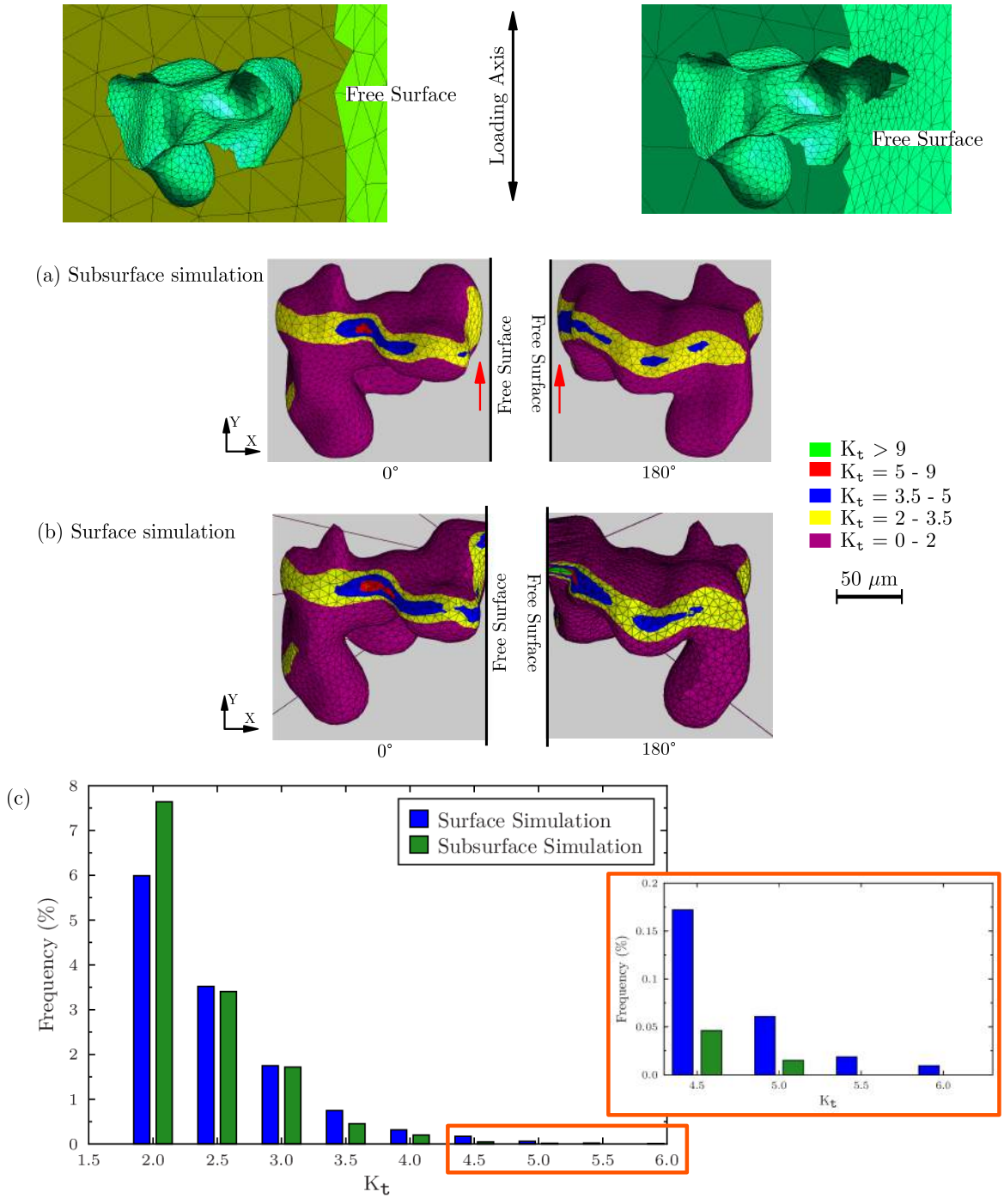

Fig. 3.26: (a) K_t evaluation obtained in a FE subsurface simulation. (b) K_t evaluation on the same pore but obtained in a FE surface simulation. (c) Histogram showing the frequency of counts against the different K_t values of FE surface and subsurface simulations performed for the same pore.

3.5.2 FE results on casting defects

Several FE simulations were performed using 3D synchrotron images although not all of them are presented in the § that follow. All the FE simulations that were performed are listed in Table 3.5. This table first introduces the only $\varnothing_{\mathtt{eq}} \approx 2$ mm internal artificial defect (CTIF-101.57 specimen) that could be simulated. Macroscopic specimens predominantly produce failure from internal defects and when this occurs the morphology of internal defects cannot be used to obtain surface meshes. Moreover, the lowest voxel size that can be obtained using laboratory tomography on a $\varnothing$ 10 mm cross section is 12 μm which impedes a realistic description of the fine details at the surface of the pores/defects. Therefore, the only macroscopic specimen available (CTIF-101.57 specimen) was sectioned using EDM in order to obtain a lower cross section of ∼4mm×4mm (allowing the use of a smaller voxel size: 4 μm). The artificial defect morphology is then introduced within an idealized $\varnothing = 10$ mm cylindrical surface mesh in order to generate the volume mesh.

Specimen name	$\sigma_{\mathtt{max}}$ **(MPa)**	**Type of simulation**	$\sqrt{A}$ **(μm)**	**Crack Inititation (cycles)**
CTIF-101.57 Defect	140	Internal Artificial Defect	2064	Crack after 938 500
SLS-445 Defect	140	Internal Artificial Defect	875	No crack after 190 000
SLS-445 Pore 1	140	Subsurface Defect	130	Crack after 20 000
SLS-445 Pore 2	140	Subsurface Defect	75	Crack after 20 000
SLS-445 Pore 5	140	Subsurface Defect	125	Crack after 170 000
SLS-449 Defect	140	Internal Artificial Defect	830	No crack after 140 000
SLS-449 Pore 1	140	Subsurface Defect	128	No crack after 140 000
SLS-449 Pore 2	140	Subsurface Defect	123	No crack after 140 000
SLS-449 Pore 3	140	Subsurface Defect	160	No crack after 140 000
ESRF-641 Defect	90	Internal Artificial Defect	790	No crack after 3 000 000
ESRF-451 Defect	95	Internal Artificial Defect	940	No crack after 1 700 000
SLS-14 Pore 3	230	Internal Natural Defect	340	Crack after 40 000
SLS-14 Pore 4	230	Internal Natural Defect	298	No crack after 73 000
SLS-40 Pore 1	240	Internal Natural Defect	350	No crack after 82 000
SLS-17 Pore 1	200	Internal Natural Defect	386	Crack after ∼60 000
SLS-22 Pore 1	200	Internal Natural Defect	314	Crack after 355 000

Table 3.5: Summary on the main characteristics of all defects used in FE simulations.

Conversely to macroscopic specimens, microscopic specimens only produced surface failure and internal nucleation was never observed. As explained above, subsurface simulations need highly refined meshed and therefore the computation of each 3mm×3mm synchrotron specimen is divided into two kinds: (i) simulations using realistic surface meshes of both internal artificial defects and free surfaces, and, (ii) simulations where the realistic morphology of small subsurface pores is introduced within an idealized 3mm×3mm free surface. The surface pores simulated were chosen because either they nucleated cracks or they were the largest non-nucleating pores present at the free surface. Finally, synchrotron specimens containing internal natural defects are listed (5 in total). Realistic surface meshes of both natural defects and free surfaces are also used in this case.

3.5.2.1 FE simulation results on internal artificial defects

A comparison between FE simulation on internal artificial defects of different sizes ($\varnothing_{eq} \approx 2$ mm and $\varnothing_{eq} \approx 1$ mm) is established in Fig. 3.27. Two 3D renderings of the artificial defect of CTIF-101.57 specimen ($\sqrt{A} = 2064$ μm, $N_f = 938\ 500$ cycles, $\sigma_{max} = 140$ MPa, see Fig. 3.27a) are first given. They show that the internal crack was nucleated along a specific site on the defect "equator". Large yellow bands (K_t=2-2.5) are observed at this region of the defect (see Fig. 3.27b) enclosing a comparatively smaller blue zones (K_t=2-3). Thus, the largest yellow-blue band matches very well the crack nucleation site. Moreover, the nucleation site also corresponds to the largest plastically strained volume that can be observed at the equator using elasto-plastic simulations (see Fig. 3.27c).

The computation results obtained for a $\varnothing_{eq} \approx 1$ mm artificial defect (corresponding to SLS-445 specimen, $\sqrt{A} = 875$ μm, $N_f = 190\ 000$ cycles, $\sigma_{max} = 140$ MPa) are presented in Fig. 3.27d-e). This defect exhibits a rougher morphology that produces slightly higher K_t values. It must be noted that the highest K_t values (blue regions between 3.5 and 4) obtained correspond to some small folds that were produced on the artificial defect during its fabrication. As a result, these blue region are very local and barely observed in Fig. 3.27d (the orange arrow indicates the location of one of these regions). The most important difference between these two artificial defects is shown in Fig. 3.27e where it can be observed that the plastically strained volume produced by the $\approx$ 1 mm artificial defect is smaller than the one produced by the $\varnothing_{eq} \approx 2$ mm artificial defect. It is thought that the ability to create large plastically strained volumes is an important parameter with respect to crack nucleation. Therefore, it can be considered that large artificial defects ($\varnothing_{eq}$ ≈ 2 mm), even if they exhibit lower K_t values (see Fig. 3.30 where other simulation results on $\varnothing_{eq} \approx 1$ mm internal artificial defects are added), are more detrimental to fatigue life. It is likely that $\varnothing_{eq} \approx 1$ mm artificial defect could eventually produce internal nucleation but at higher number of cycles than those needed to nucleate a crack with a $\varnothing_{eq} \approx 2$ mm internal artificial defect.

3.5.2.2 Subsurface FE simulation results on surface defects

The earlier crack nucleation and propagation produced by almost ten times smaller parasitic surface defects can be explained by the deleterious effect of air environment. Interestingly, all these surface pores exhibit quite similar sizes and yet some of them were able to produce earlier cracking. The FE subsurface simulations presented in what follows intend to investigate the differences in pore morphology which led to this early cracking.

Fig. 3.28b shows the K_t evaluation of SLS-445 Pore 1. A unique yellow band (K_t = 2-3.5) is observed along with two blue zones (K_t = 3.5-4) which are enclosed by the band. Two red zones (K_t = 4-5.5) are also observed, one of which has almost the same size as the blue zone that surrounds it. On the other hand, SLS-445 Pore 2 (a corner pore, see Fig. 3.28c) only exhibits a pair of small yellow zones. The experimental observations indicate that both SLS-445 Pore 1 and SLS-445 Pore 2 nucleate surface cracks between 20 000 and 70 000 cycles. The fact that the FE simulation tend to underestimate the actual severity of SLS-449 Pore 2 probably comes from the simplified mesh which is used to describe a subsurface pore while the real one is intersecting the surface; a simplification made worse by the case of a corner pore?

As for SLS-445 Pore 5, the simulation results (Fig. 3.28d, only exhibiting yellow bands) seem to be consistent with the experimental observations as this pore nucleated a crack after 170 000 cycles, which is about 100 000 cycles later than SLS-445 Pore 1. The K_t evaluations for SLS-449 Pore 1, SLS-449 Pore 2 and SLS-449 Pore 3 (presented in Fig. 3.29b-d) show similar results (only yellow bands) to those of SLS-445 Pore 5. It must be noted that no crack was observed at SLS-449 surface

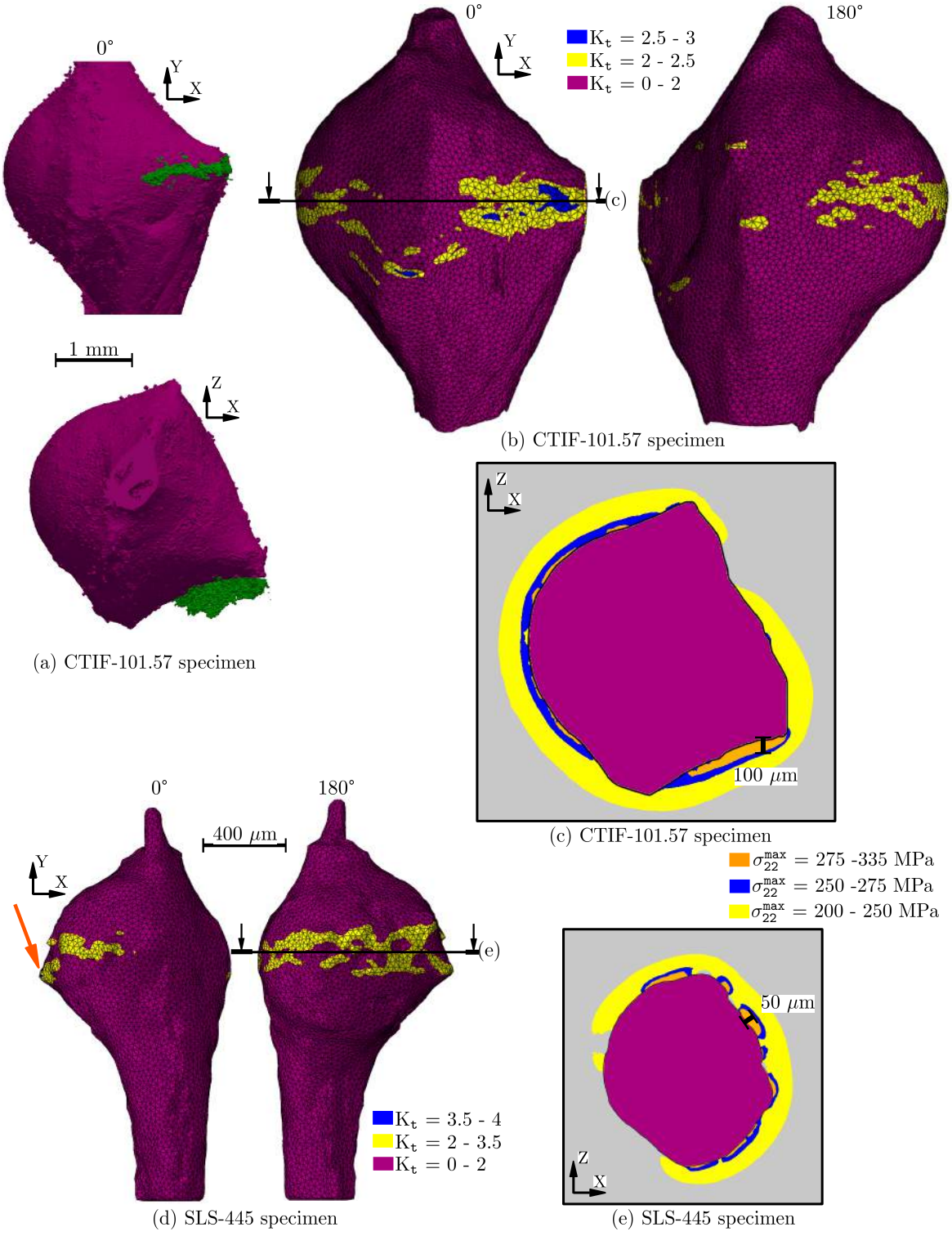

(a) CTIF-101.57 specimen

(b) CTIF-101.57 specimen

(c) CTIF-101.57 specimen

(d) SLS-445 specimen

(e) SLS-445 specimen

Fig. 3.27: (a) 3D renderings of the artificial defect of CTIF-101-57 specimen showing the internal crack (in green) formed at its equator after 938 500 cycles ($\sqrt{A}$ = 2064 μm, σ_{max} = 140 MPa). (b) K_t evaluation over the artificial defect profile of CTIF-101-57 specimen. (c) Slice performed along the "equator"of the artificial defect (CTIF-101-57 specimen) on a plane perpendicular to the loading direction showing elasto-plastic results. (d) K_t evaluation over the artificial defect profile of SLS-445 specimen ($\sqrt{A}$ = 875 μm, σ_{max} = 140 MPa). Orange arrow indicates the location of a small blue (K_t = 3.5-4) region. (e) Slice performed along the "equator"of the artificial defect (SLS-445 specimen) on a plane perpendicular to the loading direction showing elasto-plastic results.

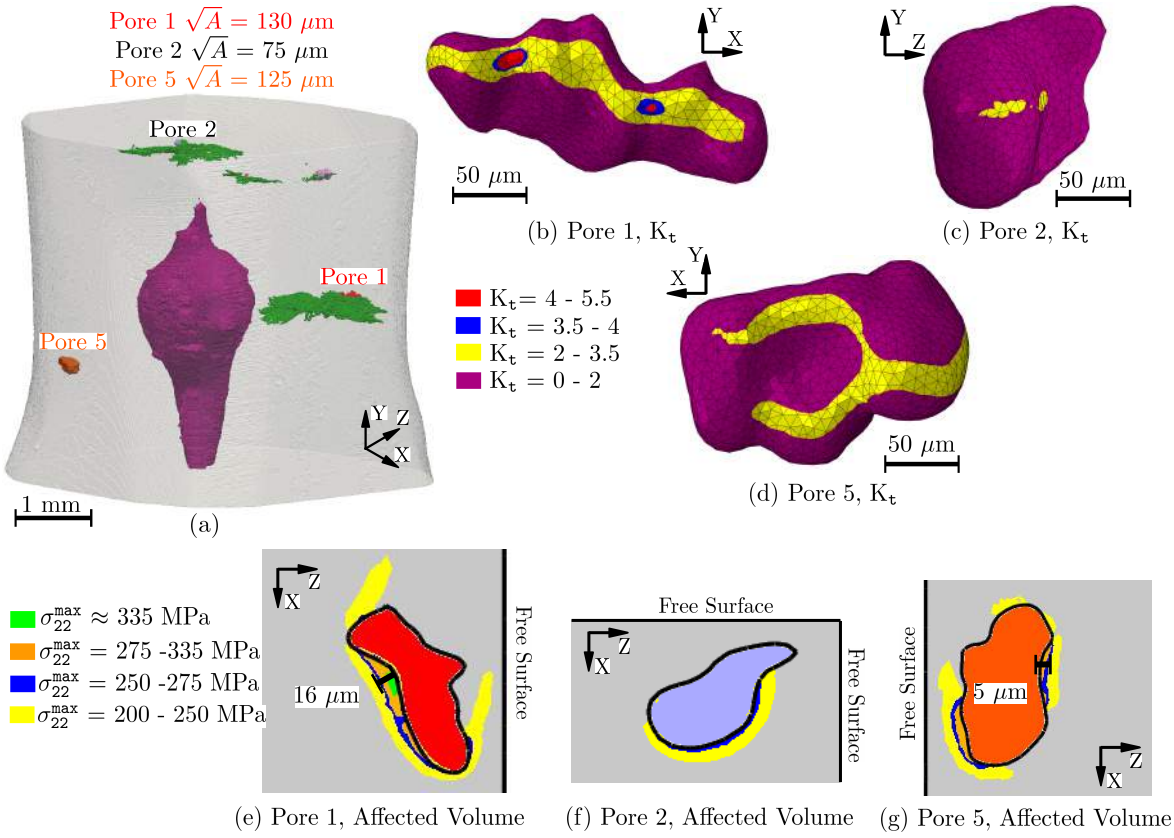

Fig. 3.28: (a) 3D rendering of SLS-445 specimen showing the artificial defect (in darkmagenta, $\sqrt{A} = 875$ μm) and the pores which nucleated surface cracks. The fatigue testing parameters are N_f = 190 000 cycles, σ_{max} = 140 MPa. (b) K_t evaluation for Pore 1 (crack nucleation after 20 000 cycles). (c) K_t evaluation for Pore 2 (crack nucleation after 20 000 cycles). (d) K_t evaluation for Pore 5 (crack nucleation after 170 000 cycles). (e) Slice performed along the middle plane perpendicular to the loading direction for Pore 1 and showing elasto-plastic results. (f) Same as before but for Pore 2 and (g) Pore 5. It must be noted that the values obtained within the ligament, between the free surface and the pore, are not taken into account.

pores after 140 000 cycles.

The elasto-plastic simulations (see Fig. 3.28e-g and Fig. 3.29e-g) show an equivalent plastically strained zone (typical sizes ranging between 5-16 μm) for all pores (except SLS-445 Pore 2) with the particularity that SLS-445 Pore 1 is the only one exhibiting a green region. Hence, it seems that a small (compared to internal artificial defects) highly strained volume suffice for an earlier surface crack nucleation.

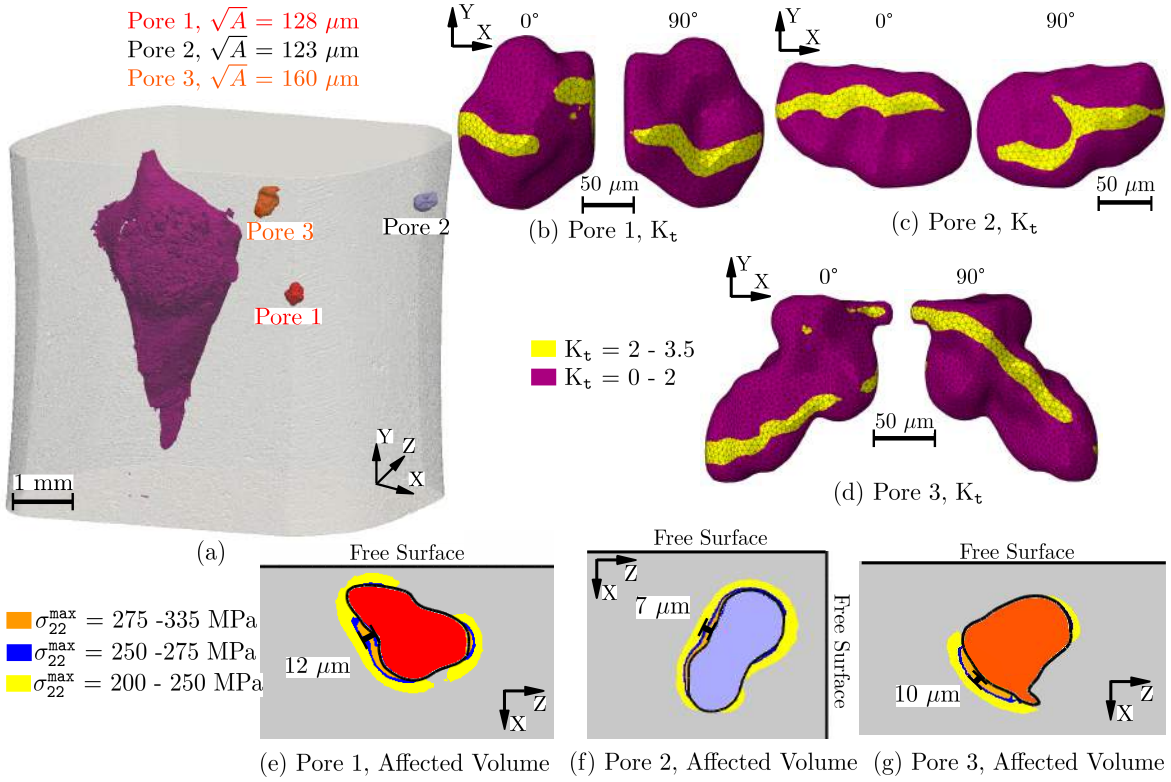

Fig. 3.29: (a) 3D rendering of SLS-449 specimen showing the artificial defect and three surface pores which did not nucleate any crack. The fatigue testing parameters are N_f = 140 000 cycles, σ_{max} = 140 MPa, Artificial Defect $\sqrt{A}$ = 830 μm. (b) K_t evaluation for Pore 1 (no crack nucleation after 140 000 cycles). (c) K_t evaluation for Pore 2 (no crack nucleation after 140 000 cycles). (d) K_t evaluation for Pore 3 (no crack nucleation after 140 000 cycles). (e) Slice performed along the middle plane perpendicular to the loading direction for Pore 1 and showing elasto-plastic results. (f) Same as before but for Pore 2 and (g) Pore 3.

Fig. 3.30 presents a summary of the K_t evaluation for the six surface pores studied along with the internal artificial defects. It can be observed that SLS-445 Pore 1 is the one exhibiting the highest K_t (with values as high as 5.0), which probably explains why this pore led to final failure (see Fig.3.20). The rest of the pores (both surface and internal) show similar K_t values even if their sizes are quite different. This figure also shows that the artificial defects tend to have, on average, lower K_t values than natural defects.

3.5.2.3 FE results on natural internal defects

As shown it Table 3.5, natural internal defects of similar $\sqrt{A}$ sizes (ranging between 300 and 400 μm) produces quite different crack initiation periods. FE simulations on this type of defects intend to elucidate the pore factors leading to these differences. SLS-14 specimen was chosen to present the main results of FE simulations. The rest of FE simulations performed for this kind of

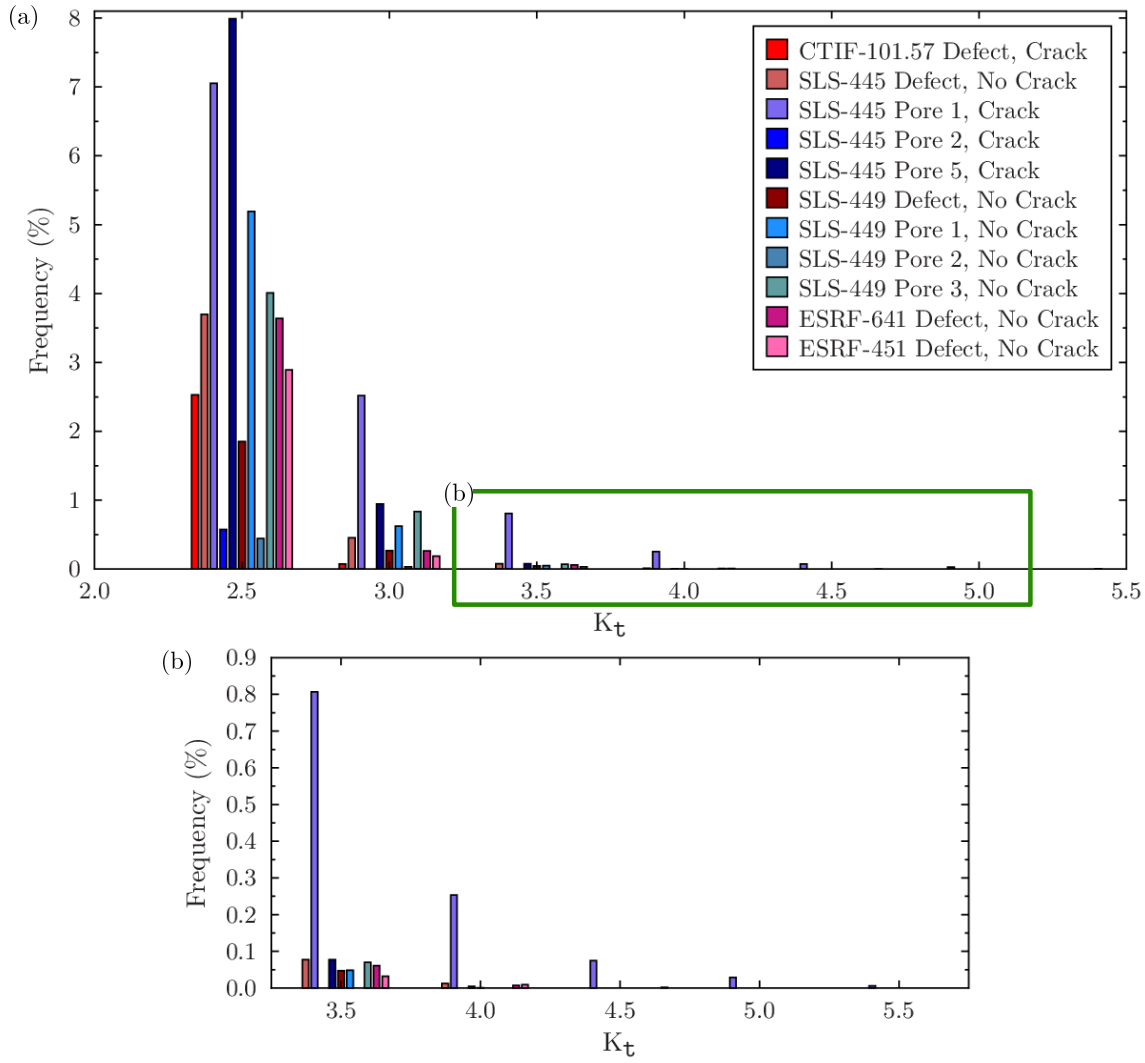

Fig. 3.30: (a) Histogram showing the frequency of counts against the different K_t values of FE simulations performed on CTIF-101.57, SLS-445, SLS-449, ESRF-641 and ESRF-451 specimens. (b) Detail on the K_t values ranging from 3.5 to 5.5.

defects are given in appendix J.

Fig. 3.31 shows the results of the elastic K_t computations over the surface of SLS-14 Pore 3 and SLS-14 Pore 4. Even though Pore 3 was able to nucleate an internal crack after 40 000 cycles and no internal nucleation was observed in Pore 4, no significant differences are observed between these two pores from a qualitative standpoint. Both of them show yellows bands (K_t = 2-2.5) extending over the pore profiles and where smaller blue zones (K_t = 3.5-5) are enclosed. Occasionally, some red (K_t = 5-9) zones are observed within the blue ones. The experimental fatigue results of Pore 3 (see appendix J) indicate that the first nucleation sites documented on Pore 3 morphology mainly correspond to these red-blue zones indicated with orange arrows in Fig. 3.31a.

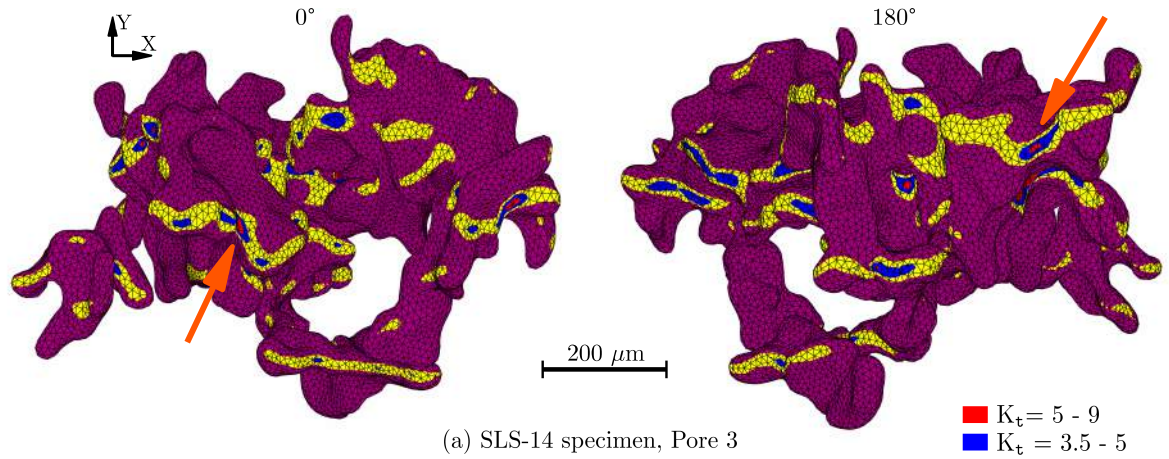

(a) SLS-14 specimen, Pore 3

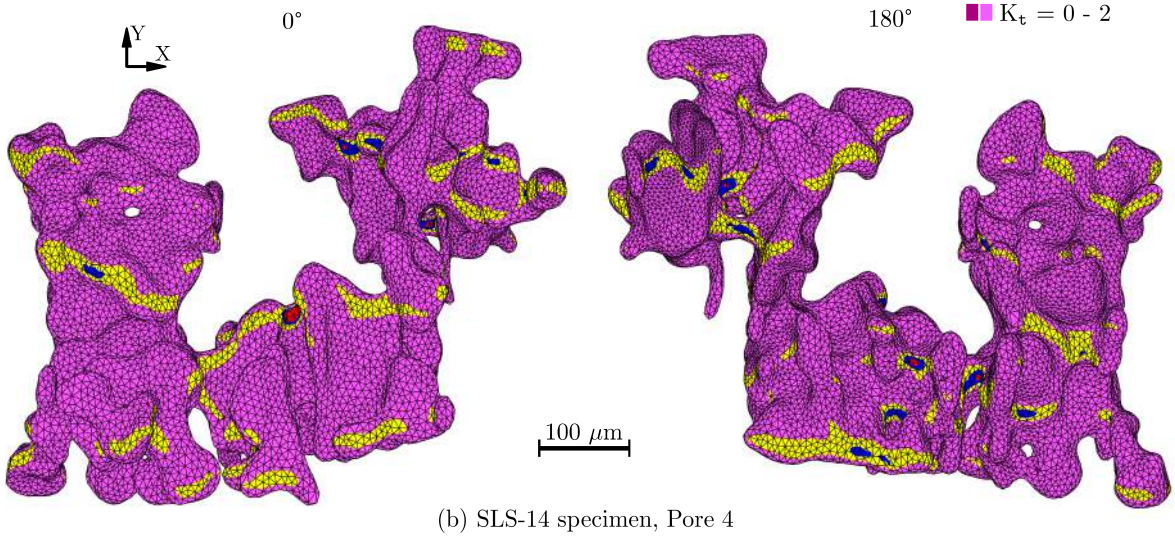

(b) SLS-14 specimen, Pore 4

Fig. 3.31: (a) 3D renderings at 0° and 180° of the K_t evaluation on Pore 3 (SLS-14 specimen). (b) The same as before but for Pore 4 (SLS-14 specimen). Orange arrows indicate some of the largest red-blue zones (K_t = 9-5) that are formed over the pore convoluted morphology.

The histogram presented in Fig. 3.32 shows the distribution of the K_t values obtained for each natural pore, intending to compare the influence of pore morphology from a more quantitative standpoint. It can be observed that those two pores initiating and propagating internal cracks in specimens SLS-14 (Pore 3) and SLS-17 (Pore 1) exhibit the highest frequencies for K_t values ranging between 3.5 and 6. Therefore, it seems that in this case the frequency of K_t values is a valid indicator of the nocivity of pores.

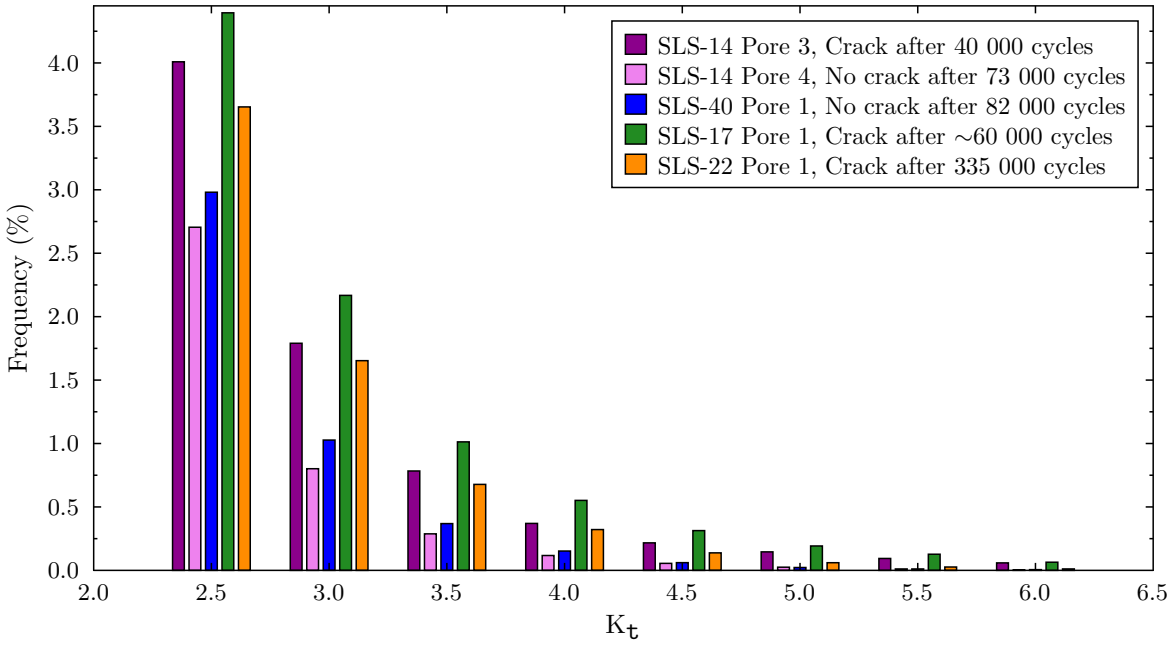

Fig. 3.32: Histogram showing the frequency of counts against the different K_t values obtained over the surface of natural internal defects.

Elasto-plastic results obtained for Pore 3 and Pore 4 of SLS-14 specimen are shown in Fig. 3.33b-c. Both pores show similar plastically strained volumes and, as for the case of K_t qualitative examinations, the qualitative comparison of elasto-plastic results on pores of similar sizes does not clearly indicate the difference in severity between each other.

Nevertheless, two main differences must be noted between these internal natural defects and the previously analysed internal artificial defects: (i) the highest K_t values obtained for internal artificial defects are lower than those obtained for internal natural defects (4 against 9), and (ii) in spite of having equivalent (case of $\varnothing_{eq} \approx 1$ mm) or larger ($\varnothing_{eq} \approx 2$ mm) plastically strained volumes, the artificial defects are not able to produce the highly plastically strained regions (∼335 MPa and shown in green) observed in natural defects. This could mean that smaller but more acute internal defects can produce lower crack nucleation periods.

The major findings regarding FE simulations can be summarised as follows:

1. A $\varnothing_{eq} \approx 2$ mm quasi-spherical internal artificial defect create a larger plastically strained volumes that a $\varnothing_{eq} \approx 1$ mm quasi-spherical internal artificial defect (cycled at equivalent stresses). This can be correlated to a higher propensity of fatigue cracks to initiate at large internal defects.
2. Surface crack nucleation from pores of similar sizes (∼120 μm) is influenced by the pore morphology. It was observed that higher frequencies of K_t values ranging between 3 and 5.5 lead to lower crack nucleation periods.
3. Pore morphology also influences the crack nucleation period of internal natural defects although in this case the higher frequencies exhibited by the most damaging defects range between 2.5 and 6 K_t values.

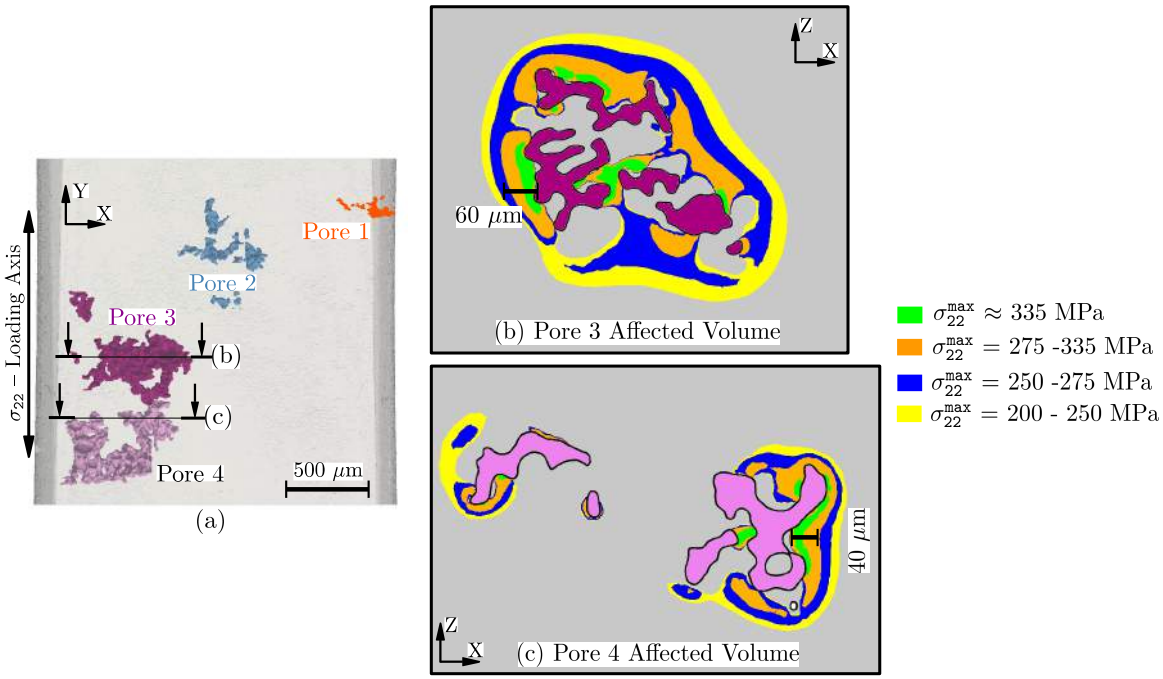

Fig. 3.33: (a) 3D rendering of the pore distribution within the gage of SLS-14 specimen where the approximate locations of images (b) and (c) are indicated. The fatigue testing parameters are N_f = 73 000 cycles, σ_{max} = 230 MPa (b) Slice performed along a random plane perpendicular to the loading direction for Pore 3 showing the elasto-plastic results. (c) The same as before but for Pore 4.

3.6 Analysis on surface v.s. interior fatigue mechanisms

To calculate stress intensity values of some of the small cracks observed in tomography, we employ the maximum stress intensity value (K_{max}) ahead of the crack front, which can be expressed by the approximate formula [MUR 85]:

$$K_{max} = 0.65 \cdot \sigma_0^{max} \cdot \sqrt{\pi \sqrt{A_{crack}}} \tag{3.2}$$

where A_{crack} is the crack area projected along the loading direction and σ_0^{max} is the maximum value of the remote stress field. The stress intensity solution for a corner crack is given by [MUR 85, NOG 01]:

$$K_{max} = 0.77 \cdot \sigma_0^{max} \cdot \sqrt{\pi \sqrt{A_{crack}}} \tag{3.3}$$

As the *surface* small cracks were able to propagate far from the influence of their nucleating pores it can be considered that they behave as microstructurally/physically small cracks (when they propagate at distances longer than at least twice the value of $\sqrt{A_{pore}}$) and so the small scale yielding criteria is somehow respected. The data obtained for the *internal* cracks corresponds to mechanically small cracks which remained engulfed within the affected field of their nucleating defects (see Fig. 3.34).

In order to establish a comparison between the internal (mechanically small) cracks and surface (microstructurally/physically small) cracks the following assumption is made: the affected field where the internal cracks evolved is considered to be an averaged value of the local stress field $\sigma_p'^{max}$. Therefore in the case of internal cracks, Eqs. 3.2 is written as follows:

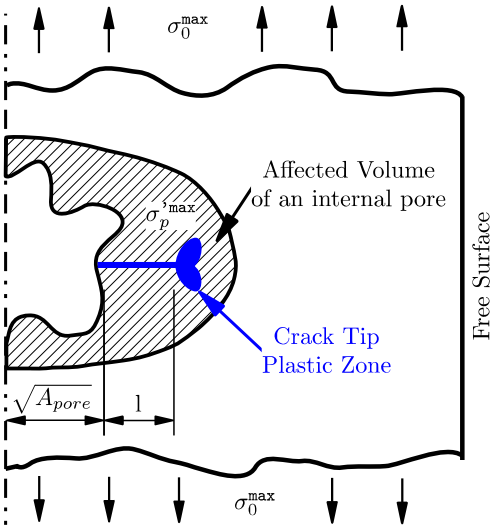

Fig. 3.34: Schematic illustration of a mechanically small crack which nucleated at an internal natural defect and remained engulfed within the affected field.

$$K_{max} = 0.65 \cdot \sigma_{\mathrm{p}}^{'\mathrm{max}} \cdot \sqrt{\pi \sqrt{A_{\mathrm{crack}}}} \tag{3.4}$$

From the FE analysis described previously, it results that the stress value for SLS-14 Pore 3 is $\sigma_{\mathrm{p}}^{'\mathrm{max}} = 288$ MPa (crack is engulfed in an affected volume where the stress ranges between 240 and 335 MPa) and that of SLS-17 Pore 1 is $\sigma_{\mathrm{p}}^{'\mathrm{max}} = 273$ MPa (210-335 MPa).

Fig. 3.35 summarises the small fatigue crack growth data obtained for synchrotron specimens using the aforementioned analysis. The long crack fatigue results were obtained at ENSMA using CT specimens for ambient air (triangle symbols) and vacuum (square symbols). It can be observed that the crack growth rates of internal small cracks vary between 10^{-9} and 10^{-8} m/cycle and that these mechanically small cracks are submitted to high stress intensity values ($\sim$7.5-8.5 MPa$\sqrt{m}$ against 3-5 MPa$\sqrt{m}$ for surface cracks) due to the local larger stress level. This means that in the studied conditions internal cracks propagate with similar growth rates than surface ones as long as they remain engulfed in the stress affected volume. Once the internal cracks propagate outside the affected volume, the crack growth rate will decrease (leading to an arrested crack in some cases). Fig. 3.35 also shows that surface crack growth rates are slightly faster than the long crack data obtained in ambient air while the experimental values obtained for internal crack growth rates fall close to the rates obtained for long cracks propagating in vacuum.

With regard to the macroscopic S-N results (see Fig. 3.5), there are some aspects that need further analysis:

• **$\varnothing_{\mathrm{eq}} \approx$ 2 mm internal artificial defects (air) v.s. reference material (air)**: The presence of large internal defects in the fatigue specimens should lead to a vertical shift on the Wöhler curve (shown in red on Fig. 3.36a) and yet the specimens containing $\varnothing_{\mathrm{eq}} \approx 2$ mm have the same fatigue lives than the reference material (see Fig. 3.36b). It was shown in the literature and by our experiment that internal cracks have a lower growth rate that cracks growing in air. Therefore, the slower propagation of the internal cracks leads to an increased fatigue life visible as an horizontal shit in the Wöhler curve (shown in green on Fig. 3.36a). Overall, the two effects must cancel each other and the Wöhler curve of both the reference material and the specimens with internal defects fall at the same place.

One puzzling question remains however: why internal crack initiation is more frequent in large samples with $\varnothing_{\mathrm{eq}} \approx 2$ mm internal artificial defects that in the small ones used in the synchrotron experiments? All the results presented until here cannot explain why macroscopic samples contain-

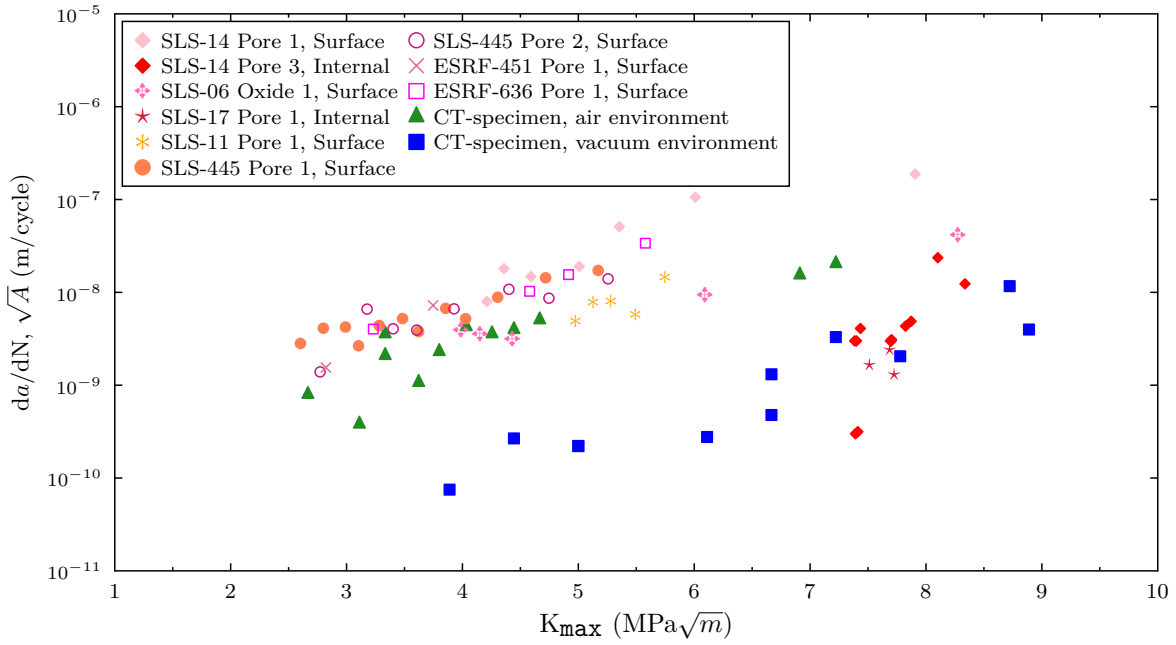

Fig. 3.35: Plot of da/dN against the stress intensity for synchrotron small cracks along with the long crack results obtained with CT specimens at ENSMA.

ing internal artificial defects fail from the propagation of an internal crack although they are likely to also contain surface/subsurface defects which have been shown to cause large stress concentration and increased slip irreversibility. Different surface conditions are suspected to influence crack nucleation in macroscopic specimens. This difference in surface conditions could be explained by the fact that 3mm×3mm specimens are carefully ground and polished while macroscopic specimens are mechanically machined. The mechanical machining could produce surface strengthening due to residual compression stresses and retard crack initiation from surface/subsurface defects.

• **$\varnothing_{eq} \approx$ 2 mm internal artificial defects (air) v.s. $\varnothing_{eq} \approx$ 2 mm surface defects (air and vacuum)**: It can be observed in Fig. 3.37 that specimens containing $\varnothing_{eq} \approx 2$ mm internal artificial defects and cycled in air produced similar fatigue lives that those with semi-spherical $\varnothing_{eq} \approx 2$ mm surface defects cycled in vacuum. This is in agreement with the fact that the stress state caused by these two defects can be considered as equivalent. However, an internal defect has larger affected volume than a surface one. It would be interesting to cycle more specimens containing surface artificial defects in order to investigate if this difference of affected volume can produce some variation in fatigue lives when compared to those of internal defects.

It was shown in § 3.2.1.1 that the environment created by the internal defect had an influence on crack propagation which is visible on the fracture surfaces (the so-called Region I). The fact that specimens with artificial internal defects and those with surface artificial defects cycled in vacuum (no Region I) fall on the same curve tends to indicate that, for the stress levels investigated, the crack growth period corresponding to the formation of Region I remains small compared to the whole fatigue life.

• **Reference material (DPI controlled, air) v.s. reference material (uncontrolled, vacuum)**: According to S-N results for a defect free material (see Fig. 3.36b), one could expect a considerable horizontal shift when the environment changes from ambient air to vacuum (red arrow on Fig. 3.38). Instead, the results of *uncontrolled* specimens cycled in vacuum fall relatively close to the reference S-N curve obtained in ambient air. It is thought that the vacuum curve is

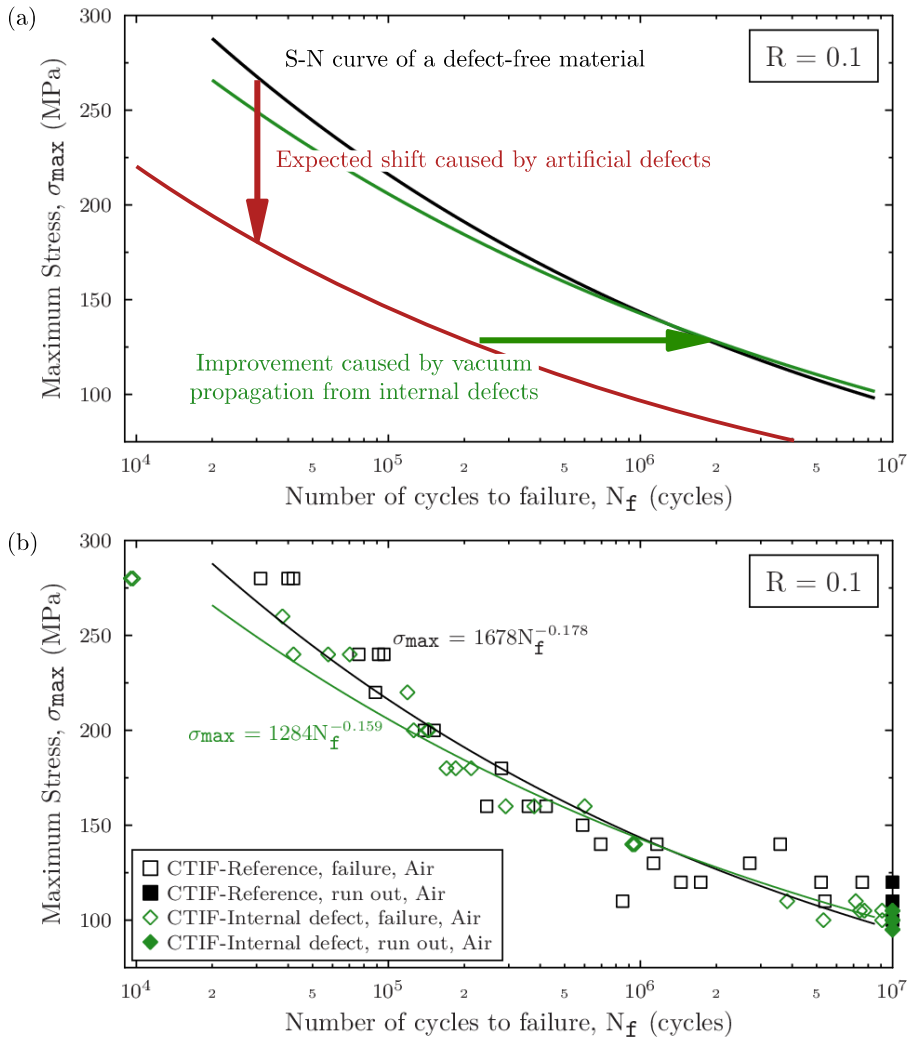

Fig. 3.36: (a) S-N curve showing the expected shifts produced by the cycling of $\varnothing_{eq} \approx 2$ mm internal artificial defect in different environments (air and vacuum). (b) S-N curves for the reference material (which is considered to be defect-free at the surface) and specimens containing internal artificial defects of $\varnothing_{eq} \approx 2$ mm cycled in ambient air.

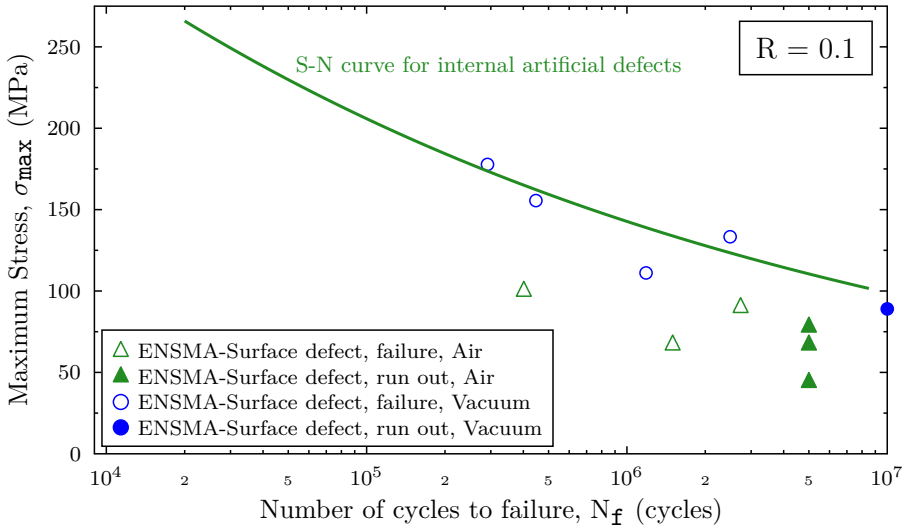

Fig. 3.37: S-N curves for specimens containing internal artificial defects of $\varnothing_{eq} \approx 2$ mm cycled in ambient air and for specimens containing semi-spherical surface artificial defects cycled in both air or vacuum environment.

shifted to a position close to the ambient air curve due to the presence of casting defects. The specimens with internal artificial defects that were used for the tests carried out in vacuum had not been screened by DPI. It is likely, therefore, that these specimens contained some natural defects at the surface or immediately below it. As shown with the synchrotron specimens, such defects, when present, tend to initiate cracks very easily. As a matter of fact, four out of the five specimens that were tested present final failure originated from such surface defects.

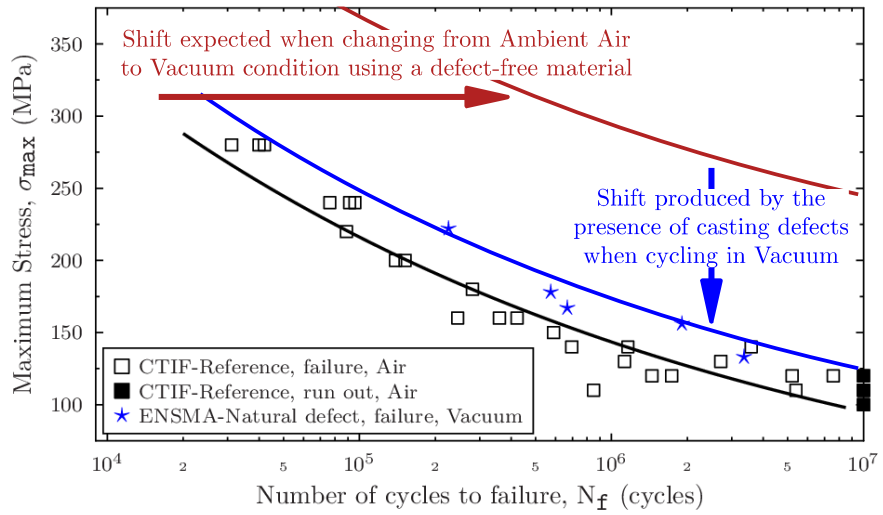

Fig. 3.38: Schematic illustration of the horizontal shift expected when environment changes from air to vacuum. It is thought that a vertical shift is produced by the deleterious influence of casting defects.

Synchrotron specimens containing $\varnothing_{eq} \approx$ **1 mm internal artificial defects** underwent early surface failure because of the presence of $\sqrt{A} \approx$ 100-200 μm. It is expected that the same type of specimen but free from any surface defect (as the case of macroscopic $\varnothing_{eq} \approx 2$ mm internal artificial defect) is capable of producing internal failure.

Finally and regarding the **effect of pore shape**, it has been shown that surface pores of

$\sqrt{A} \approx$ 100-200 μm are able to reduce the fatigue live depending on their K_t values. The higher these values are, the higher the reduction in the nucleation period is. Interestingly, Roy *et al.* [ROY 11] have shown that both natural pores and EDM semi-spherical defects of $\sqrt{A} = 400$ μm produce similar effect on the fatigue life of an A356-T6 material. As shown in the literature review, for sizes higher that this value the nucleation period can be considered negligible. These results would indicate that the pore shape is a parameter that must be taken into account only when the nucleation period influences the final fatigue life at low stress levels. This is the case of pores with sizes ranging between ∼100 μm and ∼400-500 μm.

3.7 Summary on 3D fatigue mechanisms

The fatigue results presented for different kinds of specimens containing internal and/or surface defects of various sizes and shapes tested under ambient air or vacuum conditions led to the following conclusions:

1. Macroscopic specimens containing internal artificial defects of $\varnothing_{eq} \approx 2$ mm and free from *large* surface defects ($\varnothing_{eq} \gtrsim 200$ μm) exhibit the same fatigue behaviour as the reference specimens.
2. The final failure of macroscopic specimens containing $\varnothing_{eq} \approx 2$ mm artificial defects occurs preferentially at the internal defects.
3. The internal failure presents three distinct regions of propagation (I, II and III) whose features can be clearly identified on the fracture surfaces.
4. The cause for the formation of Region I remains unclear but a limited influence of deleterious molecules somehow trapped in the internal defect is suspected.
5. The main portion of the internal crack growth occurred in the Region II under vacuum-like conditions with an intrinsic stage I-like propagation. The crack surface is formed of crystallographic facets ({111} planes) with the crack fronts being highly irregular.
6. Eventually, a Region III was formed whenever the internal crack reached the free surface and started propagation in ambient air conditions.
7. Surface artificial defects of $\varnothing_{eq} \approx 2$ mm caused a reduction in fatigue life when tested in air environment. When cycled in vacuum those specimens have fatigue lives similar to those of the reference specimens cycled in air.
8. Uncontrolled macroscopic specimens made out of the reference material and cycled in vacuum environment preferentially failed from microshrinkage defects that were located at the free surface. Longer fatigue lives (than those the reference material) were observed when using these specimens.
9. Synchrotron testing of specimens containing natural internal defects of $\sqrt{A} \approx 300$ μm shows that internal cracks have lower propagation when compared to surface cracks. The internal crack paths are (apparently) crystallographic.
10. In those synchrotron specimens crack initiation also occurs at surface natural defects. Because the propagation of those cracks are much higher, they are the ones leading to final failure.
11. Synchrotron testing of specimens containing internal artificial defects of $\varnothing_{eq} \approx 1$ mm did not produce any internal cracking; instead, crack initiation occurred on surface micropores of $\sqrt{A} \approx 120$ μm.

FE simulations were performed on pores of different kinds and sizes (*i.e.,* natural internal pores, artificial internal pores, and (parasitic) surface pores) in order to study the effects of size and shape on crack nucleation periods. The main simulation results can be drawn as follows:

1. The plastically strained volume formed around nucleating pores seems to be a valid indicator of pore severity for crack initiation because it accounts for the effect of defect size.
2. The first nucleation sites to be observed around a pore seem to correspond to the zones exhibiting the highest K_t values in both natural and artificial internal defects.
3. The K_t values (when presented using histograms) seem to be good indicators of pore severity only when comparing defect of similar sizes.
4. *Small* (almost one order of magnitude) and *acute* surface parasitic defects resulted to be more deleterious to fatigue life than *large* and *round* $\varnothing_{eq} \approx 1$ mm internal artificial defects.

Les résultats de fatigue obtenues avec différents types d'échantillons contenant des défauts internes et/ou surfaciques ayant des tailles et des natures (naturels ou artificiels) différents conduisent aux conclusions suivantes:

1. Les éprouvettes macroscopiques contenant des défauts artificiels et internes de $\varnothing_{eq} \approx 2$ mm et exemptes de grands défauts surfaciques ($\varnothing_{eq} \gtrsim 200$ μm) montrent des durées de vie similaires à celles des éprouvettes usinées avec le matériau de référence.
2. La rupture d'éprouvettes contenant des défauts artificiels de $\varnothing_{eq} \approx 2$ mm se produit préférentiellement à partir des défauts internes.
3. La rupture interne montre trois régions distinctes de propagation (I, II et III) correspondant à trois faciès de rupture caractéristiques.
4. La cause de la formation de la Région I reste peu clair, quoi qu'une influence limitée de molécules nocives pouvant être piégées dans le défaut interne est suspectée.
5. L'essentiel de la croissance interne correspond à la Région II où la propagation se produit en pseudo stade I intrinsèque et sous vide. Les faciès de rupture sont constituées de facettes cristallographiques (plans {111}) avec des fronts de fissures qui sont très irréguliers.
6. Une Région III peut être formée si la fissure interne atteint la surface libre et commence à propager sous l'influence de l'air ambiant.
7. Les défauts surfaciques et artificiels de $\varnothing_{eq} \approx 2$ mm ont provoqué une réduction de la durée de vie attendue pour le cas de tests menés à l'air ambiant. Le passage à des essais sous vide produit des durées de vie similaires à celles des éprouvettes de référence testées à l'air ambiant.
8. Les éprouvettes macroscopiques usinées avec le matériel de référence mais non contrôlées en ressuage et ayant été testées sous vide ont de préférence cassé à partir de pores qui se trouvaient à la surface. Des durées de vie supérieures à celles du matériau de référence ont été avec ces éprouvettes.
9. Les essais synchrotron réalisés en utilisant des éprouvettes contenant des défauts naturels internes de $\sqrt{A} \approx 300$ μm montrent que les fissures internes ont des vitesses de propagation inférieures à celles observées pour les fissures surfaciques. Les cheminements de fissures internes sont (apparemment) cristallographiques.
10. Dans ces éprouvettes synchrotron l'amorçage de fissures peut se produire également à partir de défauts de surface naturels. Les fissures surfaciques sont toujours responsables de la rupture finale des éprouvettes synchrotron car leur propagation est beaucoup plus rapide.
11. Les essais synchrotron réalisés en utilisant des éprouvettes contenant des défauts artificiels et internes de $\varnothing_{eq} \approx 1$ mm n'ont pas produit de fissuration interne; à la place, l'amorçage des fissures s'est produit à partir de micropores surfaciques de $\sqrt{A} \approx 120$ μm.

Des simulations EF ont été réalisées à partir de pores avec des natures et tailles différentes (c'est-à-dire, pores internes et naturels, pores internes et artificiels, et pores (parasites) en surface) afin d'étudier les effets de la taille et la forme sur l'amorçage des fissures de fatigue. Les principaux résultats de la simulation EF sont résumés de la manière suivante:

1. Le volume plastifié mesuré autour des pores étudiés semble être un bon indicateur de leur sévérité car il tient compte de l'effet produit par la taille du défaut.
2. Les premiers sites d'amorçage à être observés autour d'un pore interne semblent correspondre aux zones présentant les valeurs les plus élevées de $K_{\mathtt{t}}$ que les défauts, soient naturels ou artificiels.
3. Les valeurs de $K_{\mathtt{t}}$ semblent être de bons indicateurs de la nocivité des pores mais uniquement dans le cas de défauts de tailles comparables.
4. De *petits* défauts surfaciques présentant de faibles rayons de courbure sont plus nocifs d'un point de vue de la durée de vie que des défauts artificiels internes de $\varnothing_{\mathtt{eq}} \approx 1$ mm de taille plus importante (presque un ordre de grandeur de différence) et plutôt *ronds*.

Conclusions and Future Work

Several fatigue experiments have been carried out in this work. Surface crack monitoring was performed on macroscopic specimens (cross section ∼6mm×6mm) in order to study the influence of microstructural parameters (*i.e.,* SDAS, grain size) on small crack propagation under uniaxial loading and ambient air conditions. With regard to the effect of internal defects, macroscopic cylindrical specimens (cross section $\varnothing = 10$ mm) containing $\varnothing_{\mathtt{eq}} \approx 2$ mm artificial defects located in the bulk or at the free surface have been tested in order to establish S-N curves and to perform systematic fractographic observations on the propagation mechanisms. Microscopic specimens (cross section ∼2mm×2mm and ∼3mm×3mm) were used to try to image the nucleation of small cracks at internal defects and obtain internal crack propagation rates. FE simulations performed using 3D images of those samples allowed to evaluate the influence of defect size and shape on the ability of a pore to initiate a crack. Finally, pure torsional fatigue tests were performed on cylindrical specimens (cross section $\varnothing = 6$ mm) in order to study the influence of the underlying microstructure on crack propagation, the effects of pore presence, and to obtain torsion S-N curves.

The major conclusions of this work can be listed as follows:

- With regard to the **influence of microstructural features** on small crack propagation under **uniaxial tensile cyclic loading**:
  - The SDAS seems to be the main microstructural parameter controlling crack growth. A microstructurally small crack behaviour is observed until the size of the plastic zone at the crack-tip is equivalent to the average SDAS value (38 μm, *i.e.,* a crack length of ∼550 μm). The cracks propagate preferentially through the α-Al matrix and occasionally through eutectic particles (clusters). The eutectic crack paths mainly correspond to intergranular propagation. It must be noted that no slowing of small cracks was observed when they approached a cluster of Si particles. This is a controversial point and further investigation (by performing observations at very reduced intervals, for example every 100 cycles) have to be carried out in order to verify the interaction between microstructurally small cracks and the SDAS.
  - The grain size is considered as a second order parameter. It was observed that grain boundaries act as microstructural barriers that retard crack propagation without completely stopping it.
  - The monitored surface cracks exhibit relatively smooth crack paths (globally perpendicular to the loading direction) favoured by the multi-slip character of propagation. Crystallographic orientation is the key factor controlling the roughness of the crack path. Serrated crack paths can form when Taylor factors are high ($M_T \gtrsim 3$).
- A reference S-N curve was obtained using a surface defect-free material. The **influence of casting defects** on fatigue life under **uniaxial cyclic loading** varies depending on the nature of the defect (artificial, natural, internal and/or surface) and the surrounding environment (air or vacuum):

- ∗ It was observed that there exists a critical pore size ($\sqrt{A} \approx 400$ μm) in the case of surface natural pores cycled in ambient air and at R=0.1. Surface pores larger than this critical size significantly reduce the life expectancy of this material.
- ∗ $\varnothing_{\mathtt{eq}} \approx 2$ mm internal artificial defects cycled in ambient air produced a S-N curve similar to the reference one. For the vast majority of the studied samples, crack initiation occurs at the internal defect. The main portion of internal propagation occurs under vacuum in an intrinsic stage I-like regime where large crystallographic facets are formed and crack fronts are highly irregular. The crack growth rate is much slower than in air, therefore the corresponding S-N curves are eventually superposed with that of the reference material. Close to the defect, a small portion of the fracture surface corresponds to environment assisted propagation (termed as Region I). It is believed that this region has a negligible effect on the global fatigue life. If the internal crack front reaches the free surface before the final failure, crack propagation changes to an adsorption assisted stage II regime (Region III).
- ∗ $\varnothing_{\mathtt{eq}} \approx 2$ mm surface artificial defects cycled in vacuum produce fatigue lives similar to that of internal artificial defects. Only Region II is observed on the fracture surfaces and the crack fronts are also highly irregulars. The similarity in fatigue lives can be explained because the stress state produced by both surface and internal artificial defects can be considered as equivalent although the affected volume of the internal defect is twice that of a surface one.
- ∗ $\varnothing_{\mathtt{eq}} \approx 2$ mm surface artificial defects cycled in ambient air produced a remarkable reduction in fatigue life expectancy. This is in good agreement with the literature. A defect of this size readily produces long crack propagation and so the contribution of nucleation period and small crack propagation to fatigue life is negligible.
- ∗ The vacuum cycling of macroscopic specimens made out of the reference material and containing uncontrolled natural defects produced fatigue lives located above (but not too far from) the reference curve. The fractographic study showed that all failures were produced by intrinsic stage I like crack propagation nucleated from surface or subsurface natural defects.
- ∗ Microscopic specimens cycled in ambient air and containing internal natural defects of $\sqrt{A} = 200$-400 μm rarely produced internal crack nucleation (only 3 out of 12 specimens) and the final failure was always caused by surface defects.
- ∗ Microscopic specimens containing $\varnothing_{\mathtt{eq}} \approx 1$ mm internal artificial defects and cycled in ambient air did not nucleated any internal crack. Surface defects almost ten times smaller than the internal defects were able to produce fatal cracks.

- CT long crack testing showed that at a fixed stress intensity value, cracks cycled in ambient air produce an order of magnitude higher **crack growth rates** than those of cracks cycled in vacuum. In the case of **internal small cracks**, it was observed that for equivalent stress intensity factor values, the measured growth rates of these small cracks are similar to those of a CT long crack cycled in vacuum environment.
- It was observed that both **pore size and shape** influence the crack nucleation period. The pore size is the first order parameter. The pore shape has to be taken into account when defects are of similar sizes because this factor tends to reduce the nucleation period. It is thought that this shape influence decreases or even disappears when pores are large enough ($\sim$400 μm) to cancel the nucleation period.
- With regard to the **influence of microstructural features** on crack propagation under **pure torsional loading**:

  - Crack nucleation is multisite. Monitoring results showed that only 30% of the estimated fatigue life is devoted to nucleate cracks on crystallographic {111} planes that are close to the transverse plane. During this portion of fatigue life, the first grain boundaries have already been crossed.
  - Crack propagation depends on the stress level. In Zone 1 (high stress levels, $\tau_{\max} > 105$ MPa), crack propagation in transverse mode III is dominant and flat fracture surfaces are formed.
  - In Zone 2 (100 MPa $> \tau_{\max} >$ 85 MPa), several microcracks can be dominant. Mode III (in both transverse and longitudinal planes) is dominant although occasional mode I is observed. Grain orientation controls the mode of crack propagation and defections. Final failure occurs by the linkage of dominant cracks and tortuous fracture surfaces are formed.
  - In Zone 3 ($\tau_{\max} <$ 80 MPa), a $\sim$45° spiral-like fracture surface is observed. Mode I is dominant although some local microstepping in mode III can be observed.

- As for the **material inspection techniques**, it has been determined that *large* casting defects ($\sqrt{A} \approx 400$ μm) reduce the expected fatigue life when they are placed at the free surface but equivalent casting defects up to $\varnothing_{\text{eq}} \approx 2$ mm have a negligible effect on the fatigue life when the are placed in the bulk of the material (*i.e.,* internal defects). The following recommendations can be drawn:
  - Dye penetrant inspection (DPI) is a valid technique to detect surface casting defects. However, it fails to detect the actual severity of large subsurface defects which hide under the free surface and/or only show a small size on the free surface.
  - Tomographic controls, if possible coupled with DPI, should be able to improve the detection of surface defects.
  - The rejection rate could be decreased by accepting components containing *large* internal defects provided that they are buried deep into the bulk material.

Finally, it is proposed to pursue **further investigation** on the following topics:

- Uniaxial fatigue:
  - A reduction of the material grain size is proposed. It would be interesting to investigate an optimal grain size (for a fixed SDAS value) which could increase the barrier effect of grain boundaries. Nevertheless, it must be born in mind that by reducing the grain size, the microstructural/mechanical properties of the material can be considerably altered.
  - It would be interesting to obtain a S-N curve with a defect free material cycled in vacuum conditions in order to compare it with the curve of the reference material.
  - It is proposed to perform synchrotron experiments in vacuum conditions in order to further investigate the internal crack growth rates. Another possibility would be to apply a surface strengthening treatment on small specimens in order to favour internal crack initiation.
- Torsion fatigue:
  - Synchrotron *in situ* fatigue testing will enable to further investigate the complex nucleation and propagation mechanisms (*e.g.,* multisite cracking, linkage, branching) observed in this material. To this end, a torsion fatigue machine was commissioned (see Fig. 3.39a) and the first synchrotron experiments have been carried out in June 2014 at the ESRF using $\varnothing = 3$ mm cylindrical specimens. One of the imaged microcracks is given in Fig. 3.39b as example. It shows characteristic mode III propagation on both transverse and longitudinal planes.

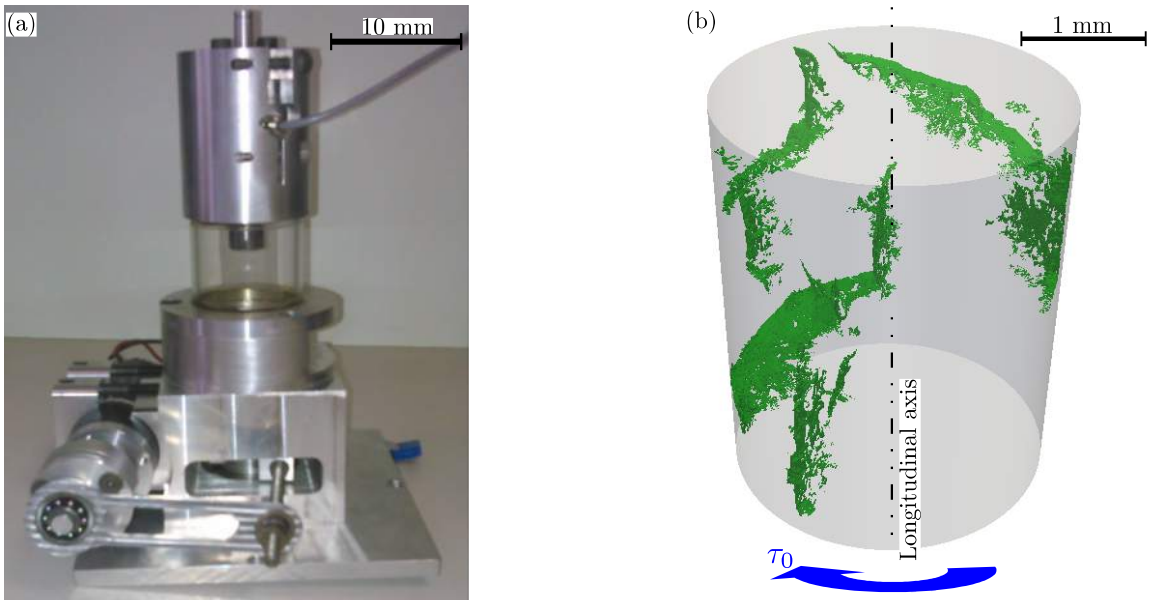

Fig. 3.39: (a) Image of the new synchrotron torsion machine. (b) 3D rendering obtained using synchrotron images of one of the first torsion microcracks imaged with the torsion machine at the ESRF.

- Surface pores are less detrimental in cyclic torsion than in cyclic tension as large surface grains seem to produce earlier crack nucleation. As future work, it is proposed to validate this point by performing tests using specimens made out of the same reference material but where artificial surface defects (produced, for example, by EDM) are present along the specimen gage length.
- It would be also interesting further investigate the influence of the grain size as well as the SDAS on the torsional fatigue life.

All in all, the main idea that must be kept in mind out of this PhD work is that the position (internal or surface) and the type of loading (uniaxial or torsional) change the influence of casting defects on fatigue life. It is reasonable to say that components presenting internal defects of considerable size (almost ten times larger that the critical defect size allowed at the free surface) can be retained during Non-Destructive Inspections (NDI). Nevertheless, attention must be paid to the shape of defects as it has been shown that smaller convoluted defects are able to produce earlier crack nucleation. New releases of current standards ((*e.g.,* reference radiographs ASTM-E155-10)) seem necessary to take into account the latest advances in NDI (*e.g.,* micro-CT) as well as the different sizes that can be allowed depending on the defect location and type of loading (uniaxial, torsion, multiaxial).

Conclusions et Perspectives

Plusieurs types d'essais de fatigue ont été menés dans ce travail. Le suivi de fissures surfaciques sollicitées en traction alternée et à l'air ambiant a été réalisé sur des échantillons macroscopiques (section transversale: ∼6mm×6mm) afin d'étudier l'influence des paramètres microstructuraux (tels que la SDAS et la taille de grain) sur la propagation de fissures courtes. En ce qui concerne l'effet des défauts internes, des éprouvettes cylindriques (section transversale: $\varnothing = 10$ mm) contenant de défauts artificiels de $\varnothing_{\mathtt{eq}} \approx 2$ mm (placés à l'intérieur ou à la surface libre) ont été testées afin d'établir des courbes S-N et d'effectuer des observations systématiques sur les faciès de rupture pour l'étude des mécanismes internes de propagation. Des éprouvettes microscopiques (section transversale: ∼2mm×2mm et ∼3mm×3mm) ont été utilisés pour essayer d'imager l'amorçage de fissures courtes à partir de défauts internes et mesurer leur vitesses de propagation. Des simulations EF effectuées avec les images 3D de ces petites éprouvettes ont permis d'évaluer l'influence de la taille et la forme du défaut ainsi que la capacité d'un pore à amorcer des fissures. Enfin, des essais de fatigue en torsion pure ont été effectués sur des éprouvettes cylindriques (section transversale: $\varnothing = 6$ mm) afin détudier l'influence de la microstructure sur la propagation des fissures en torsion, les effets de la présence de pores et d'obtenir des courbes S-N.

Les principales conclusions de ce travail de thèse peuvent être énumérées comme suit:

- En ce qui concerne **l'influence des paramètres microstructuraux** sur la propagation de fissures courtes dans le cas d'essais réalisés en **traction uniaxiale**:
  - Le SDAS semble être le paramètre microstructural contrôlant la propagation de fissures courtes. Un comportement de fissure microstructurale à pu être observée jusqu'à ce que la taille de la zone plastique en pointe de fissure soit équivalente à la valeur moyenne de le SDAS (38 μm, qui équivaut à une longueur de fissure de ∼550 μm). Les fissures se propagent préférentiellement à travers la matrice α-Al et très rarement à travers l'eutectique (amas). Le cheminement à travers l'eutectique correspond principalement à une propagation intergranulaire.
  - La taille de grain est considérée comme un paramètre de second ordre. Il a été observé que les joints de grains constituent des obstacles microstructuraux retardant la propagation de fissures courtes sans pour autant complètement l'arrêter.
  - Les fissures de surface qui ont été suivies présentent des cheminements relativement plans (qui sont globalement perpendiculaires à la direction de chargement) favorisés par le glissement multiple en poite de fissure lors de la propagation. L'orientation cristallographique est le facteur clé contrôlant la rugosité des chemins de fissuration. Il semblerait que des chemins plus rugueux (en dents de scie) aient tendance à se former lorsque les valeur de Taylor sont élevées ($M_T \gtrsim 3$).
- Une courbe S-N de référence a été obtenue en utilisant un matériau considéré libre de défauts surfaciques. **L'influence des défauts de fonderie** sur la durée de vie en **traction uniaxial** varie en fonction de la nature du défaut (artificiel, naturel, interne et/ou surfacique) et de

l'environnement (air ambiant ou vide):

* Il a été observé qu'il existe une taille de pore critique ($\sqrt{A} \approx 400$ μm) dans le cas de pores naturels en surface sollicités sous air ambiant pour un rapport de charge de R=0.1. Des pores surfaciques plus larges que cette taille critique vont considérablement réduire la durée de vie du matériau.
* Les défauts artificiels internes ($\varnothing_{\mathsf{eq}} \approx 2$ mm) testés à l'air ambiant produisent une courbe S-N similaire à celle du matériaux de référence. Pour la grande majorité des échantillons étudiés, l'amorçage de fissures se produit à partir du défaut interne. La fraction principale de la propagation interne se produit sous vide en régime pseudo stade I intrinsèque ce qui résulte en la formation de grandes facettes cristallographiques où les fronts de fissures sont très irréguliers. La vitesse de propagation d'une fissure interne est beaucoup plus lente que celle d'une fissure surfacique, ce qui conduit à la superposition des deux courbes S-N (correspondantes au matériau de référence et au matériau contenant de défauts internes de grand taille). Aux alentours du défaut, une petite portion du faciès de rupture correspond à une propagation en régime stade II assisté par l'environnent (Région I). Il parait que cette région a un effet négligeable sur la durée de vie globale des éprouvettes. Si le front de fissure interne atteint la surface libre avant que la rupture finale ne se soit produite, les fissures continuent leur propagation en changeant au régime stage II assisté par adsorption (Région III).
* Les défauts artificiels surfaciques ($\varnothing_{\mathsf{eq}} \approx 2$ mm) testés sous vide produisent des durées de vie similaires à celles des défauts artificiels et internes. Seule la Région II est observée sur les faciès de rupture et les fronts de fissure sont également très irréguliers. La similitude dans la la durée de vie s'explique parce que l'état de contraints produit par les deux type de défauts artificiels (surfaciques et internes) peut être considéré comme équivalent, bien que le volume affecté par un défaut interne soit deux fois celui d'un défaut surfacique.
* Les défauts artificiels surfaciques ($\varnothing_{\mathsf{eq}} \approx 2$ mm) testés à l'air ambiant produisent une notable réduction de la durée de vie en fatigue. Ceci est en bon accord avec les résultats de la littérature. Un défaut de cette taille peut directement produire la formation d'un fissure longue et donc la contribution de la période d'amorçage à la durée de vie est presque négligeable.
* Les essais sous vide en utilisant des éprouvettes macroscopiques usinées avec le matériau de référence et qui contaient des défaut naturels non-contrôlés produisent des durée de vie placées au-dessus (mais pas trop loin de) la courbe de référence. L'étude fractographique a montré que toutes les ruptures ont été produites par propagation en régime pseudo stade I intrinsèque à partir de défauts naturels principalement situés en surface.
* Des éprouvettes microscopiques testées à l'air ambiant et qui contiennent des défauts naturels et internes de $\sqrt{A} = 200$-400 μm ont rarement produit une propagation interne (uniquement 3 sur 12 éprouvettes) et la rupture finale a toujours été produite par des défauts naturels en surface.
* Des éprouvettes microscopiques qui contiennent des défauts artificiels et internes de $\varnothing_{\mathsf{eq}} \approx 1$ mm et cyclées à l'air ambiant n'ont amorcé aucune fissure interne. Les défauts surfaciques qui ont été capables de produire la rupture finale sont près de dix fois plus petits que les défauts internes .

- Des tests CT de fissure longue montrent que, à une valeur d'intensité de contrainte fixe, les fissures se propageant à l'air ambiant produisent **des vitesses de propagation** un ordre de grandeur plus élevées que celles de fissures se propageant sous vide. Dans le cas des

fissures coutes internes, il a été observé que, à valeurs équivalentes du facteur d'intensité de contrainte, leurs vitesses de propagation sont similaires à celles d'une fissure longue se propageant sous vide.

- Il a été observé que **la taille et la forme des pores** peuvent influencer la période d'amorçage d'une fissure en fatigue. La taille de pore est le paramètre de premier ordre. La forme des pores doit être pris en compte lorsque les défauts sont de même taille, car ce facteur a tendance à réduire la période d'amorçage. Il parait que cette influence diminue ou disparaît même lorsque les pores sont assez grand ($\sim$400 μm) pour annuler la période d'amorçage.
- En ce qui concerne à **l'influence des paramètres microstructuraux** sur la propagation de fissures en conditions de **torsion pure**:
  - L'amorçage en torsion est multiple. Les résultats de suivi de fissures ont montré que seulement le 30% de la durée de vie attendue est consacré à l'amorçage de fissures qui se produit sur des plans {111} cristallographiques proches au plan transversal. Pendant ce 30% de la durée de vie, les premiers joints de grains ont déjà été franchis.
  - La propagation de fissures dépend du niveau de contrainte. Dans la Zone 1 (niveaux de contrainte élevés, $\tau_{\mathtt{max}} > 105$ MPa), la propagation de fissures en mode III transversal est dominante et des faciès de rupture plats en sont produits.
  - Dans la Zone 2 (100 MPa $> \tau_{\mathtt{max}} >$ 85 MPa), plusieurs micro-fissures peuvent être dominantes. Le mode III (à la fois sur plans transversaux et longitudinaux) est dominant, bien que le mode I soit occasionnellement observé. L'orientation cristallographique contrôle le mode de propagation de fissures et leurs déviations. La rupture finale se produit par la liaison des fissures dominantes et des faciès de rupture tortueux sont formés.
  - Dans la Zone 3 ($\tau_{\mathtt{max}} <$ 80 MPa), un faciès de rupture à $\sim$45° en forme d'hélice est formé. Le mode I est dominant quoique quelques micro-marches produites localement en mode III peuvent aussi être observées.
- Quant aux **techniques d'inspection**, il a été déterminé que les défauts de fonderie considérés comme *larges* ($\sqrt{A} \approx 400$ μm) réduisent la durée de vie attendue quand ils sont placés à la surface libre. Par contre, les défauts ayant des tailles jusqu'à $\varnothing_{\mathtt{eq}} \approx 2$ mm ont un effet négligeable sur la durée de vie en fatigue lorsqu'ils sont placés à l'intérieur du matériaux (les cas des défauts internes). Les recommandations suivantes peuvent être tirées:
  - Le contrôle par ressuage (DPI) est une technique valable pour détecter des défauts de fonderie placés en surface. Cependant, cette technique n'est pas capable de détecter la taille réelle de quelques défauts quand ils cachent une grande partie de sa taille sous la surface libre.
  - Des contrôles tomographiques, si possible couplés avec la technique de ressuage, devraient être en mesure d'améliorer la détection de défauts surfaciques et sub-surfaciques.
  - Le taux de rejet pourrait être diminué en acceptant des composants qui contiennent de *gros* défaut internes à condition qu'ils soient placés loin de la surface libre.

Enfin, il est proposé de **poursuivre plus de recherches** sur les thématiques suivantes:

- <u>Traction:</u>
  - Une réduction de la taille de grain du matériau est proposée. Il serait intéressant d'étudier la taille de grain optimale qui pourrait augmenter l'effet de barrière de joints de grains. Néanmoins, il faut garder à l'esprit que en réduisant la taille des grains les propriétés du matériau peuvent être considérablement modifiées.
  - Il serait intéressant d'obtenir une courbe S-N avec un matériau libre de défauts naturels et qui soit testé sous vide afin de comparer ces résultats avec la courbe de référence.

∗ Il est proposé de réaliser des essais synchrotron mais sous vide afin d'approfondir l'étude des vitesses de propagation de fissures internes. Une autre possibilité serait d'appliquer un traitement de surface sur de petits éprouvettes avec l'objectif de favoriser l'amorçage interne.

- Torsion:
  ∗ Des essais synchrotron de fatigue *in situ* permettront d'approfondir l'étude des complexes mécanismes d'amorçage et propagation (par exemple, l'amorçage multiple, la jonction de fissures, la bifurcation) observés dans les essais macroscopiques de torsion. A cette fin, une machine de fatigue synchrotron dédiée à la torsion a été construite (voir Fig. 3.40a) et les premières essais ont été réalisées en Juin 2014 à l'ESRF en utilisant des éprouvettes cylindriques $\varnothing = 3$ mm . Un des micro-fissures imagées est donnée comme exemple dans la Fig. 3.40b. Celle-ci montre la propagation caractéristique de la torsion qui se produit principalement en mode III sur des plans longitudinaux et transversaux.

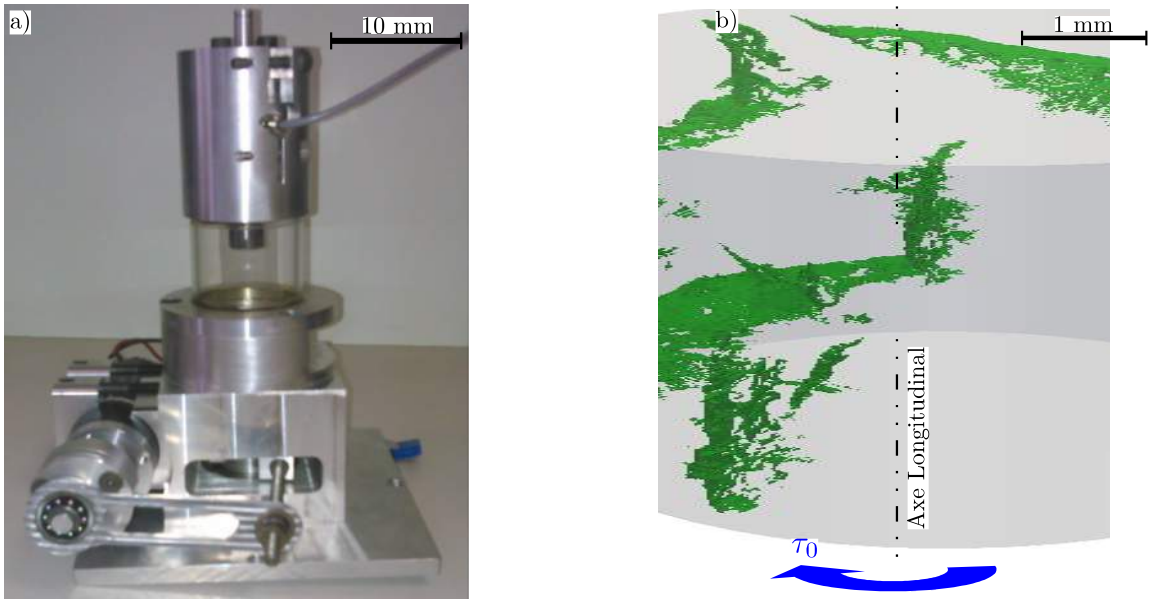

Fig. 3.40: a) Image de la nouvelle machine synchrotron dédiée à le réalisation des essais de torsion. b) Rendu 3D obtenu à partir d'images synchrotron montrant l'une des premières micro-fissures de torsion imagées avec cette machine de torsion à l'ESRF.

∗ Les pores surfaciques sont moins nocifs en torsion qu'en traction cyclique. Comme perspective, il est proposé de valider ce point par la réalisation d'essais en utilisant des éprouvettes fabriqués à partir du même matériau de référence où des défauts artificiels sont usinés (par exemple, par EDM) le long du fût.

∗ Il serait également intéressant d'étudier l'influence de la taille de grain sur les mécanismes de fatigue en torsion, en attendant à ce qu'une taille de grain plus petite puisse augmenter la période d'amorçage.

Appendix A

Synthesis of synchrotron specimens containing natural defects

Considerable work has to be done before completion of synchrotron *in situ* fatigue experiments. Preparation of specimens containing internal natural defects is laborious and time consuming, principally because of the uncertainty of defect presence within the zone of interest ($\varnothing$ = 10 mm area at the rod centre, see § 1.2.1.1 for further details). This uncertainty led to pores being randomly present in slices (∼2.5 mm width). And even when pores are present within the zone of interest, there is the possibility of them to be intercepting the free surface. Therefore, high rejection rates were obtained and a summary is given in what follows:

* ∼200 slices were mechanically sectioned (in-home process). Only 50% exhibited defects within the zone of interest.
* ∼100 specimens were produced by EDM (external provider). Only 30% contained internal defects. The rest contained surface defects or no defect at all.

Fig. A.1 shows some examples of deficient synchrotron specimens and Fig. A.2 shows some examples of optimal synchrotron specimens (∼2mm×2mm cross section). Some of the specimens shown in Fig. A.1 and Fig. A.2 (those considered as *less* interesting for synchrotron testing) were used to perform pre-synchrotron testing and so to obtain an estimation of the total number of cycles necessary to cause final failure using these type of small specimens. Finally, it must be noted that around 10-15 optimal specimens where ready for use at each SLS experiment although the limited beamtime only allowed, in total, the cycling of twelve specimens. Fig. A.2b) and Fig. A.2h shows two of the specimens that were used during synchrotron testing. Both specimens failed without producing any internal crack.

As the position of the $\varnothing_{\mathsf{eq}} \approx 1$ mm artificial defect within the rod interior was controlled, these synchrotron specimens (∼3mm×3mm cross section) were much easily produced. Fifteen of them were successfully prepared and only three rejections were obtained due to an inaccurate estimation of the defect position during tomographic inspections.

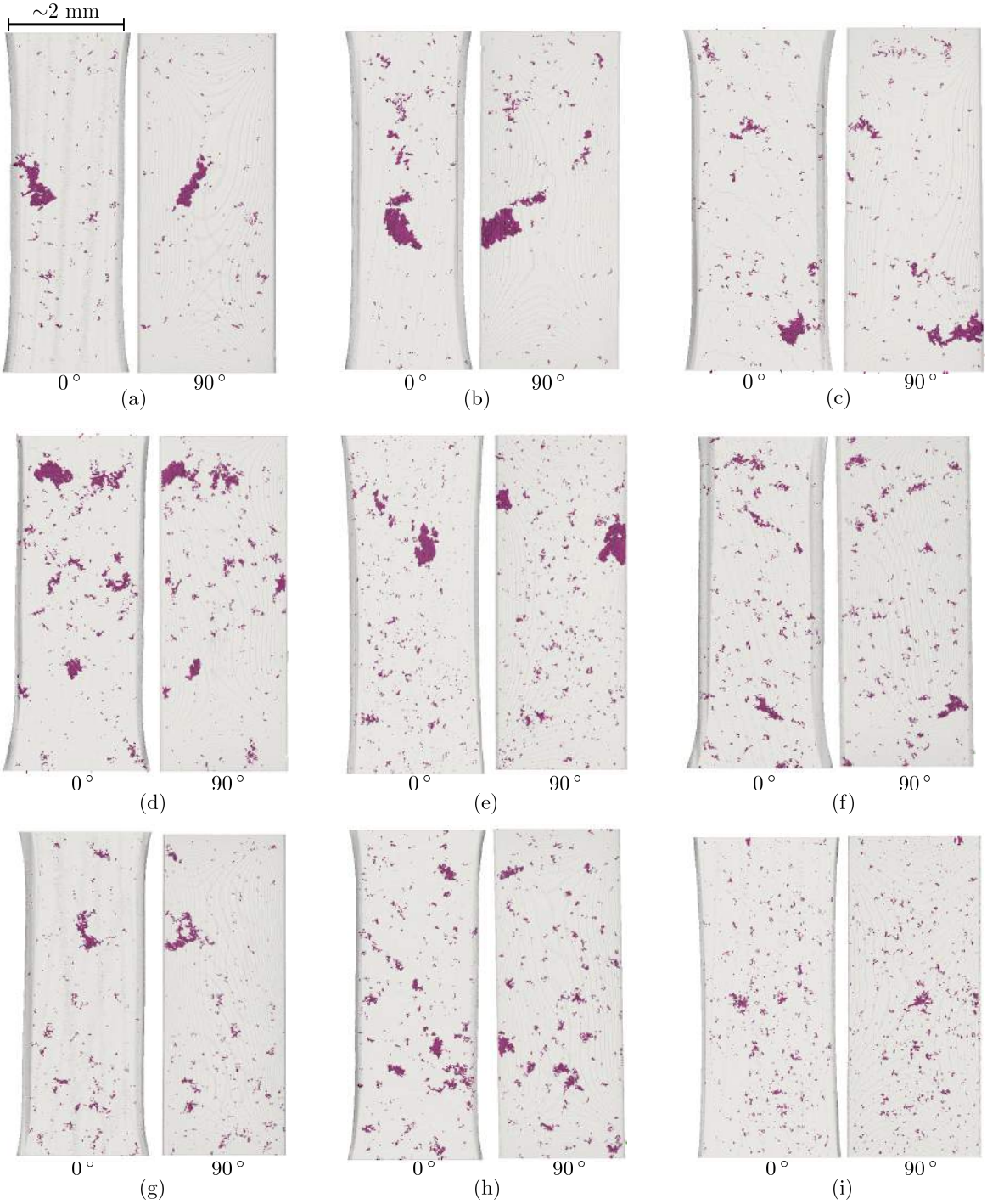

Fig. A.1: (a)-(h) Examples of deficient synchrotron specimen gages where the defect is at the free surface (surface defect). (i) This specimen is deficient because there is no important casting defect.

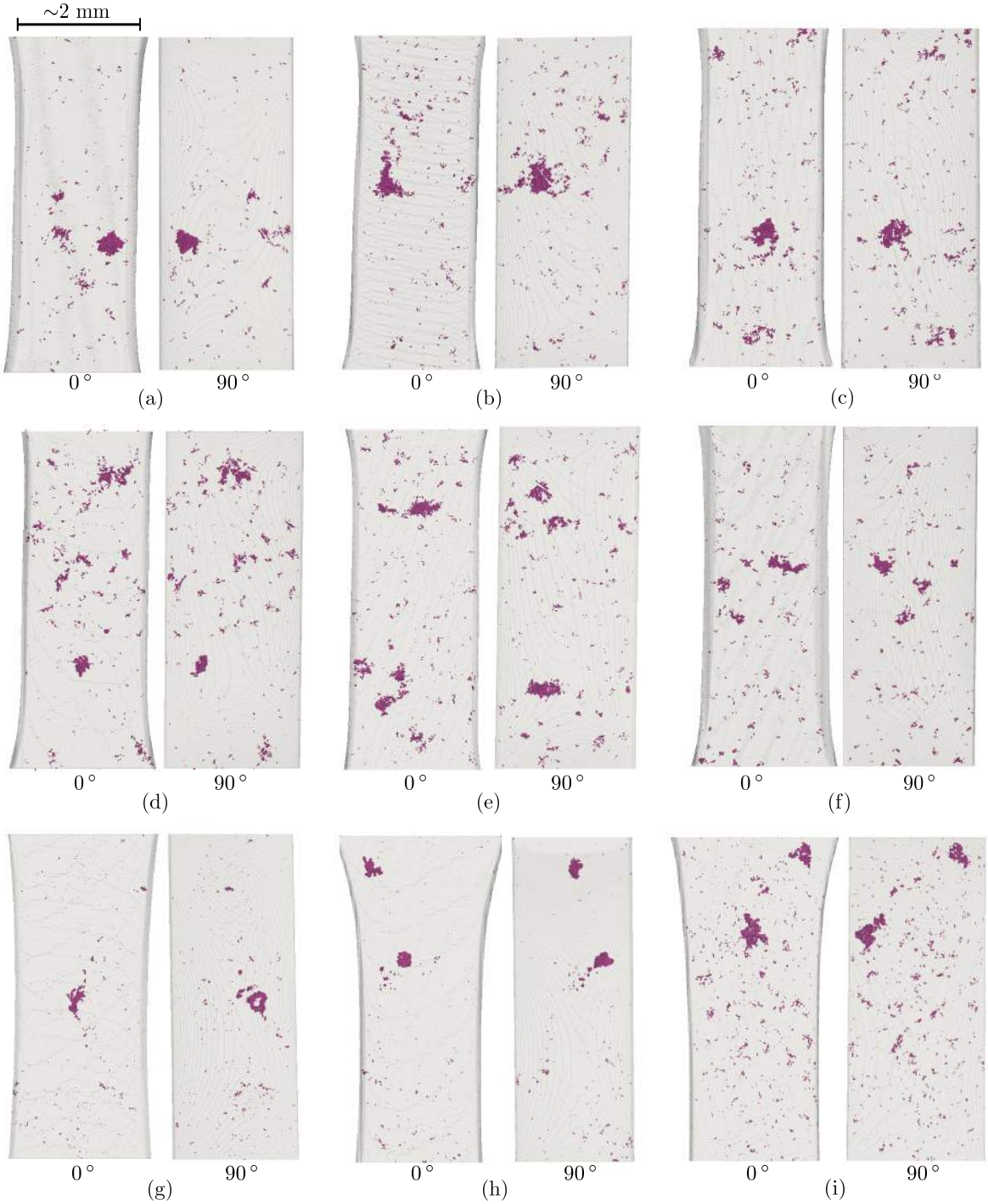

Fig. A.2: (a)-(i) Examples of optimal synchrotron specimen gages where the defect is placed in the bulk (internal defects).

Appendix B

FE analysis and profilometry on the geometry of torsion specimens

First torsion tests were performed using as-machined specimens that systematically failed at junctions. Fig. B.1 shows an example of a post-mortem as-machined specimen. In order to establish the possible causes responsible for this localised fatigue failure, it was decided to carry out a finite element study in conjunction with a profilometry analysis.

Fig. B.1: Image showing an example of a post-mortem as-machined specimen which failed at one of the junctions.

Fig. B.2 shows Von Mises results of the FE simulation performed using the torsion geometry (fine mesh of 167 000 tetrahedra) subjected to a torque of 4.24 Nm (equivalent to $\tau_{\mathtt{max}} = 100$ MPa). It was found that this specimen geometry produces 3% stress concentration at junctions.

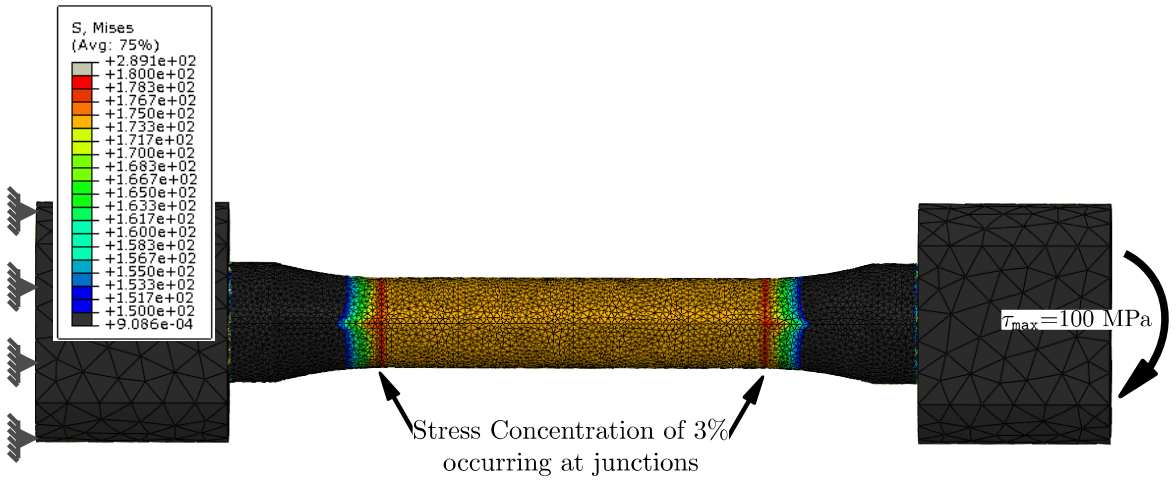

Fig. B.2: Abaqus rendering of the Von Mises results showing stress distribution along the specimen gage.

A profilometry analysis was performed at ENISE institution using a Taylor-Hobson surface profiler and a scan speed of 0.2 mm/s (see Fig. B.3). Results indicate that the mechanical machining produced $\sim$25 μm notches at the specimen junctions. The mechanisms causing these defects are so far unclear. It was observed that these notch defects were invariably present in torsion specimens even though they were machined by two different providers.

Fig. B.4 compares results obtained using as-machined specimens with those of polished ones. In general, as-machined specimens show reduced fatigue lives and flat profile morphologies where propagation in mode III was mainly dominant regardless the stress level (see Fig. B.5 and Fig. B.6). Interestingly, nucleation sites were hard to identify in most of these fracture surfaces.

Notch presence combined with the geometry stress concentration effect is therefore considered to be responsible for early crack nucleation localised at junctions. The dispersion in results suggests that the severity of notches varied from one as-machined specimen to another. All specimens exhibiting final failure at junctions were ruled out even when their fatigue lives where close to the results obtained with polished specimens.

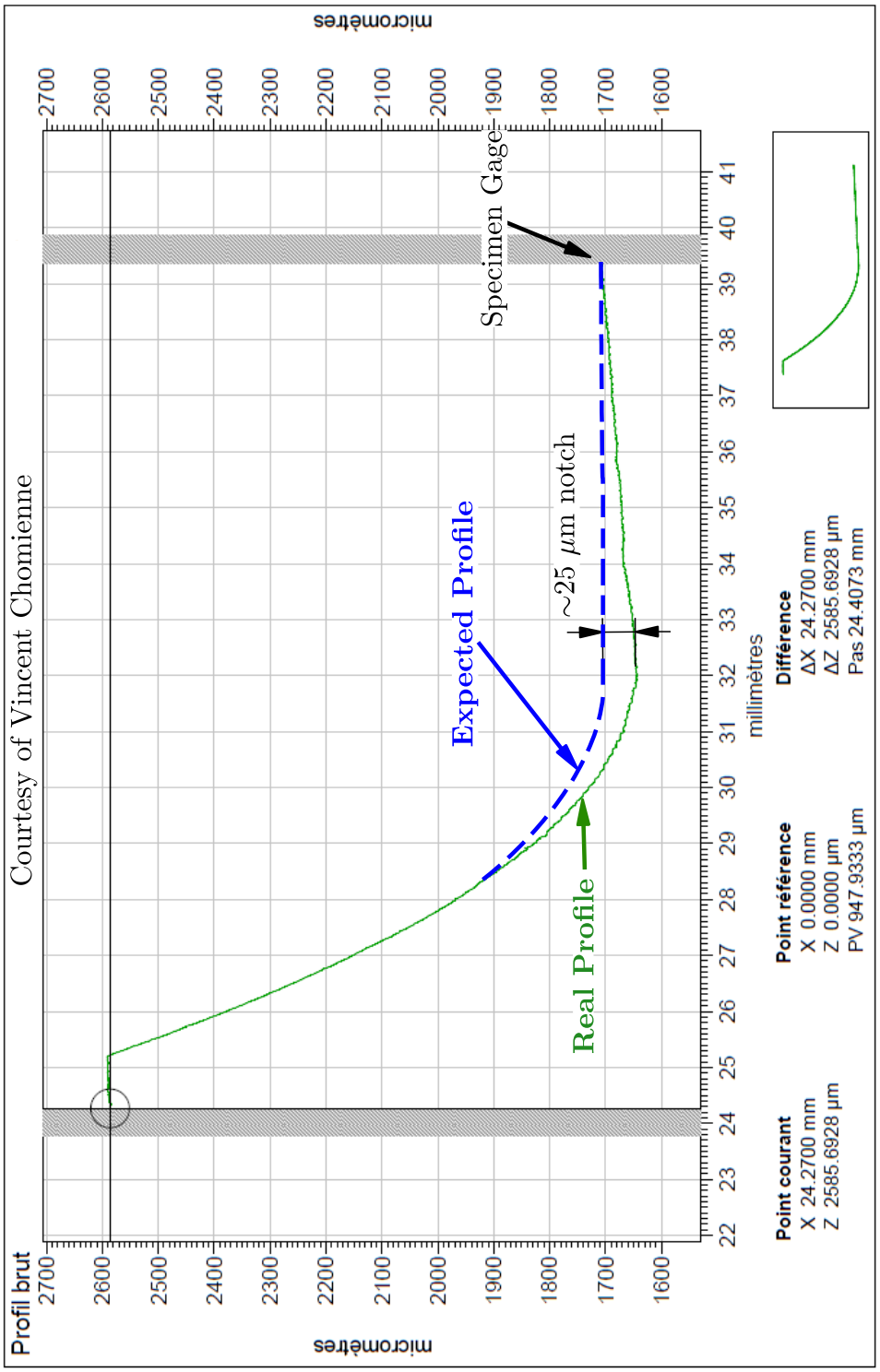

Fig. B.3: Profilometry analysis of torsion specimen geometry focused on one of the junctions. It shows a notch of $\sim 25 \mu m$ created during the mechanical machining.

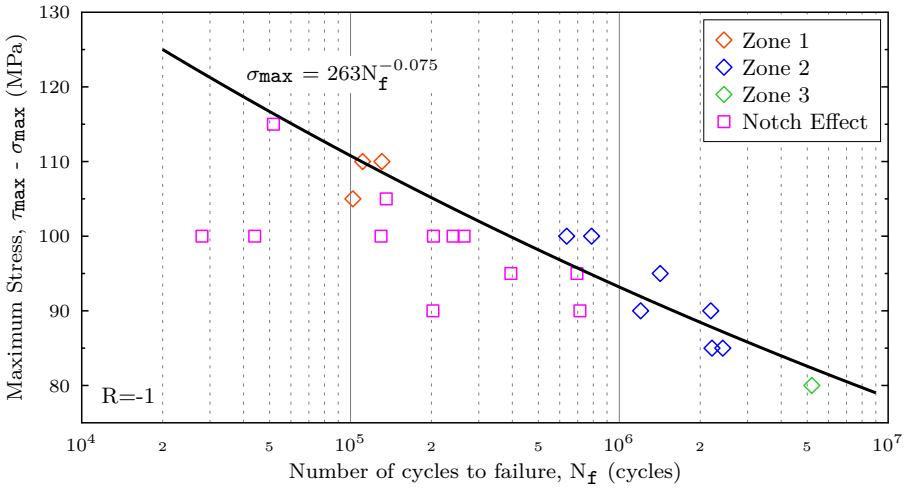

Fig. B.4: S-N curve showing results obtained using as-machined (squares) and polished (diamonds) specimens. Production of polished specimens required grinding off a superficial layer of 200 μm.

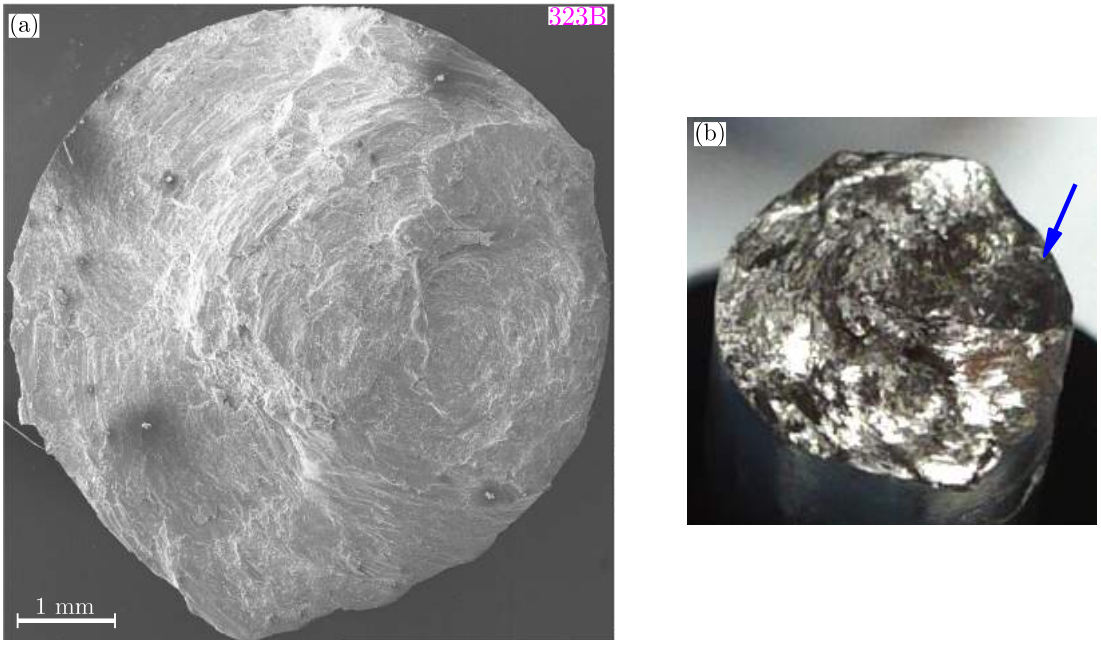

Fig. B.5: (a) SEM observation on the fracture surface of 323B specimen which occurred at one junction. Crack propagation in Mode III. The cycling parameters are: τ_{max} = 100 MPa, N_f = 203 418 cycles. (b) Optical image of the flat fracture profile where zones of murky debris (blue arrow) are visible with the naked eye.

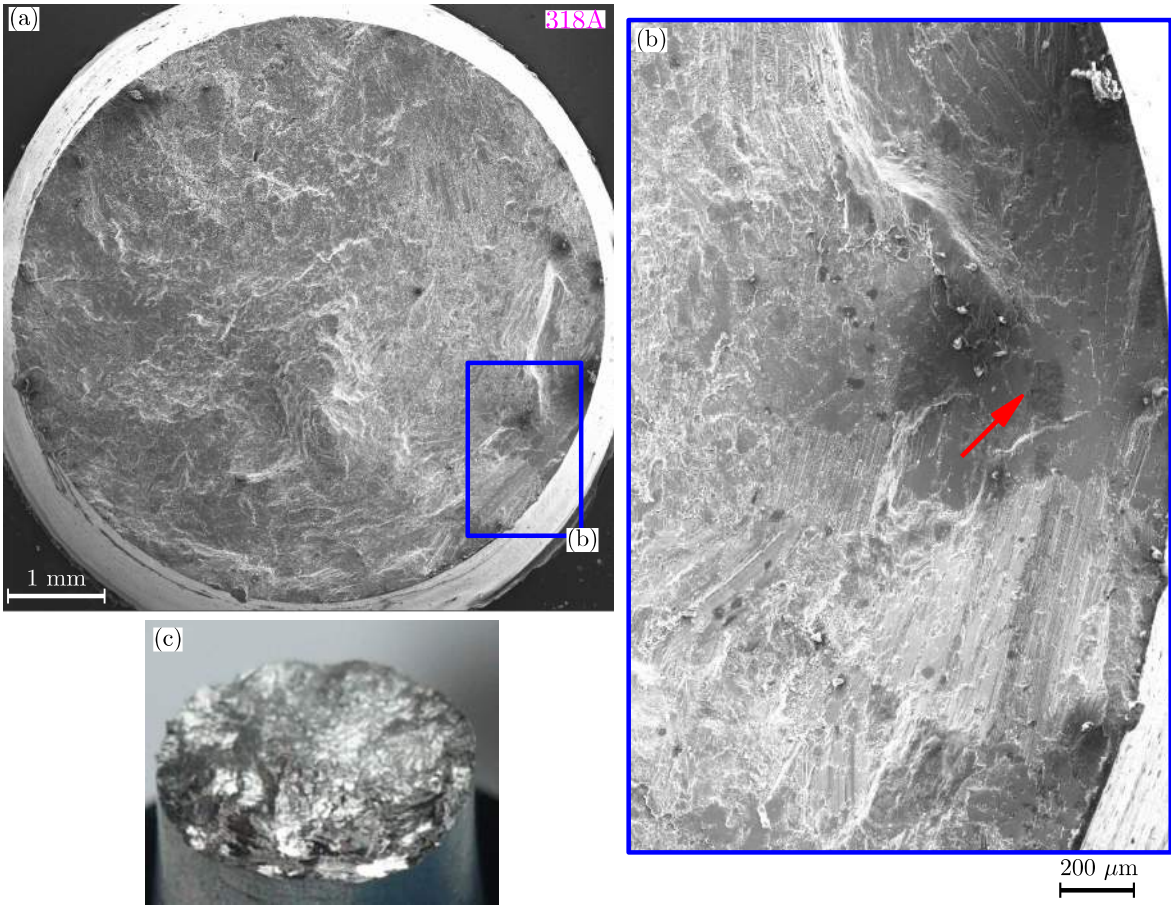

Fig. B.6: (a) SEM observation on the fracture surface of 318A specimen which occurred at one of the junctions. Crack propagation in Mode III was dominant although profile tortuosity was reduced when compared to 318A specimen. The cycling parameters are: $\tau_{max} = 100$ MPa, $N_f = 28\,012$ cycles. (b) Higher magnification on the suspected nucleation site where some crystallographic facets can be observed. The red arrow indicates a small layer of murky debris. (c) 3D optical image of this specimen flat fracture surface.

Appendix C

Additional fractographic observations on torsion specimens cycled in Zone 2

The fracture surfaces obtained in Zone 2 exhibit increased tortuousity with respect to the flat ones formed in Zone 1. Moreover, it was observed that the fracture surface topologies are considerably different from each other. Fig. C.1, Fig. C.2 , Fig. C.3 and Fig. C.4 show the additional fracture surfaces (four in total) that were ascribed to Zone 2.

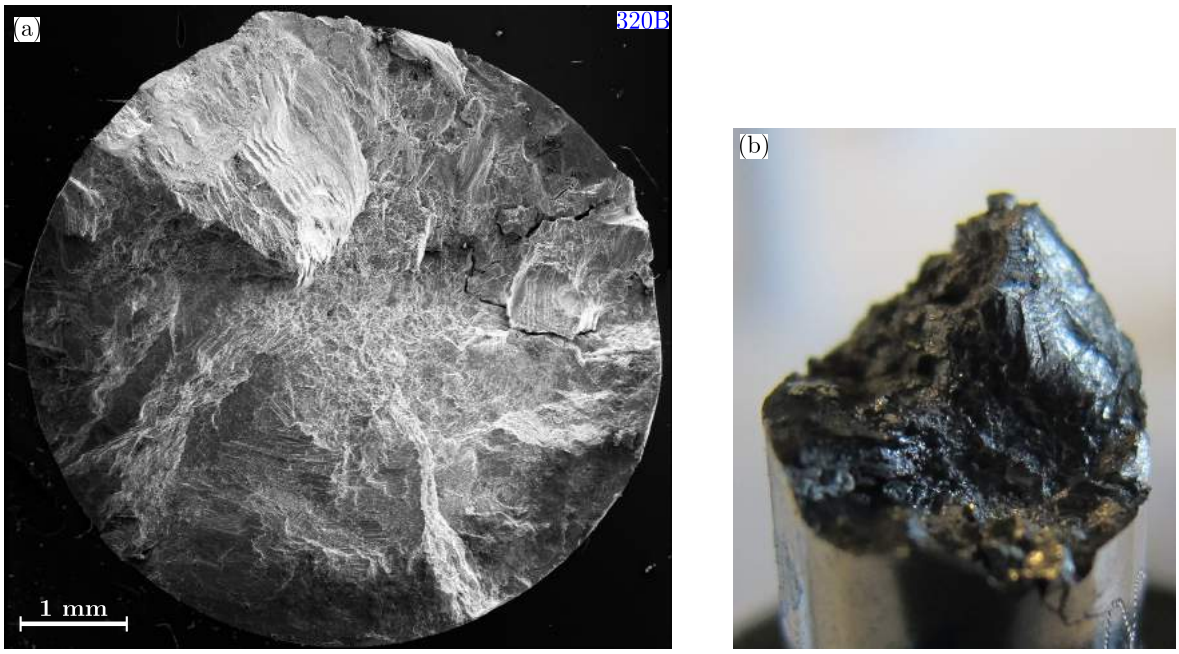

Fig. C.1: (a) SEM observation at low magnification on the fracture surface of 320B specimen. The fatigue testing parameters are: N_f = 788 444 cycles, τ_{max} = 100 MPa. (b) 3D optical observation on the fracture surface of 320B specimen.

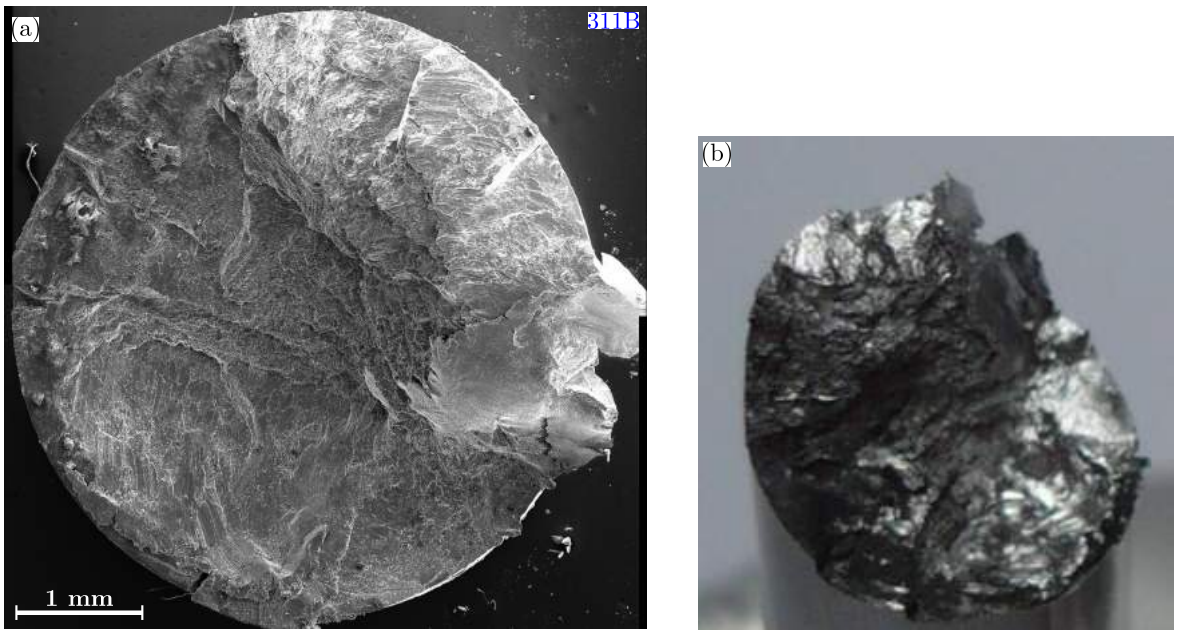

Fig. C.2: (a) SEM observation at low magnification on the fracture surface of 311B specimen. The fatigue testing parameters are: N_f = 636 925 cycles, τ_{max} = 100 MPa. (b) 3D optical observation on the fracture surface of 311B specimen.

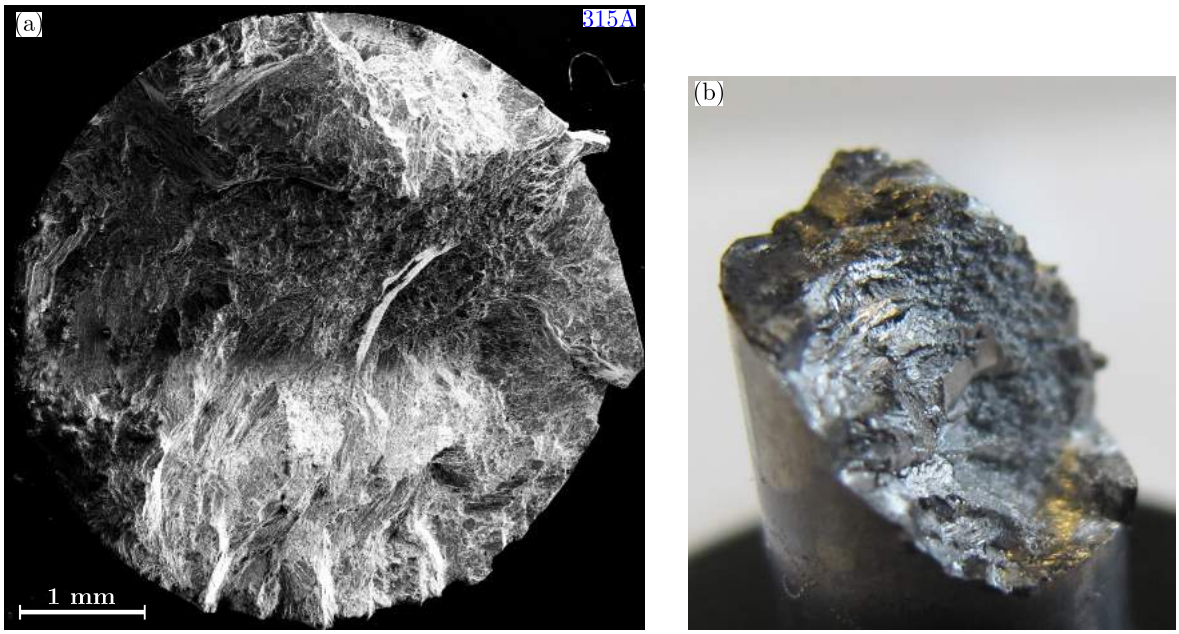

Fig. C.3: (a) SEM observation at low magnification on the fracture surface of 315A specimen. The fatigue testing parameters are: N_f = 2 188 541 cycles, τ_{max} = 90 MPa. (b) 3D optical observation on the fracture surface of 315A specimen.

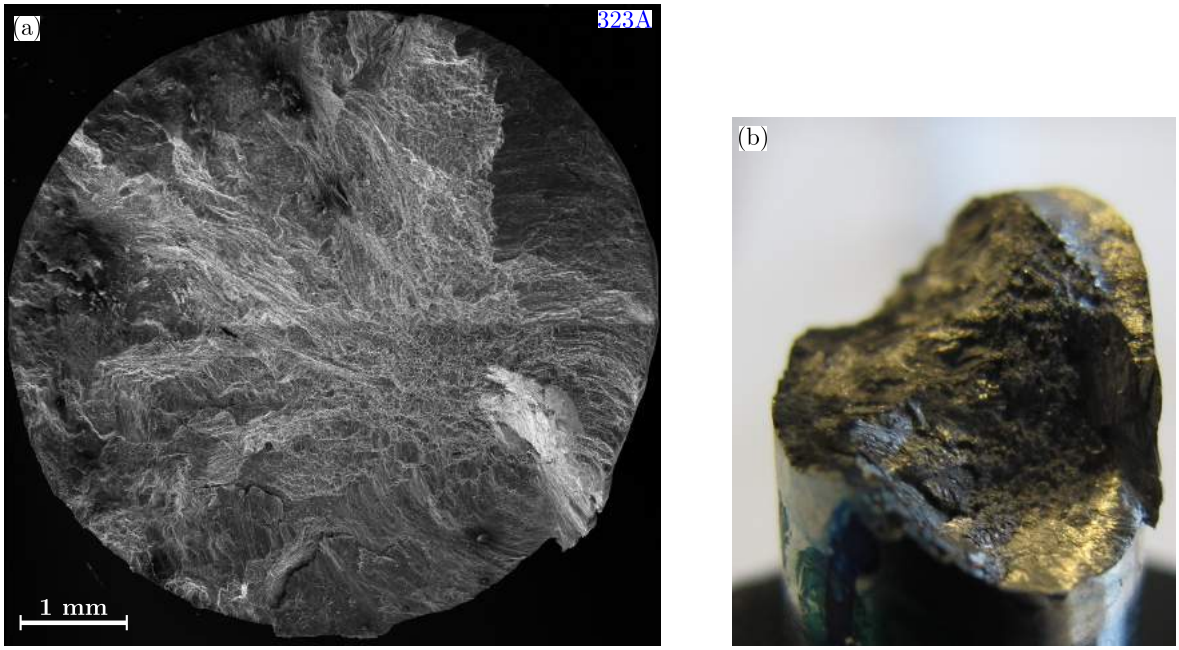

Fig. C.4: (a) SEM observation at low magnification on the fracture surface of 323A specimen. The fatigue testing parameters are: N_f = 2 425 685 cycles, τ_{max} = 85 MPa. (b) 3D optical observation on the fracture surface of 323A specimen.

Appendix D

Additional fractographic observations on $\varnothing_{eq} \approx 2$ mm internal artificial defects cycled in air environment

The figures presented in what follows (Fig. D.1, Fig. D.2, Fig. D.3 and Fig. D.4) allowed further investigation on the crack propagation features produced by internal nucleation from $\varnothing_{eq} \approx 2$ mm artificial defects. The difference between the specimen presented in Fig. D.5 and the rest is that neither Region I nor Region II are clearly observed. In addition, a small Region III area was formed from a small surface defect.

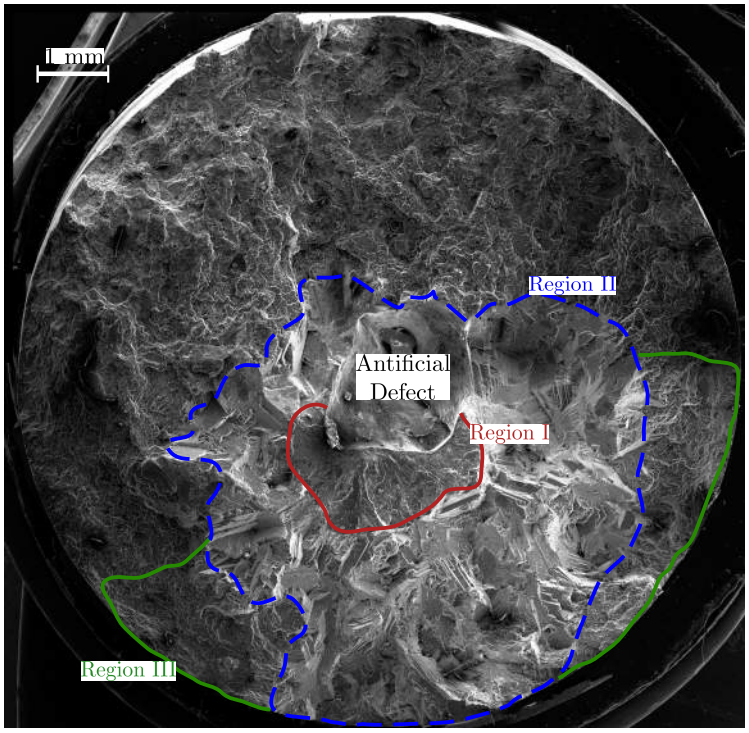

Fig. D.1: SEM observation at low magnification on the fracture surface of CTIF-131.124 specimen (ambient air) where three distinct regions can be observed. The fatigue testing parameters are: N_f = 7 423 900 cycles, σ_{max} = 105 MPa, Artificial Defect $\sqrt{A}$ = 1748 μm and Region I surface, A = 2.4 mm^2.

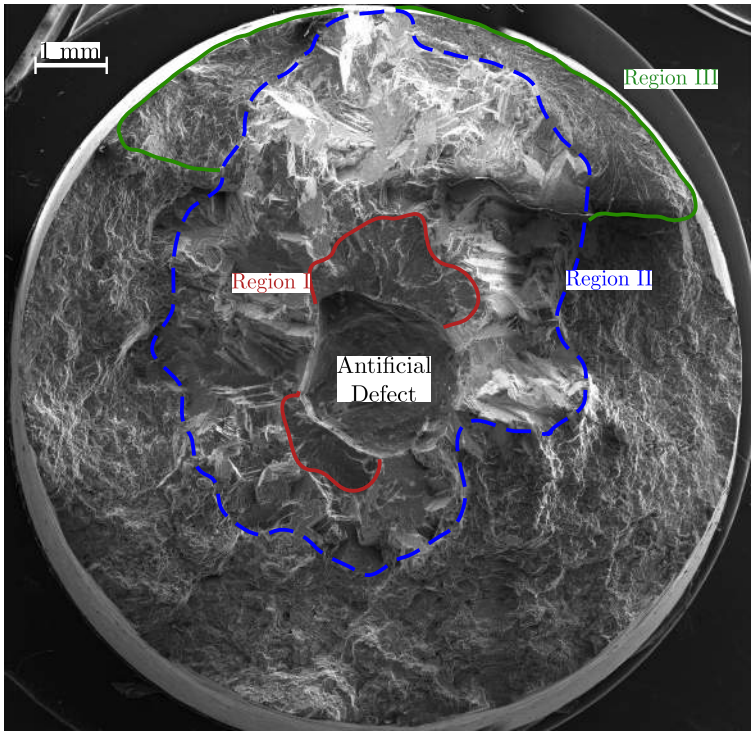

Fig. D.2: SEM observation at low magnification on the fracture surface of CTIF-131.100 (ambient air) specimen where three distinct regions can be observed. The fatigue testing parameters are: $N_f = 7\ 770\ 100$ cycles, $\sigma_{max} = 105$ MPa, Artificial Defect $\sqrt{A} = 1911$ μm and Region I surface, A = 2.6 mm^2.

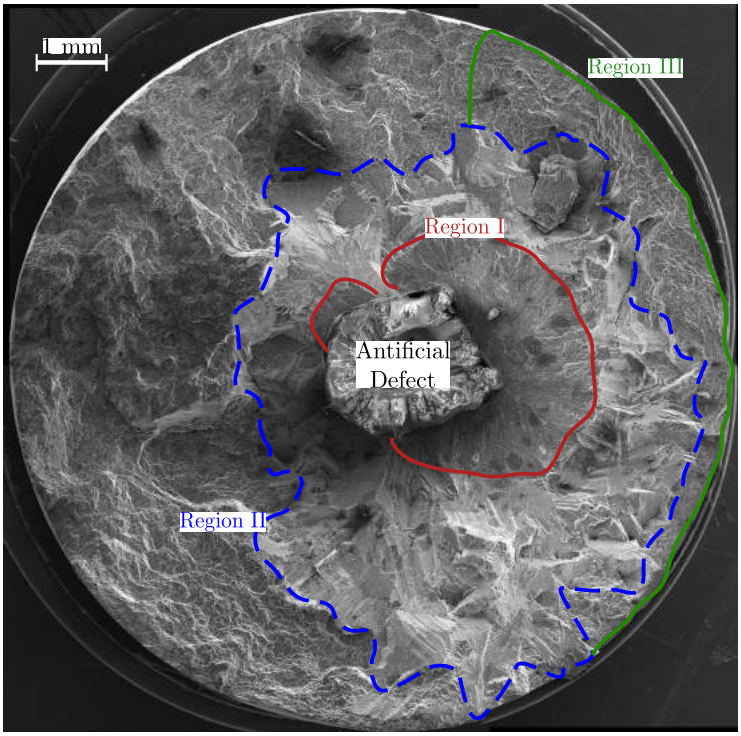

Fig. D.3: SEM observation at low magnification on the fracture surface of CTIF-131.105 specimen (ambient air) where three distinct regions can be observed. The fatigue testing parameters are: $N_f = 3\ 823\ 900$ cycles, $\sigma_{max} = 110$ MPa, Artificial Defect $\sqrt{A} = 1956$ μm and Region I surface, A = 6.2 mm^2.

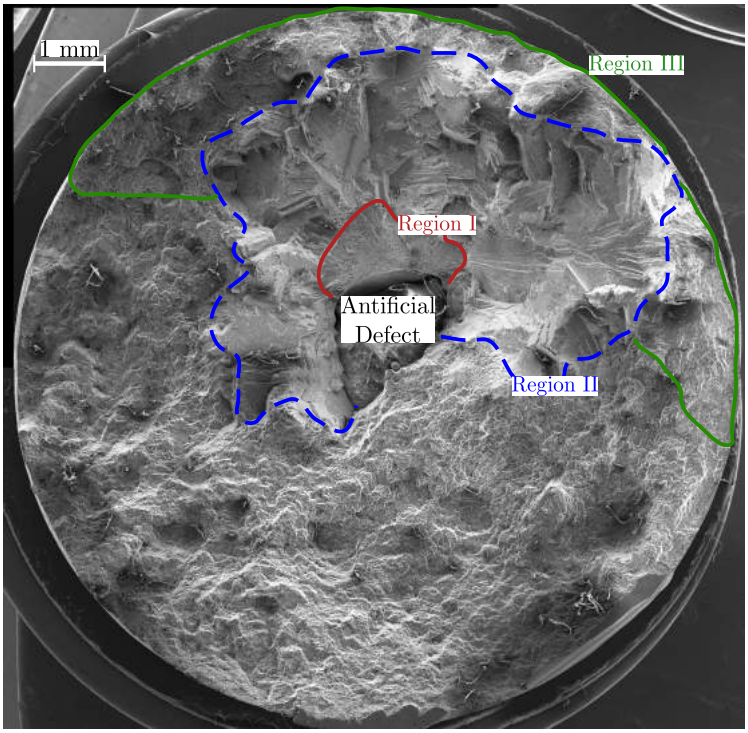

Fig. D.4: SEM observation at low magnification on the fracture surface of CTIF-131.113 specimen (ambient air) where three distinct regions can be observed. The fatigue testing parameters are: N_f = 7 151 900 cycles, σ_{max} = 110 MPa, Artificial Defect $\sqrt{A}$ = 1637 μm and Region I surface, A = 1.6 mm^2.

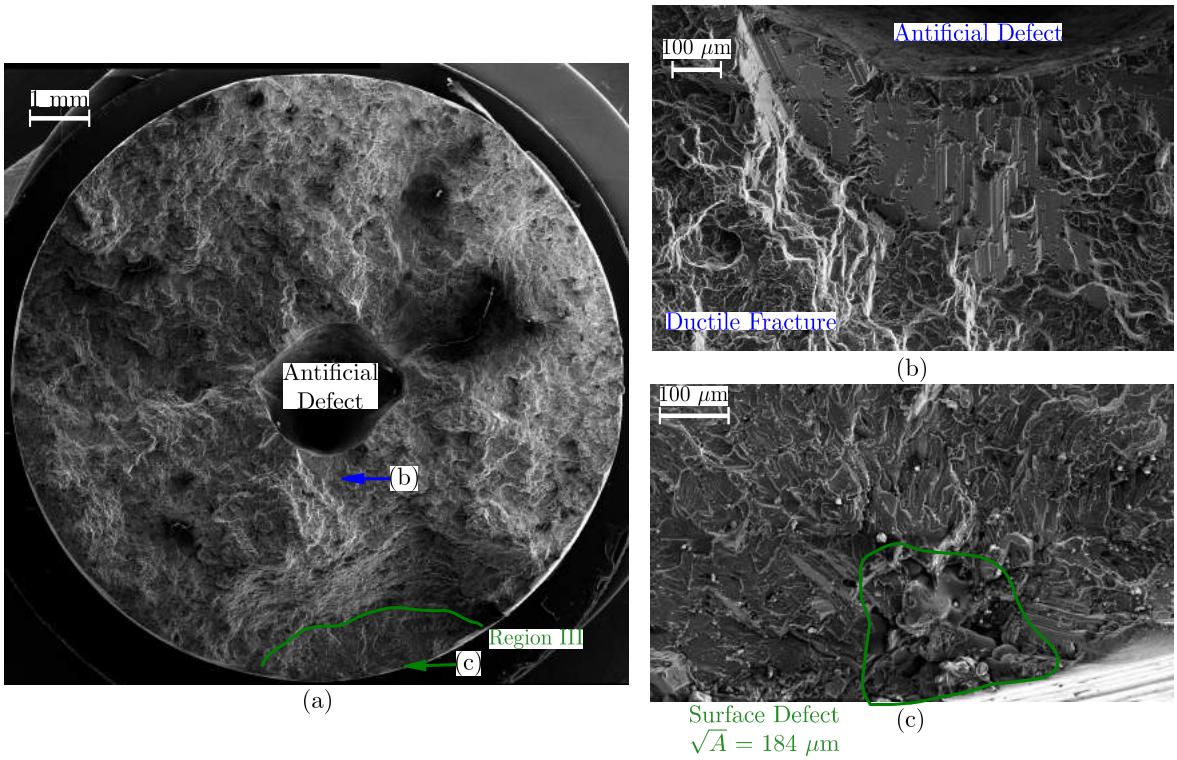

Fig. D.5: (a) SEM observation at low magnification on the fracture surface of CTIF-105.55 specimen (ambient air) where only the Region III is observed. The fatigue testing parameters are: $N_f = 38\,000$ cycles, $\sigma_{max} = 260$ MPa and Artificial Defect $\sqrt{A} = 1917$ μm. (b) A small crystallographic propagation is observed at the artificial defect. (c) A small defect of $\sqrt{A} = 184$ μm was observed to be the cause nucleation and propagation of the surface crack.

Appendix E

Additional fractographic observations on $\varnothing_{eq} \approx 2$ mm surface defects cycled under vacuum conditions

The three fracture surfaces presented bellow show exhibit features (crystallographic facets and irregular crack fronts) that are characteristic of Region II propagation. The presence of Region I or Region II is not observed in these three fracture surfaces.

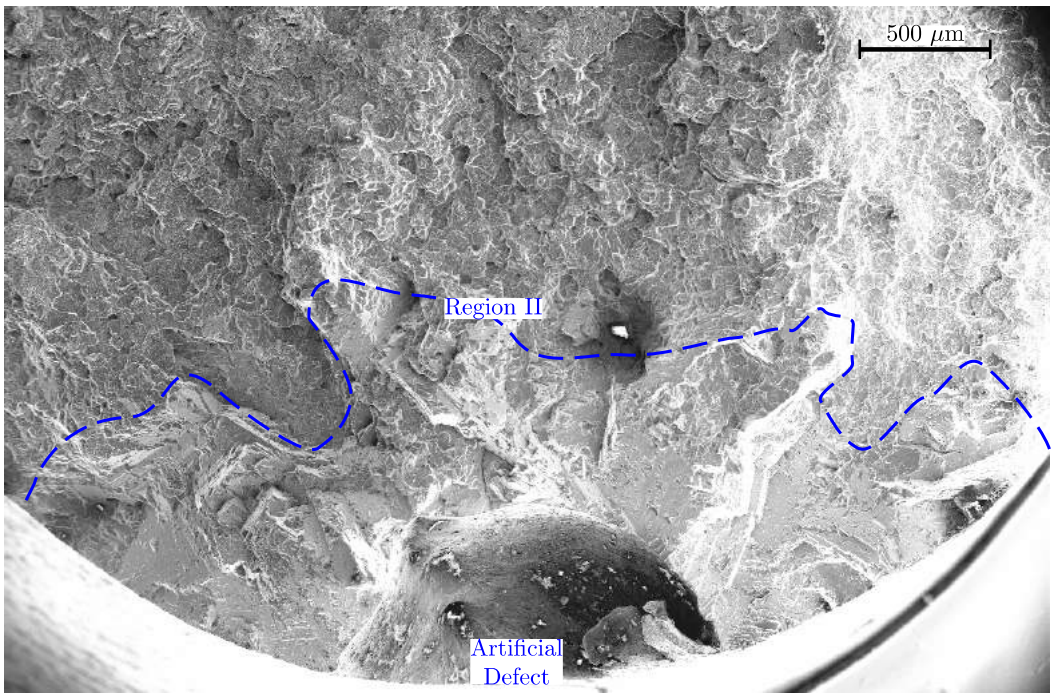

Fig. E.1: SEM observation at low magnification on the fracture surface of ENSMA-SDV-02 specimen (vacuum) where only Region II propagation is observed. The fatigue testing parameters are: N_f = 291 296 cycles, σ_{max} = 178 MPa and Artificial Defect $\sqrt{A}$ = 1220 μm.

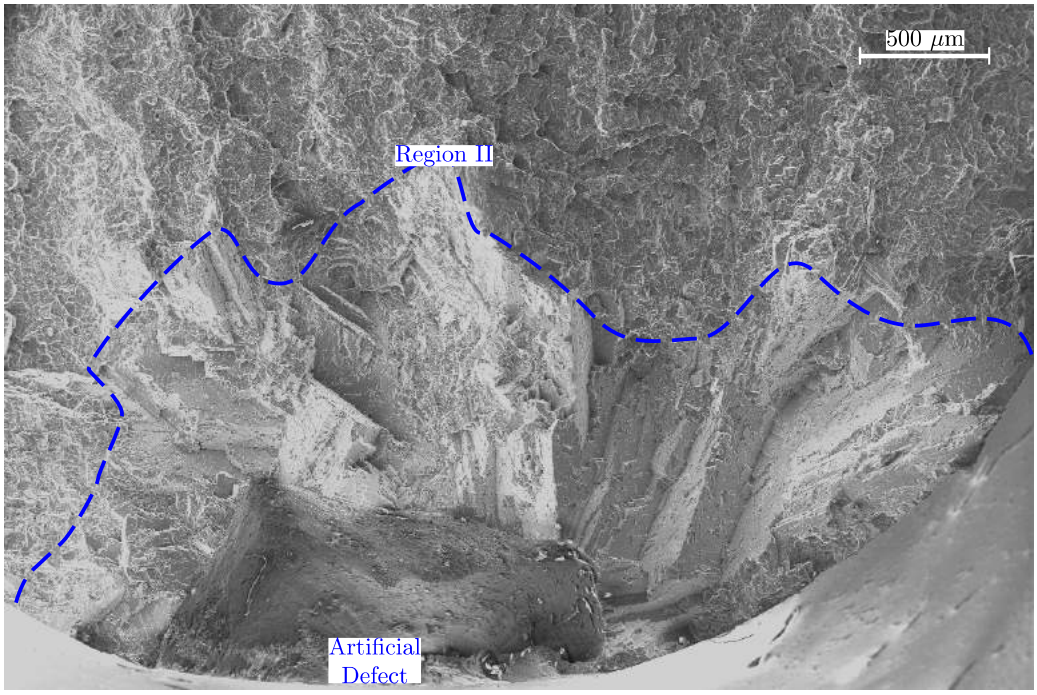

Fig. E.2: SEM observation at low magnification on the fracture surface of ENSMA-SDV-03 specimen (vacuum) where only Region II propagation is observed. The fatigue testing parameters are: $N_f = 1\ 184\ 165$ cycles, $\sigma_{max} = 111$ MPa and Artificial Defect $\sqrt{A} = 1485$ μm.

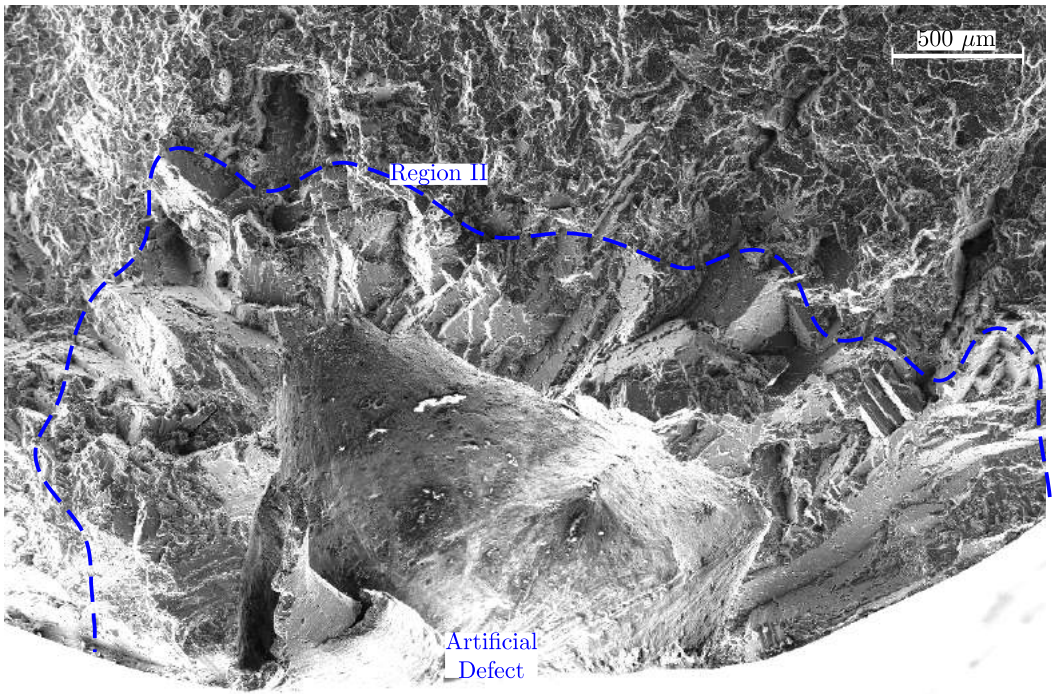

Fig. E.3: SEM observation at low magnification on the fracture surface of ENSMA-SDV-04 specimen (vacuum) where only Region II propagation is observed. The fatigue testing parameters are: $N_f = 447\ 016$ cycles, $\sigma_{max} = 156$ MPa and Artificial Defect $\sqrt{A} = 1595$ μm.

Appendix F

Additional fractographic observations on natural casting defects cycled under vacuum conditions

Fig. F.1, Fig. F.2 and Fig. F.3 shows natural surface and subsurface pores responsible for the final failure of specimens cycled in vacuum environment. Conversely to the reference specimens, these ones were not screened by DPI. Laboratory tomography controls were neither performed. Fig. F.4 presents the only case were the final failure was caused by an internal defect. Interestingly, this fracture surface also shows the presence of a smaller surface defect which was able to nucleate a microcrack.

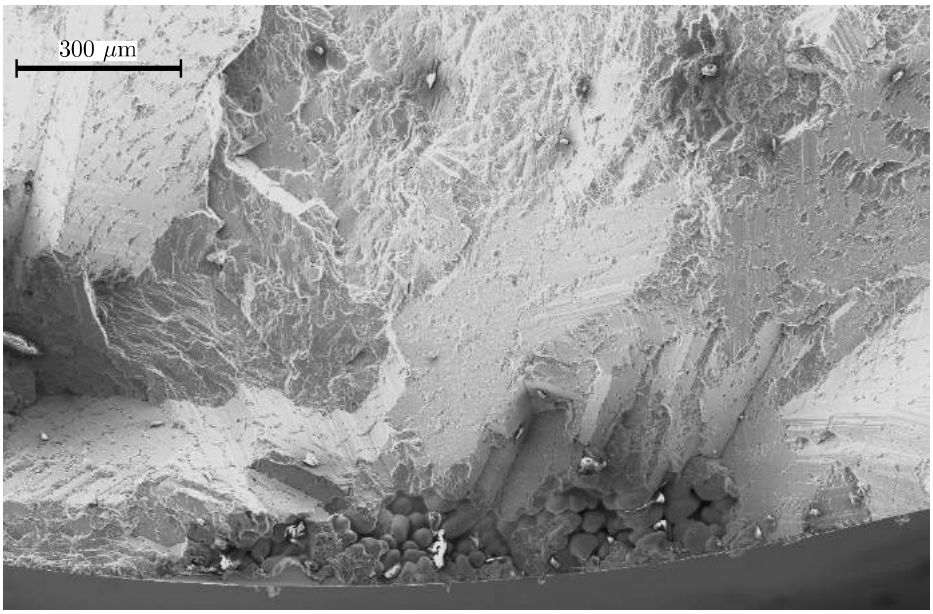

Fig. F.1: SEM enlarged view on the natural surface defect of ENSMA-SNV-02 specimen (vacuum) which nucleated and propagated the fatal crack. Only Region II propagation is observed. The fatigue testing parameters are: N_f = 225 674 cycles, σ_{max} = 222 MPa and Natural Defect $\sqrt{A}$ = 380 μm.

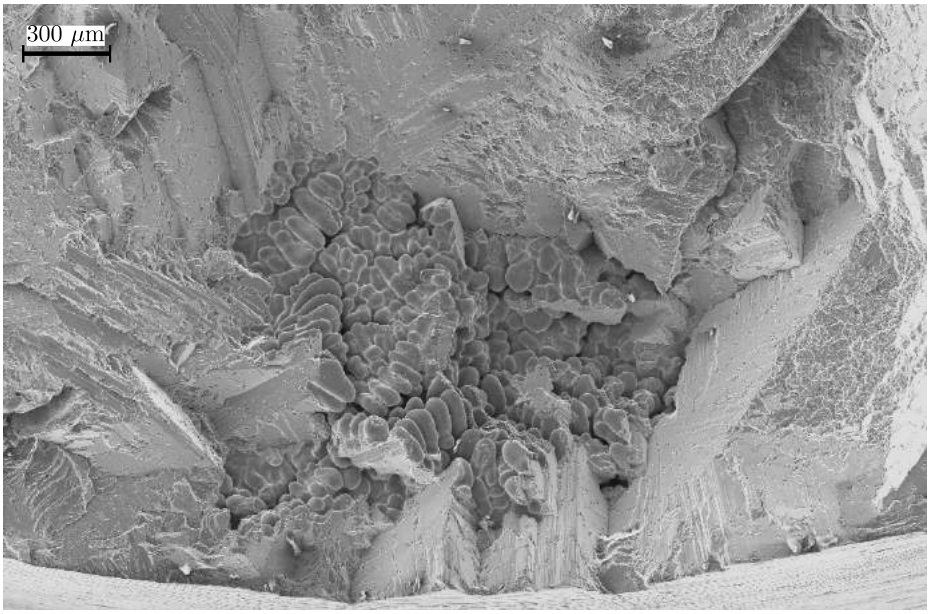

Fig. F.2: SEM enlarged view on the natural surface defect of ENSMA-SNV-02 specimen (vacuum) which nucleated and propagated the fatal crack. Only Region II propagation is observed. The fatigue testing parameters are: N_f = 574 182 cycles, σ_{max} = 178 MPa and Natural Defect $\sqrt{A}$ = 778 μm.

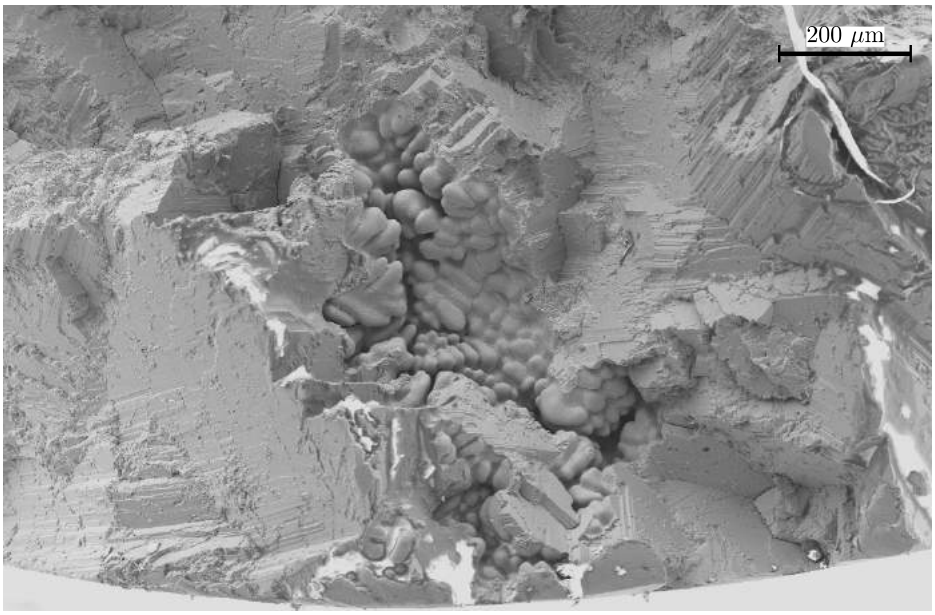

Fig. F.3: SEM enlarged view on the natural surface defect of ENSMA-SNV-05 specimen (vacuum) which nucleated and propagated the fatal crack. Only Region II propagation is observed. The fatigue testing parameters are: N_f = 667 738 cycles, σ_{max} = 168 MPa and Natural Defect $\sqrt{A}$ = 614 μm.

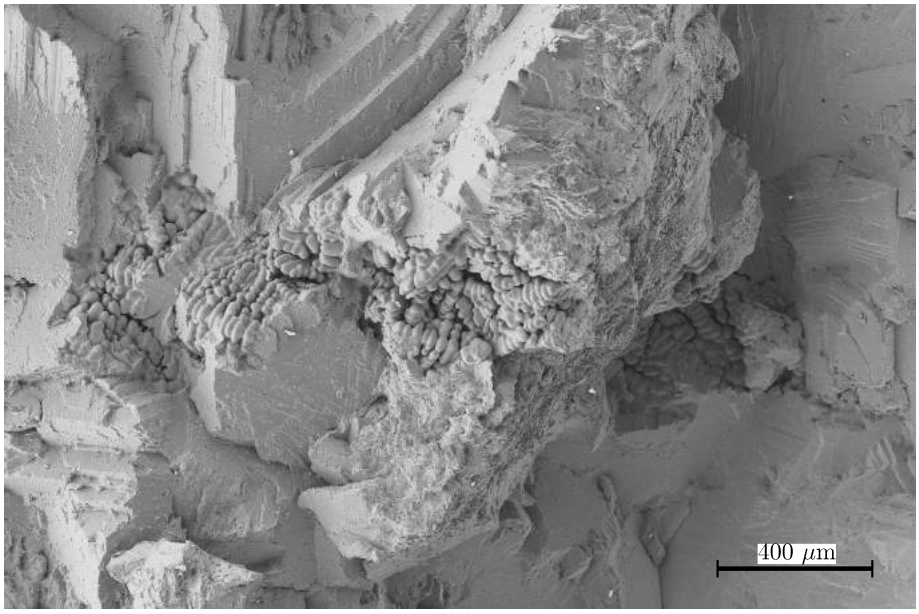

(a)

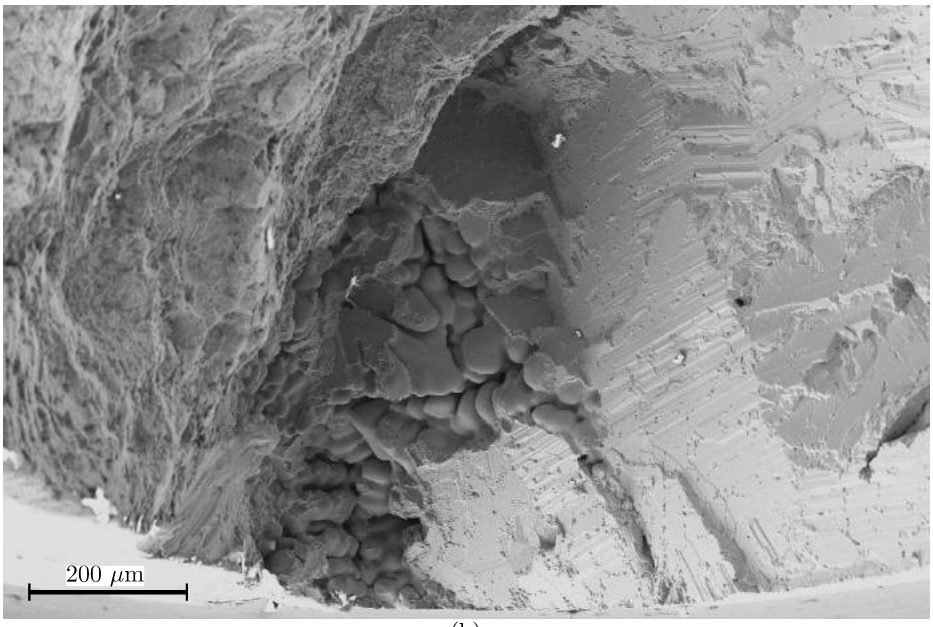

(b)

Fig. F.4: (a) SEM enlarged view on the natural internal defect of ENSMA-SNV-04 specimen (vacuum) which nucleated and propagated the fatal crack. Only Region II propagation is observed. The fatigue testing parameters are: N_f = 1 903 551 cycles, σ_{max} = 156 MPa and Natural Defect $\sqrt{A}$ = 1191 μm. (b) SEM enlarged view on a surface defect of Natural Defect $\sqrt{A}$ = 505 μm which nucleated and propagated a microcrack.

Appendix G

Linear measurement on the crack area projections of SLS-14 specimen

The methodology used to obtain linear measurement on the area projections of the cracks that nucleated at Pore 1 and Pore 3 is presented in Fig. G.1a-b. In the case of Pore 1, ten linear measures spaced at intervals of $\sim 22°$ are obtained and then averaged in each propagation interval. For Pore 3, the number of linear measures was sixteen. It must be noted that the length corresponding to the pore is systematically subtracted and that a correction of cos 45° is applied to Pore 3 results. Fig. G.1c shows the propagation curves obtained using the linear method. The averaged lengths are multiplied by two so comparison with area projection results (see § 3.3.1 in the main text) can be established. Similar propagation values are observed when comparing linear and area projection results.

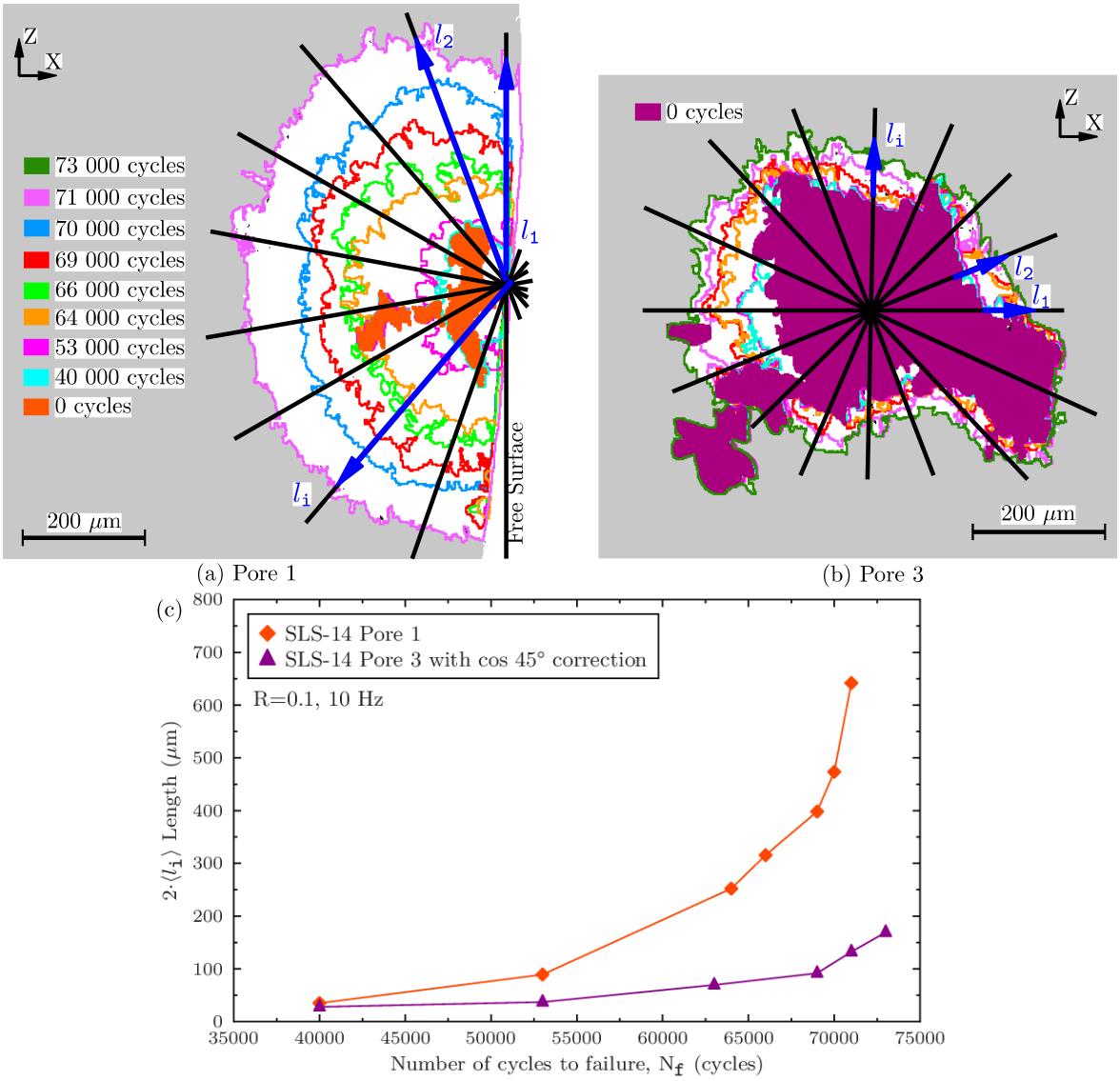

Fig. G.1: (a) Y (loading direction) projection of the main growth stages for the crack nucleated at Pore 1 (some stages were omitted for clarity). The black straight lines indicate the location of the linear traces (spaced ∼22°) performed all around the crack front. (b) Same as before but for the case of the internal Pore 3. (c) Plot of the crack propagation against the number of cycles (N_f) showing linear results of Pore 1 and Pore 3. The propagation value is the average length $2\cdot\langle l_i \rangle$ obtained for each interval.

Appendix H

Additional results on synchrotron specimens containing internal natural defects

Some additional for the case of synchrotron specimens containing internal natural defects are given in this appendix. Fig. H.1 shows the case of a synchrotron specimen that did not nucleate any internal crack while a small defect present at the free surface nucleated a microcrack. Fig. H.2 and Fig. H.3 presents the two other synchrotron specimens where internal cracks were nucleated.

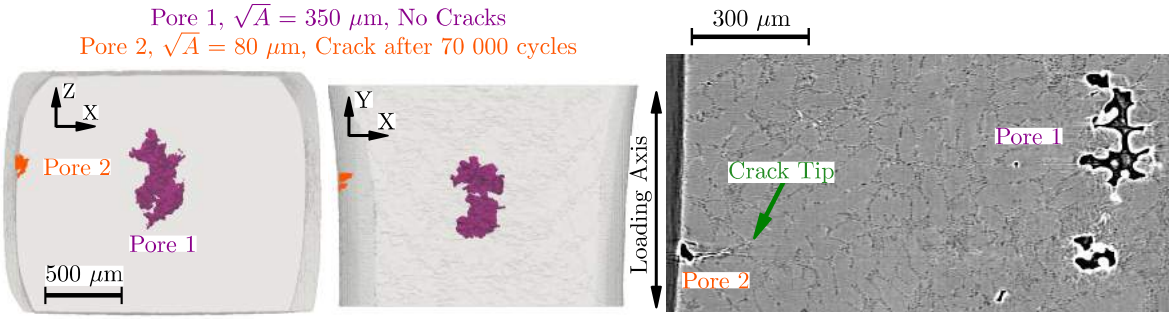

(a) (b) After 80 000 cycles

Fig. H.1: (a) Pore distribution within SLS-40 specimen gage. The fatigue testing parameters are N_f = 82 000 cycles, σ_{max} = 240 MPa (b) Tomographic image showing surface crack propagation nucleated at Pore 2. The green arrow indicates the crack tip position after 80 000 cycles.

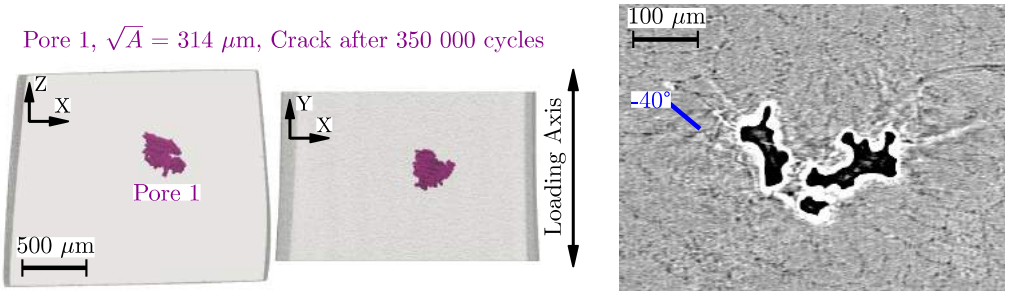

(a) (b) After 350 000 cycles

Fig. H.2: (a) Pore distribution within SLS-22 specimen gage (N_f = 355 000 cycles, σ_{max} = 200 MPa) (b) Tomographic image of Pore 1 showing a crystallographic crack formed at -40°.

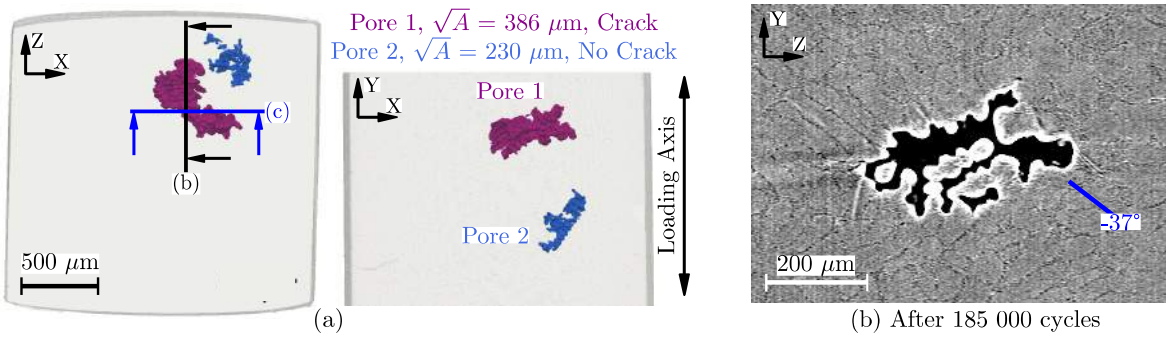

(a) (b) After 185 000 cycles

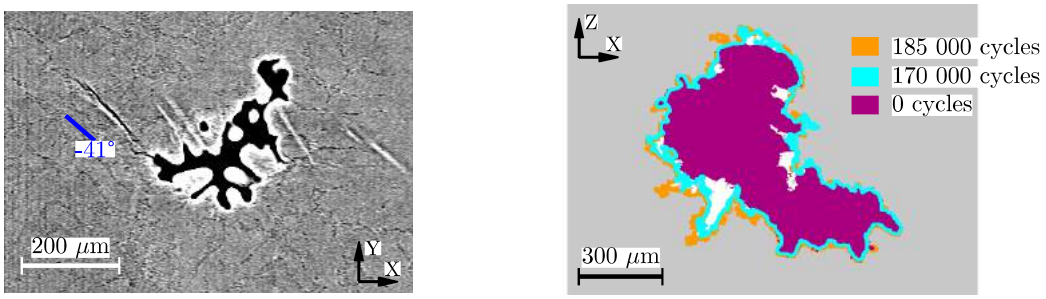

(c) After 185 000 cycles (d)

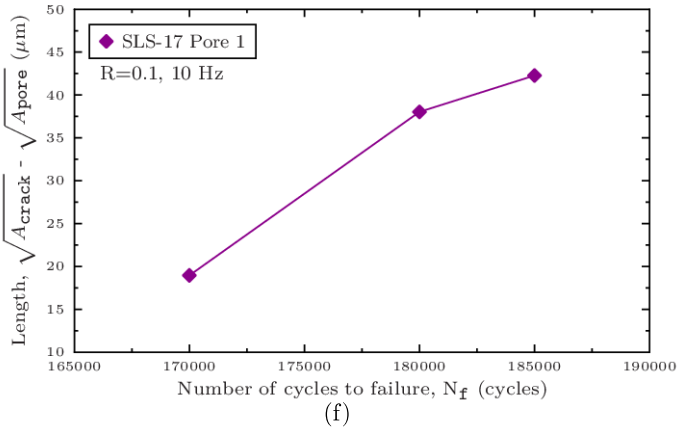

(f)

Fig. H.3: (a) Pore distribution within SLS-17 specimen gage. The straight lines indicate the approximate location of tomographic images and the fatigue testing parameters are N_f = 190 000 cycles and σ_{max} = 200 MPa (b) Tomographic slice of Pore 1 showing a crystallographic crack formed at -37°. (c) Another tomographic slice of Pore 1 showing a crystallographic crack propagating at -41°. (d) Y (loading direction) projection of the surface crack progression for all recorded spans. (f) Plot of the crack propagation ($\sqrt{A_{crack}}$ - $\sqrt{A_{pore}}$) against the number of cycles (N_f) for Pore 1.

Appendix I

Additional results on synchrotron specimens containing internal artificial defects ($\varnothing_{eq} \approx 1$ mm)

Additional results for the case of synchrotron specimens containing internal artificial defects are given in this appendix. Fig. I.1 and Fig. I.2 show the case of two synchrotron specimens that did not nucleate any internal or surface crack. Fig. I.3 is another example of a synchrotron specimen that nucleated surface cracks without nucleating any internal crack.

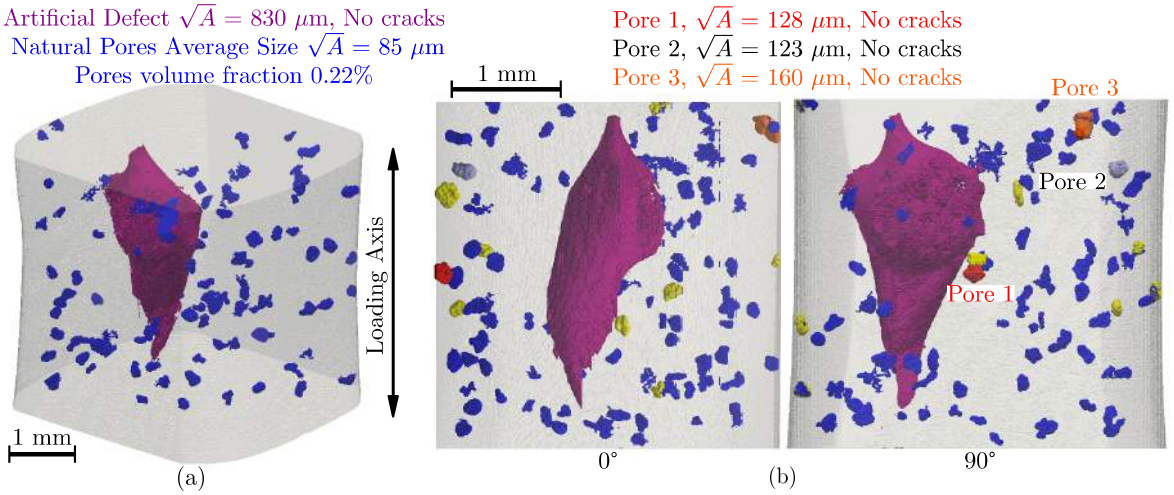

Fig. I.1: (a) Defect distribution within SLS-449 specimen gage. The fatigue testing parameters are N_f = 140 000 cycles and σ_{max} = 140 MPa. (b) 3D renderings at 0° and 90° of the artificial defect (in dark-magenta) and the parasitic pores (in blue). The $\sqrt{A}$ value for Pore 1 (in red), Pore 2 (purple) and Pore 3 (in orange) are given on the top. The pores coloured in yellow correspond to the rest (8) of surface pores which were observed.

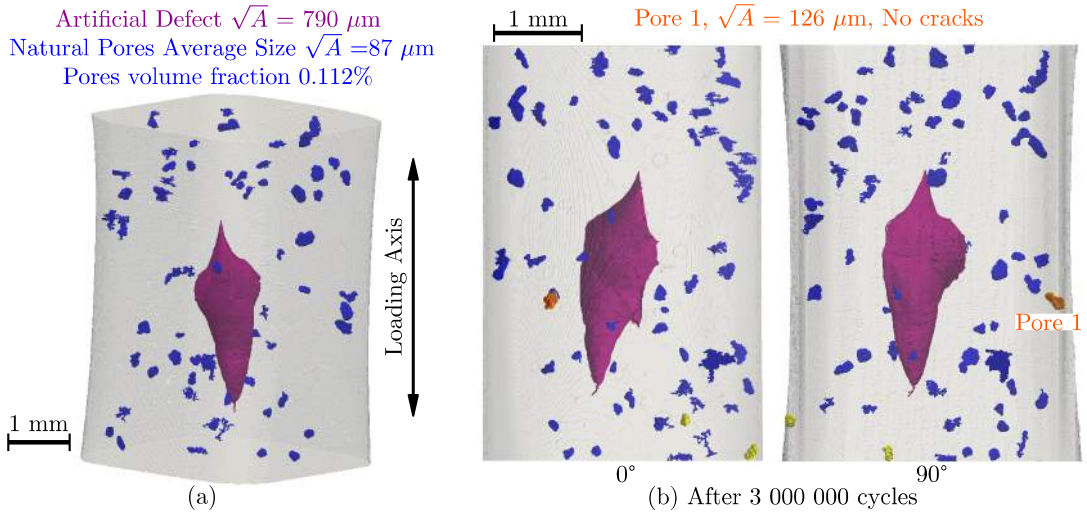

Fig. I.2: (a) Defect distribution within ESRF-641 specimen gage. The fatigue testing parameters are N_f = 3 000 000 cycles and σ_{max} = 90 MPa. (b) 3D renderings at 0° and 90° of the artificial defect (in darkmagenta) and the parasitic pores (in blue). Pore 1 (in orange) is the highest surface pore (out of three) detected in this specimen. The other two surface pores (in yellow) are smaller.

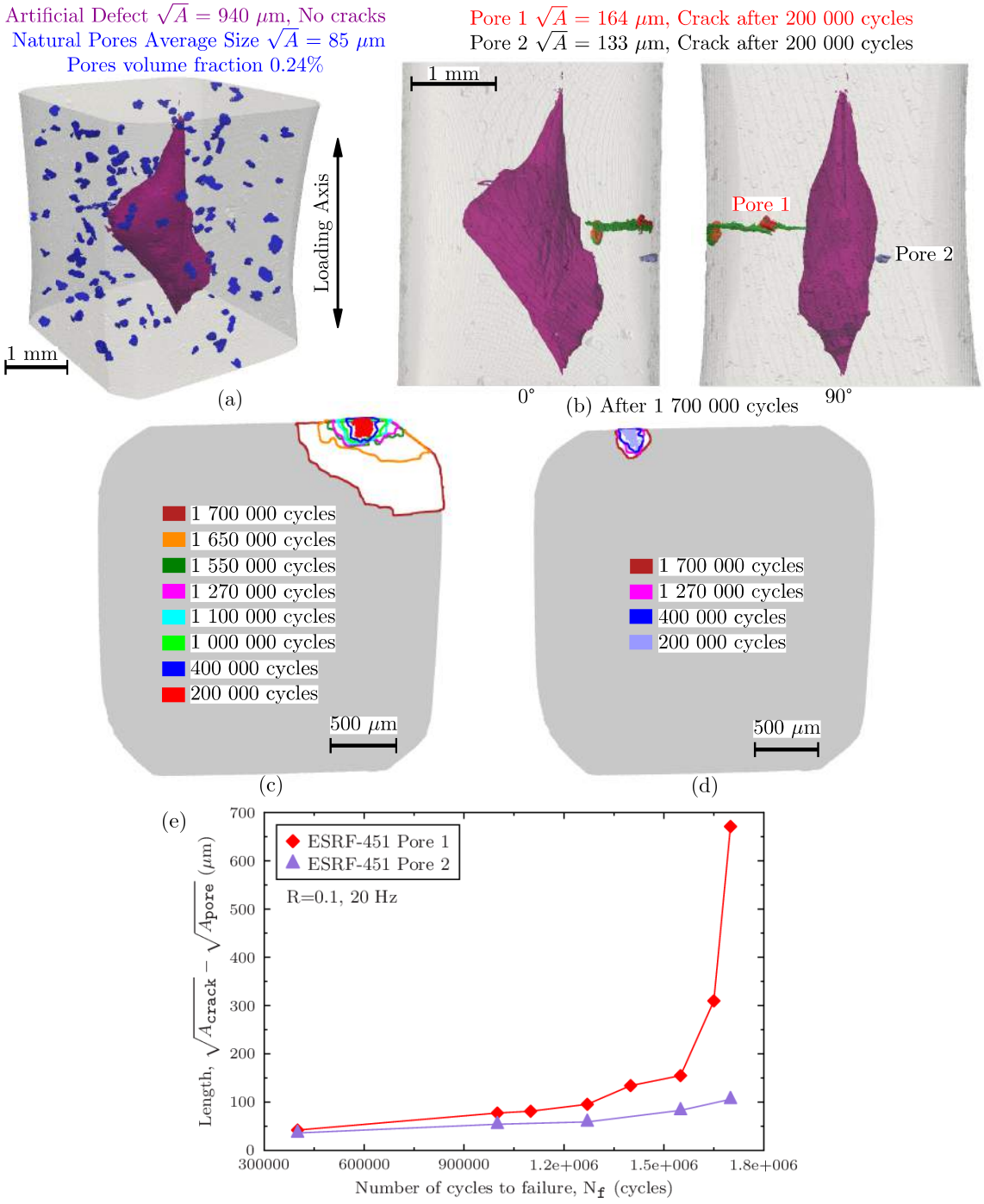

Fig. I.3: (a) Defect distribution within ESRF-451 specimen gage. The fatigue testing parameters are N_f = 1 700 000 cycles and σ_{max} = 95 MPa. (b) 3D renderings at 0° and 90° of the uncracked artificial defect and the two surface pores initiating cracks. The crack nucleating at Pore 2 was too small to be processed and it is not represented on the image. The pore presented in orange is a surface one that did not nucleated any crack but that was intersected during the propagation. (c) Y (loading direction) projection of the crack fronts nucleated at Pore 1. (d) The same as before but for Pore 2 (e) Plot of the crack propagation ($\sqrt{A_{crack}}$ - $\sqrt{A_{pore}}$) against the number of cycles (N_f) for Pore 1 and Pore 2.)

Appendix J

Additional results on FE simulations

Fig. J.1 shows a comparison between the K_t evaluations and the internal crack nucleation sites observed in SLS-14 Pore 3. The arrows indicate some of the red-blue zones obtained on the pore surface which correspond to the earliest nucleation of internal cracks. Fig. J.2 shows the same comparison but for SLS-17 Pore 1. Elasto-plastic computations are also shown in this figure.

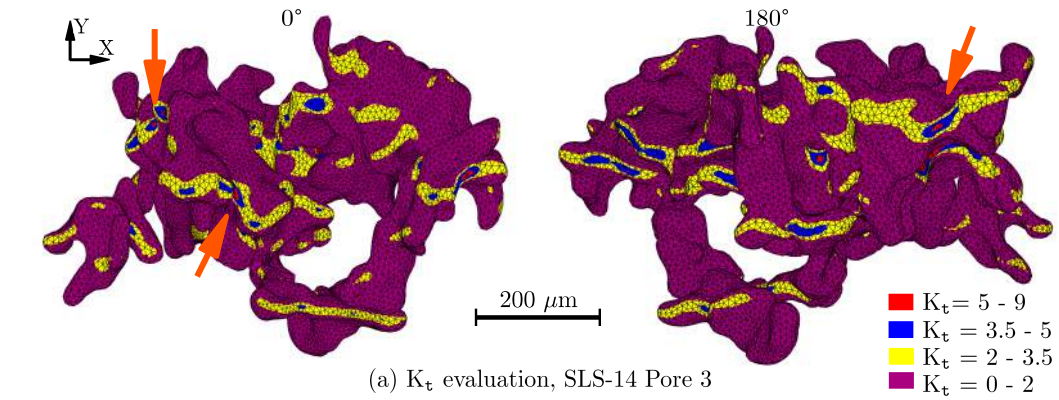

(a) K_t evaluation, SLS-14 Pore 3

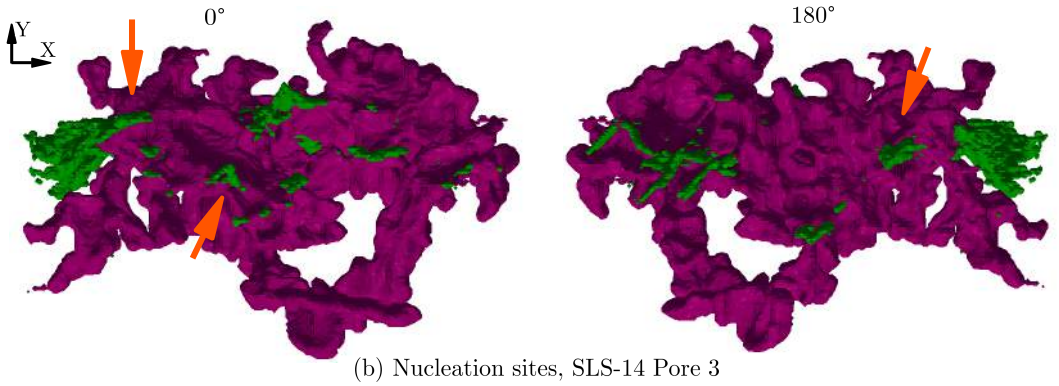

(b) Nucleation sites, SLS-14 Pore 3

Fig. J.1: (a) 3D renderings at 0° and 180° of the K_t evaluation on SLS-14 Pore 3. The fatigue testing parameters are N_f = 73 000 cycles and σ_{max} = 230 MPa. (b) 3D renderings at 0° and 180° of the crack nucleation sites (in green) after 53 000 cycles.

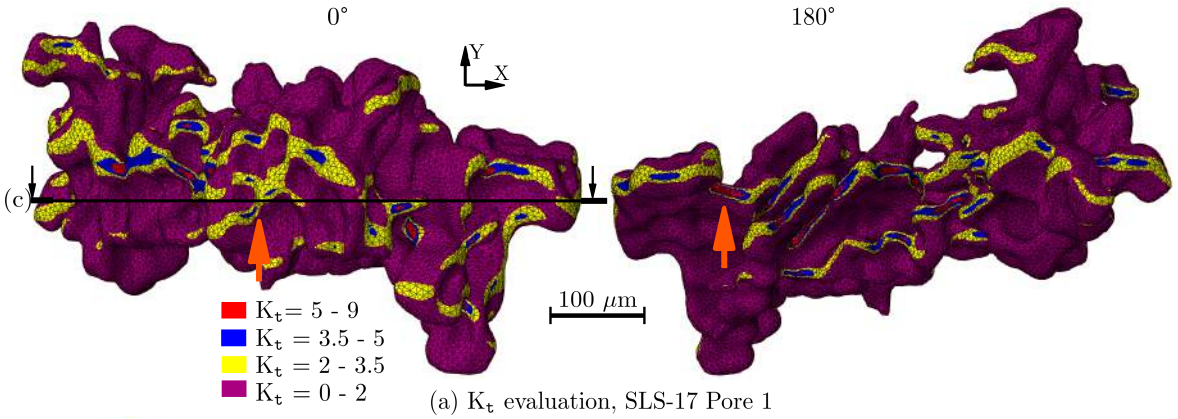

(a) K_t evaluation, SLS-17 Pore 1

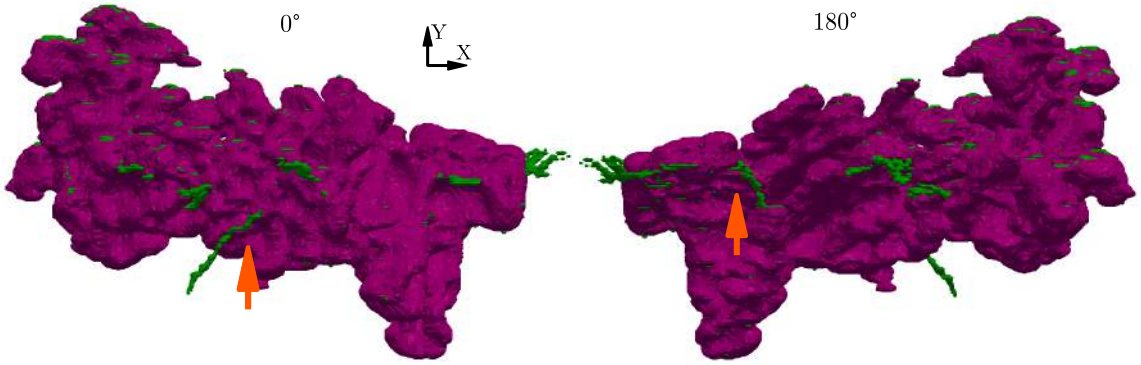

(b) Nucleation sites, SLS-17 Pore 1

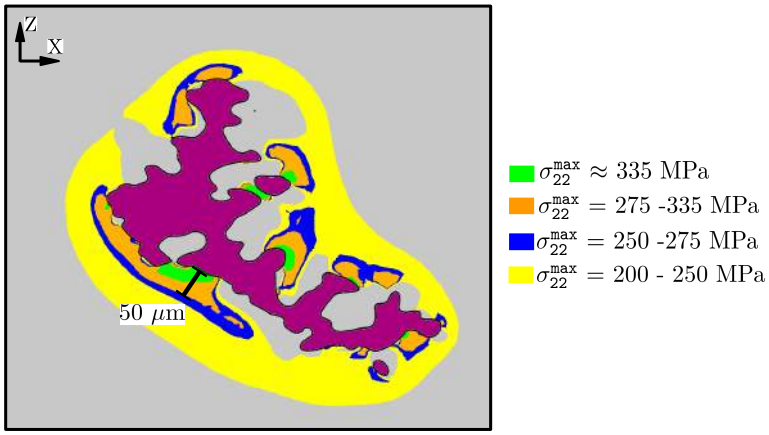

(c) Pore 1 Affected Volume

Fig. J.2: (a) 3D renderings at 0° and 180° of the K_t evaluation on SLS-17 Pore 1. The fatigue testing parameters are N_f = 190 000 cycles and σ_{max} = 200 MPa. (b) 3D renderings at 0° and 180° of the crack nucleation sites after 185 000 cycles. (c) Elasto-plastic results shown in a slice performed along a random plane (its approximate location is shown in (a)) perpendicular to the loading direction.

Finally, Fig. J.3 and Fig. J.4 show additional results on the K_t and elasto-plastic computations preformed in SLS-40 Pore 1 and SLS-22 Pore 1.

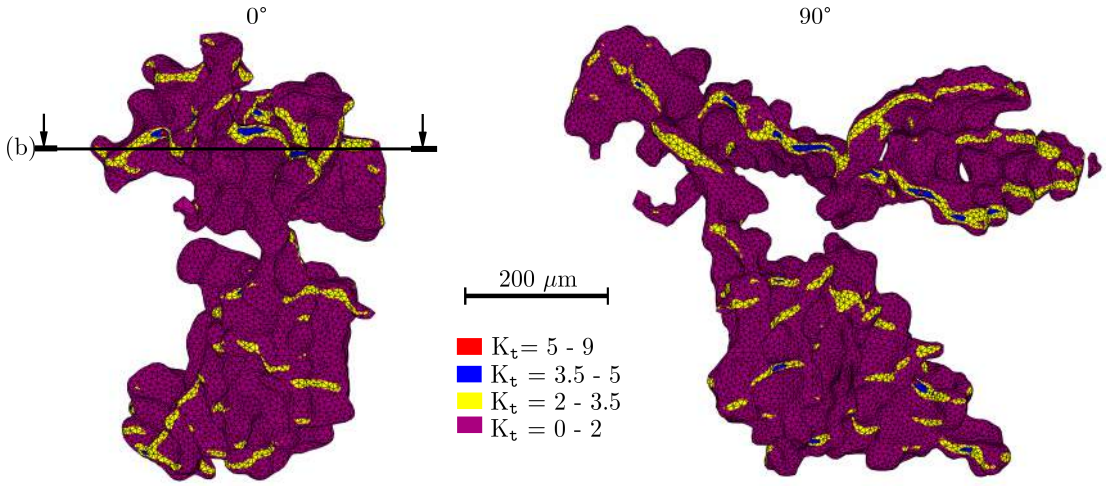

(a) K_t evaluation, SLS-40 Pore 1

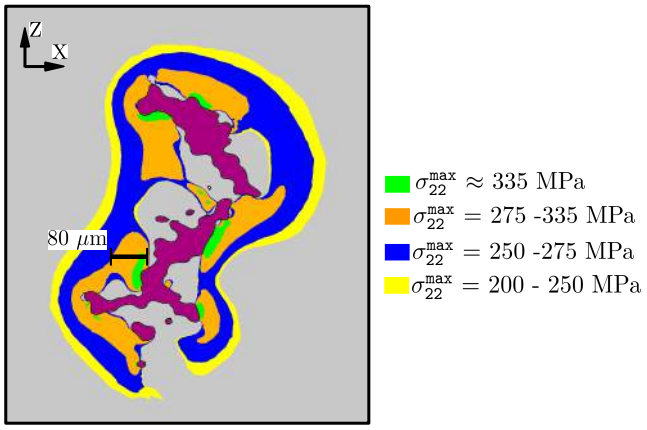

(b) Pore 1 Affected Volume

Fig. J.3: (a) 3D renderings at 0° and 180° of the K_t evaluation on SLS-40 Pore 1. The fatigue testing parameters are N_f = 82 000 cycles and σ_{max} = 240 MPa. (b) Elasto-plastic results shown in a slice performed along a random plane (its approximate location is shown in (a)) perpendicular to the loading direction.

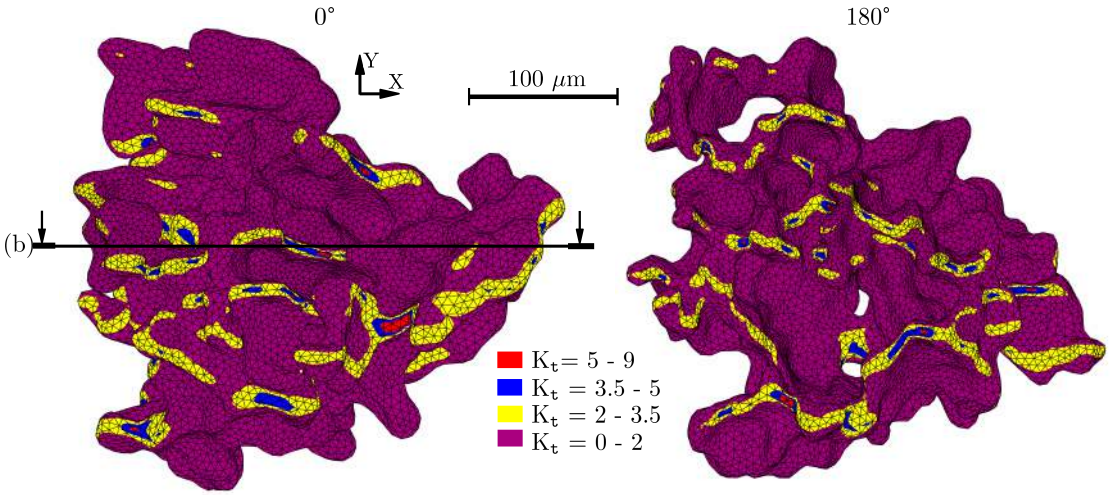

(a) K_t evaluation, SLS-22 Pore 1

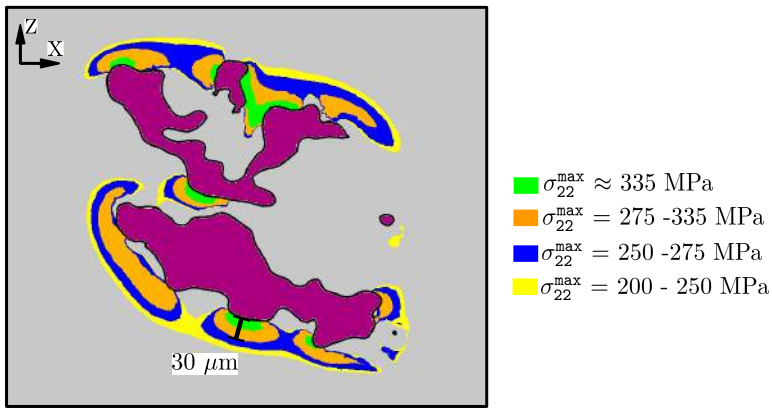

(b) Pore 1 Affected Volume

Fig. J.4: (a) 3D renderings at 0° and 180° of the K_t evaluation on SLS-22 Pore 1. The fatigue testing parameters are N_f = 82 000 cycles and σ_{max} = 240 MPa. (b) Elasto-plastic results shown in a slice performed along a random plane (its approximate location is shown in (a)) perpendicular to the loading direction.

References

[ABA 13] ABAQUS-FEA
http://www.3ds.com/products-services/simulia/overview/, 2013. 6, 121

[ALS 11] Als-Nielsen J., McMorrow D.
Elements of Modern X-ray Physics. Wiley, 2011. 6

[AMM 08] Ammar H., Samuel A., Samuel F.
Effect of casting imperfections on the fatigue life of 319-F and A356-T6 Al-Si casting alloys. *Materials Science and Engineering: A*, vol. 473, n° 1-2, 2008, p. 65-75. 39

[AND 95] Anderson T. L.
Fracture Mechanics. CRC Press, 1995. Pag. 627. 59

[ARP 07] ARP1947A
Aerospace Recommended Practice, SAE International Group, 2007. 21

[ASM 09] ASM-International
Casting design and performance. Materials Park, OH : ASM International, 2009. 18

[ATX 01] Atxaga G., Pelayo A., Irisarri A.
Effect of microstructure on fatigue behaviour of cast Al-7Si-Mg alloy. *Materials Science and Technology*, vol. 17, n° 4, 2001, p. 446-450. 39

[AVI 13] AVIZO®
http://www.vsg3d.com/, 2013. 6, 120

[BAR 57] Bartholomew R. N., Casagrande R. M.
Measuring Solids Concentration in Fluidized Systems by Gamma-Ray Absorption. *Industrial & Engineering Chemistry*, vol. 49, n° 3, 1957, p. 428-431. 5

[BEA 72] Beachem C.
A new model for hydroyen-assited cracking (hydrogen "embritlement"). *Metall Trans*, vol. 3, 1972, p. 437-451. 96

[BIR 94] Birnbaum H., Sofronis P.
Hydrogen-enhanced localized plasticity - a mechanism for hydrogen-related fracture. *Materials Science and Engineering: A*, vol. 176, n° 1-2, 1994, p. 191-202. 96

[BOR 02] Borbely A., Mughrabi H., Eisenmeier G., Hoppel H.
A finite element modelling study of strain localization in the vicinity of near-surface cavities as a cause of subsurface fatigue crack initiation. *International Journal of Fracture*, vol. 115, n° 3, 2002, p. 227-232, Kluwer Academic Publishers. 107, 119

[BRO 10] Brochu M., Verreman Y., Ajersch F., Bouchard D.
High cycle fatigue strength of permanent mold and rheocast aluminum 357 alloy. *International Journal of Fatigue*, vol. 32, n° 8, 2010, p. 1233-1242. 37, 39

[BRO 12] Brochu M., Verreman Y., Ajersch F., Bouchard D.
Propagation of short fatigue cracks in permanent and semi-solid mold 357 aluminum alloy. *International Journal of Fatigue*, vol. 36, n° 1, 2012, p. 120-129. 37, 42, 61, 62

[BUF 99] Buffiere J., Maire E., Cloetens P., Lormand G., Fougeres R.
Characterization of internal damage in a MMCp using x-ray synchrotron phase contrast microtomography. *Acta Mater*, vol. 47, n° 5, 1999, p. 1613-1625. 6

[BUF 01] Buffiere J.-Y., Savelli S., Jouneau P., Maire E., Fougeres R.
Experimental study of porosity and its relation to fatigue mechanisms of model Al-Si7-Mg0.3 cast Al alloys. *Materials Science and Engineering: A*, vol. 316, n° 1-2, 2001, p. 115-126. 19, 36, 39, 40

[BUF 06] Buffiere J. Y., Ferrie E., Proudhon H., Ludwig W.
Three-dimensional visualisation of fatigue cracks in metals using high resolution synchrotron X-ray micro-tomography. *Mat. Sc. Tech.*, vol. 22, n° 9, 2006, p. 1019-1024. 10

[BUF 08] Buffiere J.-Y., Cloetens P., Ludwig W., Maire E., Salvo L.
In Situ X-Ray Tomography Studies of Microstructural Evolution Combined with 3D Modeling. *MRS Bulletin*, vol. 33, 2008, p. 611-619. 6

[BUF 10] Buffiere J.-Y., Maire E., Adrien J., Masse J.-P., Boller E.
In Situ Experiments with X ray Tomography: an Attractive Tool for Experimental Mechanics. *Experimental Mechanics*, vol. 50, n° 3, 2010, p. 289-305, Springer US. 7, 8, 9

[BUF 14] Buffiere J.-Y., Maire E.
X-Ray Tomography in Material Science. Hermes Science, 2014. 6, 7, 10

[CAM 00] Campbell J., Ritchie R.
Mixed-mode, high-cycle fatigue-crack growth thresholds in Ti-6Al-4V - I. A comparison of large-crack and short-crack behavior. *Engineering Fracture Mechanics*, vol. 67, n° 3, 2000, p. 209-227. 34

[CAM 06] Campbell J.
An overview of the effects of bifilms on the structure and properties of cast alloys. *Metallurgical and Materials Transactions B*, vol. 37, n° 6, 2006, p. 857-863, Springer-Verlag. 19

[CAR 84] Carter R., Lee E., Starke E., Beevers C.
The effect of microstructure and environment on fatigue crack closure of 7475 aluminum alloy. *Metallurgical Transactions A*, vol. 15, 1984, p. 555-563, Springer-Verlag. 95, 96, 98

[CAT 03] Caton M., Jones J., Mayer H., Stanzl-Tschegg S., Allison J.
Demonstration of an endurance limit in cast 319 aluminum. *Metallurgical and Materials Transactions A*, vol. 34, n° 1, 2003, p. 33-41, Springer-Verlag. 94

[CHA 03] Chan K. S., Jones P., Wang Q.
Fatigue crack growth and fracture paths in sand cast B319 and A356 aluminum alloys. *Materials Science and Engineering: A*, vol. 341, n° 1-2, 2003, p. 18-34. 37

[CHA 10] Chandran K. R., Chang P., Cashman G.
Competing failure modes and complex S-N curves in fatigue of structural materials. *International Journal of Fatigue*, vol. 32, n° 3, 2010, p. 482-491. Symposium on Competing Failure Modes and Variability in Fatigue. 94

[CLO 97] Cloetens P., Pateyron-Salome M., Buffiere J.-Y., Peix G., Baruchel J., Peyrin F., Schlenker M.
Observation of microstructure and damage in materials by phase sensitive radiography and tomography. *Journal of Applied Physics*, vol. 81, n° 9, 1997, p. 5878-5886. 10

[CLO 99] Cloetens P., Ludwig W., Baruchel J., Van Dyck D., Van Landuyt J., Guigay J. P., Schlenker M.
Holotomography: Quantitative phase tomography with micrometer resolution using hard synchrotron radiation x rays. *Applied Physics Letters*, vol. 75, n° 19, 1999, p. 2912-2914. 9

[COM 10] Committee A. I. H., Ed. *ASM Handbook, Volume 02 - Properties and Selection: Nonferrous Alloys and Special-Purpose Materials*. 2010. 20

[COU 90] Couper M. J., Neeson A. E., Griffiths J. R.
Casting defects and the fatigue behaviour of an aluminium casting alloy. *Fatigue & Fracture of Engineering Materials & Structures*, vol. 13, n° 3, 1990, p. 213-227, Blackwell Publishing Ltd. 39

[CTI 13] CTIF
http://www.ctif.com/version-anglaise/, 2013. 12

[DAV 06] Davis G. R., Elliott J. C.
Artefacts in X-ray microtomography of materials. *Materials Science and Technology*, vol. 22, Number 9, 2006, p. 1011-1018(8). 7

[ENS 13] ENSMA
http://www.ensma.fr/, 2013. 13

[ESR 13] ESRF
http://www.esrf.eu/UsersAndScience/Experiments/Imaging/ID19, Accessed 2013. 9, 10

[FAN 89] Fang Q., Granger D.
Porosity Formation in Modified and Unmodified A356 Alloy Castings. *AFS Transactions*, vol. 97, 1989, p. 989-1000. 19

[FAN 01] Fan J., McDowell D., Horstemeyer M., Gall K.
Computational micromechanics analysis of cyclic crack-tip behavior for micro structurally small cracks in dual-phase Al-Si alloys. *Engeineering Fracture Mechanics*, vol. 68, 2001, p. 1687-1706. 36

[FER 05] Ferrie E., Buffiere J.-Y., Ludwig W.
3D characterisation of the nucleation of a short fatigue crack at a pore in a cast Al alloy using high resolution synchrotron microtomography. *International Journal of Fatigue*, vol. 27, n° 10-12, 2005, p. 1215-1220. 39, 40, 62

[GAL 99] Gall K., Yang N., Horstemeyer M., McDowell D. L., Fan J.
The debonding and fracture of Si particles during the fatigue of a cast Al-Si alloy. *Metallurgical and Materials Transactions A*, vol. 30, 1999, p. 3079-3088, Springer-Verlag. 36, 37, 38, 60

[GAL 00] Gall, Yang, Horstemeyer, McDowell, Fan
The influence of modified intermetallics and Si particles on fatigue crack paths in a cast A356 Al alloy. *Fatigue & Fracture of Engineering Materials & Structures*, vol. 23, n° 2, 2000, p. 159–172, Blackwell Science Ltd. 37

[GAO 04] GAO Y. X., YI J. Z., LEE P. D., LINDLEY T. C.
The effect of porosity on the fatigue life of cast aluminium-silicon alloys. *Fatigue & Fracture of Engineering Materials & Structures*, vol. 27, n° 7, 2004, p. 559-570, Blackwell Publishing Ltd. 39, 119

[GAS 05] Gasqueres C., Sarrazin-Baudoux C., Petit J., Dumont D.
Fatigue crack propagation in an aluminium alloy at 223K. *Scripta Materialia*, vol. 53, n° 12, 2005, p. 1333-1337. 98

[GRE 94] Green N., Campbell J.
The influence of oxide film filling defects on the strength of Al-Si 7-Mg Alloy Castings. *AFS Trans.*, vol. 102, 1994, Page 341. 18

[HEN 95] Henaff G., Marchal K., Petit J.
On fatigue crack propagation enhancement by a gaseous atmosphere: Experimental and theoretical aspects. *Acta Metallurgica et Materialia*, vol. 43, n° 8, 1995, p. 2931-2942. 96

[HEN 96] Henaff G., Petit J.
A logical framework for the analysis of enhancement of fatigue crack propagation by the ambient atmosphere. *Materials Science*, vol. 32, n° 2, 1996, p. 190-209, Kluwer Academic Publishers-Plenum Publishers. 96

[HKL 01] HKL-Technology
HKL Channel 5 Users Manual. Danbury, CT (USA), 2001. 24

[HOL 03] Holper B., Mayer H., Vasudevan A., Stanzl-Tschegg S.
Near threshold fatigue crack growth in aluminium alloys at low and ultrasonic frequency: Influences of specimen thickness, strain rate, slip behaviour and air humidity. *International Journal of Fatigue*, vol. 25, n° 5, 2003, p. 397-411. 98

[HOL 04] Holper B., Mayer H., Vasudevan A., Stanzl-Tschegg S.
Near threshold fatigue crack growth at positive load ratio in aluminium alloys at low and ultrasonic frequency: influences of strain rate, slip behaviour and air humidity. *International Journal of Fatigue*, vol. 26, n° 1, 2004, p. 27-38. 98

[HOS 93] Hosford W. F.
The Mechanics of Crystals and Textured Plycrystals. Oxford Science Publications, 1993. 43

[HOU 73] Hounsfield G.
Computerised transverse axial scanning (tomography): Part 1. Description of system. *BJR*, vol. 46, 1973, p. 1016-1022. 5

[HUR 82] Hurd N. J., Irving P. E.
Factors influencing propagation of mode III fatigue cracks under torsional loading. Abelkis P., Hudson C., Eds., *Desing of Fatige and Fracture Resistant Structures, ASTM STP 761*, p. 212-233 ASTM STP 761, 1982. 64

[ISO 11] ISO-1352-2011
Metallic Materials – Torque-controlled fatigue testing. International Standard, 2011. 14

[JAN 10] Jana S., Mishra R., Baumann J., Grant G.
Effect of friction stir processing on fatigue behavior of an investment cast Al-7Si-0.6 Mg alloy. *Acta Materialia*, vol. 58, n° 3, 2010, p. 989-1003. 36, 37, 39

[JIA 99] Jiang H., Bowen P., Knott J.
Fatigue performance of a cast aluminium alloy Al-7Si-Mg with surface defects. *Journal of Materials Science*, vol. 34, n° 4, 1999, p. 719-725, Kluwer Academic Publishers. 39

[KOU 13] Koutiri I., Bellett D., Morel F., Augustins L., Adrien J.
High cycle fatigue damage mechanisms in cast aluminium subject to complex loads. *International Journal of Fatigue*, vol. 47, n° 0, 2013, p. 44-57. 67, 68

[KRU 13] Krupp U., Giertler A., Siegfanz S., Michels W.
On the Micromechanisms of Fatigue Crack Propagation in Aluminum Cast Alloys. *Key Engineering Materials*, vol. 592, 2013, p. 393-396. 17, 36

[KUM 10] Kumar A., Torbet C. J., Pollock T. M., Jones J. W.
In situ characterization of fatigue damage evolution in a cast Al alloy via nonlinear ultrasonic measurements. *Acta Materialia*, vol. 58, n° 6, 2010, p. 2143-2154. 39

[LAC 12] Lachambre J., Weck A., Rethore J., Buffiere J.-Y., Adrien J.
3D analysis of a fatigue crack in cast iron using Digital Volume Correlation of X-ray tomographic images. *2012 SEM XII International Congress and Exposition on Experimental and Applied Mechanics*, Costa Mesa, CA USA, 2012. 12, 13

[LAD 04] Lados D. A., Apelian D.
Fatigue crack growth characteristics in cast Al-Si-Mg alloys: Part I. Effect of processing conditions and microstructure. *Materials Science and Engineering: A*, vol. 385, n° 1-2, 2004, p. 200-211. 36, 37

[LAD 06] Lados D. A., Apelian D., Donald J. K.
Fatigue crack growth mechanisms at the microstructure scale in Al-Si-Mg cast alloys: Mechanisms in the near-threshold regime. *Acta Materialia*, vol. 54, n° 6, 2006, p. 1475-1486. 36, 37, 38

[LAD 07] Lados D. A., Apelian D., Jones P. E., Major J. F.
Microstructural mechanisms controlling fatigue crack growth in Al-Si-Mg cast alloys. *Materials Science and Engineering: A*, vol. 468-470, n° 0, 2007, p. 237-245. 38

[LAN 82] Lankford J.
The growth of small fatigue cracks in 7075-T6 aluminium. *Fatigue & Fracture of Engineering Materials & Structures*, vol. 5, n° 3, 1982, p. 233-248, Blackwell Publishing Ltd. 36

[LEE 95] Lee F. T., Major J. F., Samuel F. H.
Effect of silicon particles on the fatigue crack growth characteristics of Al-12 Wt Pct Si-0.35 Wt Pct Mg-(0 to 0.02) Wt Pct Sr casting alloys. *Metallurgical and Materials Transactions A*, vol. 26, 1995, p. 1553-1570. 37

[LI 06] Li Y., Brusethaug S., Olsen A.
Influence of Cu on the mechanical properties and precipitation behavior of AlSi7Mg0.5 alloy during aging treatment. *Scripta Materialia*, vol. 54, n° 1, 2006, p. 99-103. 17

[LI 09] Li P., Lee P., Maijer D., Lindley T.
Quantification of the interaction within defect populations on fatigue behavior in an aluminum alloy. *Acta Materialia*, vol. 57, n° 12, 2009, p. 3539-3548. 119

[LUD 03] Ludwig W., Buffiere J., Savelli S., Cloetens P.
Study of the interaction of a short fatigue crack with grain boundaries in a cast Al alloy using X-ray microtomography. *Acta Mater*, vol. 51, n° 3, 2003, p. 585-598. 36, 37

[LYN 88] Lynch S.
Environmentally assisted cracking: Overview of evidence for an adsorption-induced localised-slip process. *Acta Metallurgica*, vol. 36, n° 10, 1988, p. 2639-2661. 96

[MAJ 97] Major J.
Porosity control and fatigue behaviour in A356-T61 aluminum alloy. *AFS Trans*, vol. 105, 1997, p. 901-906. 19

[MAR 10] Marchandise E., Compère G., Willemet M., Bricteux G., Geuzaine C., Remacle J.-F.
Quality meshing based on STL triangulations for biomedical simulations. *International Journal for Numerical Methods in Biomedical Engineering*, vol. 26, n° 7, 2010, p. 876-889, John Wiley & Sons, Ltd. 121

[MAY 03] Mayer H., Papakyriacou M., Zettl B., Stanzl-Tschegg S.
Influence of porosity on the fatigue limit of die cast magnesium and aluminium alloys. *International Journal of Fatigue*, vol. 25, n° 3, 2003, p. 245-256. 94

[MCD 03] McDowell D., Gall K., Horstemeyer M., Fan J.
Microstructure-based fatigue modeling of cast A356-T6 alloy. *Engineering Fracture Mechanics*, vol. 70, n° 1, 2003, p. 49-80. 18, 19, 40

[MEY 68] Meyn D.
Observation of micromechanisms of fatigue crack propagagation in 2024 aluminium. *Transactions of ASME*, vol. 61, 1968, p. 42-51. 94

[MIL 82] Miller K. J.
The short crack problem. *Fatigue of Engineering Materials and Structures*, vol. 5, 1982, p. 223-232. 34

[MIL 93] Miller K. J.
Materials science perspective of metal fatigue resistance. *Materials Science and Technology*, vol. 9, n° 6, 1993, p. 453-462. 35, 41

[MU 14] Mu P., Nadot Y., Nadot-Martin C., Chabod A., Serrano-Munoz I., Verdu C.
Influence of casting defects on the fatigue behavior of cast aluminum AS7G06-T6. *International Journal of Fatigue*, vol. 63, n° 0, 2014, p. 97-109. 42

[MUG 02] Mughrabi H.
On 'multi-stage' fatigue life diagrams and the relevant life-controlling mechanisms in ultrahigh-cycle fatigue. *Fatigue & Fracture of Engineering Materials & Structures*, vol. 25, n° 8-9, 2002, p. 755-764, Blackwell Science Ltd. 94

[MUR 85] Murakami Y.
Analysis of stress intensity factors of modes I, II and III for inclined surface cracks of arbitrary shape. *Engineering Fracture Mechanics*, vol. 22, n° 1, 1985, p. 101-114. 133

[MUR 98] Murakami Y., Takada M., Toriyama T.
Super-long life tension-compression fatigue properties of quenched and tempered 0.46% carbon steel. *International Journal of Fatigue*, vol. 20, n° 9, 1998, p. 661-667. 94

[MUR 00] Murakami Y. Nomoto T., Ueda T., Murakami Y.
On the mechanism of fatigue failure in the superlong life regime ($N>10^7$ cycles). Part 1: influence of hydrogen trapped by inclusions. *Fatigue & Fracture of Engineering Materials & Structures*, vol. 23, n° 11, 2000, p. 893-902, Blackwell Science Ltd. 94

[MUR 02a] Murakami Y.
Chapter 14 - Torsional Fatigue. Murakami Y., Ed., *Metal Fatigue*, p. 247 - 271 Elsevier Science Ltd, Oxford, 2002. 66

[MUR 02b] Murakami Y.
Metal Fatigue: Effects of Small Defects and Nonmetallic Inclusions. Referex Engineering Elsevier, 2002. 65, 118

[MUR 03] Murakami Y., Takahashi K., Kusumoto R.
Threshold and growth mechanism of fatigue cracks under mode II and III loadings. *Fatigue & Fracture of Engineering Materials & Structures*, vol. 26, n° 6, 2003, p. 523-531, Blackwell Science, Ltd. 67

[NAD 06] Nadot Y., Billaudeau T.
Multiaxial fatigue limit criterion for defective materials. *Engineering Fracture Mechanics*, vol. 73, n° 1, 2006, p. 112-133. 119

[NAY 01] Nayhumwa C., Green N., Campbell J.
Influence of casting technique and hot isostatic pressing on the fatigue of an Al-7Si-Mg alloy. *Metallurgical and Materials Transactions A*, vol. 32, n° 2, 2001, p. 349-358, Springer-Verlag. 18

[NEW 81] Newman Jr. J., Raju I.
An empirical stress-intensity factor equation for the surface crack. *Engineering Fracture Mechanics*, vol. 15, 1981, p. 185-192. 60

[NFE 09] NF-EN-ISO-6892-1
Matériaux métalliques - Essai de traction - Partie 1 : méthode d'essai à température ambiante, October, 2009. 20

[NIC 10] Nicoletto G., Anzelotti G., Konecna R.
X-ray computed tomography vs. metallography for pore sizing and fatigue of cast Al-alloys. *Procedia Engineering*, vol. 2, n° 1, 2010, p. 547-554. 120

[NIS 99] Nishijima, Kanazawa
Stepwise S-N curve and fish-eye failure in gigacycle fatigue. *Fatigue & Fracture of Engineering Materials & Structures*, vol. 22, n° 7, 1999, p. 601-607, Blackwell Science Ltd. 94

[NOG 01] Noguchi H., Yoshida T., Smith R.
An Analysis of a Quarter-Infinite Solid with a Corner Crack of Arbitrary Shape. *International Journal of Fracture*, vol. 112, n° 2, 2001, p. 163-181, Kluwer Academic Publishers. 133

[ODE 94] Odegård J., Pedersen K.
Fatigue Properties of an A356 (AlSi7Mg) Aluminium Alloy for Automotive Applications - Fatigue Life Prediction. *SAE International*, , 1994. Technical Paper 940811. 39

[PAD 87] Padkin A. J., Brereton M. F., Plumbridge W. J.
Fatigue crack growth in two-phase alloys. *Materials Science and Technology*, vol. 3, n° 3, 1987, p. 217-223. 36

[PEL 69] Pelloux R.
Mechanisms of formation of ductile fatigue striations. *Transactions of ASME*, vol. 62, 1969, p. 281-285. 94

[PET 91] Petit J., Hénaff G.
Stage II intrinsic fatigue crack propagation. *Scripta Metallurgica et Materialia*, vol. 25, n° 12, 1991, p. 2683-2687. 95

[PET 99] Petit J.
Influence of environment on small fatigue crack growth. K.S. Ravichandran R. R., Murakami Y., Eds., *Small Fatigue Cracks: Mechanics, Mechanisms and Apllications*, p. 167-178 Eselvier Ltd., 1999. 95

[PET 00] Petit J., G. H., Sarrazin-Baudoux C.
Mechanisms and Modeling og Near-Threshold Fatigue Crack Propagation. Newman J. C., Piascik R. S., Eds., *Fatigue Crack Growth Thresholds, Endurance Limits and Design*, p. 3-30 ASTM STP 1372, 2000. 95

[PET 06] Petit J., Sarrazin-Baudoux C.
An overview on the influence of the atmosphere environment on ultra-high-cycle fatigue and ultra-slow fatigue crack propagation. *International Journal of Fatigue*, vol. 28, n° 11, 2006, p. 1471-1478. Third International Conference on Very High Cycle Fatigue (VHCF-3). 95, 96, 97

[PET 10] Petit J., Sarrazin-Baudoux C.
Some critical aspects of low rate fatigue crack propagation in metallic materials. *International Journal of Fatigue*, vol. 32, n° 6, 2010, p. 962-970. Selected Papers of the 17th European Conference of Fracture (ECF 17). 95, 96

[PHI 98] Philibert J., Vignes A., Bréchet Y., Combrade P.
Géneralités sur la déformation plastique. Masson, Ed., *Métallurgie, du minerai au matériau*, vol. 4, Appendix 1, p. 743-754 Masson, 1998. 123

[PLU 86] Plumtree A., Schaefer S.
Initation and Short Crack Behaviour in Aluminium Alloy Castings. Miller K., de los Rios E., Eds., *The behaviour of Short Fatigue Cracks* Mechanical Engineering Publications, London, 1986, p. 215-227. 36

[POL 05] Polmear I.
Light alloys: From Traditional Alloys to Nanocrystals. Metallurgy & Materials Science J. Wiley & Sons, 2005. 15, 17

[RIC 10] Richard S., Gasqueres C., Sarrazin-Baudoux C., Petit J.
Coupled influence of microstructure and atmosphere environment on fatigue crack path in new generation Al alloys. *Engineering Fracture Mechanics*, vol. 77, n° 11, 2010, p. 1941-1952. International Conference on Crack Paths 2009. 97, 98

[ROY 11] Roy M., Nadot Y., Nadot-Martin C., Bardin P.-G., Maijer D.
Multiaxial Kitagawa analysis of A356-T6. *International Journal of Fatigue*, vol. 33, n° 6, 2011, p. 823-832. 39, 68, 138

[ROY 12] Roy M., Nadot Y., Maijer D. M., Benoit G.
Multiaxial fatigue behaviour of A356-T6. *Fatigue & Fracture of Engineering Materials & Structures*, vol. 35, n° 12, 2012, p. 1148–1159, Blackwell Publishing Ltd. 68, 69

[SCH 09a] Schijve J.
Fatigue of Structures and Materials. Springer, 2009. xix, xxiii, 64, 65, 89

[SCH 09b] Schwartz A. J., Kumar M., Adams B. L., Field D. P.
Electron Backscatter Diffraction in Materials Science. Springer, 2009. 22

[SCH 12] Schneider C. A., Rasband W. S., Eliceiri K. W.
NIH Image to ImageJ: 25 years of image analysis. *Nature Methods*, vol. 9, 2012, p. 671-675. 7

[SHI 97] Shiozawa K., Tohda Y., Sun S.-M.
Crack inititation and small fatigue crack growth behaviour of squeeze-cast Al-Si aluminium alloys. *Fatigue & Fracture of Engineering Materials & Structures*, vol. 20, n° 2, 1997, p. 237–247, Blackwell Publishing Ltd. 36, 65

[SMI 97] Smith S. W.
The Scientist and Engineer's Guide to Digital Signal Processing. California Technical Publishing, 1997. 7

[SOC 93] Socie D.
Critical plane approaches for multiaxial fatigue damage assessment, Advances in Multiaxial Fatigue. D.L. McDowell and R. Ellis. ASTM STP 1191, 1993. 65

[STA 91] Stanzl S. E., Mayer H. R., Tschegg E. K.
The influence of air humidity on near-threshold fatigue crack growth of 2024-T3 aluminum alloy. *Materials Science and Engineering: A*, vol. 147, n° 1, 1991, p. 45-54. 97, 98

[STA 95] Stanzl-Tschegg S., Mayer H., Beste A., Kroll S.
Fatigue and fatigue crack propagation in AlSi7Mg cast alloys under in-service loading conditions. *International Journal of Fatigue*, vol. 17, n° 2, 1995, p. 149-155. 37, 94

[STA 01] Stanzl-Tschegg S., Mayer H.
Fatigue and fatigue crack growth of aluminium alloys at very high numbers of cycles. *International Journal of Fatigue*, vol. 23, Supplement 1, n° 0, 2001, p. 231-237. 97, 98

[STA 06] Stanzl-Tschegg S.
Fatigue crack growth and thresholds at ultrasonic frequencies. *International Journal of Fatigue*, vol. 28, n° 11, 2006, p. 1456-1464. Third International Conference on Very High Cycle Fatigue (VHCF). 98

[SUS 08] Susmel L.
The theory of critical distances: a review of its applications in fatigue. *Engineering Fracture Mechanics*, vol. 75, n° 7, 2008, p. 1706-1724. 119

[TAY 12] Taylor J. A.
Iron-Containing Intermetallic Phases in Al-Si Based Casting Alloys. *Procedia Materials Science*, vol. 1, n° 0, 2012, p. 19-33. 11th International Congress on Metallurgy & Materials SAM/CONAMET 2011. 16

[TSC 82] Tschegg E.
A contribution to mode III fatigue crack propagation. *Materials Science and Engineering*, vol. 54, n° 1, 1982, p. 127-136. 65, 66

[TSC 83] Tschegg E.
Mode III and Mode I fatigue crack propagation behaviour under torsional loading. *Journal of Materials Science*, vol. 18, n° 6, 1983, p. 1604-1614, Kluwer Academic Publishers. 66, 89

[TSC 85] Tschegg E.
Fatigue crack growth in high and low strength steel under torsional loading. *Theoretical and Applied Fracture Mechanics*, vol. 3, n° 2, 1985, p. 157-178. 66, 67

[VAN 11] Vanderesse N., Maire E., Chabod A., Buffiere J.-Y.
Microtomographic study and finite element analysis of the porosity harmfulness in a cast aluminium alloy. *International Journal of Fatigue*, vol. 33, n° 12, 2011, p. 1514-1525. 120

[WAN 01a] Wang Q., Apelian D., Lados D.
Fatigue behavior of A356/357 aluminum cast alloys. Part II. Effect of microstructural constituents. *Journal of Light Metals*, vol. 1, n° 1, 2001, p. 85-97. 36

[WAN 01b] Wang Q., Apelian D., Lados D.
Fatigue behavior of A356-T6 aluminum cast alloys. Part I. Effect of casting defects. *Journal of Light Metals*, vol. 1, n° 1, 2001, p. 73-84. 39

[WAN 06] Wang Q., Crepeau P., Davidson C., Griffiths J.
Oxide films, pores and the fatigue lives of cast aluminum alloys. *Metallurgical and Materials Transactions B*, vol. 37, 2006, p. 887-895, Springer Boston. 19

[WEI 81] Wei R., Simmons G.
Recent progress in understanding environment assisted fatigue crack growth. *International Journal of Fracture*, vol. 17, n° 2, 1981, p. 235-247, Kluwer Academic Publishers. xx, 96

[WIL 11] Willmott P.
An Introduction to Synchrotron Radiation: Techniques and Applications. John Wiley & Sons, 2011. 9

[XU 12] Xu Z., Wen W., Zhai T.
Effects of Pore Position in Depth on Stress/Strain Concentration and Fatigue Crack Initiation. *Metallurgical and Materials Transactions A*, vol. 43, n° 8, 2012, p. 2763-2770, Springer US. 107, 119

[YAO 12] Yao J., Taylor J.
Characterisation of intermetallic particles formed during solution treatment of an Al-7Si-0.4Mg-0.12Fe alloy. *Journal of Alloys and Compounds*, vol. 519, n° 0, 2012, p. 60-66. 17

[YI 03] Yi J., Gao Y., Lee P., Flower H., Lindley T.
Scatter in fatigue life due to effects of porosity in cast A356-T6 aluminum-silicon alloys. *Metallurgical and Materials Transactions A*, vol. 34, n° 9, 2003, p. 1879-1890, Springer-Verlag. 39, 120

[YI 06] Yi J., Lee P., Lindley T., Fukui T.
Statistical modeling of microstructure and defect population effects on the fatigue performance of cast A356-T6 automotive components. *Materials Science and Engineering: A*, vol. 432, n° 1-2, 2006, p. 59-68. 18

[ZEN 14] Zeng L., Sakamoto J., Fujii A., Noguchi H.
Role of eutectic silicon particles in fatigue crack initiation and propagation and fatigue strength characteristics of cast aluminum alloy A356. *Engineering Fracture Mechanics*, vol. 115, n° 0, 2014, p. 1-12. 36

[ZHA 92] Zhang Y. H., Edwards L.
The effect of grain boundaries on the development of plastic deformation ahead of small fatigue cracks. *Scripta Metallurgica et Materialia*, vol. 26, 1992, p. 1901-1906. 34

[ZHA 00a] Zhai T., Wilkinson A., Martin J.
A crystallographic mechanism for fatigue crack propagation through grain boundaries. *Acta Materialia*, vol. 48, n° 20, 2000, p. 4917-4927. 35, 50

[ZHA 00b] Zhang, Chen, Poirier
Effect of solidification cooling rate on the fatigue life of A356.2-T6 cast aluminium alloy. *Fatigue & Fracture of Engineering Materials & Structures*, vol. 23, n° 5, 2000, p. 417-423, Blackwell Science Ltd. 39

[ZHU 06] Zhu X., Shyam A., Jones J., Mayer H., Lasecki J., Allison J.
Effects of microstructure and temperature on fatigue behavior of E319-T7 cast aluminum alloy in very long life cycles. *International Journal of Fatigue*, vol. 28, n° 11, 2006, p. 1566-1571. Third International Conference on Very High Cycle Fatigue (VHCF-3). 94

[ZOU 89] Zou J., Tynelius K., Kim D., Shivkumar S., Apelian D.
Evaluation of feeding characteristics in cast aluminum alloys. Closset B., Ed., *Production and Electrolysis of Light Metals*, Proceedings of Metallurgical Society of Canadian Institute of Mining and Metallurgy, p. 87-99 Pergamon, Oxford, 1989. 19

FOLIO ADMINISTRATIF

THÈSE SOUTENUE DEVANT L'INSTITUT NATIONAL DES SCIENCES APPLIQUÉES DE LYON

NOM : SERRANO MUNOZ DATE de SOUTENANCE : le 28 Novembre 2014

Prénoms : Itziar

TITRE : Influence of casting defects on the fatigue behaviour of an A357-T6 aerospace alloy (Étude de l'influence des défauts de moulage sur le comportement en fatigue de l'alliage aéronautique A357-T6)

NATURE : Doctorat Numéro d'ordre : 2014-ISAL–0117

École doctorale : ED Matériaux

Cote B.I.U. - Lyon : T 50/210/19 /

et bis CLASSE :

RÉSUMÉ : L'excellente coulabilité, les coûts de production relativement bas, et leurs ratios poids/résistance mécanique élevés des alliages de fonderie Al-Si-Mg une des solutions les plus intéressantes dans le secteur automobile ainsi que l'aérospatiale. Toutefois, il est bien connu que la durée de vie de ces composants moulés à haut nombre de cycles ($10^5 < N_f < 10^7$ cycles) résulte sévèrement réduite lorsque des défauts de fonderie (notamment pores et oxydes) sont débouchants et/ou subsurfaciques. Ces défauts concentrent les contraintes et peuvent considérablement réduire la période d'incubation de fissures de fatigue en fonction de leur taille, forme et des caractéristiques microstructurales du matériau. Les défauts de fonderie dénommés *internes* sont d'un intérêt particulier à ce travail car l'application de coefficients de sécurité ne tient pas compte de leur distance à la surface. C'est-à-dire, les défauts internes (correspondant au cas où l'emplacement du défaut permettrait les fissures d'amorcer et propager essentiellement sans interaction avec l'air ambiance) et les défauts de surface (ceux qui sont placés à la surface et en contact direct avec l'air ambiance) vont également nuire la durée de vie des composants moulés.

Le suivi de fissures surfaciques (effectué en éprouvettes macroscopiques de traction) indique que la présence d'un microdéfaut avec une taille supérieure à celle de petites fissures microstructurelles ($\sqrt{A} = 500$ μm, contrôlée par le SDAS) produit une remarquable réduction de la durée vie. En revanche, la durée de vie n'est pas affectée lorsqu'un défaut plus petit ($\sqrt{A} = 280$ μm) en présent à la surface car l'amorçage et les premiers stades de propagation sont encore influencés par le SDAS.

Les essaies en torsion pure montrent que la morphologie des surfaces de rupture est fortement influencée par le niveau de contrainte. En général, le comportement en torsion correspond à des périodes à l'amorçage relativement réduits (par rapport à la traction). Cet amorçage et multisite et plusieurs fissures peuvent évoluer simultanément, la rupture finale se produisant par liaison de certaines de ces fissures. La propagation de fissures en torsion est contrôlée par la cristallographie et les retassures ne semblent pas être des sites de nucléation préférentiels, contrairement à ce qui a été observé en fatigue uni-axiale.

Les durées de vie obtenues en utilisant des spécimens macroscopiques contenant défauts artificiel internes de $\varnothing_{eq} \approx 2$ mm sont similaires à celles obtenues avec un matériau de référence. L'amorçage de fissures internes a été rarement observé lors d'essais fatigue in situ caracterisés par tomographie synchrotron. Les images tomographiques montrent que, dans le cas de la propagation interne, les fissures ont une propagation cristallographique alors que les fissures surfaciques se propagent sans influence apparente de l'orientation cristalline locale (mode I). La vitesse de propagation des fissures internes est très inférieure à celle des fissures se propageant à partir de la surface. Enfin, les simulations EF obtenues en utilisant les images en 3D indiquent que le paramètre K_t est capable d'indiquer le grade de sévérité d'un pore, mais seulement quand les défauts sont d'une taille similaire.

MOTS-CLÉS: alliage d'aluminium moulé A357-T6, fissures de fatigue courtes, défaut de fonderie surfaciques et internes, essais de fatigue en traction ou en torsion, simulations par éléments finis, techniques de tomographie, EBSD.

Laboratoire(s) de recherche :

MatéIS - UMR CNRS 5510 - INSA de Lyon
25 avenue Jean Capelle
69621 Villeurbanne Cedex (FRANCE)

Directeur(s) de thèse : Jean-Yves BUFFIERE (Professeur) et Catherine VERDU (Professeur)

Président du jury : Yves NADOT (Professeur)

Composition du jury : Veronique AUBIN (Professeur, Rapporteur)
Myriam BROCHU (Maître de Conférences, Rapporteur)
Yves NADOT (Professeur, Examinateur)
Yves GAILLARD (Ingénieur, Examinateur)